HIGH PRECISION TIMING

Dissertation

zur

Erlangung des Doktorgrades (*Dr. rer. nat.*)

der

Mathematisch–Naturwissenschaftlichen Fakultät

der

Rheinische Friedrich–Wilhelms–Universität Bonn

vorgelegt von

Eleni Graikou

aus

Katerini, Griechenland

Bonn 2018

Angefertigt mit Genehmigung der Mathematisch-Naturwissenschaftlichen Fakultät
der Rheinischen Friedrich–Wilhelms–Universität Bonn

1. Referent: Prof. Dr. Michael Kramer
2. Referent: Prof. Dr. Norbert Langer
Tag der Promotion: 19.12.2018
Erscheinungsjahr: 2019

Diese Dissertation ist auf dem Hochschulschriftenserver der ULB Bonn unter
http://hss.ulb.uni-bonn.de/diss_online elektronisch publiziert

RHEINISCHEN FRIEDRICH–WILHELMS–UNIVERSITÄT BONN

Abstract

of the dissertation: "High precision timing"

by Eleni Graikou

for the degree of

Doctor rerum naturalium

Pulsars are highly magnetised, fast spinning neutron stars (NSs), formed after a supernova explosion. The core of their progenitor star, which is around 1–2 $M_\odot$, is compressed to a radius of only $\sim$10 km, making them one of the most compact objects observed. From each magnetic pole a highly magnetised beam of electromagnetic radiation is emitted, the exact emission mechanism of which is not yet fully understood. Since the magnetic axis is generally not aligned with the spin axis, the emission beam sweeps across the sky. In the cases that the emission beam crosses the line of sight of the telescope, once every rotation we detect a pulse of radiation.

The majority of science that we can do with pulsars comes from pulsar timing. With timing we compare the observed pulse arrival times to a model that contains the rotational, astrometric, interstellar medium (ISM) related, and binary (if the pulsar belongs to a binary system) properties of the pulsar. The goal is to create a model that correctly described the behaviour of the pulsar. Millisecond pulsars (MSPs), which are pulsars with spin periods of only a few milliseconds, are the ideal objects to apply timing, since their rotational stability on long timescales approaches that of atomic clocks.

Probably one of the most interesting applications of pulsar timing is the detection of gravitational waves (GWs) in the nHz regime. Main sources of these low frequency GWs are inspiraling super-massive black hole binaries (SMBHBs). GW signal can be from individual sources or from the gravitational wave background (GWB) made from the superposition of the cosmic population of the SMBHBs. A GW signal can be detected as a correlated red noise signal in the timing residuals of a pulsar timing array (PTA), formed by timing stable MSPs, almost homogeneously distributed on the sky. Since the GW signal is very weak, in order to make a detection, a timing stability of around 100 ns over a timescale of 5 years is required for PTA pulsars. The main source of red noise in pulsars that should be modeled, for achieving this high timing precision, is chromatic variations produced by perturbations on the ISM. In Chapter 3 we investigate the usage of Effelsberg and MeerKAT high-frequency receivers (both those presently used and those being commissioned) for measuring DM variations and increasing the PTA sensitivity to continuous GWs and GWBs. Six years of Effelsberg EPTA observations at 1.4 and 2.6 GHz are reviewed in this chapter, the performance of which is used to select the sources that will be observed at 4.8 GHz. 14 pulsars have been detected at these high frequencies: for the seven with the longest data set we further reported signal-to-noise ratio values, flux density measurements, and DM variation measurements. We discuss the potential of complementing the existing EPTA data set with receivers that are now in a commissioning stage. We concluded that the combination of Effelsberg 1.4 GHz and MeerKAT S-band observations, for flux density spectral indices $\lesssim -1.6$, provides the best precision for

DM variation measurements as well as the lowest uncertainty on the time-of arrival corrected from DM variations. Moreover, for the currently used Effelsberg observing combination for measuring DM variations existing from the 21 cm and the 11 cm receiver, an addition of 6.7 years for a GWB and another 80 years of observations for continuous GWs, on the top of 10, are needed in order to achieve the same sensitivity as we expect for the Effelsberg 21-cm combined with MeerKAT 11-cm observations.

In Chapter 4, we performed timing analysis of the PSR J1933−6211, a 3.5-ms pulsar with a WD companion. The observations used in the analysis were conducting with the Parkes radio telescope in Australia. The goal of this project was to reveal the nature of the WD companion. Based on scintillation and timing analysis we concluded that the pulsar has, as have very few other fully recycled MSPs, a CO companion. The formation of this system can be explained with an intermediate-mass X-ray binary. In this case the transfer of masses started when the WD companion was still in main sequence stage and thus the transfer of mass through a Roche-lobe overflow lasted long enough time scale to fully recycle the pulsar.

In Chapter 5 the relativistic effect, geodetic precession is studied in PSR B1913+16. This effect has as a result the spin axis to precessing about the total angular momentum axis. This causes the line of sight to cut different parts of the emission beam through time, making the total intensity profile and the polarisation properties to gradually change following a periodicity of around 300 years (for this pulsar). By studying these variations we can derive the emission geometry of the system. For our analysis we used observations taken with Arecibo and Effelsberg radio telescope at observing wavelength of 21 cm. The effect of geodetic precession on the separation and the relative amplitude of the two main pulse components were obvious. After applying two independent to each other models, one fitted to the total intensity and the other to our polarisation data, we concluded that the inclination angle of the PSR B1913+16 system is 132.9° and the misalignment angle $\sim$21°, and also that the emission beam is probably hollow-cone with the magnetic axis not being positioned at the center of the beam but shifted around 10° from the center.

Acknowledgment

This thesis would not be possible without the valuable help of many people that I will attempt to mention all below.

I would really want to thank Michael Kramer for all the support and help that he provided me all these years, for reading my thesis very fast and for creating the Fundamental physics group, in which I was lucky to be a member. This group is an environment that develops students into scientists, most particular the next generation of pulsar astronomers.

I would also like to thank my two advisors, David Champion and Joris Verbiest for all the support, encouragement, and guidance that they gave me all these years. Despite their very busy schedules, they always found time to answer all my questions and tolerated my mistakes. They were my motivation that kept pushing me further, without their help my PhD would not be completed.

Besides my advisors, I would like to thank all the members of the fundi group that are very willing to share their knowledge about pulsars and for creating a fun working environment. I want to particularly mention Greeegoryyy Desvignes, Paulo Freire, Ramesh Karuppusamy, Axel Jessner, and Stefan Osłowski. Also special thanks to James McKee and Nataliya Porayko who helped in proof-reading part of this thesis.

I am grateful to Kira Kühn and Le Tran for helping me with all the paper work that I had to do, so that I can only focus on my work.

I also would like to acknowledge the support of the technical staff of Effelsberg. They really made MANY of my observations a lot easier and in some cases they helped solved any problem I had right away.

I would also like to thank the officemates that I have had all these years: Carolina!, Ancor!, Philip!, Pablo!, Marina!, Alice!, Andrew!, Jason!, and last but not least Natasha!. She is the best officemate that I could ever ask for. Also, I would like to thank all the other students of the fundi group for all the scientific discussions, but also all the fun that we had. I would more particularly mention Cherry!, Mary!, Tilemachos!, Ale-Ale-Alessandro!, Henning!, Nicolas!, and especially Patrick!. And other students from the institute Hans!, WonJu!, Fateme!, Maitraiyee!, and Vica!.

A big thanks to my family, my father, my mother, and my sister Georgia. Without their guidance and support I would not have been able to start a PhD. They motivated

me to pursue my dreams even though that meant that I had to go far away from them.

I want also to thank Joey for all the support that he gave me all these years, and all the effort that he put for making me a better person.

Last but not least I want to thank my first supervisor John Seiradakis. I am feeling very lucky that I have worked with him. If it was not for him, I would not be here today.

Contents

List of Figures

List of Tables

Frequently Used Symbols

ADC	Analogue-to-Digital Converters
BAT	Barycentric arrival time
BB	Binary system barycentre
BH	Black hole
BIPM	Bureau International des Poids et Mesures
BMSP	Binary millisecond pulsars
CPSR2	Caltech Swinburne Parkes Recorder 2
CE	Common envelope
CHIME	Canadian Hydrogen Intensity Mapping Experiment
CO	Carbon-oxygen
CO WD	Carbon-oxygen white dwarf
DM	Dispersion measure
DNS	Double neutron star
EoS	Equation of state
EPTA	European pulsar timing array
FAST	Five-hundred-meter Aperture Spherical radio Telescope
FFT	Fast Fourier Transform
GR	General relativity
GW	Gravitational wave
GWB	Gravitational wave background
He GW	Helium white dwarf
HMXB	High-mass X-ray binary
IMXB	Intermediate-mass X-ray binary
IPTA	International pulsar timing array
ISM	Interstellar medium
JPL	Jet Propulsion Laboratory
LIGO	Gravitational-Wave Observatory
LISA	Laser Interferometer Space Antenna
LMXB	Low-mass X-ray binary
LNA	Low-Noise Amplifier
LOFAR	Low-Frequency Array
MCMC	Markov-chain Monte-Carlo
MJD	Modified Julian Dates
MS	Main sequence
MSP	Millisecond pulsar
NANOGrav	North American Nanohertz Observatory for gravitational waves
NIST	National Institute of Standard and Technology
NS	Neutron star
OMT	Ortho-mode Transducers
ONeMg	Oxygen-neon-magnesium
ONeMg WD	Oxygen-neon-magnesium white dwarf
PFB	Polyphase filter-bank
PK	Post-Keplerian
PPA	Polarisation position angle
PPTA	Parkes pulsar timing array
PTA	Pulsar timing array
RFI	Radio frequency interference
RFM	Radius-to-frequency mapping
RLO	Roche-lobe overflow
RM	Rotation measure
RMS	Root-mean-square timing residuals
RVM	Rotating-vector model
SAT	Site arrival times
SEP	Strong equivalent principle
SKA	Square Kilometre Array
SSB	Solar System barycentre
SSE	Solar System ephemeris
SMBH	Super-massive black hole
SMBHB	Super-massive black hole binary
S/N	Signal-to-noise ratio
SN	Supernova
SSB	Solar System barycenter
TAI	International Atomic Time
TCB	Barycentric Coordinate Time
ToA	Time of arrival
TT	Terrestrial time
UTC	Universal Coordinated Time
VLBI	Very-Long-Baseline Interferometry
WD	White dwarf

Chapter 1

Introduction

Contents

1.1 The discovery of pulsars

In 1934, only two years after the discovery of neutrons, Baade & Zwicky (1934) proposed that the outcome of a supernova explosion can be a very compact stellar remnant with density up to 10^{15} g cm^{-3}. The interior would be composed mainly from neutrons. Colgate & White (1966) predicted that the remnant would reach spin frequencies of tens to hundreds of Hz and would have strong magnetic field, due to conservation of magnetic flux and angular momentum. Later, in 1967, only a few months before the discovery of pulsars, Pacini (1967) showed that the strong magnetic field of a spinning neutron star (NS) could result in magnetic dipole emission, energetic enough to energise the surrounding remaining nebula.

Despite the growth of radio astronomy since the 1930's, more than 30 years passed until the discovery of pulsars. That was partly due to the fact that radio astronomers were not expecting to find rapid period fluctuations in the signals from any celestial source. Indeed, most radio receivers were designed to reject or smooth out impulsive signals and to measure only steady signals, averaged over several seconds of integration time.

The first pulsar was discovered unexpectedly, during a research investigation of the interplanetary scintillations carried out by Anthony Hewish and his student Jocelyn Bell at the Mullard Radio Astronomy Observatory in Cambridge. The Interplanetary Scintillation Array that was used for this research was operating at long radio wavelengths (3.7 m). At this wavelength, radio sources with very small angular diameters are affected by interplanetary scintillation. In July 1967, a month after the beginning of recording, Jocelyn Bell noticed large signal fluctuations coming from a specific location in the sky. When these fluctuations reappeared at the same sidereal time, there was no doubt that they had celestial origin. A recorder with an even faster response time was used and in November 1967, regular pulses with a period of $\sim$1.337 s were observed.

In February 1968 the discovery of this first pulsar, now known as PSR J1921+2153 (B1919+21), was announced by Hewish et al. (1968). In this paper, also, an initial interpretation about the nature of this source was presented. Hewish et al. (1968) concluded that the source lies outside the Solar System, since it was appearing at the same sidereal time every day, the observations did not show any evidence of parallax, and a frequency dispersion withing the 1-MHz band is observed. Also, based on the regularity and the rapidity of the pulsations, they argued that the source must be a radially oscillating condensed star, presumably either a white dwarf (WD) or a NS. The term "pulsar" (standing for PULSating stAR) was given to this newly discovered class of objects. By the end of the same year, three more pulsars were discovered with similar properties (Pilkington et al., 1968). In 1974 Hewish was awarded a Nobel prize in physics for this discovery.

The discovery of pulsars triggered a series of observations from all the large radio observatories at the time. By the end of 1968 more than 100 papers either reporting new discoveries or investigating pulsar properties were published. Major efforts were made to understand the nature of pulsars by, for example, observing their polarization properties, performing multi-frequency observations, and investigate their profiles. These observations challenged theoreticians to propose new models to explain the pulsar emission.

Three main mechanisms were proposed to explain the regular pulsed emission from pulsars: pulsating (Hewish et al., 1968; Burbidge, 1968), orbiting (Burbidge, 1968; Saslaw, 1968), and rotating (Ostriker, 1968; Gold, 1968) WDs or NSs. The pulsating WD and NS, and rotating WD scenarios were ruled out after the discovery of the Vela (J0835$-$4510 (B0833-45), Large et al., 1968) and Crab pulsars (J0534+2200 (B0531+21), Staelin & Reifenstein, 1968), since they have pulse periods of only $\sim$89 ms and $\sim$33 ms, respectively. According to theoretical models WDs and NSs could oscillate with periods as short as 100 ms, and $\sim$1 s (Thorne & Ipser, 1968),

respectively. Rotating WDs have also been excluded since for rotation periods of less than a second the centrifugal forces would disrupt their outer layers.

Orbiting WD and NS scenarios ruled out after an decrease in the pulsation rate was observed (Davies et al., 1969, and many others since). WD and NS systems should gradually lose orbital energy through gravitational-wave (GW) emission resulting in a gradual decrease of orbital period, which was in contradiction with the observations.

Rotating NSs remained as the only plausible explanation. Following a prediction by Pacini (1967) for the Crab pulsar, Gold (1968) was the first to identify pulsars as rotating NSs. According to his model the very strong magnetic fields, combined with high spin frequencies, result in the creation of an ionized magnetosphere which co-rotates with the NS. When the co-rotation reaches the speed of light, the plasma will escape the magnetosphere creating the emission beam. Furthermore, he predicted a decreasing spin period (due to energy loss in the form of magnetic dipole radiation), the potential existence of faster pulsars, and the association between supernova remnants and pulsars (Gold, 1969). Observations verified all his predictions. Today, even though the exact emission mechanism is not clear, there is no doubt that pulsars are rotating NSs.

1.2 The nature of pulsars and the emission mechanism

Pulsars are formed during a core-collapse supernova event. Their formation path starts with a massive main sequence (MS) star of around 8 to 15 $M_\odot$ (Woosley & Weaver, 1986; Carroll & Ostlie, 2006). As the star evolves, it fuses increasingly heavy nuclei in its core: H to He; He to C, N, O; C, N, O to Si. Finally, the fusion of the Si core result in the creation of a $^{56}_{26}$Fe rich core.

The very high temperatures reached during the nuclear fusion, give to the photons enough energy to destroy heavy nucleii; like iron, in protons and neutrons, a process known as photo-disintegration. The fusion of ^{56}Fe is an endothermic process, resulting in the removal of thermal energy, and a drop of the core radiation pressure. The electrons that supported, so far, the star from collapsing, are now captured by the atomic nuclei, and the protons that are formed by photo-disintegration. The core, having no process by which to resist gravity, starts collapsing until it reaches the Chandrasekhar mass ($\simeq 1.4\,M_\odot$). When the density of the inner core exceeds 8×10^{14} g cm^{-3}, the strong force becomes repulsive, resulting in a rebound of the in-falling matter of the outer layers. The shock wave expels the majority of the star's mass, leaving behind an ultra-dense core. The energy that is released from an explosion like this can reach values of $\sim10^{10}$ $L_\odot$ (Arnett, 1996), equivalent to the brightness of an entire galaxy. This creation scenario can be also verified from the multiple supernova remnants found to be associated with the remaining products of the explosion: pulsars (e.g. Staelin & Reifenstein, 1968; Strom, 1987; Frail & Kulkarni, 1991).

If the mass of the remaining core is less than the Tolman−Oppenheimer−Volkoff limit (Tolman, 1939; Oppenheimer & Volkoff, 1939), the collapse of the star is prevented by the neutron degeneracy pressure, leaving a NS behind. In the case where the mass is above this limit, the star is collapses further under the pressure of gravity, creating a *black hole* (BH).

NSs are highly magnetized, extremely compact objects. The remaining mass of the progenitor star, after the supernova explosion, is around $1-2$ $M_\odot$, and is contained within a radius of only $\sim$10 km (Lattimer & Prakash, 2001). The density of the star's interior is 6.7×10^{14} g cm^{-3}, comparable to nuclear density. The exact structure in the interior can be determined from the equation of state (EoS). Unfortunately, the EoS for NSs is still unclear, which prevents us from knowing their basic physical properties, like the interior mass or the radius (see Section 1.9.1).

Pulsars are a subcategory of NSs. Due to conservation of angular momentum, during the collapse of the progenitor star, they are born with spin periods ∼0.5 s. Their surface magnetic fields are strong, on the order of $\sim 10^{12}$ G. This strong magnetic field has as a result that the Lorentz force at the surface of pulsars is stronger than gravity leading to plasma extraction from the surface of the star. The plasma that escaped creates the *pulsar magnetosphere*, which co-rotates with the pulsar. When the speed of the plasma in the magnetosphere reaches the speed of light, in a distance so-called "light cylinder", the co-rotation stops and the plasma escapes the pulsar's magnetosphere following the open field lines. This open field line region, which is centred on the magnetic axis, therefore defines the emission beam. Since the magnetic axis is misaligned with the rotation axis, when pulsar's emission beam sweeps Earth's line of sight, once every rotation, we detect a periodic signal from the pulsar. This basic pulsar model is visualized in Fig. 1.1 and is called the "lighthouse model".

The exact mechanism that creates pulsar radiation is still unknown. The emission process is concluded to be coherent (e.g. maser) based on two facts: the polarization and the emission intensity. Pulsar emission is strongly polarized, which was already observed years before the discovery of pulsars, from observations of Crab nebula (Oort & Walraven, 1956). Polarization can only be explained from a process that creates radiation with some order, something that is not true for thermal radiation. The other fact that supports coherent emission is that a pulsar's emission intensity correspond to a brightness temperature that is orders of magnitude higher than the maximum possibly achieved from a thermal black body.

1.3 Pulsar model

Despite the persistent efforts from theoreticians and observers, the exact emission mechanism of pulsars is still unclear. For this reason, an empirical model was formed to explain the origin of the emitted radiation from pulsars. For this simplified model it is assumed that the magnetic field of the pulsar is purely dipolar and the pulsar is in a vacuum. In the sections below we will express some of the basic pulsar properties (spin-down luminosity, age and magnetic field) using only two observable pulsar properties: the spin period (P) and the first spin period derivative ($\dot{P}$). This section is based on the discussion of Lorimer & Kramer (2012).

1.3.1 Spin evolution

Any object, that rotates, with magnetic fields that are asymmetric about the rotation axis must radiate energy and therefore lose angular momentum. Thus, the increase of the spin period (which was observed in pulsars soon after their discovery) was expected. Pulsar spin periods gradually and steadily increase. A typical $\dot{P}$ is found to be $\sim 10^{-15}$ s s^{-1}.

If we attribute the loss of kinetic energy ($\dot{E}$) only to this magnetic dipole radiation, then:

$$\begin{aligned} \dot{E} &= -\frac{2}{3c^3} m^2 \sin^2\alpha \left(\frac{2\pi}{P}\right)^4 \\ 4\pi^2 I \dot{P} P^{-3} &= -\frac{2}{3c^3} m^2 \sin^2\alpha \left(\frac{2\pi}{P}\right)^4, \end{aligned} \tag{1.1}$$

where c is the speed of light, m is the moment of the magnetic dipole[1], α the angle between

[1]For a uniformly magnetized sphere with radius R and surface magnetic field strength B; $m = BR^3$

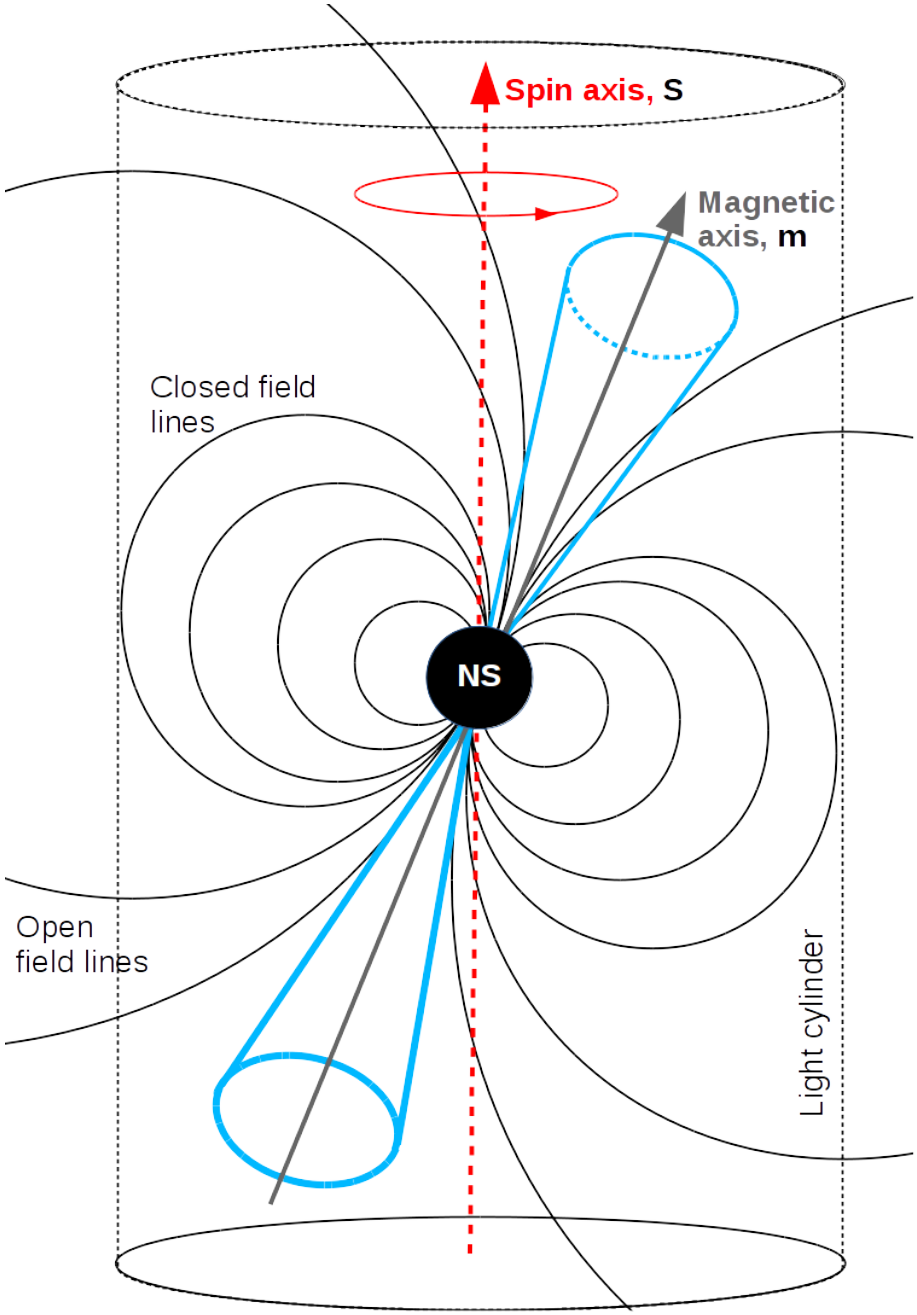

Figure 1.1: A simplified pulsar model. The NS, in the centre, is spinning about the spin axis **S**. The closed (confined inside the light cylinder) and open field lines, across which the escaping plasma travels, are presented with solid black lines. The conical emission beam (in blue) is centred on the magnetic axis (**m**) and is misaligned with respect to the spin axis. In the cases that the emission beam sweeps the line of sight from Earth we can detect a periodic signal from the pulsar. The figure is based on Fig. 3.1 from Lorimer & Kramer (2012).

spin and magnetic axis and I is the moment of inertia[2].

Based on Eq. 1.1 the rotational frequency can be, generally, expressed as:

$$\dot{\nu} = -K\nu^n, \tag{1.2}$$

where K is a constant, ν is the spin frequency, and n is the *braking index*[3]. Based on the assumptions above, the braking index is expected to be equal to 3. However, the magnetic dipole radiation is very probable to not be the only responsible for the kinetic energy loss. Other radiation processes like mass loss (pulsar wind) and quadrupole radiation, may exist, which in themselves would result in braking indices of 1 and 5, respectively.

Observationally we can measure braking indices only if the spin period, and its first and second derivatives are accurately known. Unfortunately, these values are difficult to measure, since short-term timing irregularities like glitches and long-term irregularities like timing noise contaminate the systematic trend of the spin period. Consequently, only, nine pulsars have their braking indices reliably measured, with values ranging between 0.9(2) (Espinoza et al., 2011) and 3.15(3)[4] (Archibald et al., 2016). This implies, that magnetic dipole radiation by itself cannot explain the spin down behavior of pulsars, although it is a close approximation.

1.3.2 Ages of pulsars

The age of a pulsar is a useful property but is hard to be measured directly through observations, if we exclude, of course, the cases where the pulsar is associated with a supernova remnant. Assuming again the kinetic energy loss is only due to magnetic dipole radiation and that K is a constant and $n \neq 1$, we can estimate the age of the pulsar by integrating Eq. 1.2:

$$T = \frac{P}{(n-1)\dot{P}}\left[1 - \left(\frac{P_0}{P}\right)^{n-1}\right], \tag{1.3}$$

where P_0 is the birth spin period. If we assume that $P_0 \ll P$ and $n = 3$ then we simplifies to what is called the *characteristic age*:

$$\tau_c = \frac{P}{2\dot{P}}, \tag{1.4}$$

which can be calculated very easily from P and $\dot{P}$, but, because of our assumptions, it is only an estimate of the true age, and in many cases fails to accurately predict the true age of pulsars, since our assumptions that the initial spin period is negligible and there is purely magnetic dipole radiation, are not completely true. Two pulsars: the Crab pulsar and J1801−2451 (B1757−24), both associated with supernova remnants are given as examples. For the Crab pulsar the characteristic age is ∼1238 yr, comparable to the supernova age ∼950 yr, but for J1801−2451 the characteristic age is ∼16 kyr, significant smaller than the true age 170 Myr (Gaensler & Frail, 2000).

1.3.3 Magnetic field strength

Like the age of pulsars, the strength of the magnetic field is also hard to measure through observations, except in cases where there is a detection of electron cyclotron resonance features

[2] $I = kMR^2$, where k = 0.4 and M and R are the mass and the radius of the pulsar respectively. For typical values M = 1.4 $M_\odot$ and R = 10 km, this implies $I = 10^{45}$ g cm^{-2}.

[3] $n = -\nu\ddot{\nu}/K\dot{\nu}^2$

[4] In the parentheses is the 1-σ uncertainties in the least-significant digit.

in binary X-ray pulsars (Truemper et al., 1978), or isolated NSs (Bignami et al., 2003). Thus, for radio pulsars we can only have an estimate of the magnetic field strength from applying the pure magnetic dipolar radiation model. From Eq. 1.1 we then get:

$$B = \sqrt{\frac{3c^3}{8\pi^2}\frac{I}{R^6 \sin^2\alpha} P\dot{P}}. \tag{1.5}$$

Characteristic measurements of the magnetic field strength can be obtained assuming $I = 10^{45}$ g cm^2, $R = 10$ km and $\alpha = 90°$. For typical NS properties we derive a magnetic field of 10^{12} G (12 orders of magnitude larger than the Earth's magnetic field). These values are also confirmed from the X-ray NS observations, mentioned above.

1.4 The pulsar population

Today, 50 years after the discovery of the first pulsar, there are 2627 pulsars known (based on the ATNF Pulsar Catalog v.1.57, Manchester et al., 2005). The majority of them are found isolated, with $P \gtrsim 0.1$ s, $\dot{P} \gtrsim 10^{-17}$ s s^{-1}, typical magnetic field strength 10^{12} G and characteristic age 10^7 yr. In this thesis we will refer to these as the *canonical pulsars*. It is very common in pulsar astronomy to demonstrate the, very precise, measurements of the spin period and spin period derivative in a "P–$\dot{P}$ diagram" (Fig. 1.2). In this diagram canonical pulsars occupy the upper right part.

However, in the lower right part of this diagram there is another population that is distinguished from the canonical one. Pulsars that belong to this subcategory have $P \lesssim 0.1$ s, $\dot{P} \sim 10^{-20}$ s s^{-1}, typical magnetic field of 10^8 G, characteristic age of 10^9 yr, and the majority of them belong to binary systems. These pulsars have short periods, not because they young in age but because they went through a recycling process. This formation process gives them their name: *recycled pulsars*. Especially, the recycled pulsars that have periods of a few milliseconds, are called *millisecond pulsars* (MSPs). The first MSP was discovered in 1982 (PSR B1937+21, Backer et al., 1982), much later than the first canonical pulsar. In the section below, the different formation paths that recycled pulsars may follow, determined by their different initial binary conditions, are presented.

1.4.1 Formation of recycled pulsars

Pulsars are formed in supernova explosions as explained in Section 1.2 ad as the remnant is compacted into a very small radius, we expect pulsars to be born with short spin periods and hight spin-down rates. This expectation is verified by the observations. As we see in Fig. 1.2, pulsars that are associated with a supernova remnant occupy the upper left part of the canonical pulsar population. As rotational energy is lost their spin periods increase and they move gradually to the right part of the P–$\dot{P}$ diagram.

MSPs, on the other hand, are spinning rapidly but their spin-down rates are very small. We expect small spin periods to be associated with young pulsar ages, something that is not true for MSPs. This "renewing paradox" can be explained by their formation mechanism. The story of every MSP starts with two MS stars. The most massive star of the two evolves first and explodes in a supernova, leaving a NS. Once the second star starts to evolve, mass accretes onto the NS, transferring angular momentum. This results in a spin-up of the NS (Alpar et al., 1982; Radhakrishnan & Srinivasan, 1982; Bhattacharya & van den Heuvel, 1991). All MSPs, are thought to go through that process, but the evolutionary stages that follow depend strongly on the mass of the companion and the initial orbital period of the system.

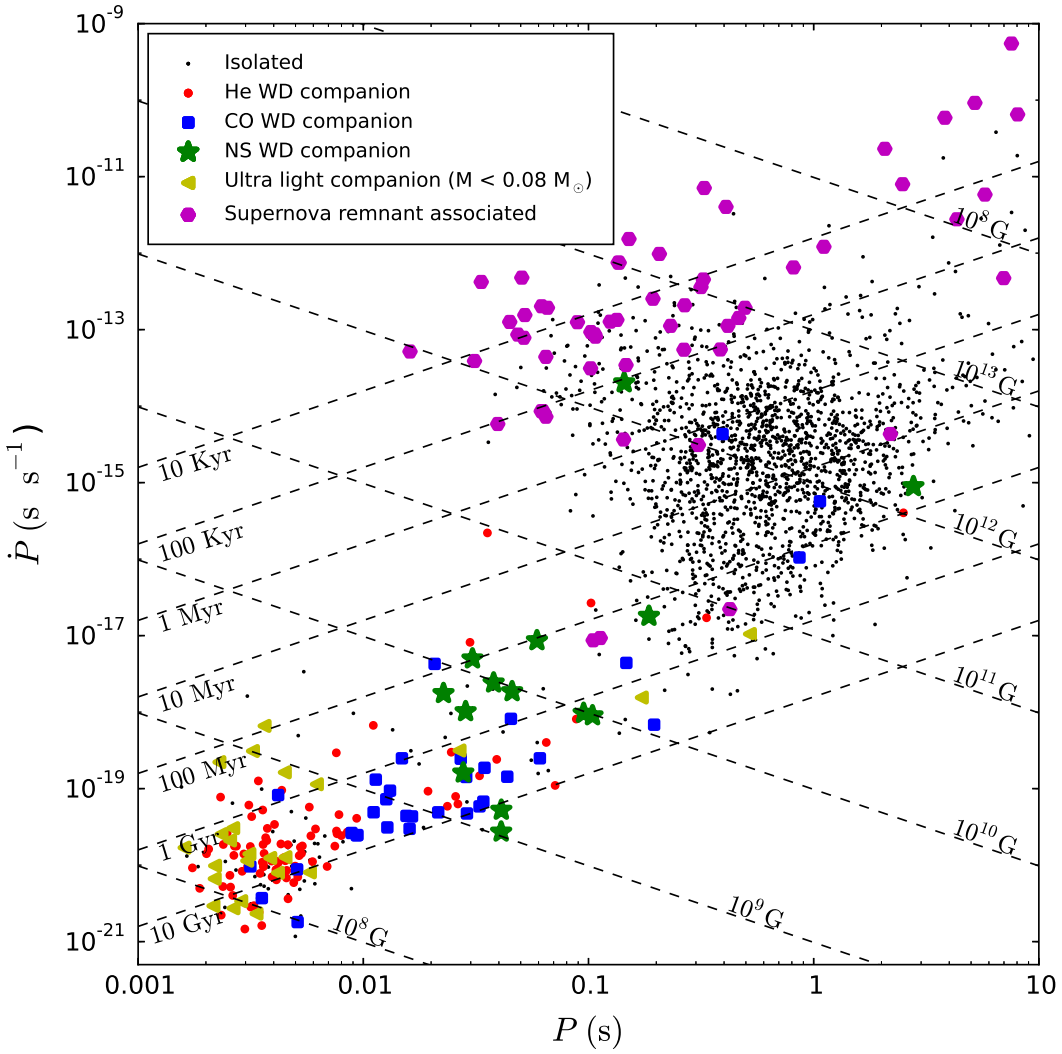

Figure 1.2: The period–period derivative diagram (P–$\dot{P}$ diagram) of the currently known pulsars (based on the ATNF Pulsar Catalog v.1.57, Manchester et al., 2005). Pulsars that belong to a binary system are presented with colored symbols. Lines of constant characteristic age (τ_c) and magnetic field strength B are also shown.

The mass and the nature of the companion, as well as the accretion history defines the type of system that we will end up with. This happens, firstly, because stars with different initial masses evolve on different time scales. The evolutionary time scale affects the mass accretion time scale and the frequency of the NS following recycling. Especially, more massive stars evolve faster, not allowing mass to accrete into the NS for a long time, resulting in a partly or "mildly" recycled NS. And secondly, because stars with different masses end in different evolution stages, collapsing into different types of degenerate stars.

In the case that the mass of the companion star is low ($\sim$1–2 $M_\odot$), the mass transfered to the NS happens in a stable mode via a Roche-lobe overflow (RLO) with a time scale of 10^7–10^9 yr. In that stage the system is observed as a low-mass X-ray binary (LMXB) (Tauris & Savonije, 1999). The X-ray emission originates from hot matter that is heated as it falls into the NS, and from thermal radiation from the hot NS and from occasional thermonuclear bursts on its surface (Lewin et al., 1997).

The result of this process is a fully recycled NS, with P $\sim$ 4 ms, and low magnetic field strength, compared to canonical pulsars ($\sim 10^8$ G), and an He WD companion. In the case that the mass of the companion star is $2 \lesssim M_\odot \lesssim 10$ an intermediate-mass X-ray binary (IMXB) is formed. In IMXBs the accretion mass stage is unstable and lasts for a short time scale $\sim 10^5$ yr. The transfer of mass happens through RLO or the system evolves through a CE. The result is a not fully recycled NS, with P $\sim$ 10 ms, a magnetic field strength of $\sim 10^9$–10^{11} G (which is stronger than LMXBs but weaker than canonical pulsars) and a massive carbon-oxygen (CO) or oxygen-neon-magnesium (ONeMg) WD companion. There are a few cases in which a fully recycled pulsar with a CO WD is observed (e.g. PSR J1614$-$2230 Demorest et al., 2010). The existence of these systems can be explained through an IMXB formed via a Case A RLO. In this case the mass transfer starts when the companion star is in the MS stage allowing the mass transfer to last significantly longer, recycling the NS fully. A example of a pulsar that belongs to this category will be discussed in Chapter 4.

In the case that the mass of the companion is $\gtrsim 12\ M_\odot$, a high-mass X-ray binary (HMXB) is formed. In this stage the NS is fed with the mass of the companion through a strong high-velocity stellar wind and/or RLO. The time scale of mass transfer can be as brief as 100 yr (Savonije, 1978). The mass transfer then follows a common envelope (CE) phase, in which the orbit shrinks rapidly due to orbital angular momentum loss. The end of the CE stage leaves us with a recycled NS and a naked He core of the component star. For one more time mass is transfered to the NS, reducing the mass of the He companion before the second supernova explosion. If the system survives, which depends on the orbital separation and the kick imparted onto the newborn NS (Flannery & van den Heuvel, 1975), a double NS (DNS) system is formed. The system will eventually collapse due to GW radiation forming a massive NS or a black hole. An event like this, has been detected through emission in γ-rays, X-rays, optical and infrared (Abdalla et al., 2017; Arcavi et al., 2017; Pian et al., 2017; Troja et al., 2017; Smartt et al., 2017; Kasen et al., 2017) as well as GWs (Abbott et al., 2017), with LIGO on 17 August 2017 (GW170817).

Due to the way that MSPs are formed, we observe many of them in binaries. However, the around 20% of them is found isolated. These pulsars are believed to be isolated because their companions have been ejected in the second supernova or destroyed or evaporated either because of X-ray irradiation when the NS was accreting mass or after the pulsar is formed due to a strong outflow of relativistic particles. The existence of ultra-light companions and planetary pulsar systems provided some evidence for these scenarios (e.g. Shaham, 1992; Tavani & Brookshaw, 1992).

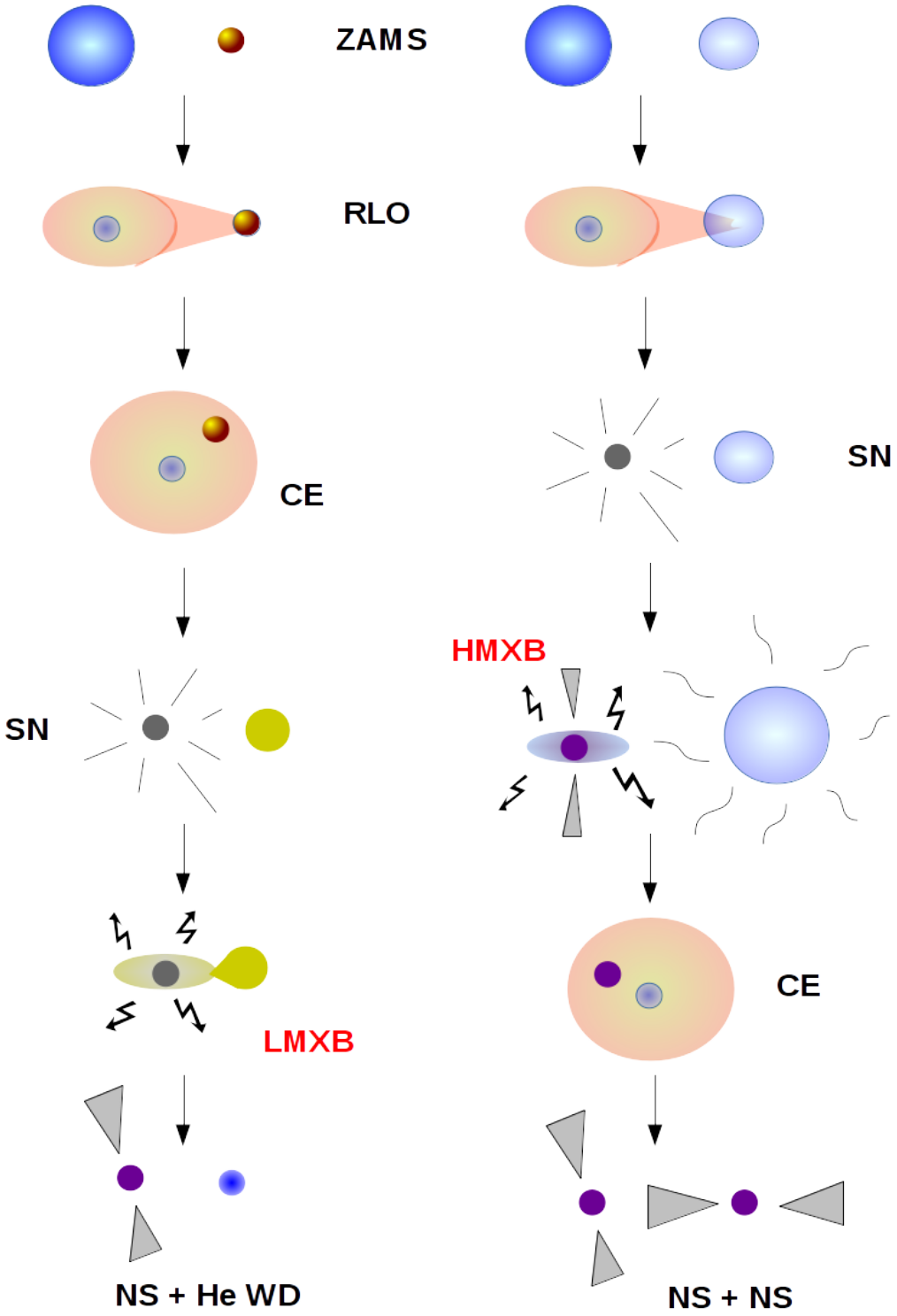

Figure 1.3: Two examples of creating a recycled NS, where the CE evolution takes a major play role. Other variations of these paths exists. Abbreviations: ZAMS–Zero age main sequence, RLO–Roche lobe overflow, CE–Common envelope, SN–supernova, LMXB–Low-mass X-ray binary, NS–Neutron star, He WD–Helium white dwarf, HMXB–High-mass X-ray binary, LMXB–Low-mass X-ray binary. The figure is based on Fig. 1 from Ivanova et al. (2013).

1.5 Observing pulsars

The first pulsars were detected at radio frequencies. Since then, pulsars have been detected in optical, near-ultraviolet, or near-infrared (Mignani, 2011), X-rays (Archibald et al., 2009; Papitto et al., 2013), and γ-rays (Abdo et al., 2009). While the radio emission is coherent, the optical–to X-ray emission comes from a combination of thermal and incoherent synchrotron radiation, and the γ-rays from incoherent curvature radiation. The observation and detection of pulsars at deferent frequencies will help us to better understand the emission mechanism of pulsars, which is still a mystery. However, optical and X-ray pulsars cover only a small fraction of the pulsar population. At the same time, with the launch of new γ-ray satellites, the γ-ray population has been growing fast but is still small compared to that of the radio pulsars. For these reasons, radio frequencies still remain the primary way to study pulsars.

The roughly 2700 radio pulsars that are known today share some basic characteristics, the most common of which is the broadband emission in a form of a periodic sequence of pulses. The study of the shape, polarization and flux density of these pulses provides us with useful information about the emission mechanism of pulsars.

1.5.1 Integrated profile

The individual pulses that are emitted in almost every pulsar rotation are often weak and, in the majority of pulsars, hardly detectable. However, there are some strong sources for which the observation of individual pulses is possible. The study of these cases has revealed that individual pulses exhibit a large diversity on morphological characteristics: *jitter noise* (Helfand et al., 1975; Cordes & Downs, 1985); on flux density: *giant pulses* (Rankin, 1970) and *nulling* (Backer, 1970); and on phase shifting: *drifting* (Drake & Craft, 1968).

Since individual pulses in most of pulsars are faint, for creating an *integrated pulse profile* it is necessary to coherent add hundreds of thousand of individual pulses. Although individual pulses reveal a large diversity, profiles are surprisingly very stable and unique for each pulsar at a specific observing frequency. We often identify a pulsar by just looking at its profile. This property allows us to attemp a technique that is called *pulsar timing*. This method (see Chapter 2) keeps track of the pulse emission time and compares it with the theoretical expectation. Pulsar timing, as will be explained in detail in Section 1.9, has many applications in fundamental physics and astrophysics, with two of the most important ones to be: testing gravitational theories and the detection of GWs in the nHz regime.

The integrated radio profiles typically cover 10° to 20° of rotational longitude, with some rare cases as narrow as 1° (e.g. PSR B1957+20, Fruchter et al., 1990) or as large as 360° (e.g. PSR B0826−34, Ashworth & Lyne, 1981). In the majority of cases the morphology of the profiles is very simple; mostly consisting of a very small number of components that can be modeled with simple Gaussians. Such a noise-free profile is called an *analytic template*. However, there are more complex cases with two or more components. Based on previous studies (Kramer et al., 1998), canonical pulsars and MSPs have not exhibited a significant difference in the number of components. The number and position of components have been associated with the structure of the emission beam (see Section 1.7). Thus, the study of the pulse shape is crucial to understand the emission mechanism of pulsars.

While the shape of the profile is very stable at specific observing frequencies, when we compare multi-frequency observations we see an evolution in shape. More precisely, for frequencies below $\sim$1 GHz the width and component separation increases at lower frequencies, a phenomenon that is more prominent in canonical pulsars (Kramer et al., 1999). This effect can be associated with changes in the emission height (Komesaroff, 1970). The empirical models

that have been created to explain this effect, and will be further discussed in Section 1.6.2, suggest that radio emission of different frequency leaves the magnetosphere at different heights (so called "frequency-to-radius mapping", Cordes, 1978).

In addition to frequency evolution (at radio frequencies), pulsars also exhibit profile evolution with time. These profile temporal changes are caused by either *mode changes* or the relativistic effect *geodetic precession*. Mode changing, first detected by (Backer, 1970) in PSR B1937+25, is the transition between two or even more different profile shapes. The origin of this effect is not yet fully understood. On the other hand geodetic precession is well studied in pulsars (e.g. Kramer, 2014). In order for this phenomenon to be measurable the spin axis of the pulsar should be misaligned to the total angular momentum of the system and the precession rate should be large compared to the observing baseline. Geodetic precession causes a change in the orientation of the radio beam in respect to the line of sight, resulting in temporal pulse profile changes. The geodetic precession rate is higher for systems with high eccentricity, short orbital periods and high masses. For this reason, this phenomenon is easier detectable in DNS systems. Today, in 5 DNS (J0737−3039A/B, Burgay et al., 2005; J1906+0746, Kasian, 2008, Desvignes et al., 2008; J2129+1210C (B2127+11C), Jacoby et al., 2006; J1915+1606 (B1913+16) Weisberg et al.; Kramer, 1998; J1537+1155 (B1534+12) Stairs et al., 2004) and one pulsar-WD system (J1141−6545, Hotan et al., 2005; Manchester et al., 2010) geodetic precession has been detected. In Chapter 5 we will present the effect of geodetic precession on PSR J1915+1606 (B1913+16) using Effelsberg observations.

1.5.2 Flux density spectra

Pulsars are weak radio sources, their flux density is typical only few a mJy[5] at observing frequency of 1 GHz. Pulsar flux densities have been measured from soon after the discovery of pulsars (Robinson et al., 1968). A lot of studies have been held for measuring multi-frequency flux densities of pulsars (e.g. Maron et al., 2000; Bates et al., 2013). Flux density measurements help us understand the pulsar emission mechanism, but also help us to derive the pulsar luminosity function over a range of radio frequencies. Luminosity (L) describes the quantity: $L = S\ d^2$, where S is the flux density, and d is the distance to the pulsar. Thus, in order to measure luminosities we need distance measurements. Direct distance measurements can only be conducted with parallax measurements. Since parallax measurements are not possible for the majority of pulsars, we can only have an estimate of the pulsar distance from the interstellar dispersion of pulsar signals, using a Galactic electron density model (Cordes & Lazio, 2002) (see Section 1.8.1). A pulsar luminosity function can then be created from these measurements. By also taking into account a beaming model, propagation effects, and flux density limitations due to telescope sensitivity, we can make a prediction about the NS birth rate and the Galactic pulsar distribution.

In literature, we can find radio pulsar detections from frequencies as low as 20 MHz (Bruck & Ustimenko, 1973) to as high as 291 GHz (Torne et al., 2017). However, the majority of pulsar observations are conducted at frequencies from 100 MHz to 2 GHz. The reason is the shape of the flux-density spectrum.

For the majority of pulsars, at frequencies between ∼100 MHz and ∼20 GHz, the flux density is inversely proportional to the observing frequency. The relation with observing frequency can be simply expressed with a single power law:

$$S_{mean}(f) \propto f^{\xi}, \tag{1.6}$$

[5] 1 Jy = 10^{-26} W m^{-2} Hz^{-1}

where ξ is the spectral index. However, there are some pulsars that exhibit more complex spectral behavior. Sieber (1973) was the first one to notice a turn over at around 100 MHz and a break at around 1 GHz. Since then, more studies have been undertaken (Lorimer et al., 1995; Maron et al., 2000; Kuniyoshi et al., 2015) revealing that the flux spectrum of the majority of pulsars can be expressed with a single power law. Attempts to correlate pulsar spectra with spin period (P), spin down rate ($\dot{P}$), characteristic age (τ), polarization fraction and profile type have been done but no significant correlation were found (Kramer et al., 1998).

The flux density spectrum is observed to be very diverse. It can be from flat ($\xi \simeq 0$) to very steep ($\xi \simeq -4$), with average values for the slope determined to be equal to -1.6 ± 0.2 (Bates et al., 2013). No significant difference in spectral behavior between canonical and MSPs has been observed (Kramer et al., 1998; Toscano et al., 1998; Burgay et al., 2013).

Observed pulsar flux densities vary not only with frequency but also with time. Time variations scale from a few minutes to months. These variations are caused by the interstellar medium (ISM) propagation effects, scintillation which will be further discussed in Section 1.8 or by intrinsic effects (nulling and intensity modulation). Time variations of shorter (Stinebring et al., 2000) and longer (year variations on the flux density of the Crab pulsar profile components Lyne et al., 2013) time scale have also been observed, but were attributed to intrinsic effects. These time variations affect how reliable the mean flux density measurements are and as a result they make it difficult to determine accurately the pulsar flux density spectrum. To obtain reliable results, we should calculate the average flux density based on multiple observations or to use observation at many frequencies that have been taken at the same time (Backer, 1972).

1.5.3 Polarization properties

Pulsars are one of the most polarized known sources in the universe. Linear polarization was detected in pulsar emission soon after their discovery (Lyne & Smith, 1968). A typical degree of linear polarization for an integrated profile is around ∼40%, but in some cases this polarization fraction can reach values of up to 100%. Circular polarization is typically less intense, covering ∼20%–30% of the total emission. No difference in the polarization intensity between canonical pulsars and MSPs has been observed.

The study of polarization properties in pulsars is very important for understanding the emission mechanism, emission geometry and ISM effects. The existence of polarization is direct evidence for the no thermal emission mechanism. The linear polarization can be explained from the ordered movement of plasma along the field lines, due to the strong magnetic field. The plane of linear polarization is tied to the magnetic field lines. This mechanism can be verified from the S-shape of the polarization position angle (PPA, see Section 1.6.1). While linear polarization can be easily explained, the existence of circular polarization is difficult to understand. Both intrinsic emission mechanisms and propagation effects have been proposed to explain it (Han et al., 1998).

The study of linear polarization can, also, reveal a lot about the strength of the Galactic magnetic field. While pulsar radiation propagates through the Galactic magnetic field, it undergoes a change in the plane of linear polarization. This effect is called *Faraday rotation* (see Section 1.8.2). Faraday rotation is a very important tool, since through the study of this effect, and the knowledge of the Galactic electron density distribution, Galactic magnetic fields can be measured.

1.6 Modeling the radio emission beam

When we investigate pulsar profiles we see a large diversity in the number of components, widths and polarization fraction. The origin of all this diversity would have been explained, if we had a theoretical model that could describe the radio emission process. Unfortunately, 50 years after the discovery of pulsars this model does not, yet, exist. Observational models come to fill this gap. These models, of course, cannot explain the nature of the radio emission process, but they can describe very efficiently some observational aspects and make some predictions.

In the sections below we will focus on two beam models: the rotating-vector model (RVM) (Radhakrishnan & Cooke, 1969), which can explain the PPA shape, and the radius-to-frequency mapping (RFM) model (Cordes, 1978) which can describe the evolution of some pulsar profiles with frequency.

1.6.1 Rotating-vector model (RVM)

The RVM is a widely accepted beam model proposed by Radhakrishnan & Cooke (1969). This model was developed to explain the behavior of the PPA in the Vela pulsar. PPA is the angle between the projected direction of the magnetic axis and the plane of linearly polarized emission. Very often in radio pulsars this angle, as a function of pulse longitude, has an S-shape. Radhakrishnan & Cooke (1969) suggested that this behavior has a geometrical origin. In their model they assumed that the radiation originates in the neighbor of each magnetic pole. The emission beam is centred on the magnetic axis and occupies a region defined by the last open magnetic field lines. The beam shape is assumed to be conical. If we assume that the plane of linear polarization is tied on the magnetic field lines as the pulsar spins the projection direction rotates with the star and the PPA varies from 0 at the profile centre to, at most, 180°. The RVM model calculates the PPA (Ψ) changes through pulse longitude using simple geometry and the Radhakrishnan & Cooke convention:

$$\tan(\Psi_0 - \Psi) = \frac{\sin\alpha \sin(\phi - \phi_0)}{\sin(\alpha + \beta) \cos\alpha - \cos(\alpha + \beta) \sin\alpha \cos(\phi - \phi_0)}, \tag{1.7}$$

where ϕ is the rotational phase, α and β are the emission geometry angles, Ψ_0 and ϕ_0 are the PPA and phase of the fiducial point, respectively.

The angles α and β as well as other important geometry angles of this model are presented in Fig. 1.4. The angle α defines the inclination of the magnetic axis with respect to the rotation axis, and the impact parameter (β) represents the closest approach of the line of sight to the magnetic axis. Due to conventional reasons, the outer line of sight β is positive when $\alpha < 90°$ and negative when $\alpha > 90°$ and for an inner line of sight and β is positive when $\alpha > 90°$ and negative when $\alpha < 90°$[6]. In order for the pulsar to be visible in all cases $\beta \leq \rho$, where ρ is the half-opening angle of the emission beam. We can detect emission for both magnetic poles (an interpulse) in cases where $\alpha \gtrsim 90° - \rho$.

According to the RVM model, the steepness and the curve shape of the PPA S-shape depends only on the emission beam geometry. The impact parameter β controls how steep the shape will be. In the cases where the line of sight cuts the emission beam close to the centre, the PPA S-shape is steeper compared to the cases where the line of sight cuts the emission beam close to the edges. The inner or outer line of sight controls the curve shape. For the outer line of sights the PPA rolls over while for the inner line of sights it continues to rise. A few examples for inner and outer lines of sight are presented in Fig. 1.5.

[6] In the case where we use an Earth-centred coordinate system (Damour & Taylor, 1992).

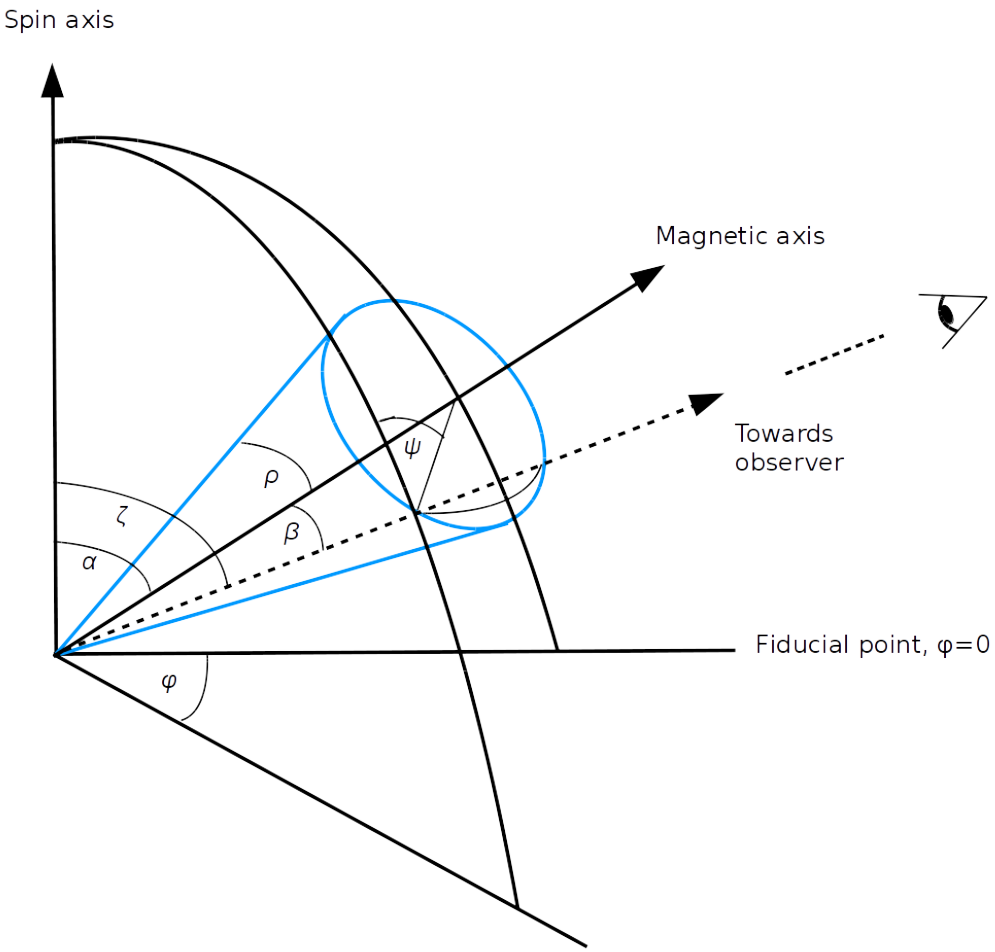

Figure 1.4: Geometry of the pulsar emission beam. The figure is based on Fig. 3.4 from Lorimer & Kramer (2012). For more details about the angles see the text.

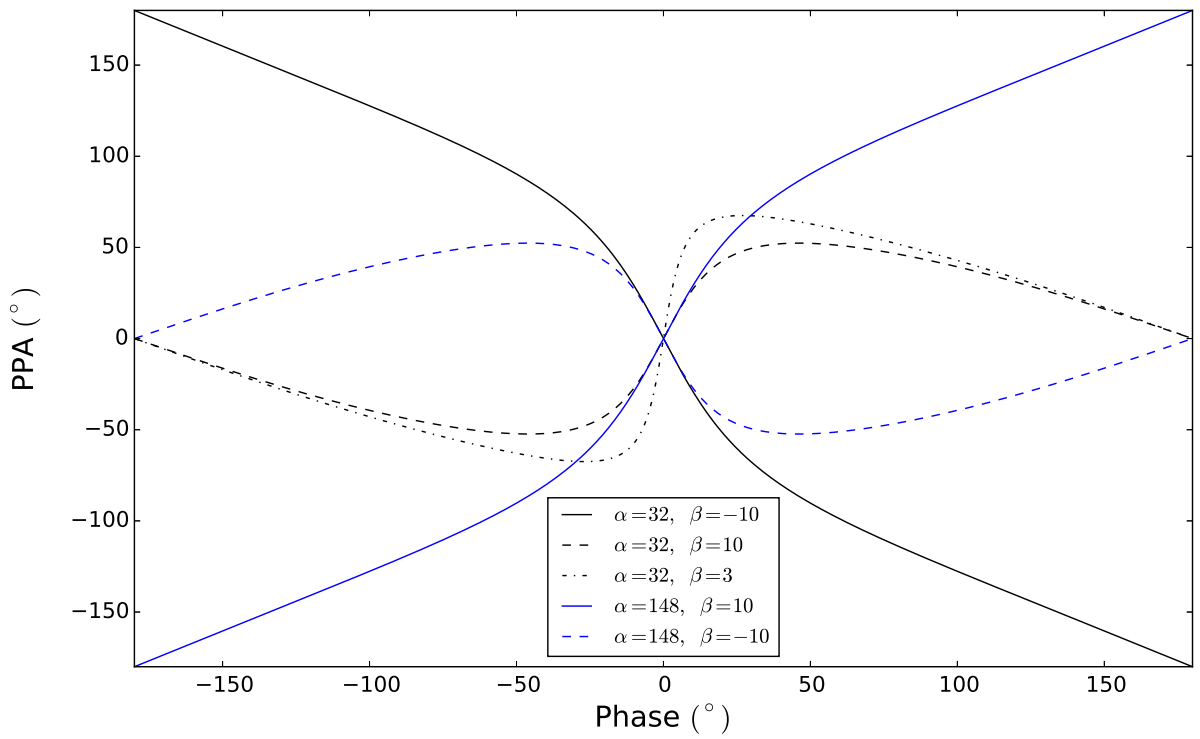

Figure 1.5: The PPA as a function of pulse longitude. With filled lines we present outer line of sights, and with dotted lines inner lines of sight. As mentioned in the text, the closer to the centre the line of sight cuts the emission beam the steeper the PPA is (see the black dot-dashed line). For pulsars with pulse width $\lesssim 30^\circ$ there is often an 180° unambiguity in α since we cannot distinguish between inner or outer line of sight (see black solid line (inner line of sight) and blue dotted line (outer line of sight)).

Each combination of the angles α and β gives a unique S-shape swing. By simple fitting of the RVM model to the observable PPA swing we can extract the geometry of the emission beam. However, very often RVM model solutions are not constrained. The reason is mostly because the emission longitude range of pulsars is small, only around 30°. Having available only a small portion of the PA swing does not allow us to distinguish between an outer or inner line of sight, creating a 180° ambiguity on α measurements (see Fig. 1.5). And partly because the PA swing is observed to deviate strongly from a simple S-shape. These deviations are caused either by propagation through the pulsar magnetosphere or thought the ISM.

With this very simple conical beam model, in which the magnetic axis is in the centre of the emission beam, we can also express the width of the pulse profile, using only the geometric angles. While the pulsar is spinning, the trajectory of the line of sight follows a curved line through the emission beam. The length of this line is the profile width (w) and can be measured by applying simple geometry:

$$\sin^2\left(\frac{w}{4}\right) = \frac{\sin^2(\rho/2) - \sin^2(\beta/2)}{\sin\alpha \sin(\alpha+\beta)}. \tag{1.8}$$

It is worth noting that this equation is independent of the beam shape. While the angles α and β depend only on the orientation of the emission beam, and can be measured through polarization observations, as described above, the opening angle is related to the shape, size and the location of the emission region. If we assume that the field lines are dipolar (a Goldreich-Julian-type beam,[7] Goldreich & Julian, 1969), the radiation region is defined by the last open field line, and the emission region is close to the polar cap, we can express the opening angle ρ with (Lorimer & Kramer, 2012):

$$\rho \approx 1.24^\circ \sqrt{\frac{r_{\rm em}}{10\ ({\rm km})}\ \frac{1\ ({\rm s})}{P}}. \tag{1.9}$$

It should be noted that this expression is only valid for $\rho \lesssim 30^\circ$. In different cases the full last opening angle as expressed from Goldreich-Julian model should be applied. According to Eq. 1.9, the knowledge of the opening angle requires an accurate measurement of the emission height ($r_{\rm em}$). The lack of a theoretical model, as mentioned above, requires emission heights to be determined observationally.

1.6.2 Radius-to-frequency mapping (RFM)

As mentioned earlier, the radio emission of pulsars is believed to originate in the open field lines in the magnetosphere. Even though the region of emission is known, the exact emission height[8] is still unknown but generally accepted to be within 10% to 30% of the light-cylinder radius for canonical pulsars and MSPs, respectively (Kijak & Gil, 1998). Observationally (Rankin, 1983; Gould & Lyne, 1998; Johnston et al., 2008), we see that in general as the observing frequency increases profiles become narrower, outer components are more prominent, double peaks move closer together and the polarization fraction declines.

The model that is used to explain these observational facts is the RFM model (Cordes, 1978). The main idea is that high frequencies are emitted closer to the pulsar surface compared

[7] General relativistic effects add, only, a 4% distortion on the Goldreich-Julian-type beam (Kapoor & Shukre, 1998).

[8] With emission heights we are referring to the heights in which the radiation leaves the magnetosphere. The region where the radiation is actually emitted is still unclear.

to low frequencies. Although the details of this map depend on the emission mechanism, a power law is typically assumed:

$$r_{\rm em} \propto f^{-p}, \tag{1.10}$$

where $p = 0$ in the case of a stable profile across frequency and $p = 0.66$ in the case of a dipolar magnetic field.

Kijak & Gil (1998) undertook a large study to create an observational relation of emission heights with frequency. In their study they included both canonical pulsars and MSPs for which the emission geometry angles, α and β are known. By measuring profile widths they concluded that the emission heights depend not only on the observing frequency (f) but also on the spin period and period derivative, through the equation:

$$r_{\rm em} \approx (400 \pm 80){\rm km}\, f^{-0.26\pm0.09}({\rm GHz})\, \frac{\dot{P}^{0.07\pm0.03}}{10^{-15}}\, P^{0.30\pm0.05}({\rm s}). \tag{1.11}$$

According to this empirical formula the emission originates higher in the magnetosphere for long-period pulsars and closer to the surface for short-period pulsars. High frequencies originate lower in the magnetosphere, as proposed by the RFM model. More precisely, the emission region for frequency ranges from 0.3 to 32 GHz is around 500 km for canonical pulsars and around 100–200 km for MSPs. This very narrow emission region in MSPs can explain why we do not observe many profile width changes with frequency in the majority of these pulsars. In addition to the studies that approach the problem geometrically, there have been studies that use polarization information, timing or scintillation to investigate emission heights. All of them give strong support to the RFM model, as detailed above.

In addition to the studies that assume that the emission at a specific frequency comes from a particular height, there are others that investigate the differences of the emission heights between profile components. In one of them, Gangadhara & Gupta (2001) analyzed observations of PSR J0332+5434 (B0329+54) at 325 and 606 MHz. They included aberration and retardation effects due to rotation in their emission geometry model. The aberration and retardation shift that they measured increased from the inner to the outer cone and are more prominent at lower frequencies. These facts, first of all, give direct evidence in support of the RFM model since it indicates that for the same cone components[9] the emission at lower frequencies originates from greater heights compared to the emission at higher frequencies. Secondly, they showed that for the same emission frequencies not all profile components originate at the same height. More precisely the outer cones originate at higher altitudes compared to the inner cones. Finally, they concluded that for the same frequency the same cones associated with the same sets of field lines which are located not at, but close to the last opening angle.

Pulsars for which the RFV model cannot explain frequency profile changes also exist (Hassall et al., 2012), and so alternative models have been proposed. According to some of these (e.g. Barnard & Arons, 1986; Petrova, 2000; Weltevrede et al., 2003) magnetosphere propagation effects should be taken into account. The radio emission originates in a small region in the magnetosphere but propagation effects like refraction and dispersion are responsible for the frequency evolution of different profile components.

In conclusion, emission heights and the cause of profile evolution in frequency are still not fully understood. In the next section, beam structure models will be presented. These models, as well, try to explain the observational facts mentioned above.

[9] Profile components that originate from the same emission cone.

1.7 Pulsar beam structure

Another unresolved question is how the emission beam is structured and how this structure is related to the profile diversity and profile changes with frequency. Unfortunately, the emission region structure is hard to be revealed since the observations that we have corresponds only to one-dimensional cut of the two-dimension emission beam. Despite this limitation, three major observational emission beam structure models have been proposed.

The first model was proposed by Rankin (1983) and is highly influenced by the morphology of pulsar profiles. According to this model the emission beam has, apart from a conal structure (which was already proposed by Komesaroff, 1970; Backer et al., 1976), a core structure as well, arising close to the magnetic pole. Depending on how the line of sight cuts the emission beam, a profile with one or multiple components is created. It is also proposed that the emission process of the core components is not the same as the outer cone components. At low frequencies core emission is more prominent than cone emission. Expanded versions of this model have been proposed. According to these models the cone region, consisting of multiple or single structures, surrounds the core component. Unfortunately, this model has difficulties in explaining some very complex pulse profiles, for example PSRs J1239+2453 (B1237+25) (Hankins & Wright, 1980) and J2048−1616 (B2045−16) for which the which the core component is considered to be displaced from the centre of the profile (Lyne & Manchester, 1988).

A few years after the proposal of this model, a second one was suggested by Lyne & Manchester (1988). According to their model, the radio emission zones are distributed randomly, instead of occupying discrete regions. The intensity of radiation within these regions is patchy, so that profile components that correspond to different part of the beam may appear stronger or weaker. An example that supports beam patchiness is the asymmetry in pulsar profiles, in which only the trailing or leading component can be observed (Han & Manchester, 2001). Unfortunately, this model cannot explain the profile evolution with frequency and the predicted and observed relation of opening angle with spin period (e.g. Gil et al., 1993).

Karastergiou & Johnston (2007) proposed another model which is a combination of the two previously mentioned. For their model they assumed that there are core and conal zones (as proposed by Rankin, 1983), but the emission of a given zone is patchy (as proposed by Lyne & Manchester, 1988). The new idea that the model brought is that a specific radio emission frequency originates on wide range of heights in the magnetosphere. This stands in contrast with previous models that assume that radio emission, at specific frequencies, rises from many locations across the polar cap, but which have a uniform height. The emission region is very close to the last open field line. They also claim that the emission height range is correlated with the pulsar spin-down energy, with young, short-period pulsars emitting only in a narrow range.

1.8 Interstellar medium effects

The radiation emitted from pulsars passes through the ISM before it is detected with radio telescopes on Earth. The ISM consists partially of a cold, ionized plasma, which is inhomogeneous and turbulent. The interaction of pulsar radiation with the charged particles of the ISM results in intensity variations, polarization changes, and frequency-dependent delays. These effects should be taken into account and carefully removed when we study a pulsar's signal (see Chapter 2). The study of these effects can reveal some pulsar properties, like distance and velocity, and can also help us monitor ISM properties, like the Galactic distribution of free electrons and the Galactic magnetic field. In the sections below we will describe four ISM

effects: dispersion, Faraday rotation, scattering, and scintillation.

1.8.1 Dispersion

Pulsar radiation propagates through the ISM. Since the ISM is not a vacuum, but partially consists of ionised plasma, the group velocity of radio propagation v_g, is not equal to the speed of light, but it is reduced by a frequency-dependent factor, which is called the *refractive index*, μ:

$$v_g = \mathrm{c}\ \mu. \tag{1.12}$$

The exact value of μ depends on the physics of the ISM. For our case it can be expressed as (Lorimer & Kramer, 2012):

$$\mu = \sqrt{1 - \left(\frac{f_\mathrm{p}}{f}\right)^2}, \tag{1.13}$$

where f is the observing frequency and f_p is the plasma frequency, which is equal to:

$$f_\mathrm{p} = \left(\frac{\mathrm{e}^2 n_\mathrm{e}}{\pi m_\mathrm{e}}\right)^{1/2} \approx 8.97\ \mathrm{kHz} \left(\frac{n_\mathrm{e}}{\mathrm{cm}^{-3}}\right)^{1/2}, \tag{1.14}$$

where n_e is the electron number density and e and m_e are the charge and the mass of the electron respectively.

The delay that is introduced to an electromagnetic wave of frequency f, with respect to a signal of infinity frequency, is (based on Eq. 1.12):

$$t = \left(\int_0^d \frac{\mathrm{d}l}{v_\mathrm{g}}\right) - \frac{d}{c}, \tag{1.15}$$

where d is pulsar–Earth distance. For pulsar observations $f_\mathrm{p} \ll f$, we can expand Eq. 1.13 into a Taylor series. Thus, the delay between two observing frequencies (f_high and f_low) becomes:

$$t = \frac{e^2}{2\pi m_\mathrm{e} \mathrm{c}} \left(\frac{1}{f_\mathrm{low}^2} - \frac{1}{f_\mathrm{high}^2}\right) \int_0^d n_\mathrm{e}\ \mathrm{d}l. \tag{1.16}$$

From the equations above it is obvious that higher frequencies arrive to the observer earlier. This frequency-depended delay is called *dispersion* and is quantified by the integrated column density of free electrons along the line of sight, called the *dispersion measure* (DM):

$$\mathrm{DM} = \int_0^\mathrm{d} n_\mathrm{e}\ \mathrm{d}l \quad (\mathrm{pc\ cm}^{-3}). \tag{1.17}$$

The DM is a very important quantity in astronomy at radio wavelengths. It can be easily measured by comparing the pulse arrival time at different frequencies. DM measurements to pulsars vary from ∼2 to 1700 pc cm^{-3}. From these measurements we can obtain a first estimate of the distance of pulsars, and make a rough prediction about the existence of some ISM effects like scintillation or scattering which are strongly dependent on distance (see Section 1.8.3). However, exact distance measurements require knowledge of the Galactic electron density distribution, n_e.

Pulsar observations can contribute to the opposite procedure: the creation of a Galactic electron density distribution model. One of the most widely used is the 'NE2001' model (Cordes & Lazio, 2002). The observations used in the construction of this model are mostly radio. The radio observations are mostly pulsar-independent distance measurements (from

timing parallax, associations with globular clusters and supernova remnants and HI measurements), pulsar DM measurements, and scattering and scintillation studies from pulsars with high and low DM. Apart from the 'NE2001', a new model, 'YMW16' (Yao et al., 2017) was introduced recently, which is also based on new pulsar distance measurements, since the pulsar population increases rapidly, but not on scintillation measurements as the 'NE2001'. These models can provide an estimate of pulsar distances with just the knowledge of their DM and Galactic position.

1.8.2 Faraday rotation

The Galactic magnetic field crosses the ISM. In the presence of this field, the free electrons are forced to move circularly, due to the Lorentz force, perpendicular to the magnetic field direction. The cyclotron frequency (f_B) of this motion is:

$$f_{\rm B} = \frac{{\rm e}B_{||}}{2\pi m_{\rm e} c}, \tag{1.18}$$

where $B_{||}$ is the Galactic magnetic field in the direction of the wave propagation. The result is the electrons in the right and left hand circularly polarized waves, oscillate with frequencies $f + f_B$ and $f - f_B$, respectively. Thus, we have two refractive indices for the circularly polarized wave, since the refractive index depends on the propagation frequency. The result is that the right and left hand circularly polarized waves propagate with different speeds in the magnetized ISM. Since a linearly polarized wave is the sum of right and left hand circularly polarized waves, these two different speeds will cause a change in the angle of the linear PPA. This rotation is called *Faraday rotation*, and is a tool that can be used to measure the Galactic magnetic field in the direction of the radiation propagation.

The differential phase rotation between the right and left circular polarization can be expressed as:

$$\Delta\Psi_{\rm PPA} = \frac{1}{2}\frac{{\rm e}^3}{\pi m_{\rm e}^2 c^2 f^2} \int_0^d n_{\rm e} B_{||}\, {\rm d}l \equiv \lambda^2\, {\rm RM}, \tag{1.19}$$

where λ is the wavelength of radiation and RM is the *rotation measure*:

$${\rm RM} = \frac{{\rm e}^3}{2\pi m_{\rm e}^2 c^4} \int_0^{\rm d} n_{\rm e} B_{||}\, {\rm d}l. \tag{1.20}$$

As expressed in Eq. 1.19, PPA rotation increases at lower observing frequencies, and with a strong magnetic field and high electron density in the direction of propagation.

Another very interesting application of this effect is that together with the knowledge of the RM and DM we can estimate the average[10] intensity of the Galactic magnetic field component along the line of sight:

$$\langle B_{||} \rangle = \frac{\int_0^d n_{\rm e} B_{||}\, {\rm d}l}{\int_0^d n_{\rm e}\, {\rm d}l} = 1.23\,\mu{\rm G} \left(\frac{\rm RM}{\rm rad\ m^{-2}}\right) \left(\frac{\rm DM}{\rm pc\ cm^{-3}}\right)^{-1}. \tag{1.21}$$

Extended studies based on numerous pulsar rotation measures and distance measurements have revealed the strength (few μG) and the direction of large-scale field structures (Han et al., 2006, 2018).

[10] We can only measure the average value of $B_{||}$, since we can only measure the integrated Faraday rotation along the line of sight.

1.8.3 Scattering and scintillation

For the two phenomena that we described above, we assumed that the ISM is homogeneous. In reality the electron density along the line of sight varies due to, for example, HII regions or supernova shock fronts. The result of these variations is that the refractive index changes continuously (see Eq 1.13 and 1.14). The propagation of a wave with frequency f through an inhomogeneous medium with multiple refractive indices is not straight but can experience multiple bends. Since the propagation time is no longer the same for all the rays, the signal appears scattered. The radiation that arrives later forms a scattering "tail" in the pulse profile.

If we assume that the thin-screen model (Scheuer, 1968) is valid, and the turbulent plasma located in a thin screen mid-way between the pulsar and observer, then the scattering time scale is proportional to:

$$\tau_s \propto d^2 f^{-4}. \tag{1.22}$$

Scattering is general more intense for distant pulsars, and at low observing frequencies. At lower frequencies (< 1 GHz) scattering can be longer than a pulse period and therefore smear out a pulsar's signal. Thus, for selecting the optimal observing frequency, in addition to the flux density spectral index of pulsars, scattering effects should be taken into account.

Another effect that results from the ISM inhomogeneities is *scintillation*. Scintillation is a well-studied phenomenon in astronomy. An example of this effect at optical wavelengths, is the twinkling of stars due to scintillation in the Earth's atmosphere.

Scintillation is a frequency-dependent effect that can easily be described with the same model applied to scattering. As the pulse wave-front crosses the scattering medium a phase shift $\delta\Phi \sim 2\pi f \tau_s$, is introduced to the signal. The interference of this signal can be constructive or destructive, creating a pattern of enhanced and reduced intensities (you can visualize this effect as similar to Young's split experiment). In the case of a transverse motion of the pulsar, observer or ISM, we can also have temporal intensity variations, apart from spatial. The timescale Δt of the pattern movement, depends on the relative motion.

Interference of the signal is possible when the phase differs by less than one radian:

$$2\pi \Delta f \tau_s \sim 1. \tag{1.23}$$

This relation implies that there is a limited bandwidth, over which intensity variations occur. This bandwidth is called the *scintillation bandwidth*, Δf. The scintillation pattern that is created, by the interference, consists of regions with increased and reduced intensity. This pattern can be demonstrated in the from of a *dynamic spectrum*, which is a 2-D plot of pulse intensity as a function of observation time and frequency. In this plot, the regions of enhanced intensity are called *scintles*. The size of these regions reveals the scintillation time and frequency scales of the pulsar.

Scintillation can be either *weak* or *strong*, depending on the size of the electron density inhomogeneities, pulsar distance, and observing frequency. Strong scintillation can be split into *diffractive* and *refractive*, with time scales of minutes and weeks, respectively (for a review see Rickett, 1977; Narayan, 1992)

At an observing frequency of ∼1 GHz, the majority of pulsar observations are affected by diffractive scintillation. Intensity variabilities due to this effect, were the first to be detected in pulsars (Rickett, 1969). A typical time and frequency scale for ∼1 GHz observations is ∼ minutes and ∼1 MHz, respectively.

Diffractive scintillation occurs when the diffractive length scale ($r_{\rm diff}$), which represents the transverse separation for which the root-mean-square phase difference is equal to one radian, is way smaller than the first *Fresnel zone* ($l_{\rm F}$). Since the frequency, $\Delta f_{\rm DISS}$, and time scale, $\Delta t_{\rm DISS}$, of this effect can be easily measured from a pulsar observation which lasts more

than a few minutes, we can easily determine the transverse velocity to the line of sight of the pulsar, $V_{\rm ISS}$ (Gupta et al., 1994):

$$V_{\rm ISS} = A\ ({\rm km\ s^{-1}}) \sqrt{\frac{d}{\rm kpc}} \sqrt{\frac{\Delta f_{\rm DISS}}{\rm MHz}} \left(\frac{f}{\rm GHz}\right)^{-1} \left(\frac{\Delta t_{\rm DISS}}{\rm s}\right)^{-1}, \tag{1.24}$$

where A depends on the distribution of scattering material along the line of sight and on the wavenumber spectrum of electron density irregularities. Different values of A can be found in literature (Rickett, 1970; Gupta et al., 1994; Cordes & Rickett, 1998), based on different assumptions. Eq. 1.24 was derived assuming that there is a single scattering screen which is located in the mid-way between pulsar and the Earth.

1.9 Pulsar applications

Even though the exact emission mechanism of pulsars is not yet completely understood, pulsars have been used to study a wide range of physical and astrophysical problems. In the majority of these applications we only need to consider pulsars as very rotationally stable, polarized sources. Many of the applications are based on timing techniques (see Chapter 2). This means that they require a long-term observation campaign, and a model that can predict every single pulsar rotation. Bellow we pick some of the many pulsar applications, both timing and non-timing based.

1.9.1 Mass measurements and equation of state

Mass measurements are important for understanding the formation and evolution of pulsars, constraining theories of gravity, and the EoS. The methods that we have available only allow us to measure masses of pulsars that share an orbital system with a companion (or companions). Since only a small fraction of pulsars have a companion, only few pulsars have their mass measured.

The most common method is pulsar timing. In order to provide precise measurements, timing requires very hight rotational stability from pulsars, which can, most often, be achieved from MSPs. Through timing we can measure precisely the orbital and astronomical characteristics of pulsars, such as the orbital period (P_b) and the semi-major axis ($\alpha_{\rm p}$). Based on Kepler's third law, we can combine P_b, and $\alpha_{\rm p}$ into the *binary mass function*:

$$f(m_{\rm p}, m_{\rm c}) = \frac{(m_{\rm c}{\rm sin}i)^3}{(m_{\rm p}+m_{\rm c})^2} = \frac{4\pi^2}{\rm G}\frac{(\alpha_{\rm p}{\rm sin}i)^3}{P_{\rm b}^2} = \frac{4\pi^2}{\rm T_\odot}\frac{x_{\rm p}^3}{P_{\rm b}^2}, \tag{1.25}$$

where $m_{\rm p}$ and $m_{\rm c}$ are the masses of the pulsar and its companion measured in $\rm M_\odot$, respectively, $x_{\rm p} = a_{\rm p}{\rm sin}i/{\rm c}$ is the projection of the semi-major axis onto the observer's line of sight, and $\rm T_\odot \equiv GM_\odot/c^3 = 4.925490947\mu s$ is the mass of the Sun in time units and i the inclination angle. $m_{\rm c}$, $m_{\rm p}$ and i are the three unknowns. If the companion mass cannot be measured through other means (like optical spectroscopy), and there is no sign of Shapiro delay, in order for the inclination angle to be determined, we can only put a limit on the pulsar's mass.

In the case that the pulsar belongs to a relativistic system, its motion deviates from a Keplerian orbit. Post-Keplerian (PK) parameters are required in order to describe the orbit (Damour & Taylor, 1992). If we assume that general relativity (GR) is the correct theory of gravity the five PK parameters needed are related to the Keplerian parameters: P_b, x, e, and the system masses. Precise measurements of Keplerian parameters through timing allow us to determine the mass of the pulsar with high precision. Indeed, the first system for which

masses were measured precisely, was the first discovered binary pulsar: PSR J1915+1606 (B1913+16 Hulse & Taylor, 1975). Of the 15 DNS systems known today (see Tauris et al., 2017, for a review), half of them have very accurate mass measurements, through the method described (Özel & Freire, 2016).

NS mass measurements range from ≈1.1 to 2.0 $M_\odot$, with especially MSP mass measurements giving evidence for a bimodal distribution with peaks at 1.39 $M_\odot$ and 1.81 $M_\odot$, and standard deviations of 0.06 $M_\odot$ and 0.18 $M_\odot$ (Antoniadis et al., 2016), respectively. These observational measurements agree with theoretical measurements, which are based on quantum mechanics, predicting 1.4 $M_\odot$ for NSs (Oppenheimer & Volkoff, 1939).

PSR J0348+0432 presently holds the record for the maximum pulsar mass: M = 2.01 ± 0.04 $M_\odot$ (Antoniadis et al., 2013). Pulsars with high masses, are particularly interesting since they directly help us to put constraints on the EoS. Pulsars like PSRs J0348+0432, and J1614−2230 (with 1.928(7) $M_\odot$, Fonseca et al., 2016), can rule out "soft" EoSs at high densities.

Apart from masses, pulsar radii are also important to constrain the EoS. However, radius measurements are very difficult to obtain. Almost all methods used rely on the observation of thermal emission from NS's surfaces at optical wavelengths and X-rays. Most often, these measurements apply spectroscopic techniques, like is done for a normal star, in order for the apparent angular size to be measured and from this to extract the radius. The theoretical models, combined with observations, set pulsar radii in the 10 – 12 km range (Özel & Freire, 2016).

1.9.2 Binary and stellar evolution

The discovery of the first pulsar in a binary system raised the question of how this system was formed. With the discovery of even more diverse systems, like the first MSP in a globular cluster (J1824−2452A (B1821−24A) Lyne et al., 1987), triple (e.g. Ransom et al., 2014), and eclipsing systems (e.g. Lyne et al., 1993; Altamirano et al., 2011), the field of binary and stellar evolution became even more fascinating.

The standard model is that MSPs are created by a recycling process occurring in X-ray binary systems (see section 1.4.1). This model was first proposed by Smarr & Blandford (1976). With the discovery of the first MSP (PSR B1937+21), this model was subsequently extended (Srinivasan & van den Heuvel, 1982; Radhakrishnan & Srinivasan, 1982). Since then, the discovery of more diverse systems, with different environments (for example globular clusters), companion masses, orbital periods etc., helped to investigate and extend the initial conditions of the formation models (see for a review Tauris & van den Heuvel, 2006). The connection between MSPs and X-ray binary systems found more evidence with the discovery of three systems: PSRs J1023+0038 (Archibald et al., 2009), J1824−2452I in M28 (Papitto et al., 2013) and J1227−4853 (Roy et al., 2015). All of these were discovered in a swapped phase between a radio MSP and an X-ray binary stage, all detectable in both radio and X-rays.

However the discovery of new systems challenged this model. One of these examples is the highly eccentric binary PSR J1903+0327 with a MS star companion, most probably originating from a hierarchical triple system (Freire et al., 2011). Also PSRs J2234+06 and PSR J1946+3417 are both members of eccentric systems with WD companions, believed to be formed after a direct collapse of a spinning super-Chandrasekhar mass WD (Freire & Tauris, 2014).

All these pulsar systems and other systems that we will be, definitely, discovered in the future bring us one step closer to understanding how binary systems are formed and evolve.

1.9.3 Tests of gravity theories

The first binary and the DNS ever discovered was the J1915+1606 (B1913+16) system (Hulse & Taylor, 1975). This system consists of a mildly recycled pulsar, with spin period 59 ms, and a canonical slow pulsar, tightly together with an orbital period of only 7.75 h. This system along with similar DNS systems that were discovered later are ideal to test GR in the strong-field regime.

For a pulsar that belongs to a relativistic system, its motion deviates from a Keplerian orbit. As mentioned above, PK parameters are required to describe the orbit (Damour & Taylor, 1992). All the PK parameters are related to system masses, as well as to the Keplerian parameters: $P_{\rm b}$, x, e, $\Omega_{\rm asc}$, and T_0. By just measuring two of the PK parameters, and assuming a theory of gravity, we can calculate the system masses. For PSR B1913+16, three PK parameters are measured precisely: periastron precession ($\dot{\omega}$), relativistic time dilation (γ), and orbital decay ($\dot{P}_{\rm b}$) (Weisberg & Huang, 2016), with this last one to be better than 0.2% in agreement with GR predictions. For even more relativistic systems, like the DNS system J0737−3039A/B (Burgay et al., 2003; Lyne et al., 2004), three more PK parameters can be measured associated with the Shapiro delay, r and s (Kramer et al., 2006), and geodetic precession rate (Breton et al., 2008). All these measurements can be plotted on a "mass–mass" diagram. Every PK parameter defines a zone in the diagram, where masses are allowed. In the case that a correct theory of gravity is applied to the analysis, all the PK parameter zones will intersect to a single region, within the uncertainties, which defines the system masses. For the J0737−3039A/B system, especially, the mass ratio can be obtained, from Kepler's third law based on the accurate measurements of the projected semi-major axes of both orbits. This measurement, unlike PK parameters, is independent from gravity theories to first order. Mass ratio value combined with the mass measurements obtained with PK parameters, provides us with stringent constraint on gravity theories. For this system, it is concluded that GR can describe the motion of the two stars with a precision of 0.05% (Kramer et al., 2006).

GR has passed, so far, successfully all the tests made with DNS systems, however, there are alternative gravitational theories that have assumptions that can be better tested with NS–WDs systems. Many of these theories predict the existence of gravitational dipolar radiation. The PSR J1738+0333 system has set the most stringent limits, so far, on dipolar radiation (Freire et al., 2012), with other similar systems also providing tight constraints (Bhat et al., 2008; Lazaridis et al., 2009). There is another set of alternative theories of gravity, to which most alternative metric theories and the scalar–tensor theories of gravity belong, that violate the *strong equivalence principle* (SEP). A key implication of SEP is that strong and week self-gravity bodies fall in the same way in an external gravitational field. Thus with some binary pulsars, as well as with the triple system J0337+1715 (Ransom et al., 2014) we can probe SEP (see Shao & Wex, 2016, for a recent review). Zhu et al. (2018) studying the change rate in the orbital periodicity and eccentricity of the pulsar–WD binary PSR J1713+0747, derived the most precise limit, so far, on the degree of SEP violation: $\Delta < 0.002$ (95% CL).

Apart from binary systems, also isolated pulsars can be used to test alternative theories of gravity. By studying the profile variations of the two solitary pulsars PSRs B1937+21 and J1744−1134, Shao et al. (2013), for example, put limits on the isotropic violation of the local Lorentz invariance of gravity.

1.9.4 Searching for gravitational waves

GWs are "ripples" in the fabric of space-time. The cause of GWs is accelerated objects, such as NSs or BHs. The inspiral or decrease of orbit of these interactions will have as a result the radiation of energy in a form of "waves". These waves will propagate through the Universe

at the speed of light, carrying information about the objects of their origin. Albert Einstein predicted the existence of GWs in 1916 in his GR theory. They were detected indirectly with the binary pulsar PSR B1913+16 (Hulse & Taylor, 1975). While studying this pulsar they realized that the way that the orbit of the system decays was due to energy emission in a form of GWs, exactly as predicted by GR (see Chapter 5). In September 2015 the Laser Interferometer Gravitational-Wave Observatory (LIGO) made the first direct detection of GWs (Abbott et al., 2016), initializing the era of GW astronomy. The source was the coalescing of two $\sim$30 $M_{\odot}$ BHs. LIGO consists of two laser interferometers, one located in Livingston Louisiana and the other in Hanford Washington State. Each interferometer consists of two perpendicular arms 4 km each. A laser beam is splitted into two beams. Each of these beams travels through one of the arms, is reflected back by a mirror, and finally recombined again. The space-time distortion that is caused by a GW passage, resulting in arm length changes. Since the two laser beams travels through different length arms if there is a GW present, when they are recombined they are not in phase, but an interference pattern is created. The strain sensitivity achieved with LIGO at 100 Hz is better than $10^{-23}/\sqrt{\text{Hz}}$, high enough in order length changes of the order of 10^{-19} m to be detected (Martynov et al., 2016).

GWs (exactly as electromagnetic radiation, which is the conventional way to observe the Universe) have a frequency-dependent behavior. Observing different frequency bands of electromagnetic radiation enables us to observe different physical events, revealing something new about the Universe. The same applies to GW observations.

The spectrum at GWs ranges from 10^{-20}–10^{6} Hz and can be split in high, intermediate and low frequencies. Three different experiments have been formed in order to detect GWs in these three different bands. LIGO observes GWs ar high frequencies (50–500 Hz). The source of these GWs are single spinning, not perfectly spherical, massive objects like NSs (emitting continuous GWs), or coalescence of massive objects in binary orbits: NS–NS, binary BH (BBH), and BH–NS. The Laser Interferometer Space Antenna (LISA, Amaro Seoane et al., 2013a; Amaro-Seoane et al., 2013b) aims to detect intermediate GWs (0.1 – 100 mHz). Such a detector, when it is launched, will observe signals from ultra compact binaries, supermassive BH mergers and extreme-mass-ratio inspirals and bursts produced by a stellar-mass compact objects orbiting supermassive BHs. Pulsar timing arrays (PTAs, Romani, 1989) are able to detect low frequency GWs, in the nanoHertz regime (10^{-9}–10^{-7} Hz). The primary sources of GWs at these frequencies are expected to be inspiralling super-massive BH binaries (SMBHBs). The GW signal may be from individual, massive nearby systems (e.g. Sesana, 2013) or from a stochastic GW background (GWB), made up from the cosmological population of gravitationally bound SMBHBs in the cores of distant galaxies (e.g. Sesana et al., 2008). Other potentials sources for PTAs are cosmic strings (e.g. Sanidas et al., 2012) and GWs from the inflationary epoch, arising from the era of graviton decoupling in the early Universe (e.g. Grishchuk, 2005; Boyle & Buonanno, 2008).

1.9.4.1 PTA experiments

It was first proposed by Sazhin (1978) and Detweiler (1979) that the detection of GWs is possible through an experiment that uses Earth and pulsars in order to monitor changes in their apparent motion of pulsars, though changes in the period of detected pulses. The discovery of MSPs (Backer et al., 1982), opened new possibilities for GW detection with pulsars, since they have such great spin stability, that a GW passage can cause measurable changes in their arrival times, affecting their timing.

The effect of GWs, from sources like binary SMBHs, is expected to be significant over cosmological distances, affecting the timing of all pulsars. Indeed, Hellings & Downs (1983),

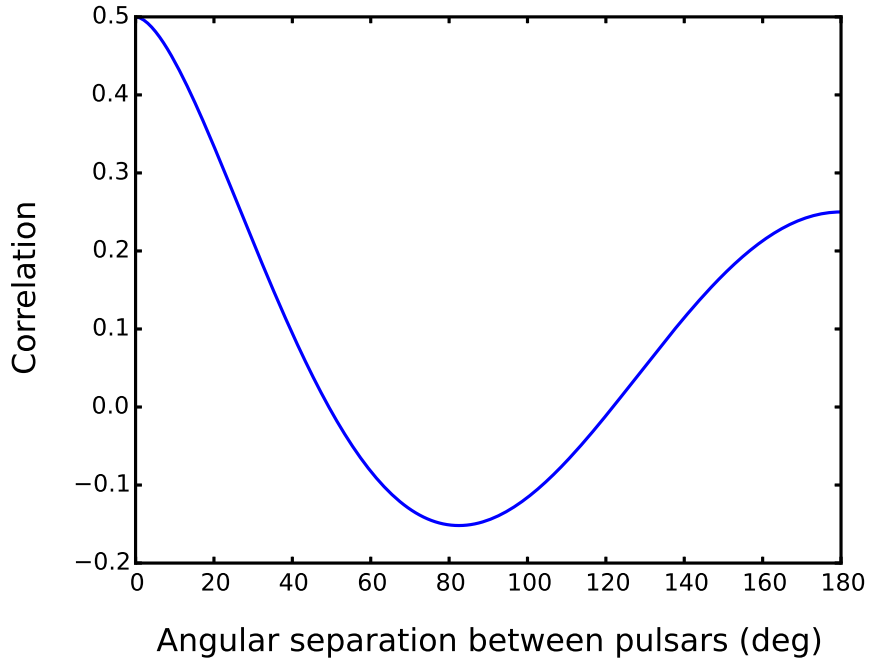

Figure 1.6: The correlation of timing residuals with respect to the angular separation between pair of pulsars in the case of an isotropic, stochastic GWB.

used timing data on four pulsars with residual rms between 10 μs and 2 ms, put the first upper limit on the stochastic GWB. The key point to their analysis is that the signal of the stochastic GWB should have a correlated response between pairs of pulsars. In the case of an isotropic, unpolarized background the gravitational radiation has a quadrupole signature, composed of plus (+) and a cross ($\times$) polarization modes as predicted by GR. The correlations between pairs of pulsars, in the presence of this signal, is expected to follow the *Hellings and Downs curve*[11]. In Fig. 1.6 this curve as a function of the angular separation between pulsars is presented. In order to understand this correlation we can assume a propagation of a single GW. Since the gravitational radiation is quadrupolar and perpendicular to the GWs propagation direction, pulsars in opposite parts of the sky undergo similar effects, while pulsars with $\sim$90° offsets undergo opposite effects. For the pulsars along the direction of propagation there is no impact. A mathematical expression of the Hellings and Downs curve is given by (e.g.) Jenet et al. (2005) and has the following form:

$$r(\theta) = \frac{1}{2} - \frac{1}{4}\left(\frac{1-\cos\theta}{2}\right) + \frac{3}{2}\left(\frac{1-\cos\theta}{2}\right)\ln\left(\frac{1-\cos\theta}{2}\right), \tag{1.26}$$

where θ is the angle between the pair of pulsars.

PTAs are presently the only way to detect the GWB. A PTA consists of highly stable MSPs, ideally uniformly spread across the celestial sphere. The comparison of the correlated deviations on the arrival times of pulses, with that expected from the Hellings and Downs curve, reveals the existence or observe, of an isotropic, stochastic GWB in the data. In 2005 it was estimated that in order to achieve this goal, regular observations of around $\sim$20–40 stable MSPs,

[11] A GWB predicted from alternative theories of gravity, which have different polarization modes, or GWBs from anisotropic GW distributions predict different correlation signatures.

in a time span of ∼10 years are required (Jenet et al., 2005).

Currently three PTAs experiments, with main goal to detect GWs, exist: the European PTA (EPTA) (Desvignes et al., 2016), the North American Nanohertz Observatory for GWs (NANOGrav) (Arzoumanian et al., 2015) and the Australian Parkes PTA (PPTA) (Reardon et al., 2016). The EPTA consists of the 5 largest radio telescopes in Europe: the Effelsberg 100-m Radio Telescope in Germany, Lovell Telescope in the UK, the Nancay Radio Telescope in France, Westerbork Synthesis Radio Telescope, and the Sardinia Radio Telescope in Italy. NANOGrav uses the Robert C. Byrd Green Bank Telescope and the 305-m William E. Gordon Telescope of the Arecibo Observatory and the PPTA uses the Parkes Radio Telescope. All combine their efforts under the International PTA (IPTA) (Verbiest et al., 2016).

So far no correlated signal among PTA pulsars, has been found. However, a limit on the strength of GWs in the nanoHertz regime can be placed by studying the power spectrum of the timing residuals of either all or only the best PTA pulsars. The power spectrum of the timing residuals, induced by a GWB, is expected to be (e.g. Jenet et al., 2006):

$$R(f_{\rm GW}) = \frac{h_c(f_{\rm GW})^2}{12\pi^2 f_{\rm GW}^3}, \tag{1.27}$$

where h_c is the characteristic strain spectrum, which describes the spacetime fluctuations induced by the GWB, and can be defined by:

$$h_c(f) = A_{\rm GW}\ (f_{\rm GW})^{\alpha}, \tag{1.28}$$

where $A_{\rm GW}$ is the amplitude of the GWB, $f_{\rm GW}$ is the frequency of GWs in yr^{-1}, and α is the power-law index. Depending on the origin of the stochastic GWB the power-law index is expected to have a different value. For a SMBHB background $\alpha = -2/3$, for the cosmic string background $\alpha = -7/6$, and for a GWB generated from cosmological perturbations $\alpha = -1$. Any GWB amplitude limit derived from timing residuals should assume a value for the spectral index, or it can measure it.

The most stringent upper limit on the amplitude of the GWB from SMBHBs is given by Shannon et al. (2015), based on 3-GHz observations of the four least noisy pulsars in the PPTA, and is equal to $A_{\rm GW} < 1.0 \times 10^{-15}$ (with 95% confidence) in the reference frequency of 1 yr^{-1}. The other PTAs set their own upper limits, the EPTA's upper limit is $< 3.0 \times 10^{-15}$ in the reference frequency of 1 yr^{-1}, based on a 18-year, 6 pulsar dataset (Lentati et al., 2015), and NANOGrav's is $< 1.45 \times 10^{-15}$ at a frequency of also 1 yr^{-1}, based on the NANOGrav 11-year dataset (Arzoumanian et al., 2018). Even before a GWB detection, some SMBH models that are inconsistent with these limits can be ruled out (Chen et al., 2017; Ravi et al., 2014)

1.9.4.2 Sensitivity to detect GWs

It is clear that in order to achieve a nanoHertz GW detection, increased IPTA sensitivity is needed. Siemens et al. (2013) calculated the signal-to noise ration (S/N) of PTAs detection sensitivity. In the case that the GWB contribution to the noise is dominant, the S/N of detection sensitivity is proportional to:

$$N \left(C \frac{A_{GW}^2}{\sigma^2} \right)^{1/2(3-2\alpha)} T^{1/2}, \tag{1.29}$$

where N is the number of pulsars in the array, C is the cadence, σ is the timing residual rms and T the length of the pulsar timing data set. In the case where the GWB contribution is below the white noise level the S/N is given by:

$$N\, C\, \frac{A_{GW}^2}{\sigma^2}\, T^{3-2\alpha}. \tag{1.30}$$

It is clear that in this case the contribution of cadence and the rms of timing residuals is very important in contrast with the case where the GWB has significance presence in the noise where the number of pulsars in the array starts to be more important. The reason is that within an array with more pairs of pulsars it is easier to discriminate GWs with quadrupolar spatial correlations from red noise. Taylor et al. (2016) came to the same conclusion in their analysis.

In the case of single SMBHB sources the sensitivity of the array will also strongly scale with the rms of timing residuals (Lee et al., 2011).

Based on the analysis above, the best way to increase the sensitivity to detect GWs is to add more good timers in the array. Since the GW signal is very weak, the required timing stability of pulsars is $\sim$200 ns, for more than 10 years of observations (Taylor et al., 2016). In order to achieve this goal, a lot of stable pulsars with hight flux densities and low red noise levels should be constantly added in the array. Also, the observing systems should be characterized by low system temperature and broad-band receivers. For this reason the best MSP timers are observed by the largest radiotelescopes in the world, chosen to be part of PTA projects. It is, also, the reason why new facilities like the South African telescope array MeerKAT (Booth et al., 2009), the Chinese Five-hundred-meter Aperture Spherical radio Telescope (FAST, Nan et al., 2011), and eventually the Square Kilometre Array (SKA, Kramer, 2004; Cordes et al., 2005; Janssen et al., 2015), combining with the already existing PTAs, will almost certainly detect GWs in the nanoHertz regime.

Chapter 2

Timing a pulsar

The majority of the science that we can do with pulsar observations comes from pulsar timing. For applying timing we need to measure the times of arrival (ToA) of the emitted pulse and compare this to a theoretical model. This theoretical model, which is referred to as a *timing solution* or *ephemeris*, contains all the rotational, astronometric, ISM related, and binary properties of the pulsar. After observing the pulsar multiple times, we create a series of ToAs. By comparing these ToAs with the ephemeris predictions we can fit the model parameters in order to minimize these differences. The aim is to create a phase-coherent solution that is able to account for every pulse emitted. This process is called pulsar timing.

MSPs are the ideal objects to apply this method to, since they have very stable rotation (comparable to atomic clocks) and exhibit little (if any) timing noise. However, there are effects that can introduce unexpected perturbations to ToAs, degrading timing precision. The most common are processes intrinsic to the pulsar, like spin and spin-down irregularities, ISM effects like scattering or DM variations, jitter noise caused by S/N and pulse-shape variations of single pulses, and radiometer noise. Fortunately, the high precision to which ToAs are measured, enables us to model most of these effects (or example DM variations), and even to mitigate some of them (for example jitter noise).

With pulsar timing we can very accurately measure the timing model. This precision can be used to study a wide range of effects (as discussed in Section 1.9). The study of the orbit, and limits on the mass of the NS-WD system J1933−6211, based on results obtained with timing techniques, are presented in Chapter 4.

Contents

2.1 Timing observations

To successfully plan a timing campaign we should take into account the observing system (e.g. gain, sensitivity, bandwidth), the pulsar characteristics (e.g. flux density spectrum, and DM), and the project requirements (e.g. cadence).

The majority of pulsar observations are performed between ∼300 MHz to 3 GHz. The reason is the pulsar flux density spectrum, which is inversely proportioned to the observing frequency, as well as the sky background noise, which has a steep spectrum ($\propto f^{-2.7}$). The flux density spectral index (but also ISM effects, like scattering and scintillation, which are more intense at lower frequencies) should be taken into account when picking the observing frequency so that high ToA precision can be achieved. For projects that require high timing precision without ISM noise (for example PTA projects for detecting GWs), multiple frequency observations, or broad-band receivers are required (see, e.g. Janssen et al., 2015).

The duration of pulsar observations is mostly determined by the gain of the observing system, the available observing bandwidth, the pulsar flux density, the required S/N, and whether there is a well-known timing solution for the pulsar. Systems with high gain and wide bandwidth require less observing time to achieve the same ToA uncertainty when observing the same pulsar.

Pulsars without well-known timing solutions require high cadence observations with a duration that depends on their spin precision and orbital characteristics (isolated or binary pulsar, and orbital period). As soon as the pulsar has a good timing solution, repeated observations are still required in order to maintain phase connection. However, even when a phase-connected solution is available, pulsars may be needed to be observed more often, in the case that a particular phenomenon is investigated. One example is the investigation of the relativistic effect Shapiro delay in binary pulsars. Shapiro delay is caused by the curvature of the space-time due to the gravitational field of the companion. In order this effect to be detectable the pulsar orbit should be seen edge-on, and the observations should cover the whole pulsar orbital phase.

2.1.1 Frontend

Since pulsars are weak radio sources, large collecting areas are required to achieve a high S/N. For single-dish telescopes, that have active pulsar timing programs, the telescope diameter range from ∼64 m (e.g. Parkes radio telescope) to 500 m (FAST radio telescope). The shape of the dish is usually parabolic, except for the Arecibo Observatory and FAST radio telescopes. Since radio telescopes operate from radiowaves with wavelength of a few millimeters to a few meters, and since the dish surface should be smoother than a fraction of the wavelength, an accuracy of less than a few mm is required.

The signal that is collected from the dish is reflected to the primary or secondary focus of the telescope. There, through the *feed horn* the signal is channeled into the *receiver*. The signal in the receiver is converted to electric voltages, separated into two orthogonal (linear or circular) polarisations by a Separating polarisations–Ortho-mode Transducers (OMTs), and is amplified by a Low-Noise Amplifier (LNA). The receiver is usually cryogenically cooled to

about 10 Kelvin using helium gas refrigerators, in order to minimize the thermal noise in the electronics that could cover the signal. The amplified signal is transmitted from the receiver by a fiber-optic cable. Then it passes through a bandpass filter so that frequencies outside the band of interest are rejected.

The signal is then converted to lower frequencies. This procedure is done by the *mixer*, which blends in a monochromatic signal of a specified frequency provided by the *local oscillator*. The signal that is produced from this procedure consists of the sum and the difference of these two frequencies. By applying another bandpass filter we usually reject one sideband. At the end of this stage the signal is, usually, amplified again before it is sent to the *backend*.

2.1.2 Backend

The output of the frontend system is usually a signal in an analog form. How this signal will be further analyzed depends on what type of backend we use and how the backend works. Pulsar backends, typically, work in three modes: baseband, searching, and timing mode. With baseband mode all the information of the emitted signal is recorded, so this mode is used for specific pulsar projects where the raw data for reprocessing later are needed. In searching mode the backend records data suitable for pulsar searching, and in timing mode suitable for pulsar timing. In this thesis only timing mode is used.

The analog signal from the frontend will be further analyzed by computers, thus a conversion from analog to digital is required. This procedure is done by two (for the two orthogonal polarisation modes) Analogue-to-Digital Converters (ADCs), which have a sampling rate described by the Nyquist–Shannon sampling theorem. The emitted pulsar signal is affected by dispersion (an ISM effect described in Section 1.8.1). This effect introduces a frequency-dependent delay that smears the signal across the whole band. The correction process of this effect is called de-dispersion. The most efficient way to de-disperse the signal is to split the observing band into frequency channels. This process is done by a polyphase filter-bank (PFB) which performs a Fast Fourier Transform (FFT). For de-dispersing the signal in each channel we can either apply an *incoherent* or *coherent de-dispersion* approach, both techniques will be described in the next section.

As in timing mode, in searching mode the bandwidth is also split into channels, but in this mode no de-dispersion is applied, since pulsar's DM is an unknown in pulsar searching.

2.1.2.1 Incoherent and coherent de-dispersion

Incoherent de-dispersion is the simplest and less computationally expensive method that is used to remove the effect of dispersion from the signal (see Fig 2.1). In this method a time shift that corresponds to the delay derived from the pulsar's DM, is subtracted from each channel. The delay is calculated using Eq. 1.16. The disadvantage is that while the signal is aligned across the whole band, inside the individual frequency channels dispersion remains uncorrected, causing some pulse smearing (dependent on the channel width and DM).

With advances in electronics and computing power, coherent de-dispersion, that can completely restore the original signal without any intra-channel smearing, can be performed in backends (Hankins, 1971). According to this method the ISM can be modeled as a filter. The emitted signal can be represented as a sequence of Fourier components. As this signal propagates through the ISM, the phase of each frequency component in the sequence changes, proportionally to the DM of the pulsar. By applying the inverse filter to the Fourier transform of the input signal, we can remove the dispersion delay. Since multiple FFTs are applied, this method is computationally expensive, but it gives us back a signal with the same time

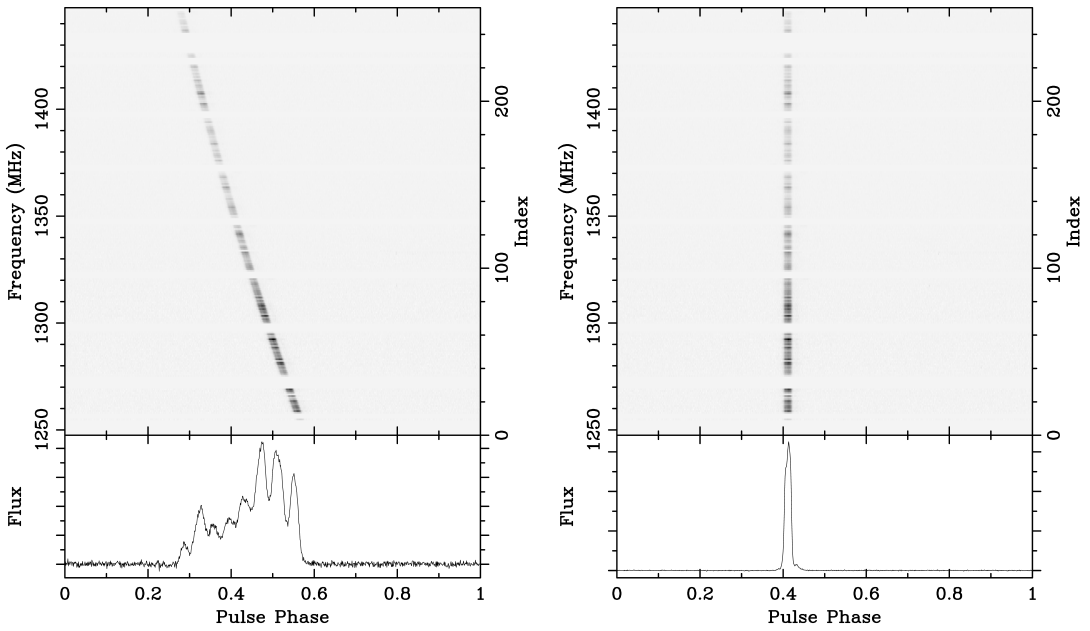

Figure 2.1: The effect of ISM dispersion on timing data of PSR J1935+1616 (B1933+16). The observation is taken with the 'P217 mm' Effelsberg receiver. In the left plot, the frequency-dependent delay introduced by dispersion is demonstrated in the top panel, and the integrated smeared-out profile due to this effect is given on the bottom. In the right plot, the same observation but this time dedispersed with the correct DM ($= 158.52$ pc cm^3), and the integrated profile with all its features, are given on the top and bottom panels, respectively.

resolution as the original. Although, after coherent de-dispersion the signal is completely recovered and there is no need for high frequency resolution, we still retain some. The reason is to further correct the DM, when we get a better timing solution or when DM variations are measured, and for the case that a channel is affected by RFI to be removed without losing a lot of signal.

2.1.2.2 Folding mode

After the de-dispersion stage, each frequency channel contains a time series, which is then split into intervals of the length of the pulsar spin period. These individual pulses are phase-aligned, with a phase that is obtained from the pulsar timing solution, and coherently summed to form a *sub-integration*. Since the typical length of a sub-integration is $\sim$10–120 s, hundreds or thousands of single pulses (depending on the pulsar spin period) are added in a sub-integration. This procedure, that in timing mode is usually done in real time, is called *folding*. The result is a folded archive which contains a phase-aligned signal as a function of both observing time and frequency. The folded profile contains, in the majority of times, the polarisation information of the initial signal as well.

The pulse phase is recorded in bins, which, usually, number between 512 or 4096. Such high phase resolution allows small details in the profile structure to be recorded.

2.2 Data reduction

Before the creation of ToAs we should make sure that we have processed the data in a way that we can get the most information from them. Artifacts that have been introduced to the signal, due to ISM, instrumental, or terrestrial effects, have changed its intrinsic characteristics and should be removed. The steps that are usually followed for processing folded data into ToAs, are presented below.

2.2.1 RFI mitigation

RFI is any transmission within the observing band, other than the astronomical source of interest. Even though radio telescopes are typically located far from urban facilities, and specific important frequencies for radio astronomy are protected by law, the extended, and growing use of telecommunication devices, as well as the use of broad-band receivers, make radio observations vulnerable to terrestrial and non-terrestrial RFI. Among terrestrial RFI we can name digital video or digital audio transmitters, and ground-based aviation radars as examples.

Since RFI signals are produced from a wide range of devices, their morphological characteristics are diverse. In the frequency domain RFI usually affects only a small part of the band (narrow-band), but there are cases in which bursts can affect the whole band (broad-band). In the time domain, the number of sub-integrations that will be affected depends on the duration of the signal, which can be short or persistent. In the worst case, the affected channels introduce artifacts into the integrated profile that can hide small features in the profile, or the RFI signal could even be so strong that it can completely hide any pulsar signal. RFI mitigation is necessary for recovering the emitted pulsar signal.

Techniques to deal with RFI can be hardware and software based. For cases in which the RFI is persistent in specific frequencies, and/or is stronger than the receiver can handle, a filter is installed to avoid saturation. The frequencies that are filtered out can then not be observed with this receiver any more.

For not so strong, temporary RFI, we apply a software approach. This software can work manually and/or automatically. Since the effect of RFI on the channel and sub-integrations of an integrated profile can often be identified by eye, RFI mitigation can be done by a manual inspection that zero-weights the indicated affected files (e.g. using PSRCHIVE, Hotan et al., 2004; van Straten et al., 2012). However, this procedure is time consuming especially for projects that require observations of multiple pulsars on a regular basis (for example PTA projects). For this reason, before a manual check of the observations, an automatic algorithm, sophisticated enough to work with diverse RFI signals is normally applied (e.g. Lazarus et al., 2016). For an example of RFI mitigation in a pulsar observation see Fig. 2.2.

2.2.2 Polarisation calibration

Pulsars are highly polarised sources. However, both the ISM (Faraday rotation), and instrumental effects (caused by the telescope observing and recording system) modify the polarisation properties of the emitted signal. The correction of intensity variations introduced to the linear polarisation by Faraday rotation will be discussed in Section 2.2.3. In this section the instrumental effects that introduce intensity and shape variations to the Stokes parameters, as well as *polarisation calibration*, the method used in pulsar astronomy to correct these effects, will be presented.

The instrumental effects that can modify the observed pulsar polarisation properties, are four and can be expressed as interdependent Mueller matrices (see, e.g. Heiles et al., 2001), which all together form a single 4 x 4 Mueller matrix, which is used to transfer from the observed ($S_{\rm observed}$) to the initial stokes parameters ($S_{\rm true}$):

$$S_{\rm observed} = M \times S_{\rm true}. \tag{2.1}$$

The first observing effect accounts for the differences of the orientation of the receiver and the pulsar. Since pulsar observations can take place at any time of year and at different times of day, the rotation of the receiver feed with respect to the plane of polarisation changes by an amount that is called the *parallactic angle*.

The second and the third instrumental effects account for the geometry of the feed. Nowadays, the majority of radio telescopes have either two orthogonal linear or circular feed receptors. However, feeds are not perfect. Electric power leakage from one feed to another and/or imperfections in the orthogonality of the feed receptors, can lead to *cross-coupling* effects.

The last effect originates from the fact that the two orthogonal signals pass through two different amplifier chains. The two feed receptors can have slightly different gains, and the differences in the length of the cables that carry the two polarisation signals can introduce phase differences on the signal. This effect is also called "differential gain and phase".

Polarisation calibration is the method with which we measure and correct these effects, in order to reconstruct the intrinsic Stokes vector of the emitted pulsar signal. Polarisation calibration is important for pulsar polarimetry studies, but also for precise timing. The reason for the latter is that some of the instrumental effects that we mentioned above, can change, among others the Stokes parameter I, that corresponds to the total intensity of the pulse profile. Since total intensity is the quantity that is commonly used to create ToAs, the lack of (or wrong) polarisation calibration will lead to distortions of the pulsar profile, introducing systematic timing errors.

The basic polarisation calibration techniques for pulsar data, are the same for both the orthogonal linear and circular feeds. The simplest method requires only a few-minute noise diode observation just prior to, or immediately after the pulsar observation. A noise diode produces an 100% linearly polarised signal that illuminates both feeds equally. The gain and

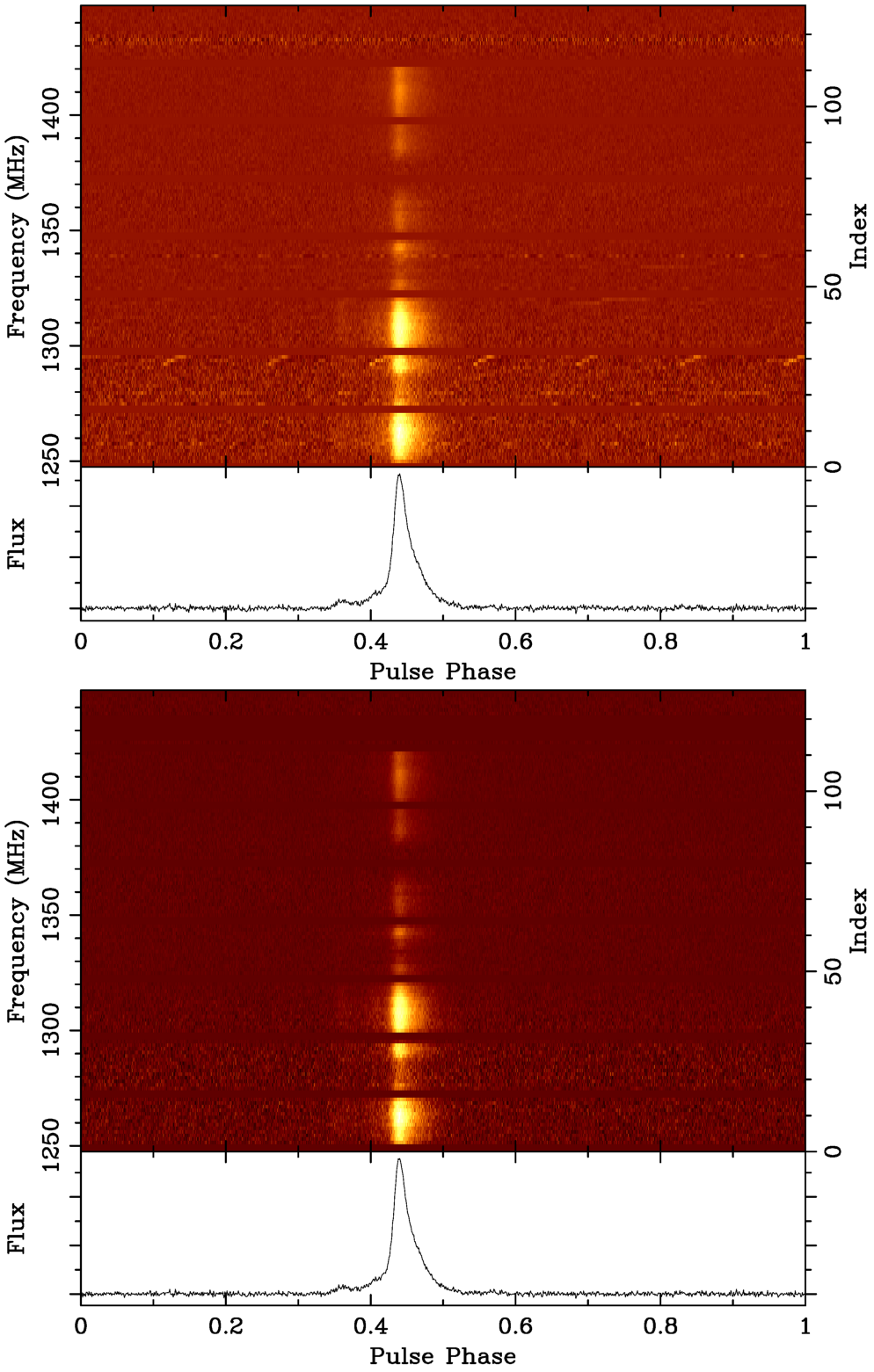

Figure 2.2: In the top plot, the intensity as a function of frequency and phase is shown, for a 30-min observation of PSR J1713+0747 taken with the 'P217 mm'. The corresponding frequency and time integrated profile, is presented bellow this colour plot. At ∼1.29 GHz, ∼1.34 GHz, and ∼1.43 GHz the frequency channels are affected by narrow-band RFI. In the bottom plot, the same observation is shown after RFI removal.

phase differences between the two feeds can then be measured in a form of a Mueller matrix which acts as a transfer function between the measured and the input Stokes parameters of the initial noise diode signal. Apart from the noise diode there are other polarisation calibration methods like Measurement Equation Modeling (van Straten, 2004) and the Measurement Equation Template Matching (van Straten, 2013). The first one requires observations of a strongly polarised pulsar, and a source with a well-determined degree of circular polarisation across a wide range of parallactic angles. The latter requires an observation of a highly polarised pulsar, as well as calibrated observations of the same pulsar.

2.2.3 RM correction

After applying the polarisation calibration all the instrumental effects that modify the polarisation properties of the pulsar will have been corrected. However, in a calibrated polarised pulsar profile the intensity of the Stokes parameters Q and U, which contain information about the linear polarisation, is not that intrinsic to the pulsar. The reason is the ISM effect of Faraday rotation. As mentioned in Section 1.8.2, and expressed in Eq. 1.19, the PPA of the linear polarisation rotates due to Faraday rotation by an amount which is proportional to the square root of the observing wavelength. If the pulsar signal is observed with wide-band receivers, each recorded frequency channel has a different PPA value. This bandwidth depolarisation effect will make the linear polarisation to appear reduced.

To reconstruct the emitted linear polarisation, we need to measure the RM and to apply this value to each polarisation channel. There are different methods to do this. One of the most common is to investigate the RM parameter space with a brute-force method in which we change the RM values until we find the one that maximizes the linear polarisation.

The RM-corrected file can then used for studying the polarimetric properties or effects that require the correct polarisation properties of the pulsar, as, for example, to extract the emission geometry of pulsars that exhibit geodetic precession, by monitoring the changes on the PPA through time. A study like this, applied to PSR B1913+16, in given in Chapter 5.

2.2.4 Flux calibration

So far the pulse profile's intensity is scaled in arbitrary units. With *flux calibration* we convert this arbitrary scale to a Jy scale. Flux calibration in pulsars requires a series of observations that will be explained below.

When we observe an astronomical source the recorded number of the machine counts received is equal to:

$$\mathrm{Level} = G(\mathrm{S_{sys}} + \mathrm{S_{src}}), \tag{2.2}$$

where G is the gain of the system, $S_{\rm sys}$ is the system temperature (also known as system-equivalent flux density, SEFD), and $S_{\rm src}$ is the flux density of the source. As can be seen from the equation above, the quantity that is needed to be measured in order to determinate the flux of the source is $S_{\rm sys}$.

A straightforward method for measuring $S_{\rm sys}$ is to perform two observations, one pointing at a reference source ($\mathrm{Level_{ON}}$) and one pointing away from this source, in the sky where no strong radio source exists ($\mathrm{Level_{OFF}}$). The two machine count levels observed by these observations can be expressed as:

$$\begin{aligned} \mathrm{Level_{ON}} &= G\,(S_{\rm sys} + S_{\rm src}) \\ \mathrm{Level_{OFF}} &= G\,(S_{\rm sys}), \end{aligned} \tag{2.3}$$

respectively. By comparing these two levels we can determinate the $S_{\rm sys}$. In order to avoid miscalculations, the source of reference should have a very well-known, stable flux density (e.g a quasar).

In the approach above we have assumed that the contribution of the system temperature is the same when we observe the pulsar and the calibrator. However, the orientation of the telescope during the observation can change the system sensitivity. Moreover, the attenuation of the signal can also change from observation to observation. To avoid these errors, which can introduce systematics on pulsar flux measurements, a noise diode signal is injected into the receiver during the flux calibration scans. The flux density scale factor, in this case, contains also the noise diode flux ($\rm S_{cal}$). The machine levels are measured with (H) and without (L) the noise diode signal and on and off the calibrator source, can be expressed as:

$$\begin{aligned} \rm H_{ON} &= G\,(S_{sys} + S_{cal} + S_{src}) & \rm H_{OFF} &= G\,(S_{sys} + S_{cal}) \\ \rm L_{ON} &= G\,(S_{sys} + S_{scr}) & \rm L_{OFF} &= G\,S_{sys} \end{aligned} \tag{2.4}$$

By comparing these levels, we measure the $\rm S_{src}$ and $\rm S_{cal}$, independently from the $\rm S_{sys}$ and the gain. With these simple few-minute observations of the noise diode before the pulsar observation, we can create a conversion factor, with which a conversion from the arbitrary flux density units to flux densities in Jy can be achieved.

While flux density measurements are important for understanding the emission mechanism and the NS population in the Galaxy, they are not critical for timing analysis.

2.3 Timing analysis

After being cleaned of RFI, and polarisation and flux density calibrated, the folded profiles are ready to be used for applying timing techniques. Pulsar timing requires an initial timing model, and multiple ToA measurements. By comparing the predicted and measured pulse rotational phases, we refit our initial model until these differences are minimized. The aim is to create a model that account for every emitted pulse. With this method, we can measure the pulsar spin period and spin-down rate, the astrometric parameters like the position and proper motion, the ISM electron density, and binary parameters, at a very high precision. The position and proper motion, for example, can be measured with precisions of microarcseconds and microarcseconds per year, respectively, quite comparable to Very-Long-Baseline Interferometry (VLBI) results. All these extracted parameters can be used for further studying the pulsar's evolution and its environment.

Timing analysis includes the implementation of Keplerian and relativistic effects into the model; fitting procedures; modeling, and mitigation of red noise, introduced by various effects. Most of these steps are carried out with well-tested timing programs. The most widely used are TEMPO[1] and TEMPO2 (Edwards et al., 2006; Hobbs et al., 2006).

2.3.1 ToA measurement

ToAs are the fundamental data of timing. A ToA is defined as the time that a pulse profile arrives, relative to a reference phase. The reference phase is set by a *template*. A cross-correlation of this template with the pulsar profiles creates the ToAs.

Each integrated pulse profile created in an observation, is a coherent addition of usually $\geq 10^4$ single pulses. We use integrated profiles because they are morphologically stable, in contrast to single pulses, which exhibit large variations in their S/N and in their morphological

[1] http://tempo.sourceforge.net/

characteristics from pulse to pulse, due to jitter noise. Jitter noise causes a wrong measurement of ToA values as well as wrong estimate of their uncertainties, which leads to incorrect determination of the uncertainties of the timing parameters. For each integrated profile, we measure the time ($t_{\rm fiducial}$) at which a chosen reference point, called fiducial point, arrives to the telescope. This point is usually near the mid-point of the time interval.

As mentioned above, all pulse profiles are correlated with a template. A template is, typically, an addition of multiple good S/N pulse profiles at a particular observing frequency, noised-free by either fitting Gaussian functions (Kramer et al., 1994), or wavelet transforms (Demorest et al., 2013) to the pulse profile. With this process we create a noise-free template, avoiding any correlation between the noise components of the template and the profile. Each integrated pulse profile $P(t)$ can be expressed as a scaled and shifted version of the template $T(t)$, with the addition of a radiometer and background noise $N(t)$ (Lorimer & Kramer, 2012):

$$P(t) = \mathrm{a} + \mathrm{b}T(t-\tau) + N(t), \tag{2.5}$$

where a, b, and τ the time shift between the fiducial point and the profile.

A cross-correlation of the template with the profile defines the phase shift between their fiducial points. The phase shift is traditionally calculated in the phase domain with the Fourier phase gradient algorithm. With this method a precision smaller than a tenth of the sampling bin size can be achieved (Taylor, 1992). The phase shift is converted to a time offset, τ, by multiplying it with the pulsar period. An addition of τ to the fiducial observing time defines the ToAs also referred to as the site arrival times (SAT):

$$t_{\rm SAT} = \tau + t_{\rm fiducial}. \tag{2.6}$$

ToAs are typically reported in Modified Julian Dates (MJD).

Due to frequency evolution of pulse profiles (see Section 1.6.2), the template can only be used for cross-correlating observations of the same frequency. Especially with the recent development of broadband receivers this issue is very important. New sophisticated techniques to create 2D templates, which can be used to measure the pulse phase but also the DM, have been introduced to account for this effect (Pennucci et al., 2014; Liu et al., 2014).

Advanced cross-correlation techniques for increasing the ToA precision and reducing systematic effects, have been introduced through the years. Here we will mention specifically a technique developed by van Straten (2006), in which not only the total intensity, but also the polarisation information of the profile and template are used for cross-correlation. With this method systematic effects that occasionally introduced when we use only the total intensity, are avoided. An application of this technique can be seen in Chapter 4.

The precision with which we can measure a ToA is proportional to the pulse width (W) divided by the average S/N of the pulse profile, using radiometric equation[2] (Lorimer & Kramer, 2012):

$$\sigma_{\rm ToA} \approx \frac{W}{S/N} \propto \frac{S_{\rm sys}}{\sqrt{t_{obs}\Delta f}} \frac{1}{S_{\rm mean}} \frac{W}{\sqrt{P}}, \tag{2.8}$$

where t_{obs} is the integration time, P the spin period, Δf the bandwidth, and $S_{\rm mean}$ the mean flux density of the pulsar.

[2]The radiometer equation, a basic measurement of system sensitivity, can be expressed as (Dicke, 1946):

$$\Delta_{\rm sys} = \frac{T_{\rm sys}}{\sqrt{n_{\rm p} t \Delta f}}, \tag{2.7}$$

where $t_{\rm obs}$ is the integration time, Δf is the observing bandwidth, and $n_{\rm p}$ is the number of polarisation.

Thus, the most precise ToA measurements are to be expected from bright rapidly spinning pulsars, with narrow pulse profiles, for some pulsars $\sigma_{\rm ToA}$ can be as low as a few tens of ns (e.g. Shannon et al., 2015; Verbiest et al., 2009). For pulsar observations with more sensitive systems we expect an improvement in ToA precision. However, the full expected benefit from new observing systems has not been observed in ToAs, due to the presence of jitter noise which is unaffected by sensitivity improvements (see Section 2.3.4).

2.3.2 Timing model

With template matching we measure ToAs in the telescope frame (topocentric frame). The topocentric ToAs should be converted to a pulse emission time at the pulsar. This conversion is not simple, since many effects both Newtonian and relativistic, introduce delays to the ToAs, like for example the existence of massive bodies in the Solar System, or in the pulsar's environment (a companion star or planet), and ISM propagation effects. However, since the number and the nature of these effects are diverse, the conversion from the Earth to the pulsar's frame is more efficiently done in a series of frame transformations.

First, the ToAs are transversed to the Solar System barycentre (SSB) ($t_{\rm SAT} \rightarrow t_{\rm BAT}$), then, in the case that the pulsar has a companion, to the binary system barycentre (BB) ($t_{\rm BAT} \rightarrow t_{\rm BB}$), and last to the pulsar emission time ($t_{\rm BB} \rightarrow t_{\rm em}$). The frame transformations, following Taylor (1992), can be expressed as:

$$t_{\rm SSB} = t_{\rm SAT} - t_0 + \Delta_{\rm CLK} - D/f^2 + (\Delta_{\rm R\odot} + \Delta_{\rm E\odot} - \Delta_{\rm S\odot}) - (\Delta_{\rm R} + \Delta_{\rm E} + \Delta_{\rm S} + \Delta_{\rm A}), \quad (2.9)$$

where t_0 is a reference ToA; $\Delta_{\rm CLK}$ term corrects the telescope time to the terrestrial time standard; D/f^2 is the dispersive delay due to pulse propagation through ISM; $\Delta_{\rm R\odot}$, $\Delta_{\rm E\odot}$, and $\Delta_{\rm S\odot}$ terms are the Römer, Einstein, and Shapiro delay, respectively, that are correspond to propagation delays inside the Solar System; $\Delta_{\rm R}$, $\Delta_{\rm E}$, and $\Delta_{\rm S}$ are the same corrections corresponding to pulsar's orbital motion; and $\Delta_{\rm A}$ is a term related to aberration effects. All these terms, are expressed with more detail in the Sections below.

2.3.2.1 Barycentric corrections

ToAs measured with atomic clocks in the Earth frame are affected by the spin and orbital acceleration, and variations in gravitational potential, due to the elliptical motion of the Earth. To avoid these effects, ToAs should be transformed from a telescope frame to a frame defined by an observer located at a fixed point in the Solar System, the SSB. To do so, we first convert the site time, to terrestrial time (TT). TT is referred to the geocentre, in order to correct time dilation effects caused by altitude differences in the locations of different atomic clocks.

Initially, the ToAs are time stamped with the maser clock at the observatory. Maser clocks are very good frequency standards, over time scales of a few days. But we also need a precise time standard that is stable over longer time scales, so we constantly compare the observatory time to the GPS-based Coordinated Universal Time, measured by the US National Institute of Standard and Technology (NIST): UTC(NIST). The offsets of these two time standards are stored, regularly, to a clock file. The UTC(NIST) time is, then, converted to UTC. UTC is based on the International Atomic Time (TAI). But, while TAI is smooth, UTC is adjusted by leap seconds in order to take into account the decreasing rotational rate of Earth. TAI, the most precise real time standard available, is a weighted average of the time kept by over 400 atomic clocks in over 50 national laboratories worldwide. The conversion from UTC to TAI is done by just the subtraction of the leap seconds. Once published by the Bureau International des Poids et Mesures (BIPM), TAI is not revised again for taking into account small instabilities,

for this reason a better realisation of TT (TT(BIPM)) which takes into account these errors is needed. TT is a theoretical time standard, tied to TAI by a constant number of seconds (TT = TAI + 32.184 s). It is defined as the ideal time of an atomic clock located at the geocentre, and is consisted with GR. TT(BIPM), in contrast, is a yearly corrected version of TT(TAI). See Hobbs et al. (2012) for more details about time standards on pulsar timing.

So far, ToAs converted to TT are still referring to the Earth's frame. By taking into account the *Römer delay* and relativistic effects of *Shapiro delay* and *Einstein delay*, we can convert them to the SSB frame. The Einstein delay is caused by the relativistic time dilation, due to the orbital acceleration of the Earth, and gravitational redshift, caused by the bodies in the Solar System. To apply this correction we need accurate measurements of the masses and the positions of the major bodies in the Solar System. The Jet Propulsion Laboratory (JPL) provides these measurements regularly, in a Solar System ephemeris (SSE), for example 'DE405' and 'DE421'. The SSE model that is used in timing analysis is specified in the timing model. After correcting for the Einstein delay, the ToAs are referred to Barycentric Coordinate Time (TCB). TCB represents the time that is measured by an observer located at the SSB, without being influenced by the gravitational fields of the Sun and the planets.

Two further corrections should be applied to the TCB time in order to accurately convert ToAs from site arrival time (SAT) to SSB. The first one is another relativistic effect: the *Shapiro delay*, and the other one is a geometric effect: the *Römer delay*.

The Römer delay is a classical effect which accounts for the differences between the arrival of the pulse at the observatory and at the SSB, due to the orbital motion of the Earth, without taking into account the pulsar binary motion, and extra delay introduced by nearby pulsars[3]. If this effect is not taken into account, we observe annual variations in the pulse arrival times, since ToAs arrive earlier when the Earth is closer to the pulsar, and later when the Earth is away from the pulsar. These delays can introduce deviations of ToAs up to $\sim$500 s, much larger than the period of known pulsars. The correction of this delay requires an accurate pulsar position, and precise knowledge of the Earth's motion. But since the motion of the Earth is affected by the other masses on the Solar System, a SSE should be included in the timing model, so that the Römer delay can be measured accurately.

2.3.2.2 Interstellar corrections

Interstellar dispersion affects the arrival time of the pulsar's emitted signal. As described in Section 1.8.1, dispersion is caused by the fact that different electromagnetic frequencies travel at different speeds in an ionized, cold plasma. The delay introduced by these differences in group velocity, depends on the electron density in the direction of the pulsar (DM), and is inversely proportional to the observed frequency squared. However, the observed frequency in the telescope reference frame is different from the frequency at the SSB, due to the Doppler shift caused by the Earth's motion and relativistic effects. As for all effects mentioned above, an accurate SSE should be used in order to calculate the velocity of the telescope, so that the Doppler shift can be corrected.

Unmodeled DM variations can also cause delays in ToAs. DM variations are caused by

[3] Another delay, which is not part of barycentric corrections, introduced only for pulsars close enough to the Solar System is the *annual parallax*. For these pulsars we are able to observe the curvature of the pulse wavefront. The curvature shape of the wavefront causes another delay, which is not correctable by Römer delay, but which also depends on the orbital position of Earth during the observations. The effect has a half-year period, and causes variations in ToAs which amplitude equal to $l^2\ cos\beta/(2cd)$ (Lorimer & Kramer, 2012), where l is the Sun-Earth distance, d is the pulsar distance, and β is the pulsar's ecliptic latitude. Clearly, the parallax effect is stronger for nearby pulsars that are close to the ecliptic plane.

spatial variations in the ISM density, are often found to be at magnitude of order 10^{-3} pc cm^{-3} per year (Keith et al., 2013). Unmodeled DM variations introduce red noise in the timing residuals, and for projects like PTAs in which high precision is needed, this should be corrected. A way to correct these variations is to regularly monitor the pulsar at multiple frequencies, since ISM effects are mostly frequency dependent (see for example Keith et al., 2013; Lee et al., 2014; Lam et al., 2016). When DM variations are measured, a DM model can be created and added in the pulsar ephemerides. In Chapter 3, an investigation of the usefulness of existing and future observing systems for correcting DM variations, is presented.

2.3.2.3 Binary corrections

In case the pulsar is isolated, the arrival time at the SSB, which is measured after the corrections mentioned above, is only a constant offset away from the pulse emission time. However, when the pulsar is in a binary system further corrections due to binary motion should be included. This series of corrections follows the same concept as SSB corrections due to the orbital motion of the Earth. Thus, since in SSB corrections a precise model of the Earth's motion is needed, correspondingly in BB corrections a precise model of the pulsar's orbital motion is required.

This model can be purely Newtonian, if relativistic effects can be ignored. In this case the binary motion of the pulsar can be described with 5 Keplerian parameters:

1. the *orbital period* ($P_{\rm b}$), measured in days,
2. the *projected semi-major axis* ($x_{\rm p} = a_{\rm p}{\rm sin}i/{\rm c}$), measured in light seconds,
3. the *orbital eccentricity* (e), which ranges between 0 (for circular orbits) and 1,
4. the *longitude of periastron* ($\omega_{\rm p}$), measured from the ascending node to the periastron, only defined for $e > 0$,
5. and the *epoch of periastron passage* (T_0), measured in MJDs.

The temporal position of a pulsar in an elliptic orbit is described by Kepler's equation:

$$M = E - e \sin E, \tag{2.10}$$

where M is the mean anomaly, and E is the eccentric anomaly. M defines the angular distance of the pulsar's position across the ecliptic orbit, from the periastron as measured from the centre of the orbit. While E, defines the angular distance of a fictitious body which moves in an auxiliary circle of a radius equal to semi-major axis as measured from the centre of the orbit (see Fig 2.3). The relation of M with time can be expressed as (Roy, 1988):

$$M = \frac{2\pi}{P_b}(t - T_0). \tag{2.11}$$

Kepler's equation can only be solved numerically after having first measured the mean anomaly through Eq. 2.11.

In addition to M and E there is a third anomaly: true anomaly, A_T, which, as M, defines the angular distance from the periastron to the pulsar position, as seen, in this case, from the BB. The relation between true anomaly and the eccentric anomaly is (Roy, 1988):

$$\tan\left(\frac{A_{\rm T}}{2}\right) = \sqrt{\frac{1+e}{1-e}}\,\tan\left(\frac{E}{2}\right). \tag{2.12}$$

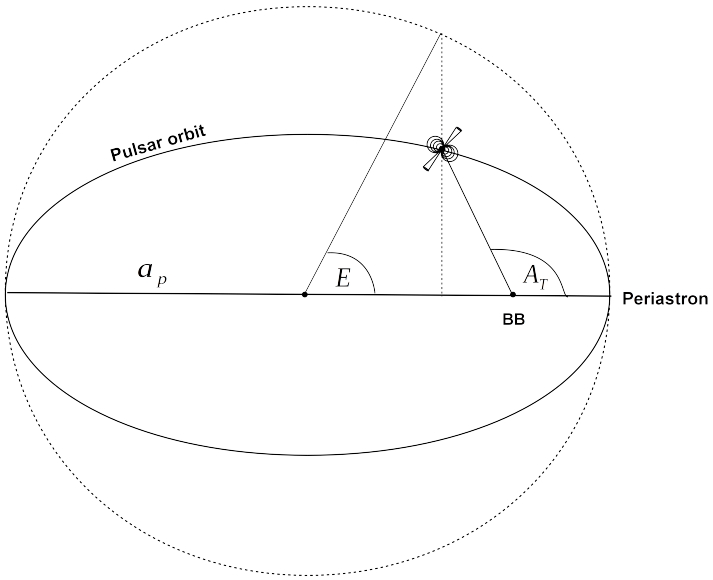

Figure 2.3: The eccentric (E) and the true anomaly ($A_{\rm T}$) of the pulsar at the specific orbital point is presented (For the definition of these angles see text.). The figure is based on Fig. 2.10 of Ridolfi (2017).

Having solved Kepler's equation we can further describe the pulsar's motion with Kepler's third law:

$$4\pi^2 \frac{\alpha_{\rm R}^3}{{\rm G}(m_{\rm p}+m_{\rm c})} = P_{\rm b}^2, \tag{2.13}$$

where $m_{\rm p}$ and $m_{\rm c}$ are the mass of the pulsar and the companion, respectively, and $\alpha_{\rm R}$ the semi-major axis of the relative orbit. Based on this, we can express the size of the pulsar's and the companion's orbit, $\alpha_{\rm p}$, and $\alpha_{\rm c}$ respectively, with respect to the centre of mass as a function of the masses:

$$\begin{aligned} \alpha_{\rm p} &= \alpha_{\rm R} \frac{m_{\rm c}}{(m_{\rm p}+m_{\rm c})} \\ \alpha_{\rm c} &= \alpha_{\rm R} \frac{m_{\rm p}}{(m_{\rm p}+m_{\rm c})} \end{aligned} \tag{2.14}$$

For a Keplerian pulsar orbit, the five Keplerian parameters can be determined through timing. The inclination angle remains unknown, unless the orbit can be seen nearly edge-on so the Shapiro delay effect, due to companion's mass, has a measurable impact on ToAs. Without the inclination angle, the system masses are also unknown. By associating them through the mass function (Eq. 1.25), we can, only, set, limits on their values.

In the case that relativistic effects cannot be ignored, PK parameters should be introduced to describe the corrections that need to be made to a Keplerian orbit. PK parameters depend on the system masses and the Keplerian parameters, which are easily measured from timing. The five PK parameters that have to date been measured with timing are: the rate of periastron advanced, $\dot{\omega}_{\rm p}$; the time dilation and gravitational redshift parameter, γ; the orbital decay, $\dot{P}_{\rm b}$; the range, r, and shape, s, of the Shapiro delay (Damour & Taylor, 1992).

The relation of PK parameters with masses can be demonstrated on a "mass-mass" diagram. If more than two lines which correspond to the region allowed by PK parameters, intersect within the uncertainties, then the theory of gravity used is consistent with the observations. The intersection point defines the system masses. For a relativistic system if two (at least) of the PK parameters are measured, system masses can be determined, for a given theory.

With the analysis above we can describe the orbit of the pulsar with respect to the BB. However, further corrections should be applied in order to transform from the BB to the time of pulsar emission. The basic corrections are: Römer, Shapiro, and Einstein delay. The Römer delay is caused by the orbital motion of the pulsar around the BB, and the difference that this motion causes in the pulse arrival time at the BB. Shapiro delay is caused by the extra time that the pulse takes, when it passes close to the curved spacetime of the companion. Einstein delay, is a result of the delay introduced by the time dilation, due to the pulsar orbital acceleration, and gravitational shift, due to the companion's mass.

2.3.3 Timing residuals

With the corrections mentioned above, the pulse emission time ($t_{\rm em}$) is derived. If we assume that the spin-down process in pulsars is only due to dipolar radiation (see Section 1.3), and for every rotation a single pulse is emitted, then the rotational phase evolution can be expressed with a Taylor expansion as:

$$\phi(t_{\rm em}) = \nu t_{\rm em} + \frac{1}{2}\dot{\nu} t_{\rm em}^2 + \frac{1}{6}\ddot{\nu} t_{\rm em}^3 + ..., \tag{2.15}$$

where ν, $\dot{\nu}$, and $\ddot{\nu}$ are the spin frequency and its first and second derivative, respectively. Since for every rotation a single pulse is emitted, the phase difference between any two ToAs should be an integer number of rotations.

The $\phi(t_{\rm em})$ of each ToA is then compared with the corresponding phase, predicted by the theoretical model ($\phi_{\rm theo}$), to form the *timing residual*:

$$R_i = \phi_i(t_{\rm em}) - \phi_i(t_{\rm theo}). \tag{2.16}$$

Our goal is to create a timing model for which the rms of the timing residuals has a minimum value. This timing model, also referred to as the *phase-coherent solution*, as it is able to account for every rotation of the pulsar, within a small fraction of the pulsar spin. The most common method to evaluate the quality of the timing model is the reduced χ^2 (e.g. Taylor & Weisberg, 1989):

$$\chi^2 = \frac{1}{N_{\rm free}} \Sigma_i \left(\frac{\phi_i(t_{\rm em}) - \phi_i(t_{\rm theo})}{\sigma_i} \right)^2, \tag{2.17}$$

where σ_i is the uncertainty of the ith ToA, and $N_{\rm para}$ the number of degrees of freedom. For a correct and complete timing model we expect $\chi^2 \approx 1$, and the residuals to be Gaussianly distributed around zero with a root mean square comparable to the ToA uncertainties.

In practice, at the end of this process, we may observe deviations from $\chi^2 \approx 1$. These deviations can come from either overestimation or underestimation of ToA uncertainties, or non-Gaussian noise. ToAs are formed after template-matching techniques as explained in Section 2.3.1. However, noise introduced by effects that are either intrinsic to the pulsar or extrinsic (which will be discussed in Section 2.3.4) as well as not properly removed RFI, lead to underestimated ToA uncertainties. To solve this problem either an 'EFAC' or an 'EQUAD',

(or both) can be added into the timing model. The 'EFAC' accounts for incorrect ToA uncertainty scaling, so it just multiplies the measured ToA uncertainties: $\sigma^2 = \mathrm{EFAC}^2 * \sigma^2_{\mathrm{ToAs}}$. The 'EQUAD', on the other hand, accounts for unmodeled sources of noise, so it is added in quadrature to the measured ToA uncertainties: $\sigma^2 = \mathrm{EQUAD}^2 + \sigma^2_{\mathrm{ToAs}}$.

Deviations from $\chi^2 = 1$, or clear trends in the residuals can also be observed in cases where timing parameters, like for example pulsar position or proper motion, are not correctly taken into account, or are unmodeled. This is often observed in newly discovered pulsars and/or in pulsars for which ToAs have insufficient cadence, and/or the timing span is not enough to model all physical properties that can fully predict the pulse emission time.

The least-squares method is the most popular process of fitting model parameters, and is usually performed with the TEMPO or TEMPO2 packages. However, with this technique it is assumed that there are no covariance matrices and non-linearities in the timing parameters, and that ToA uncertainties are only due to white noise. To measure correctly ToA uncertainties in the presence of covariances we can apply a brute force method like a χ^2 map, with which we create a grid of values and we calculate the χ^2 in each point, or we can use a Bayesian approach with a package created for pulsar timing called TEMPONEST (Lentati et al., 2014). TEMPONEST is a combination of TEMPO2 and the Bayesian tool MULTINEST (Feroz & Hobson, 2008; Feroz et al., 2009a). With this package timing parameters can be measured and also limits on an isotropic stochastic GWB have been set (Lentati et al., 2015).

2.3.4 Sources of noise

Time-correlated structures in timing residuals that cannot be explained by the timing model can originate from noise. If noise is not taken into account in the timing analysis, it can lead to underestimation of ToA uncertainties, causing degradation of timing accuracy. Noise can be either intrinsic to the pulsar or extrinsic, and can be influenced by (chromatic) or be independent of (achromatic) observing frequency. The noise power spectrum can be either white (a flat spectrum at all spectral frequencies) or red (increasing power at lower spectral frequencies). Since the stochastic GWB is expected to have a red spectrum, it is very important for red noise from other sources to be understood, and even mitigated (e.g. Rajagopal & Romani, 1995; Sesana et al., 2004).

While the noise origin is still poorly understood, possible intrinsic and extrinsic red noise sources have been identified. Among possible intrinsic sources are spin noise (Lentati et al., 2016), and magnetospheric torque variations (Lyne et al., 2010). Some of the extrinsic sources are DM variations (e.g. Keith et al., 2013), ISM propagation effects (Hemberger & Stinebring, 2008), possible errors in TT standards (Hobbs et al., 2012), and errors in the SSE (Champion et al., 2010).

The dominant source of extrinsic red noise is DM variations (e.g. Lentati et al., 2016; Verbiest et al., 2016). DM variations are caused by temporal variations on the observed column density of electrons along that line of sight, due to the pulsar's motion. Typical DM variations are from 10^{-4} to 10^{-3} pc cm^{-3} per year (e.g. Keith et al., 2013), with power spectrum $\propto f^{-8/3}$, if a Kolmogorov spectrum is assumed (Armstrong et al., 1995). During a typical observing session, DM variations are too small to be detected, but high-precision timing requires the removal of DM variations between epochs (Liu et al., 2011). Unlike spin noise, DM variations are frequency dependent. The reason for this frequency dependency is that the refractuin makes the group velocity frequency-dependent. Thus, a way to mitigate DM variations is to perform quasi-simultaneous multi-frequency observations (e.g. Keith et al., 2013).

A strong source of red noise in canonical pulsars is *spin noise*. Spin noise is caused by

rotational irregularities of the pulsar. These irregularities probably come from changes in magnetospheric torque, and are often observable in canonical pulsars, but also in some MSPs (e.g. PSR J1939+2134 (B1937+21)). Moreover, rotational irregularities can be the result of a glitch event. Glitches are spin-up events more probably originating from internal torques from crust-superfluid interactions. Glitches have been observed in canonical pulsars, but also in two MSPs so far (PSRs B1821−24A, and J0613−0200, Cognard & Backer, 2004; McKee et al., 2016). These stochastic spin variations are a source of red noise in pulsars. There is no current method for removing spin noise from timing residuals. However, since the spin noise spectrum is red and for some MSPs can be even steeper than the expected spectrum from the stochastic GWB, the GWB signal will be highly correlated with the spin noise of each pulsar in the data set. Thus, the characterization of spin noise spectrum properties of MSPs is important for estimating the time of GW detection with PTAs.

Radiometer noise, is white. It is uncorrelated in time, and originates from the fact that the sky background, like pulsar flux density, has a frequency dependence ($T_{\rm sky} \propto f^{-2.7}$). Thus depending on the pulsar flux density spectral index, sky brightness can introduce an error in ToAs. Radiometer noise can be reduced by increasing the integration time per ToA, and by observing the pulsar with more sensitive systems (larger collecting area, lower system temperature, and wider recording bandwidth), obtaining using Eq. 2.7.

Jitter noise is white. It is caused by stochastic, broadband, pulse-shape variations intrinsic to the pulse emission process. In nearly every pulsar, observed with sensitive systems, single pulses show variations beyond those expected from radiometer noise. These variations can be in amplitude and in phase, and can be either correlated or uncorrelated from pulse to pulse. For jitter noise, it is uncorrelated from pulse to pulse, so the rms contribution to residuals scales as $1/\sqrt{N}$, where N is the number of pulses added to the integrated profile. Jitter noise is expected to significantly affect timing of pulsar observations for which the single-pulse S/N exceeds unity (Osłowski et al., 2011; Shannon & Cordes, 2012). A few studies have investigated the contribution of jitter noise to the timing of MSPs (Liu et al., 2011; Osłowski et al., 2011; Shannon & Cordes, 2012; Shannon et al., 2014). The MSPs included in those studies, are the brightest ones for obvious reasons (PSRs J0437−4715, J1022+1001, J1603−7202, J1713+0747, J1744−1134, J1909−3744, J1939+2134, and J2145−0750). In these pulsars, the limits on timing precision introduced by jitter noise, for 1-hr integration time, scales from few tens to few hundreds of ns. Thus, the timing precision that can be achieved with very sensitive telescopes (larger collecting areas, lower system noise, and broader bandwidth), will be limited by the jitter noise. The increase of integration time per ToA, will be the only recourse to increase the timing precision.

Chapter 3

Prospects of determining DM variations with Effelsberg multi-frequency observations

Part of the results that are presented in this chapter have been published in:

Lazarus P., Karuppusamy R., **Graikou E.**, Caballero R. N., Champion D. J., Lee K. J., Verbiest J. P. W., Kramer M., *"Prospects for high-precision pulsar timing with the new Effelsberg PSRIX backend"*, 2016, MNRAS, 458, 868

For this publication, I performed and I reduced part of the observations, and I measured the phase-averaged flux densities of observed pulsars at 1.4 GHz.

Abstract

In this chapter we investigate the usage of Effelsberg and MeerKAT high-frequency receivers (both those presently used and those being commissioned) for measuring DM variations and increasing the sensitivity to continuous GWs and GWBs. We review the existing multi-frequency Effelsberg EPTA data set, which consists of monthly observations at 1.4, 2.6, and 4.85 GHz. The phase-averaged flux densities of 33 pulsars at 21 cm are reported and compared with previously published measurements. For five of these pulsars these kinds of measurements are reported for the first time. For the pulsars with the longest data set we further report S/Ns, ToA uncertainties, phase-averaged flux densities, flux spectral indices, and DM variation measurements. We discuss the potential of complementing the existing EPTA data set with receivers that are now in a commissioning stage. We concluded that for the currently used Effelsberg 11-cm receiver combined with the 21-cm receiver, an addition of 6.7 years of observations for GWB and another 80 years for continuous GWs are needed in order to achieve the same sensitivity as we expect for the Effelsberg 21-cm combined with MeerKAT 11-cm observations.

Contents

3.1 Introduction

The main goal of the EPTA is to detect GWs in the nanohertz regime. The expected GW signal is very weak. Thus, in order to be detected in the timing residuals, timing stability of more than 10 ns over a timescale of more than five years (Jenet et al., 2005), is required. The integral requirement of such high precision timing is very accurate deterministic timing models, which account for all known physical effects, which affect ToAs. However, such high precision is not so easily achieved, as besides of deterministic processes present in pulsar timing data, timing precision is perturbed by stochastic processes: uncorrelated (white) and correlated (colored) in time. The dominant source of the colored noise in MSPs is DM variations (Lentati et al., 2016).

When the pulsar signal propagates through the ISM, due to the electron density along the line of sight a group delay is introduced, which, as mentioned in the introduction, is proportional to: $\tau_{\rm DM} \propto {\rm DM} f^{-2}$. In the majority of studies DM is treated as a constant. However, as pulsars move fast, their line-of-sights cross different parts of the ISM at different times resulting in DM variations. Thus, for studies that long-term monitoring of pulsars is required, like PTAs, temporal DM variations should be taken into account. These variations, as has shown in multiple studies (e.g. Lam et al., 2016), and supported by theory, have access of power at low frequencies.

The primary source of DM variations is thought to be plasma turbulence in the ISM[1]. Such turbulence usually has a Kolmogorov power spectrum, meaning that variations are larger over longer time scales. In addition to Kolmogorov turbulence, local structures introduce DM variations. Some examples of such local structures are: supernova remnants (e.g. in the Vela pulsar the DM decreased by 0.04 pc cm^{-3} yr^{-1}, Hamilton et al., 1985), the ionised envelope of a companion star (e.g. for PSR J0023−7203J in 47 Tuc DM changes of 0.0065 pc cm^{-3} have been observed, Freire et al., 2003), and the solar wind (Tiburzi & Verbiest, 2018). The amplitude of DM variations depends on the distance and the velocity of the pulsar, ranging from 10^{-4} to 10^{-3} pc cm^{-3} per year (Keith et al., 2013). If variations of this amplitude are not taken into account at a typical observing frequency of 1.4 GHz, for example, a delay of $\sim$2 μs will be added to ToAs. For PTA projects, DM variations require correction within few days or weeks.

Another ISM effect that introduces delays in ToAs is scattering. Scattering, as introduced in more detail in Section 1.8.3, broadens the pulse shape. The broadening is chromatic, scaling as $t \propto f^{-X}$, where X = 4.4 for a Kolmogorov medium in moderate scattering regime. However, deviations from this picture has been observed (e.g. Bhat et al., 2004, X = 3.86), which

[1]Changes of the electron content in the ionosphere also cause (mostly insignificant) DM variations (10^{-5} pc cm^{-3}) that do not have to be corrected (Bilitza et al., 2016).

also shown a DM dependence, with high DM (> 400 pc cm^{-3}) pulsars show significant departures from the Kolmogorov spectrum (Löhmer et al., 2004). For example, in the case of a pulsar with DM 30 pc cm^{-3} observed at 1.4 GHz the pulse broadening is ∼34 ns and if observed at 4.5 GHz, it would be ∼0.4 ns. For the current ToA uncertainties that we have with PTAs, scattering delay variations are not significant, partly also because PTA MSPs are typically nearby sources, and the PTA observing frequency range.

Since both the delays introduced to ToAs by DM variations and scattering are smaller at higher frequencies (> 2.0 GHz), it is natural to assume that by observing at these frequencies the amount of red noise introduced by DM variations in the residuals will be reduced as well. However, the radio flux density spectrum of pulsars in not flat but approximately follows a power law: $S(f) \propto f^{\xi}$, where $-4 \leq \xi \leq 0$ is the spectral index (Maron et al., 2000), with mean value -1.4 ± 0.2 (Bates et al., 2013). The negative spectral index means that at high observing frequencies the S/N is lower and since ToA uncertainty is inversely proportional to S/N, high precision timing is more easily achieved at frequencies around 1.0 GHz. For the reasons mentioned above, ISM variations can not be completely ignored by observing at high frequencies but instead they should be carefully measured and removed from our data.

The only way to measure DM variations is to perform multi-frequency observations (see for example extended studies by You et al., 2007; Keith et al., 2013; Demorest et al., 2013). In order to increase our sensitivity to DM variations we should put emphasis on picking the right observing frequencies when we perform these observations.

The ideal case is when these observations are done simultaneously, since small DM variations over a period of a few days (∼10^{-4}–10^{-5} pc m^{-3}) can add significant noise to ToAs. The best solution to this problem is observations with receivers that cover more than one frequency band (broadband [2] or dual/triple-band receivers). In this case for each part of the frequency band different ToAs can be calculated. But when broadband receivers are not available we cannot avoid inner-day differences between observations and, as a result, a remaining error in the DM estimate. Lam et al. (2015) assuming that the ISM is a Kolmogorov medium concluded that for nearby pulsars a timing error of about 10 ns is introduced for observations taken within one day. While for observations further apart the timing error introduced increases following a $\tau^{\beta-2}$ scaling, where $2 < \beta < 4$. While this error limits the timing precision that required for GWs detection, with current PTAs we have not reached this timing precision in order to be sensitive to DM variations caused on a time scale of few days.

Apart from picking the right time difference, it is also very important to choose the best observing frequencies that minimize the error in the DM measurement. In this concern we should also take into account frequency-dependent DM variations. Chromatic DM variations are caused by ISM electron density micro-structure fluctuation. Diffraction and scattering effects cause from these fluctuations create a multi-path propagation that is strongly frequency dependent. Cordes et al. (2016) in their analysis after modeled frequency-dependent screen-averaged DM they concluded that for nearby pulsars (DM $\lesssim$ 30 pc m^{-3}) observed with bandwidths exceeding an ovtave in frequency range, an error of 100 ns is introduced in the timing residuals. While for pulsars with larger DMs, observed with wider frequency ranges this error increased to microseconds and more.

In the following sections we will investigate the usage of the existing and future Effelsberg receivers, with central frequencies ranging from 1.3 GHz to 5 GHz, in measuring and correcting ISM variations. We will start by describing the observations and data analysis in Section 3.2. Next, in Section 3.3.1, we will present the pulsar selection procedure based on

[2] With broadband receiver we mean a fractional bandwidth (bandwidth divided by the central frequency) of 1/3 or more.

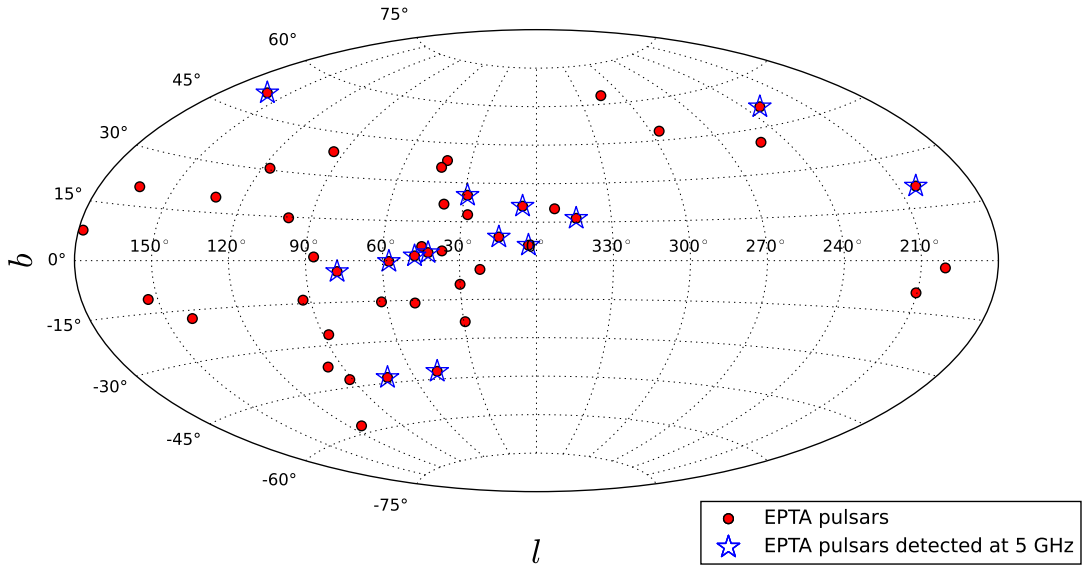

Figure 3.1: The galactic distribution of the EPTA pulsars observed regularly with the Effelsberg radio telescope at 1.4 GHz, is presented with red circles, while the subset of these pulsars that are also monitored at 4.85 GHz are shown with blue stars.

Effelsberg flux density measurements. In Section 3.3.2 we will compare the profile evolution and ToA uncertainty of our multi-frequency observations. In Section 3.3.3 the DM variations based on our observations are given, followed by DM variations based on simulated data in Section 3.3.4. The implication for the existing Effelsberg and new Effelsberg and MeerKAT receivers being commissioned for detecting continuous GWs and the GWB are presented in Section 3.4, followed by concluding remarks in Section 3.5.

3.2 Observations and data analysis

For our analysis we used EPTA observations with the Effelsberg radio telescope recorded with the PSRIX backend from 2012 January to 2016 December. The Effelsberg EPTA campaign consists of monthly observations of around 42 pulsars at ∼1.4 GHz and around 20 pulsars at ∼2.6 GHz (see Fig. 3.1). For the 1.4-GHz observations either the central beam of the 7-beam receiver 'P217 mm' or the single-feed receiver 'P200 mm' is used, providing a recording bandwidth of 200 MHz and 140 MHz respectively. The 2.6 GHz observations are done with the 'S110 mm' secondary-focus receiver. The maximum time span between those two frequencies was two days. All receivers mentioned have circularly polarised feeds. In all cases the data were recorded with the PSRIX backend, which provides a coherently de-dispersing real-time folding mode. For more details about the receivers used see Table 3.1.

Since 2015 August, we have included the observing frequency of 4.85 GHz in our monthly Effelsberg EPTA observations (Lazarus et al., 2016). For these observations the 'S60 mm' secondary-focus receiver is used combined with the PSRIX backend. The recording bandwidth provided is 500 MHz, much broader than the 80 MHz bandwidth available with the 'S110 mm' receiver. The main goal of these observations was to investigate and compare the performance of the 'S60 mm', with the 'S110 mm' receiver, for mitigating ISM effects.

Table 3.1: The characteristics of systems used for the Effelsberg EPTA observations.

	Receiver			
	P200 mm	P217 mm	S110 mm	S60 mm
Receiver band (MHz)	1290–1430	1240–1480	2599.5–2679.5	4600–5100
Recorded band (MHz)	1247.5–1447.5	1247.5–1447.5	2527–2727	4607.8–5107.8
Bandwidth used (MHz)	140	200	80	500
SEFD (Jy)*	13	17, 16	11	18
System temperature (K)	20	23, 22	17	27
Gain (K/Jy)	1.54	1.37	1.5	1.55

Note: * The two values correspond to the two polarisation channels. For historical reasons, for each channel is assumed that the full quasar flux density is recorded instead of the half which is the correct assumption. Thus an additional correction of a factor of two is needed to SEFD values that are given here.

In a typical EPTA observing session, pulsars are observed for around 30 min. For polarisation calibration purposes, before each observation scan a 100% linearly polarised signal, which illuminates both circular feeds equally, and is produced by a noise diode, is observed. This scan is performed 0.5° away from the pulsar for a duration of 2 minutes. For flux calibration purposes, since the middle of 2012, a source of well-known flux is observed once in each EPTA session and at each observing frequency. This source was either the quasar 3C 286 or 3C 218 (Hydra). The quasar scan consists of three 2-min noise diode scans, one on-source and two 1.0° off-source[3].

The PSRIX backend records data using 8 machines with the 'P200 mm', 'P217 mm', and 'S110 mm' receivers and 16 machines with the 'S60 mm' receiver. The time resolution of recording is 10 s for each of the 25-MHz frequency sub-bands. All time sub-integrations are combined into a single file that has full frequency and phase resolution. One ToA is formed from each 30-min pulsar observation.

The main method used for our analysis is timing. The data reduction process that is followed for the creation of ToAs is discussed in Chapter 2. The basic steps are: RFI excision, polarisation calibration, and (noise-free) template creation. The software packages that are used for the data reduction process along with a small description are summarised in Table 3.2.

Flux calibration is not part of the standard timing analysis thus should be done manually. Based on the flux density measurements of pulsars at 1.4 and 2.6 GHz, and previously published flux density spectral indices, we choose the pulsars that are expected to have sufficient S/N, at a typical EPTA integration time, to be observed at 4.8 GHz. Flux calibration requires a series of observations that include a noise diode observation off the pulsar source, and a series of noise diode observations on and off a quasar. A comparison of these observations, that in more details is explained in Section 2.2.4, will convert the arbitrary scale to Jy scale. In order to make sure that there was no saturation of the system during our pulsar observations we used only the quasar on and off scans for measuring the SEFD. These straightforward measurements that require only a comparison of intensity levels of noise diode observations, on and off the quasar are given by Eq. 2.4. The result of this analysis are presented in Fig. 3.2. From 2013 November to 2014 August and at 2.6 GHz since 2015 December signs of saturation, that have been attributed to insufficient attenuation, are observed. The attribution of these variations to differences of the quasar elevation during these observations is excluded,

[3] 1.0° deviation is needed, since active galactic nucleus are more extended sources than pulsars.

Table 3.2: List of softwares used in this analysis for cleaning, polarisation and flux calibration, and creating ToAs.

Process	Tool	Software	Description
RFI mitigation	clean.py PAZI	COASTGUARD[4] PSRCHIVE	Frequency channels and time sub-integrations with signal strength beyond the receiver response are automatically zero weighted with COASTGUARD. Any remaining RFI channels are manually zero weighted with PAZI.
Polarisation calibration	PAC	PSRCHIVE	The model that is used for polarisation calibration is called 'SingleAxis', as explained in Johnston (2002).
Flux calibration	FLUXCAL PAC	PSRCHIVE PSRCHIVE	FLUXCAL compares the power levels on- and off- the standard candle in order to derive the SEFD and the flux density of the receiver noise source. This information is used by the PAC program to measure the absolute pulsar flux density.
Noise-free template	PAAS	PSRCHIVE	A set of von Mises functions are fitted to a profile formed from high-S/N observations. A different profile is created for each observing frequency band.
ToA creation	PAT	PSRCHIVE	The ToAs and their uncertainties are measured with the one-dimensional Markov chain Monte Carlo (FDM) method. This method provides more reliable uncertainties for low S/N observations, compared to χ^2 minimisation.

[4] COASTGUARD (https://github.com/plazar/coast_guard) is an automatic reduction pipeline which uses PSRCHIVE packages (Hotan et al., 2004).

since firstly none of the quasars has very low declination, and secondly since for EPTA observations roughly the same observing schedule is used each month, thus pulsars are observed at roughly the same sidereal time in every session. Also, flux density variations of these quasars at our observing frequencies are also excluded from independent observations (NASA/IPAC Extragalactic Database (NED)). Since no irregular artifacts in the observed pulse profiles have been observed at these epochs, since only the calibration observations (of very bright sources) appear to be affected allowing these observations to be used for timing.

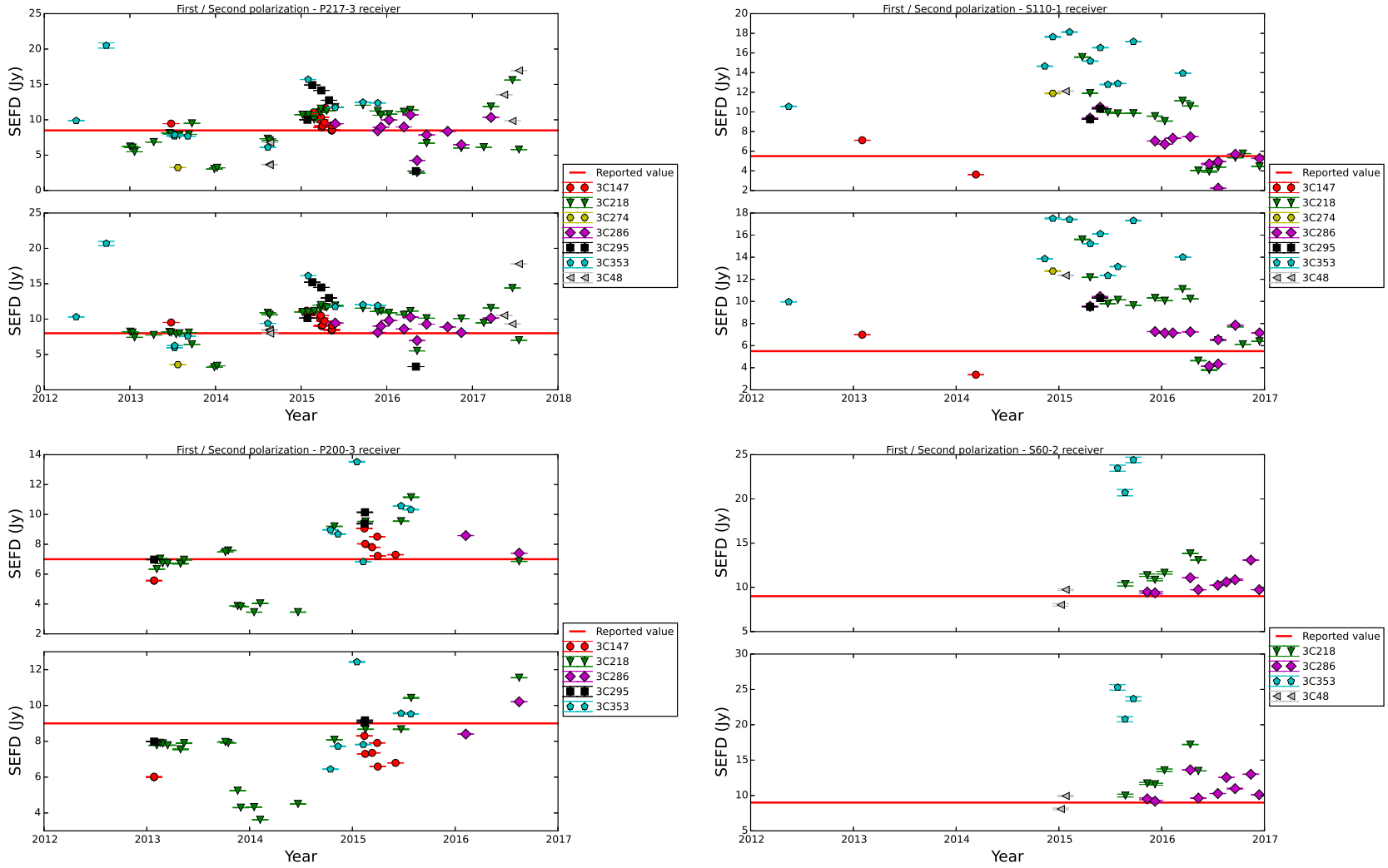

Figure 3.2: SEFD measurements of the receivers used for EPTA observations: two primary 1.4-GHz receivers ('P200 mm' and 'P217 mm'), and the secondary receivers centered at 2.6 GHz ('S110 mm') and 4.85 GHz ('S60 mm'), as measured from different quasar observations. At 1.4 GHz from 2013 November to 2014 August, and at 2.6 GHz since 2015 December SEFD measurements significantly smaller than the lab expected (red line) are attributed to saturation of the telescope signal.

3.3 Results

In the next sections we report five years of EPTA Effelsberg observations at 1.4 and 2.6 GHz. We present that is feasible to achieve high S/Ns for 15 of EPTA pulsars at frequencies as high as 4.85 GHz. For the pulsars with the longer dataset at all these three frequencies we further report flux densities, flux spectral indices, profile stability, ToA uncertainties, and DM variations. Motivating from the good quality that we can achieve in timing data at 4.85 GHz we further investigate the usage of other, under commissioning, high frequency receivers for measuring DM variations.

3.3.1 Flux density and spectral indices measurements

As mentioned above, the flux density spectrum of pulsars is not flat but follows a power law. Pulsars with flatter spectral indices are more easily detected at high frequencies, since they retain S/N, which is needed for high-precision timing (see Eq. 2.8). In order to optimally pick pulsars for our analysis we used the Effelsberg telescope to measure the flux densities of EPTA pulsars at 1.4 GHz. the pulsars with the highest flux densities at this frequency and flatten spectral indices are ideal for further observing at 4.8 GHz.

In Table 3.3 and Fig. 3.3 we present the mean flux density measurements (the integrated intensity of the pulse profile divided by the pulse period) of 33 EPTA pulsars at 1.4 GHz. We report both the mean and median flux density values. The uncertainties on the values is the standard error on the mean ($\sigma_{\rm s}/\sqrt{N_{\rm obs}}$, where σ_s is the standard deviations of the individual flux density measurements and $N_{\rm obs}$ is the number of observations used). In Fig. 3.3 we also compare our measurements with previously published values. Most of our measurements are consistent with previously published values that are based on data calibrated against observations of standard calibrators. Inconsistencies may be attributed to scintillation that can affect both the flux density and the uncertainties. Scintillation is expected to be stronger for low DM pulsars and is more prominent in our data when the integration time or the bandwidth is limited.

15 of the 33 pulsars have been detected at 4.85 GHz: PSRs J0751+1807, J1012+5307, J1022+1001, J1518+4904, J1600−3053, J1643−1224, J1713+0747, J1730−2304, J1744−1134, J1857+0943, J1911+1347, J1939+2134, J2045+3633, J2145−0750, and J2234+0611. For seven (PSRs J1600−3053, J1643−1224, J1713+0747, J1730−2304, J1744−1134, J1857+0943, and J1939+2134) of them we continued further analysis since we had longer data sets among the rest. Their flux densities based on our and previously published analyses at 2.6 GHz and 4.85 GHz are given in Tables 3.4 and 3.5, respectively. In most of the pulsars our flux densities aggree with previously published values within the errors, with the exception of PSR J1857+0943 at both frequencies and PSR J1939+2134 at 4.85 GHz. We mostly attributed these inconsistencies to scintillation since PSR J1857+0943 has very low DM, combined with the fact that the dataset that was available for these pulsars is consisted of a small number of flux calibrated observations.

Based on these measurements and previously published flux densities at different frequencies we can study the flux density spectra of these pulsars. As shown in Fig. 3.4 the flux densities decrease with frequency following a power law, as expected. A turnover, only, on PSRs J1643−1224 and J1744−1134 have been observed around 100 MHz (Kuniyoshi et al., 2015). No high-frequency cut off (at around 1.0 GHz) has been observed. We also measured the flux density spectral indices of these pulsars, using our and previously published flux measurements. We assumed that a simple power law, without cut-offs, can describe our data. The model that we used to fit our measurements is the least-squares method. The

Table 3.3: Phase-averaged flux density measurements of 33 EPTA pulsars with the Effelsberg radio telescope at 1.4 GHz. See Fig. 3.3 for a graphical representation of these data. With bold fonts pulsars for which multi-frequency observations are available are presented.

Name	DM (pc cm^{-3})	N_{obs}	S/N*	S median (mJy)	<S> (mJy)	<$S_{published}$> (mJy)	Reference
J0023+0923	14.3	14	25.5	0.46	0.54(8)	0.48	Levin et al. (2016)
J0030+0451	4.3	13	42.7	0.83	1.05(2)	0.6(2)	Lommen et al. (2000)
J0218+4232	61.3	13	56.1	1.01	1.00(8)	0.9(2)	Kramer et al. (1998)
J0340+4129	49.6	12	30.8	0.43	0.43(3)	–	–
J0348+0432	40.5	88	34.1	0.49	0.52(2)	–	–
J0613−0200	38.8	17	117.3	1.8	1.7(1)	2.3(3)	Manchester et al. (2013)
J0621+1002	36.3	18	83.7	1.27	1.22(7)	1.9(3)	Kramer et al. (1998)
J0751+1807	30.2	28	74.9	1.02	1.05(6)	3.2(7)	Kramer et al. (1998)
J1012+5307	9.0	15	154.5	3.4	3.7(6)	3.2	Levin et al. (2016)
J1022+1001	10.3	20	274.8	1.1	2.2(7)	6.1(54)	Manchester et al. (2013)
J1024−0719	6.5	22	96.4	1.1	1.7(3)	1.5(11)	Manchester et al. (2013)
J1518+4904	11.6	152	300.4	1.7	2.5(2)	4(2)	Kramer et al. (1998)
J1600−3053	**52.3**	**32**	**118.1**	**2.2**	**2.3(1)**	**2.5(4)**	Manchester et al. (2013)
J1640+2224	18.4	16	60.6	0.3	0.6(1)	2(1)	Kramer et al. (1998)
J1643−1224	**62.4**	**33**	**233.4**	**4.18**	**4.0(1)**	**4.8(4)**	Manchester et al. (2013)
J1713+0747	**16.0**	**44**	**628.1**	**3.4**	**6.2(2)**	**10.2(108)**	Manchester et al. (2013)
J1730−2304	**9.6**	**13**	**201.1**	**3.5**	**4.7(11)**	**3.9(19)**	Manchester et al. (2013)
J1738+0333	33.8	8	40.1	0.49	0.49(5)	0.68	Levin et al. (2016)
J1741+1351	24.0	12	25.3	0.54	0.48(6)	0.93	Jacoby et al. (2007)
J1744−1134	**3.1**	**32**	**191.6**	**1.30**	**2.1(3)**	**3.1(26)**	Manchester et al. (2013)
J1853+1303	30.6	9	25.9	0.49	0.59(9)	0.4(2)	Stairs et al. (2005)
J1857+0943	**13.3**	**32**	**152.9**	**4.4**	**6.2(16)**	**5.0(35)**	Manchester et al. (2013)
J1911+1347	31.0	9	50.8	0.7	0.8(1)	0.08	Lorimer et al. (2006)
J1918−0642	26.6	13	61.0	1.2	1.6(3)	0.58(2)	Janssen et al. (2010)
J1939+2134	**71.0**	**28**	**438.6**	**12.8**	**18.3(53)**	**13.2(50)**	Manchester et al. (2013)
J2010−1323	22.2	10	54.6	0.58	0.61(8)	1.6	Jacoby et al. (2007)
J2017+0603	23.9	12	24.0	0.40	0.45(8)	0.5(2)	Cognard et al. (2011)
J2043+1711	20.7	8	13.5	0.26	0.25(2)	–	–
J2145−0750	9.0	12	325.0	2.6	2.9(5)	8.9(125)	Manchester et al. (2013)
J2229+2643	23.0	11	86.1	0.5	1.2(8)	0.9(2)	Kramer et al. (1998)
J2234+0944	17.8	17	53.5	0.8	0.8(1)	–	–
J2317+1439	21.9	13	52.7	0.3	0.7(2)	4(1)	Kramer et al. (1998)
J2322+2057	13.4	6	20.1	0.3	0.5(2)	–	–

Note: * The S/N is scaled to observational length of 28min, which is the typical observing length in Effelsberg EPTA campaign.

Table 3.4: Flux density measurements of seven EPTA pulsars with the Effelsberg radio telescope at 2.6 GHz.

Name	DM (pc cm^{-3})	N_{obs}	S/N*	S median (mJy)	<S> (mJy)	<$P_{published}$>	Reference
J1600−3053	52.3	7	22.7	1.05	0.93(8)	-	-
J1643−1224	62.4	4	51.2	1.50	1.27(8)	1.4(5)	Kramer et al. (1999)
J1713+0747	16.0	7	237.0	1.0	3.3(7)	2.7(9)	Kramer et al. (1999)
J1730−2304	9.6	2	47.6	1.4	1.4(3)	-	Kramer et al. (1999)
J1744−1134	3.1	7	26.8	0.61	0.7(1)	0.7(4)	Kramer et al. (1999)
J1857+0943	13.3	4	43.7	0.8	1.1(2)	2.3(7)	Kramer et al. (1999)
J1939+2134	71.0	11	72.7	1.5	1.7(2)	2.0(4)	Kramer et al. (1999)

Note: * The S/N is scaled to observational length of 28 min, which is the typical observing length in Effelsberg EPTA campaign.

Table 3.5: Flux density measurements of seven EPTA pulsars with the Effelsberg radio telescope at 4.85 GHz.

Name	DM (pc cm^{-3})	N_{obs}	S/N*	S median (mJy)	<S> (mJy)	<$P_{published}$>	Reference
J1600−3053	52.3	6	17.2	0.43	0.49(6)	-	-
J1643−1224	62.4	6	24.9	0.44	0.44(4)	0.4(2)	Kramer et al. (1999)
J1713+0747	16.0	6	111.6	1.2	1.2(2)	0.8(2)	Kramer et al. (1999)
J1730−2304	9.6	7	22.7	0.8	1.0(3)	-	-
J1744−1134	3.1	6	22.4	0.42	0.40(2)	-	-
J1857+0943	13.3	3	35.8	0.65	0.67(9)	1.12(9)	Kramer et al. (1999)
J1939+2134	71.0	5	20.9	0.4	0.5(1)	1.0(2)	Kramer et al. (1999)

Note: * The S/N is scaled to observational length of 28 min, which is the typical observing length in Effelsberg EPTA campaign.

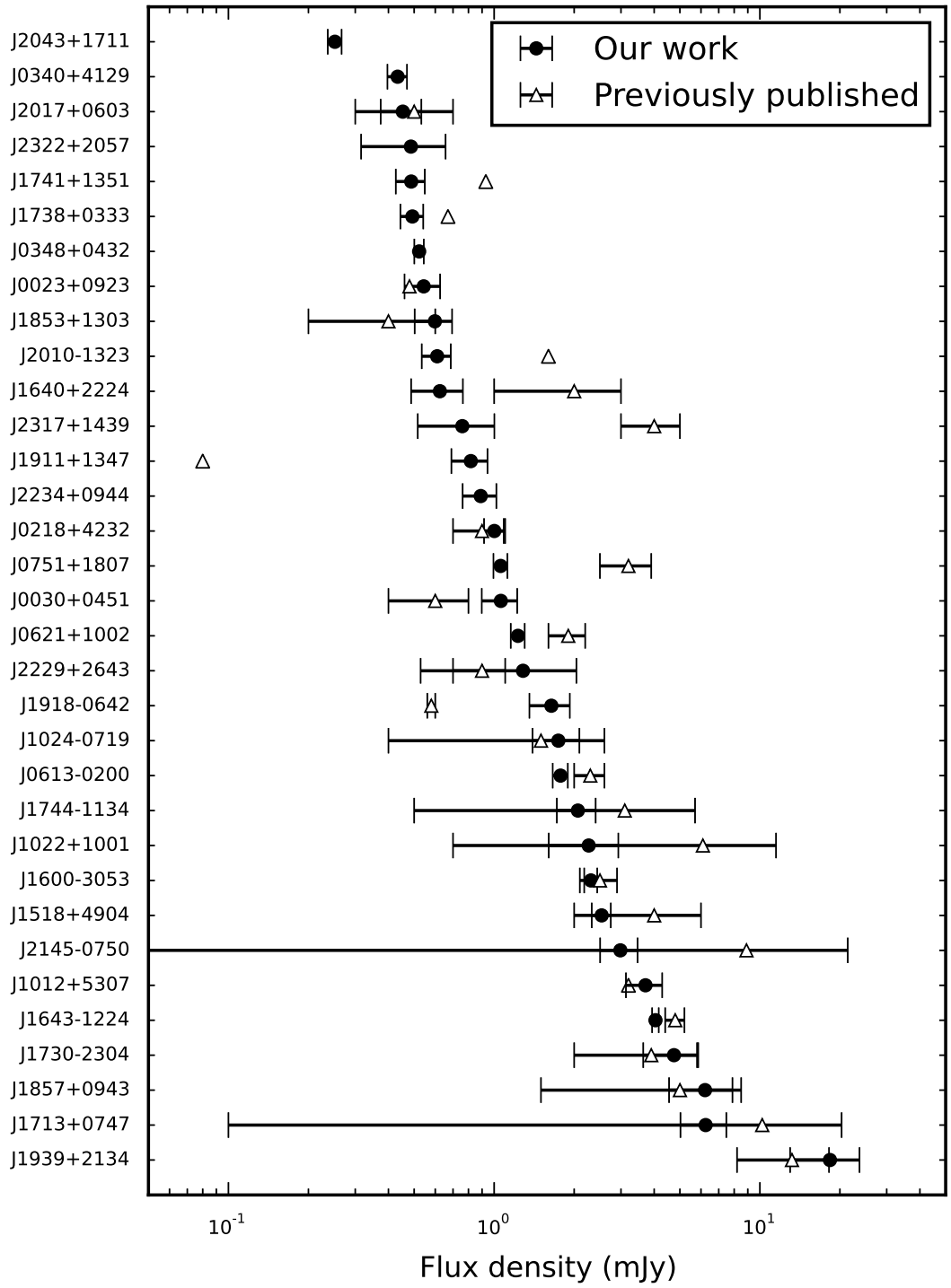

Figure 3.3: Flux density measurements of 33 pulsars at 1.4 GHz. Our measurements with the 'P217 mm' and 'P200 mm' Effelsberg receivers are presented with black circles. While measurements based on previous publications are shown with open triangles (see Table 3.3). The lack of uncertainties for some of these values is because these measurements are based on the radiometer equation and not on real flux-calibrated observations. For five pulsars we report flux density measurements for the first time.

Table 3.6: Spectral indices of seven EPTA pulsars based on Effelsberg PSRIX observations and previously published flux densities.

Name	Frequency range (MHz)	Flux spectral index (ξ)	χ^2	Published ξ	Reference
J1600−3053	700 – 5000	-1.1(1)	2.9	-	-
J1643−1224	75 – 5000	-1.85(7)	2.6	$-2.11^{+0.03}_{-0.04}$	Kuniyoshi et al. (2015)
J1713+0747	100 – 5000	-1.3(1)	2.2	-1.4(1)	Kuzmin & Losovsky (2001)
J1730−2304	100 – 5000	-1.7(1)	1.3	$-1.85^{+0.06}_{-0.08}$	Kuzmin & Losovsky (2001)
J1744−1134	100 – 5000	-1.54(7)	1.7	-1.8(1)	Kuzmin & Losovsky (2001)
J1857+0943	100 – 5000	-1.59(9)	0.9	-1.6(1)	Kuzmin & Losovsky (2001)
J1939+2134	10 – 5000	-2.7(3)	3.8	-2.59(4)	Kuniyoshi et al. (2015)

best flux density spectral indices, along with the corresponding goodness-of-fit χ^2 values, are presented in Table 3.6.

3.3.2 Comparison of multi-frequency observations

3.3.2.1 Profile evolution with frequency

In order to calculate ToAs a noise-free pulsar template in necessary. Since pulsar profiles exhibit changes in shape and number of profile components as a function of observing frequency (e.g. Kramer et al., 1999), it is necessary to create different templates for each observing frequency and bandwidth used. In Figs. 3.5–3.6 we present our templates as created with the method explained in Section 3.2. Differences in the pulse phase of the fiducial point between multi-frequency observations are measured with the PAS package in PSRCHIVE.

All seven pulsars observed at three frequencies are very rapidly spinning millisecond pulsars, with spin periods less than 10 ms. For two of them (PSRs J1643−1224 and J1744−1134) we did not observe any significant changes either in the shape or in the profile width over frequency. For the remaining five (PSRs J1600−3053, J1713+0747, J1730−2304, J1857+0943, and J1939+2134) profile changes are more obvious. In PSR J1600−3053 the leading component becomes stronger at higher frequencies compared to the trailing component. In PSR J1713+0747 both the two leading components and the trailing one become stronger at higher frequencies. In PSR J1730−2304, even though no changes in the overall profile width are observed, the number and the relative strength of the profile components change across different frequencies. PSR J1857+0943 is an orthogonal rotator (Thorsett & Stinebring, 1990; Kramer et al., 1999). In our analysis, as in the previous ones, the interpulse is observed to be brighter at higher frequencies. No changes in the width or in the separation of the main pulse and interpulse are observed. Another pulsar in which we detect emission from both magnetic poles is PSR J1939+2134. In contrast to PSR J1857+0943, in PSR J1939+2134 the inter-pulse becomes weaker at higher frequencies.

In Figs. 3.7 and 3.8 we present width changes in the main component of pulsar profiles at two different intensity levels: 10% and 50%, which are defined as the furthest most point from the position of the peak flux. The intensity levels have as a reference the normalized peak of the most prominent component. In contrast to slow pulsars, in millisecond pulsars, as shown is older studies (Kramer et al., 1999), no significant changes in the profile width have been observed. We did not observe any significant changes in the profile widths either, with the exception of PSRs J1600−3053 and J1713+0747. At the 10% intensity level, in both pulsars, the existence of and additional component that appears at high frequencies influences the results. For PSR J1600−3053, at the 50% intensity level, we observe a gradual increase in profile width.

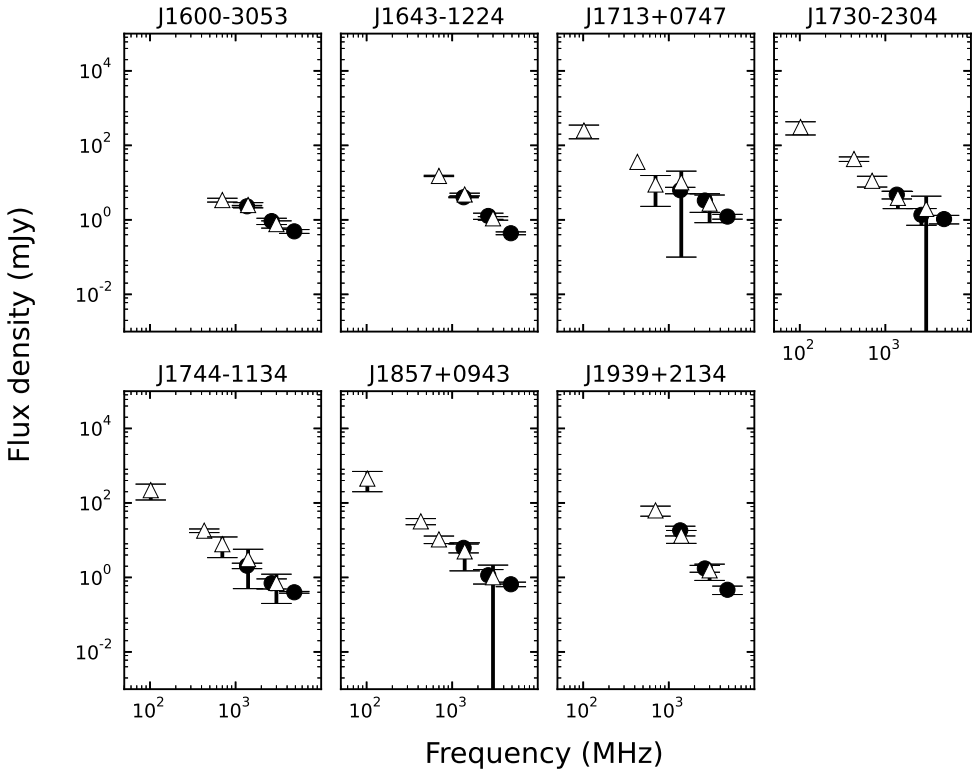

Figure 3.4: Flux density spectra for seven EPTA pulsars from ∼100 MHz to 4.85 GHz. With filled circles our flux-density measurements, based on the analysis described in Section 3.2, are presented. With open triangles we give the previously published flux density measurements (data taken from the ATNF Pulsar Catalog, Manchester et al. (2005)).The flux density upper limit at 75 MHz for PSR J1643−1224 and the flux density values of PSR J1939+2134 at 10–100 MHz, that are not presented in this figure, can be seen in Figs. 4 and 1, respectively in (Kuniyoshi et al., 2015).

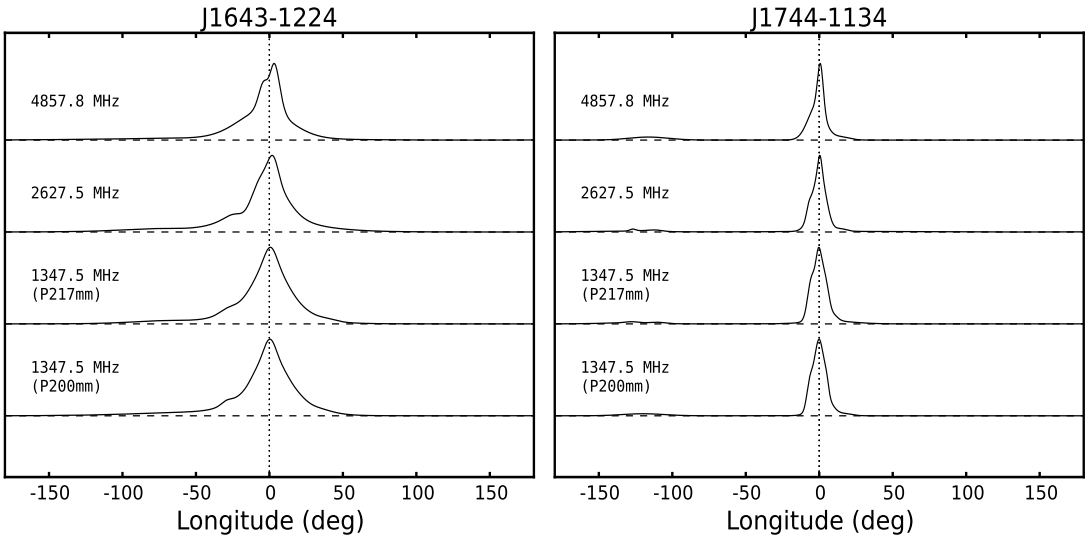

Figure 3.5: Multi-frequency noise-free templates for the PSRs J1643−1224 and J1744−1134, in which no significant changes on the shape or in the profile width have been observed on the PSRIX Effelsberg observations. The templates are based on the addition of multiple high-S/N polarisation-calibrated observations, to which von Mises functions were fitted. All the observations are taken with the Effelsberg radio telescope and PSRIX backend. Templates are aligned in phase with respect to a fiducial point.

This happens because the leading component at higher frequencies becomes stronger, exceeding the 50% level. Thus, while the 50% intensity level at frequencies < 2.6 GHz corresponds only to the main profile component, at higher frequencies it corresponds to both components (Fig 3.6).

3.3.2.2 ToA uncertainties

The last stage of data reduction is to create ToAs. As explained in Section 3.2, ToAs are determined by cross-correlating the pulsar template with observations. In Table 3.7 we present the mean ToA uncertainties at 1.4, 2.6, and 4.85 GHz. The general conclusion is that the best ToA precision can be achieved at 1.4 GHz and the worst at 4.85 GHz. This finding is not unexpected since the ToA uncertainty is inversely proportional to the profile S/N (see Eq. 2.8). However, when observe at lower frequencies DM variations become more severe and the precision of ToAs degrades. Thus, DM variations should be measured precisely in order the red noise introduced due to DM variations at lower frequencies to be reduced.

Although large ToA uncertainties have a negative effect on how precisely we can measure the astrometric, spin and binary parameters of pulsars since they are determined through timing, (which is a least-squares fit analysis of ToAs, see for more details Sec. 2.3.3), they do not have straightforward affect on the precision of DM determination. The reason is that DM delays scale as $\propto f^{-2}$ thus the propagation effects are easier to be probed at low frequencies but the precision with which DM variations can be measured is a multiple factor effect that depends on the flux density spectral index of the pulsar observed and the bandwidth of the

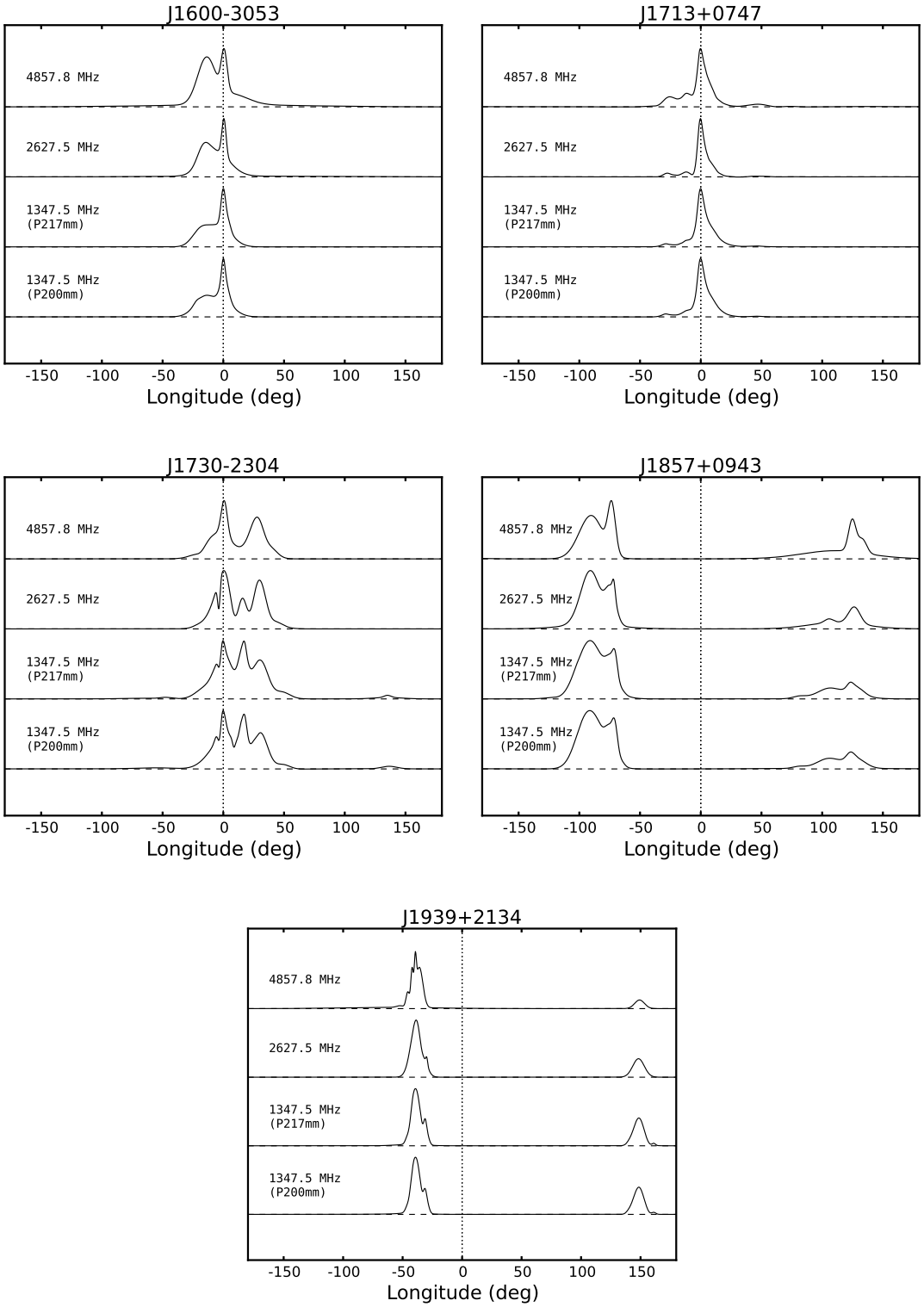

Figure 3.6: Multi-frequency noise-free templates for the PSRs J1600−3053, J1713+0747, J1730−2304, J1857+0943 and J1939+2134, in which significant changes on the shape or in the profile width have been observed on the PSRIX Effelsberg observations. Since for PSR J1857+0943 at 4.85 GHz the noise rms on pulse is comparable to rms off pulse it suggests that the leading part of the interpulse is fitted noise. While for PSR J1939+2134 the noise rms on pulse is lower than the rms off pulse it suggests that the extra components that appear on the peak of the main component are real. See Fig. 3.5 for further details.

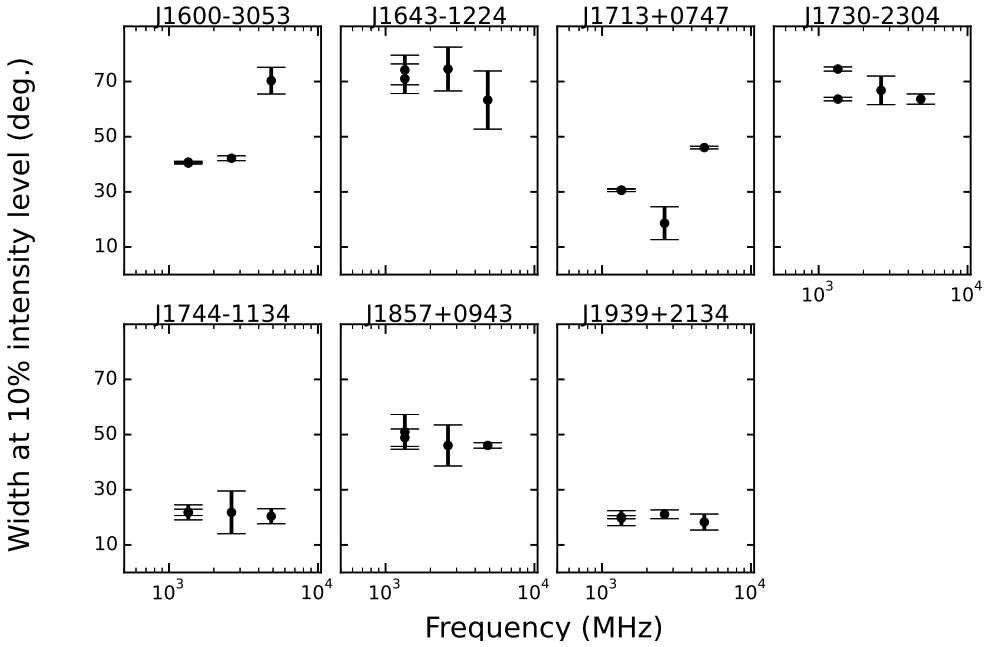

Figure 3.7: Profile width measurements at 10% intensity level.

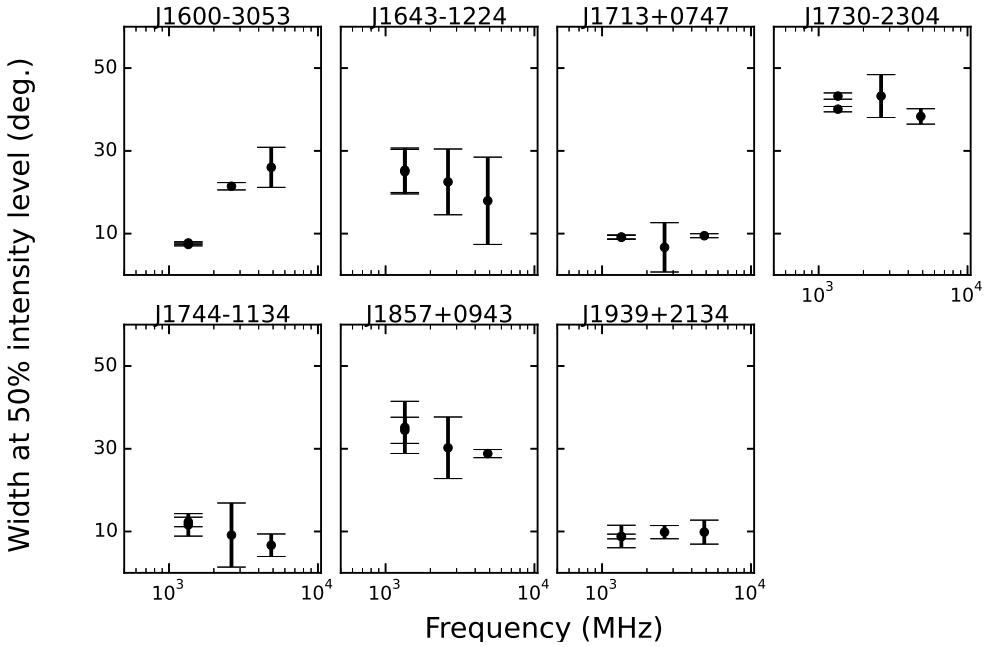

Figure 3.8: Profile width measurements at 50% intensity level. This level defines the furtherest most point from the position of the peak flux.

Table 3.7: The median ToA uncertainties, scaled to 28-min integration time, of seven pulsars in μs. The measurements are based on PSRIX observations taken at three different frequencies and four different receivers (at 1.4 GHz we used both the single-beam 'P200 mm' and the 7-beam 'P217 mm' receiver). In the parentheses are the nominal 1-σ uncertainties in the leas significant digit quoted.

	Receiver			
Name	P200 mm	P217 mm	S110 mm	S60 mm
J1600−3053	0.5(4)	0.4(2)	2.1(6)	0.3(2)
J1643−1224	0.9(2)	0.9(4)	3(1)	3(2)
J1713+0747	0.3(5)	0.2(5)	0.3(4)	0.6(2)
J1730−2304	1.2(9)	1.2(7)	1.3(5)	1.5(8)
J1744−1134	0.5(4)	0.5(7)	1.8(4)	1.0(9)
J1857+0943	0.6(6)	0.9(5)	1.9(6)	1.9(7)
J1939+2134	0.02(12)	0.02(10)	0.2(5)	0.4(8)

observation. In the next sections we will investigate how ToA uncertainty, of the existing and future receivers, affect our ability to measure and correct DM variations.

3.3.3 DM time variations

The ToAs measured above were further analysed with the TEMPO2 package (Hobbs et al., 2006). The initial timing models were taken from the EPTA data release (Desvignes et al., 2016). These timing models contain the spin, astrometric and orbital parameters of each pulsar. DM time derivatives were not part of the timing models. We also included in the models arbitrary time offsets (JUMPS) between the reference observing system and the other systems. The origin of these JUMPS is differences in instrumental delays, and the use of different templates for each system.

We fitted the spin period and period derivative, and proper motion only to ToAs obtained from the 1.4 GHz observations. The post-fit residuals were Gaussianly distributed around zero, the root-mean-square was comparable to the ToAs uncertainties, and the reduced $\chi^2 \sim 1$. In order to obtain DM time variations, we split our observations in time segments, where each segment contains one observation at 1.4 GHz and either one at 2.6 GHz or 4.85 GHz. In each segment we used the best timing model, as resulting from our analysis, and fitted only for DM. In all cases 1.4 GHz was the reference frequency. Our DM variation results are presented in Fig. 3.9. In the case of PSR J1744−1134, around epoch 56700 MJD we observed large variations in DM, their origin is presumably a scattering event. In all the other cases the DM varies by about 0.001 to 0.05 pc cm^{-3}.

3.3.4 DM time variations with future receivers

The development of new receivers, with wide recording bandwidths, high gains and low system temperatures is always an ongoing goal of each observatory. Effelsberg is no exception to this rule. For our analysis we picked two high-frequency receivers that are planned to be available soon for pulsar observations. The first one is the 'C+' receiver ('S45 mm'), with recording bandwidth 4.0–6.0 GHz. The second one is the S-band MeerKAT receiver designed by MPIfR, also with a wide recording bandwidth of 700 MHz centered at 1.95 GHz. Both are

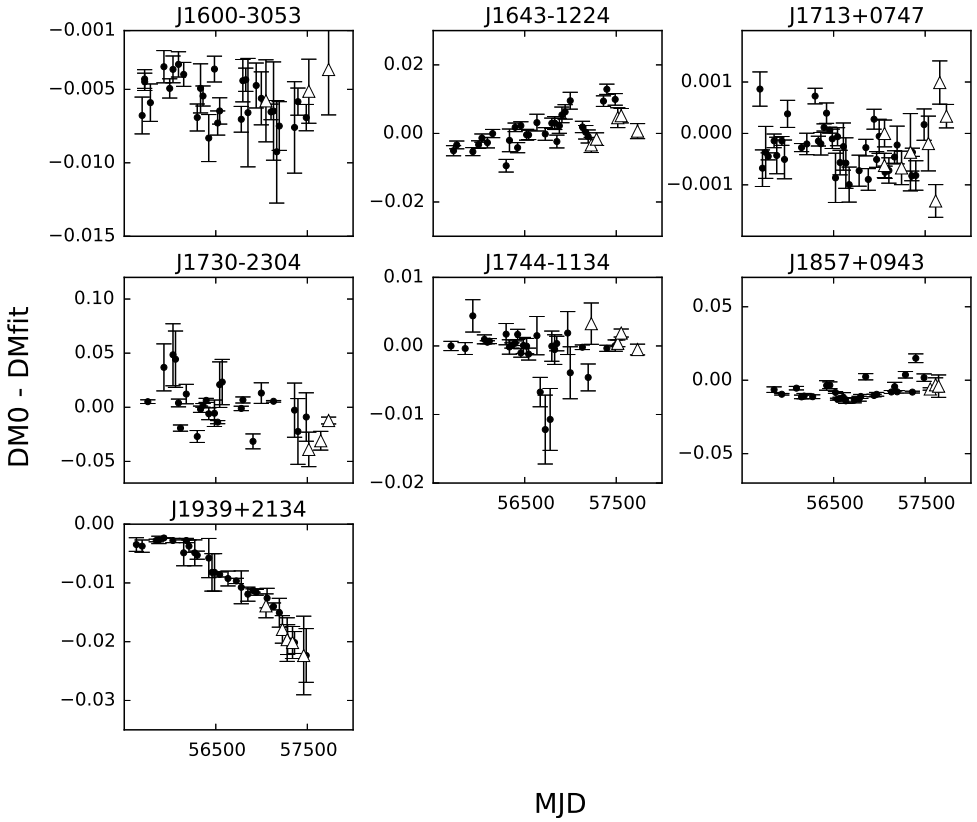

Figure 3.9: DM variations as a function of time for seven EPTA pulsars. DM variations measured based on 1.4 GHz and 2.6 GHz observations are indicated with filled circles. While DM variations based on 1.4 GHz and 4.85 GHz observations are indicated with open triangles.

Table 3.8: The technical characteristics of future systems planned to be used for pulsar observations.

	Receiver	
	S45 mm	MeerKAT S-band
Receiver band (MHz)	4000–9300	1600–3500
Recorded band (MHz)	4000–6000	1600–2300
Bandwidth used (MHz)	2000	700
SEFD (Jy)	18.5	10
System temperature (K)	∼25	<25
Gain (K/Jy)	∼1.35	2.5

presently in a commission phase. The expected parameters of these receivers are presented in Table 3.8.

For these two receivers and the already existing ones we calculated the theoretical ToA uncertainty assuming observations with 28-min length, typical for EPTA observing sessions (Desvignes et al., 2016). Using the 'P217 mm' observations as a reference, we can calculate the theoretical ToA uncertainties by comparing the expected S/N [4]:

$$\begin{aligned}\frac{\sigma_{\rm A}}{\sigma_{\rm P217mm}} &= \frac{({\rm S/N})_{\rm P217mm}}{({\rm S/N})_{\rm A}} \\ &= \frac{{\rm S}_{\rm sys,A}}{{\rm S}_{\rm sys,P217mm}}\sqrt{\frac{\Delta f_{\rm A}}{\Delta f_{\rm P217mm}}}\left(\frac{1.4475^{(\xi+1)}-1.2475^{(\xi+1)}}{f_{\rm hi,A}^{(\xi+1)}-f_{\rm lo,A}^{(\xi+1)}}\right),\end{aligned} \tag{3.1}$$

where 'A' is referring to the system of interest, $\rm S_{sys}$ is the system temperature (see Tables 3.1 and 3.8), Δf is the recorded bandwidth, ξ is the pulsar flux density spectral index and $f_{\rm hi}$ and $f_{\rm lo}$ are the higher and lower recording frequencies, respectively. For Eq. 3.1 we assumed that the pulse profiles have the same width at all frequencies and across the whole frequency recording bandwidth, and the observing duration in both frequencies is the same.

We applied Eq. 3.1 to the different existing and future systems, leaving the pulsar flux density spectral index as a free parameter. The theoretical ToA uncertainties are presented in Fig. 3.10. In this plot we assumed that one ToA is created for the whole band. In all cases the 4.85 GHz receiver ('S60 mm') gives worse ToA uncertainties than the rest. The 2.6 GHz receiver ('S110 mm') provides better ToA precision than the 4-to-9 GHz 'C+' receiver for pulsars with $\xi \leq -2.1$. In Fig. 3.11 we compare these theoretical measurements for the 'S110 mm' and 'S60 mm' receivers with the values that we obtained from the observations.

In the next stage of our analysis we simulated the arrival times of the same seven pulsars. We used the FAKE plug-in of the TEMPO2 package and generated ToA uncertainties based on Eq. 3.1 to create a fake dataset. We picked the cadence to be one observation per month. The length of the simulated datasets covers the years from 2012 January to 2016 December. The only noise that we added in the residuals was DM noise, with the plug-in ADDDMVAR. The input that we gave in this plug-in was the structure function of DM variations. The DM structure function is related to the diffractive time-scale ($\tau_{\rm diff}$) through:

$$D_{\rm DM}(\tau) = \left(\frac{Kf}{2\pi}\right)^2\left(\frac{\tau}{\tau_{\rm diff}}\right)^{\beta-2}, \tag{3.2}$$

[4] This is the same equation as Eq. 3 in Lazarus et al. (2016).

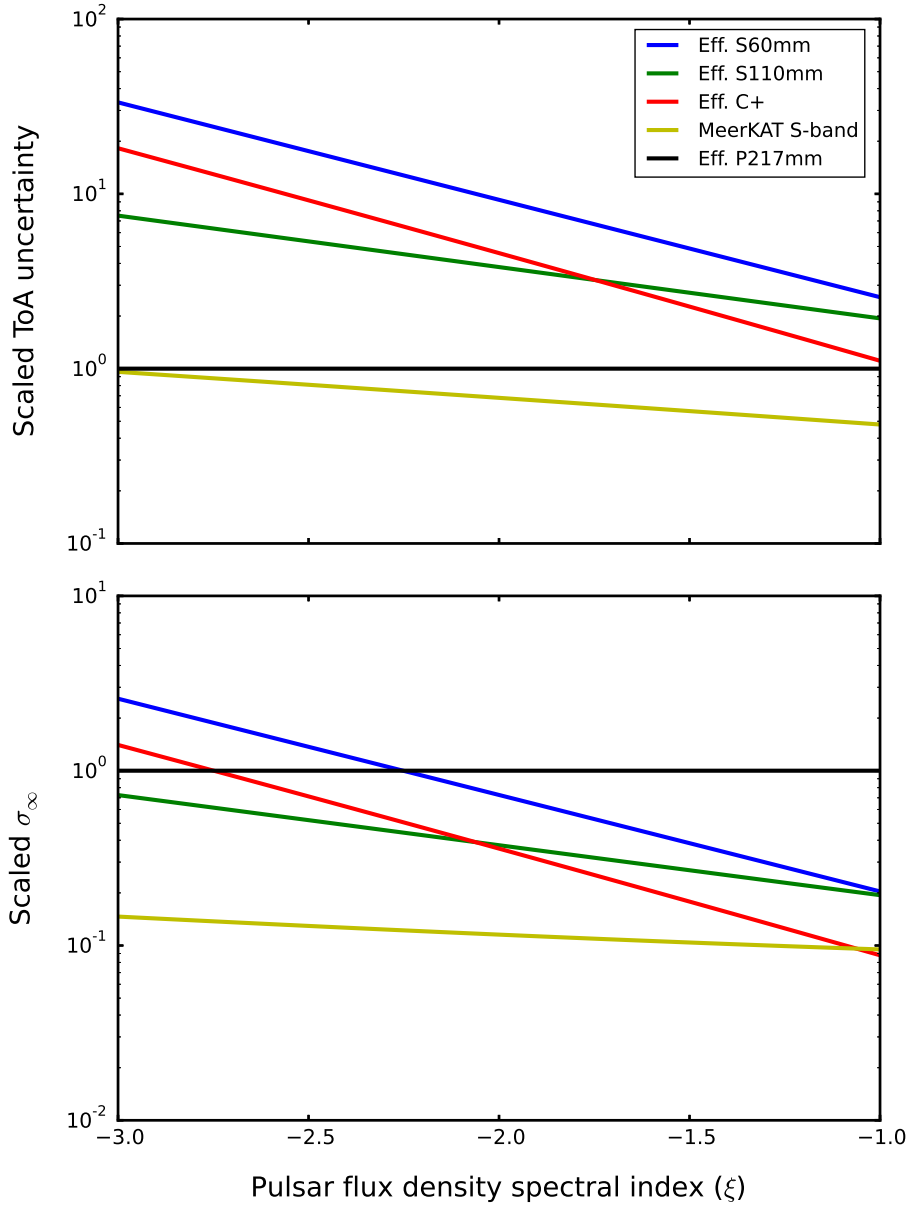

Figure 3.10: Top panel:ToA uncertainties of the existing and future receivers as a function of flux density spectral index. All the measurements are based on theoretical calculations, scaled to 'P217 mm' values achieved with PSRIX in Effelsberg. Low values indicate better precision in ToA estimation. Bottom panel: The uncertainty of the infinite-frequency ToAs as a function of the flux spectral index relative to the self-corrected 'P217 mm' observations. The self-corrected 1.4 GHz ('P217 mm') Effelsberg observations (which measure the DM variations with the 200'MHz band only) are presented with the black line, while the combination of these observations with the other receivers: 'S110 mm', 'S60 mm', 'C+', and MeerKAT S-band are presented with green, blue, red, and yellow, respectively. For the self-correction, the frequency band is split into two sub-bands, while for the rest we assumed one ToA for each band.

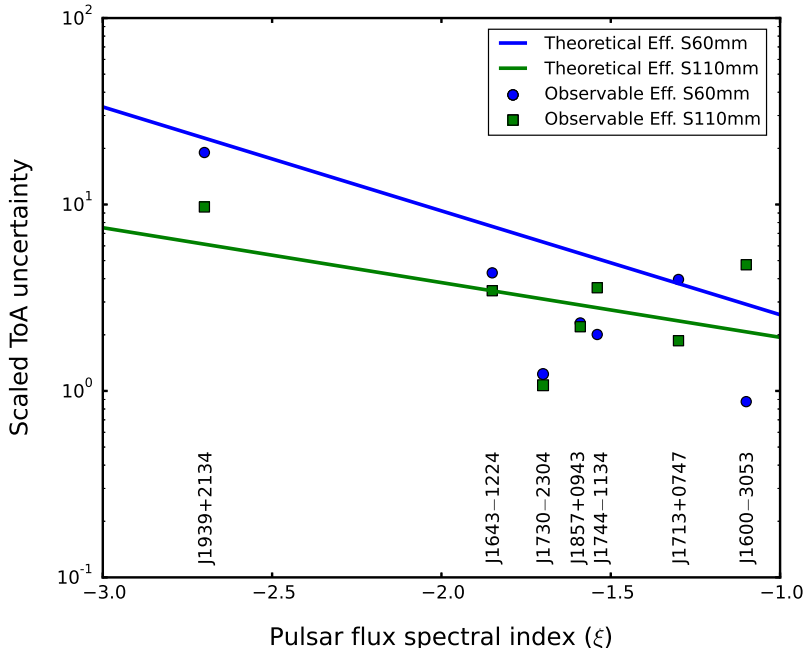

Figure 3.11: The ToA uncertainties of the 'S110 mm' and 'S60 mm' receivers scaled to 'P217 mm' values, as a function of pulsar flux density spectral index. With the solid green and blue lines 'S110 mm' and 'S60 mm' theoretical measurements are presented. While with green squares and blue circles the observable median ToA uncertainties, scaled to 28-min integration time, of seven pulsars are given as measured with the 'S110 mm' and 'S60 mm' receiver respectively. Inconsistencies between theoretical and observable ToA measurements are attributed to scintillation time scale, profile evolution through frequency that is not taken into account on the theoretical measurements. Characteristic example is PSR J1600−3053 for which the intensity increase of the trailing component at 4.85 GHz (Fig. 3.6) resulted to maximization of template-profile cross-correlation, and thus to decrease of ToA uncertainty.

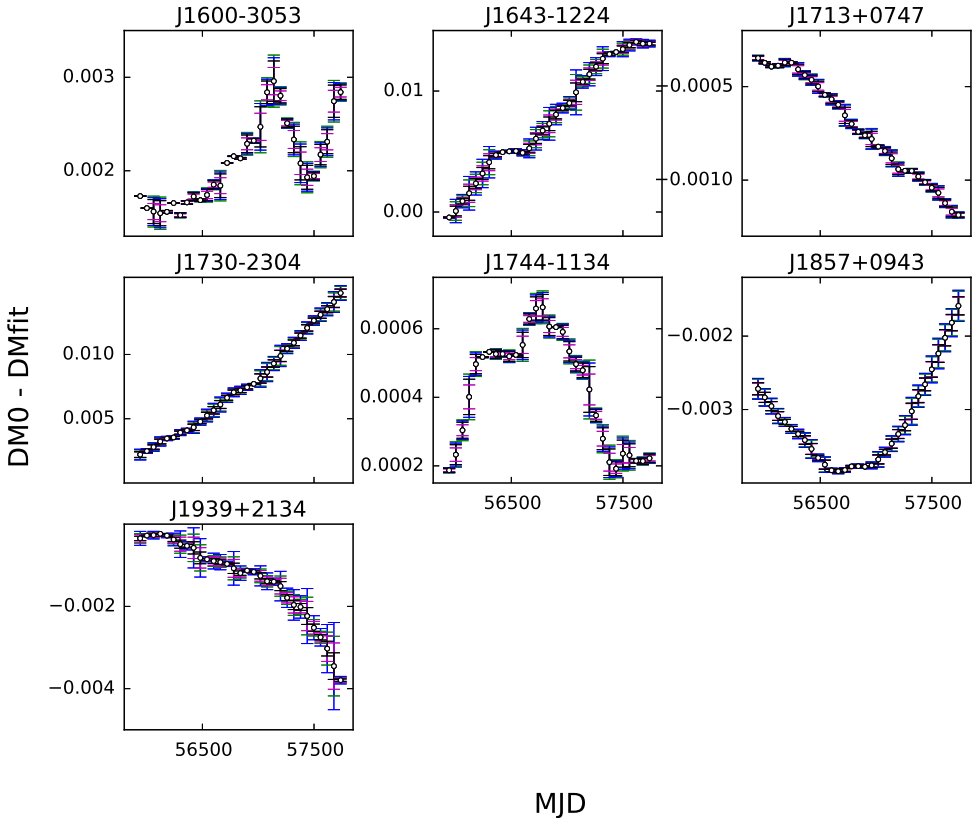

Figure 3.12: Simulated DM variations as a function of time for seven EPTA pulsars. For the calculations we used the ToA uncertainties measured with 'P217 mm' real observations as reference to calculate the expected ToA uncertainties for the different systems. The only noise that we added to residuals was DM noise.

where $\beta = 11/3$, if we assume a Kolmogorov spectrum (Armstrong et al., 1995). For our analysis we used the $\tau_{\rm diff}$ values as measured in the Keith et al. (2013) analysis (see their Table 2).

After creating the simulated ToAs we measured the temporal DM variations following the technique that has been described in Section 3.3.3. The results are presented in Fig. 3.12. The quantity that we are most interested in is $\sigma_{\rm DM}$, which shows how precisely we can determinate DM variations (ΔDM). In Fig. 3.13 we present the uncertainty in DM variation measurements as a function of pulsar flux density spectral indices (ξ). As we can see in the plot there is not a single receiver that is ideal for measuring DM variations with all the pulsars. For pulsars with $\xi \gtrsim -1.6$ using the Eff. 'P217 mm' combined with the Eff. 'C+' receiver we can determine DM variations with very low uncertainty compared with the rest of the receivers. On the other hand, for $\xi \lesssim -1.6$ the Eff. 'P217 mm' combined with the S-band MeerKAT receiver appears to give the most accurate DM variation measurements. However, since the majority of EPTA pulsars have $\xi \sim -1.8$ (see Fig. 3.14) the MeerKAT receiver appears to give more accurate DM measurements.

By combining the uncertainty in ToAs and in DM variations (top part of Fig. 3.10 and

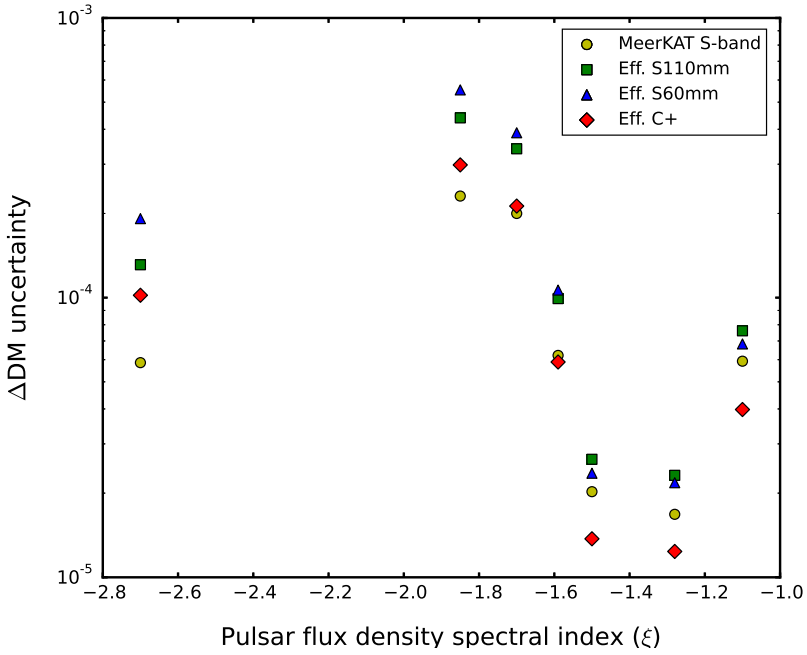

Figure 3.13: The uncertainty in the DM variation measurements as a function of pulsar flux spectral index based on simulated data of seven EPTA pulsars. In all cases, the primary receiver is the 'P217 mm' and as a secondary the: 'S110 mm' (green square), 'S60 mm' (blue triangle), 'C+' (red diamond), and MeerKAT–S-band (yellow circle). Lower values indicate more precise DM variation measurements. The fact that some of the pulsars can achieve more precise measurements than others is associated with the magnitude of noise introduced by the ISM effects and the pulsar flux density.

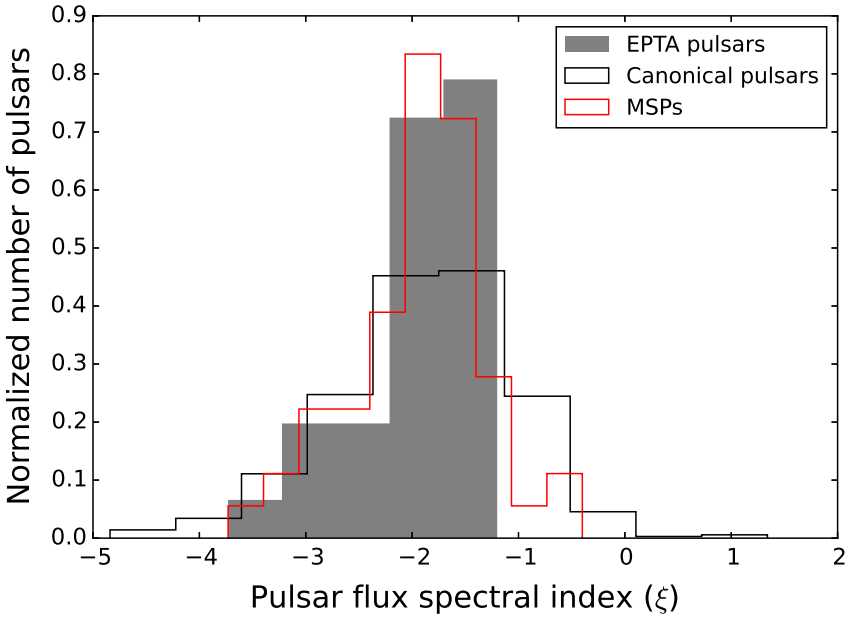

Figure 3.14: Distribution of published pulsar flux spectral indices for 569 canonical (black line), 54 MSPs (red line), and 42 EPTA pulsars (filled gray). Spectral index values are taken from the ATNF catalogue (Manchester et al., 2005).

Fig. 3.13) we can calculate the infinite-frequency ToA (T_∞), in other words: the ToA corrected from DM variations. For measuring T_∞ we followed the analysis by Lazarus et al. (2016). We assumed that, in all cases, a combination of the 'P217 mm' receiver with the receivers 'S110 mm', 'S60 mm', 'C+', and MeerKAT S-band are used for correcting DM variations. We picked as primary the receiver which in each combination has the lowest input ToA uncertainty. The T_∞ is given by (Lee et al., 2014):

$$< \delta T_\infty^2 >= \frac{f_1^4\ \sigma_1^2 + f_2^4\ \sigma_2^2}{(f_1^2 - f_2^2)^2}, \tag{3.3}$$

where f_i and σ_i are the central frequency and ToA uncertainty of the two receivers used. The uncertainty of T_∞ ($\sigma_\infty = \sqrt{< \delta T_\infty^2 >}$) scaled to the self-corrected 'P217 mm' observations is presented in the lower part of Fig. 3.10. One ToA is measured for the whole recorded frequency band, the uncertainty of which is calculated theoretically as shown in Eq. 3.1. From the figure it is clear that the 'P217 mm'+MeerKAT S-band combination provides the most precise DM-corrected ToA, while the 'P217 mm'+'S60 mm' combination the worst, regardless of the flux density spectral index.

We should point out that the correction of DM variations is a process that while decreases red noise, always adds white noise to the residuals. This fact should be taken into account for GW detection studies, for which high ToA precision is needed. In order to investigate by which factor the uncertainty of the infinite-frequency ToA will be increased by this process, we applied Eq. 3.3 assuming that the ToA uncertainty with 'P217 mm' receiver observations is 100 ns, while the uncertainty of the other receivers is calculated theoretically based on Eq. 3.1. In Fig. 3.15 our results are presented. We concluded that using 'P217 mm' observations as our primary receiver and 'S110 mm', 'S60 mm', and 'C+' for correcting DM variations, the

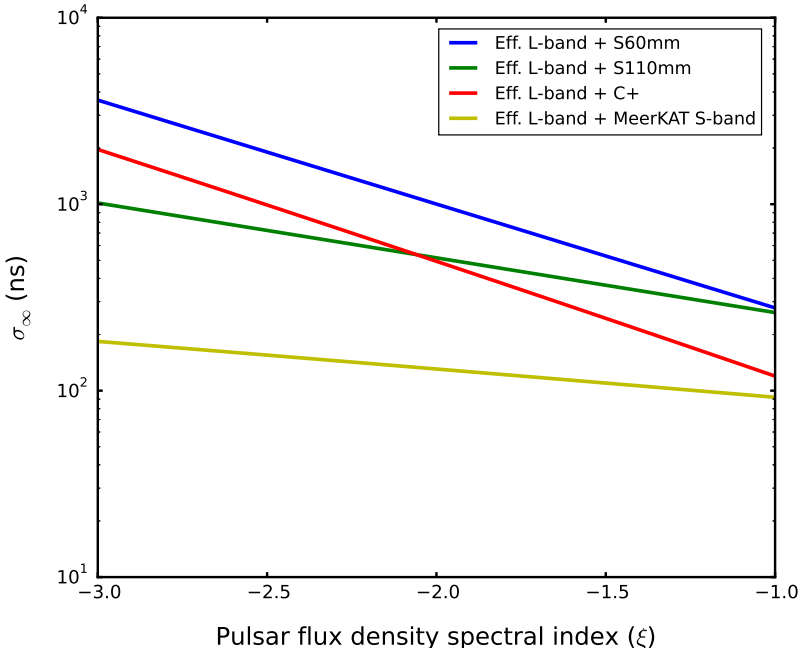

Figure 3.15: The uncertainty of the infinite-frequency ToAs as a function of pulsar flux density spectral index. We assumed ToA uncertainty of the DM variations pre-corrected ToA uncertainty of the 'P217 mm' observations equal 100 ns, while for the rest of the receivers presented the ToA precision is measured theoretical based on Eq. 3.1. From the figure it is obvious that DM correction process adds white noise in the timing residuals, since in all cases the post-corrected ToA uncertainty is higher than 100 ns.

uncertainty of the infinite-frequency-DM-corrected ToA increases by a factor of 4.5, 7.7, and 3.7, respectively, for a pulsar with flux density spectral index equal to -1.8 (which is the median value of EPTA pulsars, see Fig. 3.14). This means that in order to get 100 ns post-correction timing residuals at 21 cm, we would need pre-correction ToA precision at 21 cm on the order of 22 ns, 13 ns, and 26 ns, using the secondary receivers 'S110 mm', 'S60 mm', and 'C+', respectively. In the case that we use the combination of 'P217 mm' with the MeerKAT S-band receiver, our primary observations will be the MeerKAT S-band. For reaching post-correction ToA precision of 100 ns we need actual pre-correction ToA precision on the order of 53 ns with MeerKAT S-band, only a factor of 1.2 better than the theoretically expected with this receiver. We should notice that since the current residual rms that we can achieve with IPTA pulsars at 1.4 GHz is typically not yet of the order of ≤ 100 nanoseconds (Verbiest et al., 2016), we should focus on achieving high timing precision at high frequencies as well, in order to get post-DM-correction timing residuals of 100 ns at 1.4 GHz.

3.4 Implication for continuous GWs and GWB detection

One of the primary goals of PTAs is to detect very low frequency GWs, emitted by individual sources and a stochastic GWB. Here, we estimate how the sensitivity to monochromatic

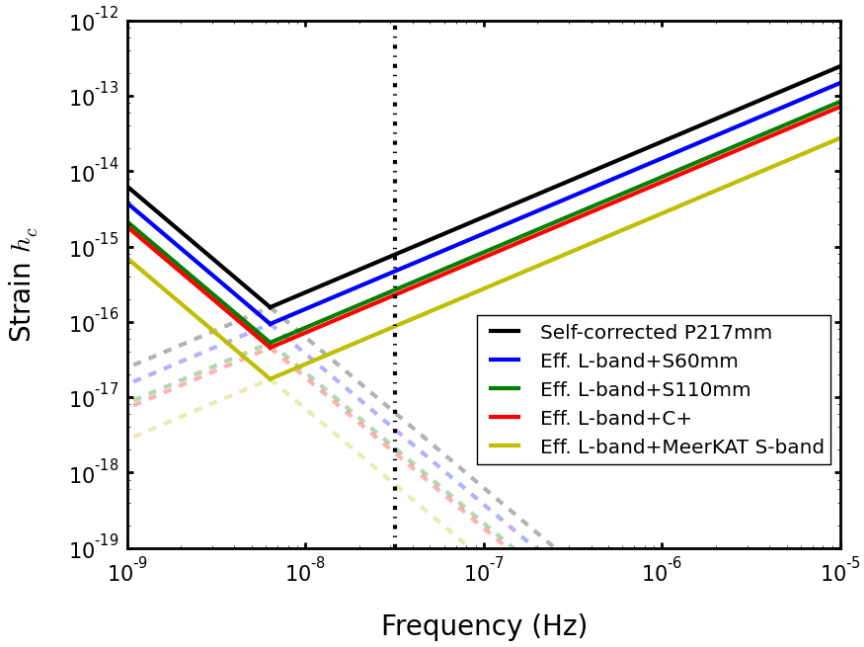

Figure 3.16: Sensitivity curves to continuous GWs for a fictional PTA discussed in the text, with the presence of only Gaussian, uncorrelated white noise in the timing residuals. The solid lines show the predictions based on a frequentist analysis in the time domain, as described in Eqs. (14) and (16) of Moore et al. (2015). The black solid line corresponds to self-DM-corrected P217 mm observations, while the blue, green, red, and yellow solid lines corresponds to 'P217 mm' observations corrected for DM with 'S60 mm', 'S110 mm', 'C+', and MeerKAT S-band observations, respectively. The dot-dashed vertical black line indicates the strain of the signal at $f = 1$ yr^{-1}.

waves and the GWB will be improved by removing DM variations. For the analysis we assumed that the noise in the timing residuals is only white, Gaussian and uncorrelated between pulsars. The timing residual rms of the self-DM-corrected 'P217 mm' observations was assumed equal to 200 ns, while the observing combination of 'P217 mm' with 'S110 mm', 'S60 mm', 'C+', and MeerKAT S-band receivers improves this rms by a factor of 2.9, 1.6, 3.4, and 8.9, respectively. These improvement factors were obtained from the σ_∞ measurements (see Sec. 3.3.4 and lower part of Fig. 3.10) at a flux density spectral index equal to the EPTA pulsars' median value (-1.8). For the calculations a fictional PTA was formed, consisting of 15 pulsars[5] randomly distributed on the sky, observed once per month over 10-year period.

The sensitivity curve (the minimum characteristic strain as a function of frequency) to continuous GWs is formed based on the Moore et al. (2015) analysis. For the calculation a frequentist framework in the time domain, using analytic methods was used.The characteristic strain obtained for a detection threshold 3-σ, is presented in Fig. 3.16. The 'P217 mm'+MeerKAT combination provides us with the best sensitivity to continuous GWs, with characteristic strain equal to 8.7×10^{-17} at 1 yr^{-1} frequency, and the 'P217 mm'+'C+' combination follows with strain 3.3×10^{-16}. For the 'S110 mm' receiver currently used in Effelsberg for removing DM variations, an additional 4 and 80 years of observations are needed to achieve the same

[5]This is the total number of EPTA pulsars that can be detected at 4.85 GHz with the 'S60 mm' receiver.

sensitivity as expected for the 'C+' and MeerKAT S-band, respectively, if we assume only white noise in the timing residuals.

For calculating the detection sensitivity for a stochastic GWB we followed the Siemens et al. (2013) analysis. The amplitude of the background was set equal to $4{\times}10^{-16}$ (Sesana et al., 2016) and the power law index equal to $-2/3$. In the weak signal regime S/N $\propto N\,C\,(A^2_{GW}/\sigma^2)\,T^{3-2\alpha}$, where N is the number of pulsars in the array, C is the cadence, σ is the timing residual rms and T the length of the pulsar timing data set. Since in this regime the S/N is inversely proportional to the square root of the residual rms, an improvement in rms by a factor of 1.16, which can be achieved by changing from 'P217 mm'+'S110 mm' to 'P217 mm'+'C+' observations can be compensated by adding 7 more months of 'P217 mm'+'S110 mm' observations to the data set. While an improvement in rms by a factor of 3 can be achieved by changing from 'P217 mm'+'S110 mm' to 'P217 mm'+MeerKAT S-band observations, or can be compensated by adding 6.7 more years, on the top of 10, of 'P217 mm'+'S110 mm' observations to the data set.

3.5 Conclusions

In this chapter we presented the usage of currently available, and currently being commissioned Effelsberg high-frequency receivers for measuring DM variations and increasing the sensitivity to continuous GWs and the GWB. We have shown that at 4.85 GHz ('S60 mm' receiver observations) 15 EPTA pulsars can be detected with high S/N and with low ToA uncertainties. For seven pulsars with the longest data set we measured DM variations with the existing 'S110 mm' and 'S60 mm' receivers, as well as (based on simulations) for the future receivers 'C+' and MeerKAT S-band. We also calculated the uncertainty of the infinity-frequency ToA by combining the L-band Effelsberg observations with different receivers. We concluded that at flux spectral indices $\gtrsim -2.0$ the combination of Effelsberg L-band with the MeerKAT S-band receiver provides the most precise DM-corrected ToAs, with the Effelsberg L-band combined with the 'C+' receiver to follow.

The correction of DM variations is a process that removes red noise from the residuals but always adds white noise. This effect should be always taken into account, for studies like GW detection in nHz regime, for which high ToA precision is required. We calculated the amount of noise that is added to the residuals after correcting DM variations with the Effelsberg and MeerKAT receivers. We concluded that for pulsars with spectral index -1.8 in order to achieve post-correction ToA precision with Effelsberg 1.4 GHz ('P217'mm") observations combined with the secondary frequency observations at 2.6 GHz ('S110 mm'), 4.85 GHz ('S60 mm'), and 5 GHz ('C+'), a pre-correction ToA precision of 22 ns, 13 ns, and 26 ns is needed respectively. While in the case of MeerKAT S-band observations combined with Effelsberg 1.4 GHz observation, in which the MeerKAT observations will be the primary, the needed pre-correction ToA precision with MeerKAT should be equal to 53 ns. Since the timing precision that we can achieve with PTAs in not yet of the order of nanoseconds, we should also focus on achieving high timing precision with high frequency observations as well.

We finally investigated how by removing DM variations we can increase the sensitivity to continuous GWs and to the GWB. Assuming only white, Gaussian uncorrelated noise, and following the Moore et al. (2015) and Siemens et al. (2013) studies, we concluded that for both continuous GWs and for the stochastic GWB, best sensitivity can be achieved with MeerKAT S-band receiver, with the receivers 'C+', 'S110mm', and 'S60 mm' to follow in order. We concluded that for the currently used 'S110 mm' receiver combined with the 'P217 mm', an addition of 80 years of observations for continuous GWs and another 6.7 years for a GWB are needed in order to achieve the same sensitivity as we expect for the Effelsberg 21-cm

combined with MeerKAT 11-cm observations.

Chapter 4

Limits on the Mass, Velocity and Orbit of PSR J1933−6211

This chapter is based on:

Graikou, E., Verbiest, J. P. W., Osłowski, S., Champion, D. J., Tauris, T. M., Jankowski, F., Kramer, M. *"Limits on the mass, velocity and orbit of PSR J1933−6211"*, 2017, MNRAS, 471, 4579

For this publication I reduced the observations, I performed the timing analysis, I studied the scintillation properties of the pulsar, and I set limits on the WD and pulsar masses.

Abstract

We present a high-precision timing analysis of PSR J1933−6211, a millisecond pulsar (MSP) with a 3.5-ms spin period and a white dwarf (WD) companion, using data from the Parkes radio telescope. Since we have accurately measured the polarization properties of this pulsar we have applied the matrix template matching approach in which the times of arrival are measured using full polarimetric information. We achieved a weighted root-mean-square timing residuals (rms) of the timing residuals of 1.23 μs, 15.5% improvement compared to the total intensity timing analysis. After studying the scintillation properties of this pulsar we put constraints on the inclination angle of the system. Based on these measurements and on χ^2 mapping we put a 2-σ upper limit on the companion mass (0.44 $M_\odot$). Since this mass limit cannot reveal the nature of the companion we further investigate the possibility of the companion to be a He WD. Applying the orbital period-mass relation for such WDs, we conclude that the mass of a He WD companion would be about 0.26±0.01 $M_\odot$ which, combined with the measured mass function and orbital inclination limits, would lead to a light pulsar mass $\leqslant 1.0\ M_\odot$. This result seems unlikely based on current neutron star formation models and we therefore conclude that PSR J1933−6211 most likely has a CO WD companion, which allows for a solution with a more massive pulsar.

Contents

4.1 Introduction

MSPs are rapidly rotating neutron stars that have spin periods shorter than ∼30 ms. It is thought that they obtain their short spin periods from angular-momentum increases during mass transfer from their companions (Bisnovatyi-Kogan & Komberg, 1974; Alpar et al., 1982). The majority of MSPs have WD companions which can be either massive CO or ONeMg WDs or lower-mass He WDs. CO or ONeMg WD companions are less common in binary MSPs (BMSPs), originating from intermediate-mass progenitor stars which transfer their envelope mass on a short time leaving a partly recycled MSP (with a spin period of a few tens of ms; Tauris 2011). In contrast, He WD companions are the most common and originate in low-mass X-ray binaries (LMXBs). Their time scale of evolution is long enough to allow significant amounts of matter to accrete onto the pulsar and to fully recycle them to spin periods of a few milliseconds.

PSR J1933−6211 was discovered in 2007 at the Parkes radio telescope in the high Galactic latitude survey (Jacoby et al., 2007). Soon after the discovery it was clear that the spin period was only 3.5 ms and the orbital period was 12.28 days, which in combination with the position of the pulsar in a spin period – period derivative ($P - \dot{P}$) diagram, makes this system a typical example of a BMSP (Fig. 4.1). Pulsars that belong to this category, along with double neutron-star systems, are the most well-studied so far. If BMSPs are formed in an LMXB, their resulting He WDs follow a tight correlation between their mass and orbital period (Savonije, 1987; Tauris & Savonije, 1999). This relation can be a useful tool to probe the origin of a given BMSP and place constraints on the component masses of the system. In addition, their orbital eccentricity is also predicted to be correlated with their orbital period (Phinney, 1992).

Based on equation of state and evolutionary models the minimum allowed mass for rotating neutron stars is around 0.1–0.3 $M_\odot$ depending on their spin period (Colpi et al., 1993; Haensel et al., 2002). However, from current theories on stellar evolution and supernova (SN) explosion physics, minimum neutron star masses are expected to be larger than at least 1.0 $M_\odot$ (Timmes et al., 1996). Direct pulsar mass measurements can be achieved with post-Keplerian parameter measurements through timing (Lorimer & Kramer, 2012). These measurements require an eccentric, tight system, with preferably an edge-on orbit orientation. In edge-on orbits Shapiro-delay detection is often possible. Shapiro delay is a time-delay that arises from the photon's passage through the gravitational field of the companion star. This effect is strongest in edge-on orbits and is typically sharply peaked, with the largest delays inflicted on observations at time of superior conjunction. Efforts to measure the Shapiro delay (and thereby the companion and pulsar masses) therefore typically benefit from intense observations around superior conjunction, although full orbital coverage is typically needed to break covariances with other orbital parameters (Freire & Wex, 2010).

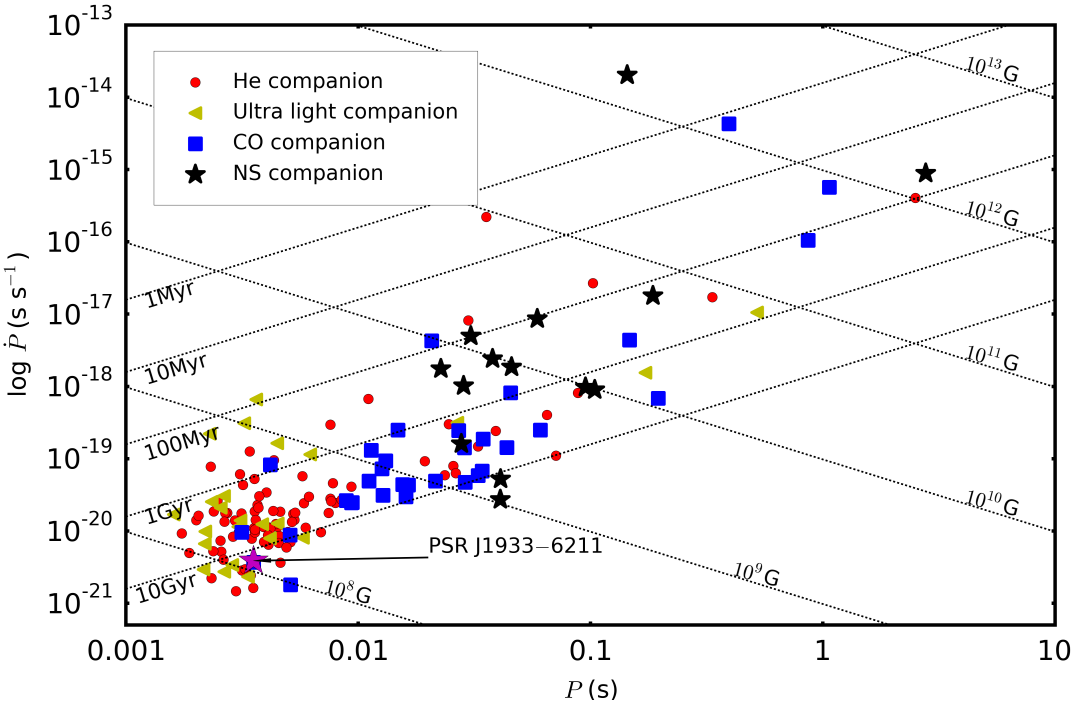

Figure 4.1: The position of PSR J1933−6211 in the period - period derivative diagram. In the plot we present also the position of all known pulsars that have a companion. Circles indicate He WD companions, squares CO WD companions, diamonds neutron star companions and triangles ultra-light or planetary companions (data taken from the ATNF Pulsar Catalog, Manchester et al. (2005)), see definition of companion stars in Tauris et al. (2012).

In the cases that neither the orbit is relativistic nor the inclination of the system is high, indirect limits on the mass can be derived from the mass function. The mass function defines a relation between the Keplerian parameters with the system inclination angle and the system masses. Unlike Keplerian parameters that can be accurately measured through timing, the inclination angle and companion mass are very difficult to measure directly. In cases of close, massive WDs, optical observations, in combination with WD cooling models, may reveal the mass of the companion. When no direct measurements are feasible, pulsar timing can still be used to derive limits on the masses and orbital parameters. In those cases where the companion is a He WD, a mass estimate can be obtained from the correlation between WD mass ($M_{\rm WD}$) and orbital period ($P_{\rm b}$).

Strong scintillation of the pulsar signal can be a big observational challenge. Scintillation, which has as a result that the observed signal intensity varies, is caused by inhomogeneities and turbulence in the interstellar plasma. How strong this phenomenon is, depends on the size of inhomogeneities, the distance of the pulsar, the observing frequency and the peculiar velocity. PSR J1933−6211, having a low dispersion measure of 11.520(2) pc cm^{-3}, is expected to scintillate strongly at 1.3 GHz frequency (Rickett, 1977). Scintillation time scale analysis can be used in order to measure the transverse velocity of the pulsar. Scintillation transverse velocity is an interstellar medium effect that is caused by the pulsar's orbital velocity, the proper motion, Earth's orbital motion, the velocity of the scattering screen and the peculiar velocity. Transverse velocity measurements allows us to put constraints on the orbital inclination of the system (Lyne, 1984; Ord et al., 2002) leading us to better understand the masses of the system.

In this paper we present an updated timing analysis and mass limits for PSR J1933−6211. The observations and data reduction are described in Section 5.2, while the overall timing solution and the pulsar's usefulness for pulsar timing arrays (PTAs) are discussed in Section 4.3. Our attempts to measure the mass of this pulsar were seriously hampered by strong scintillation around the time of superior conjunction. An analysis of these scintillation measurements is given in Section 4.4. Next, we present the pulsar's proper motion and transverse velocity in Section 4.4.1. Constraints on the mass of the pulsar – and the implications for binary evolution models, are outlined in Section 4.5, followed by some concluding remarks in Section 4.6.

4.2 Observations and data reduction

Our observations of PSR J1933−6211 were performed with the Parkes 64-m radio telescope. The total span is ∼10 years divided into two epochs of ∼1 year of observations each (Fig. 4.3). In the first epoch the pulsar is observed as part of the high Galactic latitude survey follow-up observations (Jacoby et al., 2007). These archival data, biblically available, were recored with the Caltech Swinburne Parkes Recorder 2 (CPSR2) coherent dedispersion backend (Hotan et al., 2006) that provides two dual-polarization bands of 64 MHz, each centred on 1341 and 1405 MHz respectively. Each of the bands was split into 128 frequency channels using a polyphase filterbank.

The aim of the second epoch of observations was to precisely measure the orbital parameters of the system and the masses. The observations were performed with the CASPSR backend (Hickish, 2016), which provides a 256-MHz bandwidth, centred at 1382 MHz, resulting in a significant increase in sensitivity. All the observations were taken at wavelength of 21cm with the central beam of the Parkes multibeam receiver (Staveley-Smith et al., 1996).

Since one of our goals is to measure the system masses we picked our observations strategy in a way that we were sensitive to Shapiro-delay detection. This phenomenon maximally affects pulse arrival times at superior conjunction. Superior conjunction is the point in the orbit where the pulsar is behind its companion. Consequently we defined our observing

Table 4.1: The timing data characteristics, as observed with two different observing systems.

	Data range (MJD)	Data range (Gregorian)	Number of ToAs	Central frequency (MHz)	Bandwidth (MHz)	Average ToA uncertainty (μs)[1]	EFAC	Weigthed rms timing residual (μs)
CPSR2	52795.7–53301.4	2003 Jun.–2004 Oct.	52	1341/1405	2 x 64	3.686	0.8/1.4	1.254
CASPSR	55676.0–56011.0	2011 Apr.–2012 Mar.	96	1382	256	3.393	0.9	1.057

[1] These values correspond to the mean ToA uncertainty for 15-min integration time observations. For more typical 1-hour integrations, the ToA uncertainty (and timing RMS) should decrease by up to a factor of two.

strategy to have uniform coverage through 75% of the orbit, but increased observing cadence during the 25% of the orbit surrounding superior conjunction. The length of a typical observing scan was 30min.

We divided each observation into 15-min segments. Each of these 15-min sub-integrations were weighted by their signal-to-noise ratio (S/N) before the segments were integrated in time and frequency. The observations that provided the best S/N were combined and von Mises functions were fitted in order to create an analytic template. We followed the same procedure to create templates for each of the two backends for which the data were available. We measured the pulse times-of-arrival (ToAs) with two different methods. In the first method we correlated the analytic templates with the observations by applying goodness-of-fit statistics in the frequency domain (Taylor, 1992) and in the second method we applied the matrix template matching approach for which we used the full polarization information of the pulsar signal in the template.

In order to optimise the sensitivity of our analysis, we performed full polarimetric calibration following the methods described by (van Straten, 2004, 2013). Specifically, a time-dependent receiver model was derived from long-track observations of PSR J0437−4715 following the polarimetric calibration-modelling technique described by van Straten (2004). This solution was then applied to the PSR J1933−6211 data using the measurement-equation template-matching technique of van Straten (2013). The Stokes parameters in the calibrated data follow the conventions defined by van Straten et al. (2010).

Based on the polarized pulse shape (see Fig. 4.2), we performed the analysis of van Straten (2006), which suggests a theoretical $\sim 25\%$ improvement in ToA precision, depending on the degree of polarization and the variability of the polarization vector as a function of pulse phase, can be obtained if ToAs were derived by using the full polarization information (instead of deriving ToAs from the total-intensity profile only, as is common in pulsar timing). To verify this result, we derived two sets of ToAs: one set based on the total-intensity pulse profile and one based on the full polarimetric polarization, using the van Straten (2006) timing method. In the remainder of the paper we use full polarimetric polarization residuals unless otherwise stated.

The resulting phase-connected full polarimetric polarization ToA residuals are presented in Fig. 4.3. The comparison with the total-intensity residuals led to an overall improvement of 15.5% in timing residuals and 20% in ToAs uncertainty.

The packages that were used for the analysis described above are PSRCHIVE (Hotan et al., 2004; van Straten et al., 2012) and TEMPO2 (Hobbs et al., 2006).

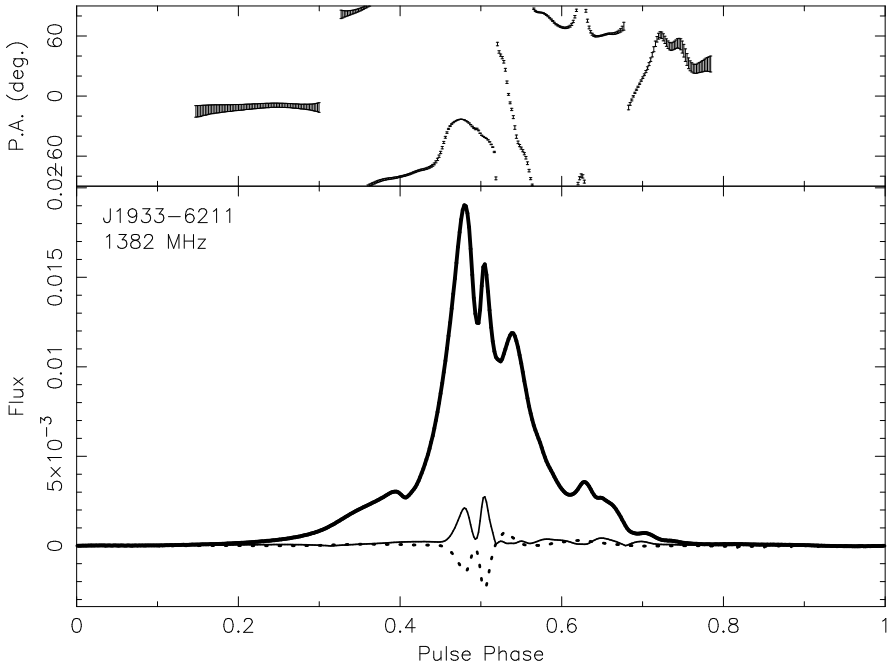

Figure 4.2: Average polarization calibrated pulse profile from the CASPSR backend data at 1382 MHz central frequency (averaged across a bandwidth of 256 MHz). In the plot the linear (solid) and circular polarization (dotted) profiles are presented as well as the total intensity profile (bold). The flux scale is arbitrary. The fact that the main pulse is sub-divided into three individual, sharp, components, greatly aids the timing precision achievable in this system. This resolved main pulse was not presented in the discovery publication (Jacoby et al., 2007), which used data from the analog filterbank, which does not perform coherent dedispersion and thereby smears out the fine structure in the pulse profile.

Table 4.2: The timing parameters of the system that correspond to the best-fit residuals.

General information	
MJD range.....	52795 - 53301
	55676 - 56011
Number of ToAs.....	148
Weigthed rms timing residual (μs)....	1.23
Measured Quantities	
Right ascension, α (J2000).....	19:33:32.42668(5)
Declination, δ (J2000).....	$-$62:11:46.876(1)
Proper motion in α, μ_α (mas yr^{-1})....	$-$5.54(7)
Proper motion in δ, μ_δ (mas yr^{-1})....	10.7(2)
Total proper motion (mas yr^{-1})	12.1(2)
Spin frequency, ν (Hz).....	282.21231361528(2)
Spin down, $\dot{\nu}$ ($\times 10^{-16}$ Hz s^{-1}).....	$-$3.0828(7)
Dispersion measure, DM (pc cm^{-3})...	11.520(2)
Orbital period, $P_{\rm b}$ (d).....	12.8194067183(8)
Time of ascending node, T_{asc} (MJD) ...	53000.4952524(2)
Projected semi-major axis, a$_p$=a sin$i$ (lt-s).	12.2815745(3)
$\eta = e\,\sin\omega$ ($\times$ 10^{-6})	1.36(4)
$\kappa = e\,\cos\omega$ ($\times$ 10^{-6}).....	$-$0.32(3)
Derived Quantities	
Epoch of periastron passage, T_0 (MJD) ..	53004.17(5)
Longitude of periastron, ω (deg).....	103(1)
Orbital eccentricity, e ($\times$ 10^{-6}).....	1.40(4)
Mass function, $f(M_\odot)$	0.0121034(2)
2-σ limits from χ^2 mapping	
Longtitude of the ascending node, Ω (deg)	4–148
Companion mass, M_{wd} (M$_\odot$)	<0.44
Distance, d (kpc)	>0.11
Assumptions	
Clock correction procedure	TT(BIPM(2013))
Solar system ephemeris model.....	DE421
Binary model	ELL1

Note: Figures in parentheses are the nominal 1-σ TEMPO2 uncertainties in the least-significant digits quoted.

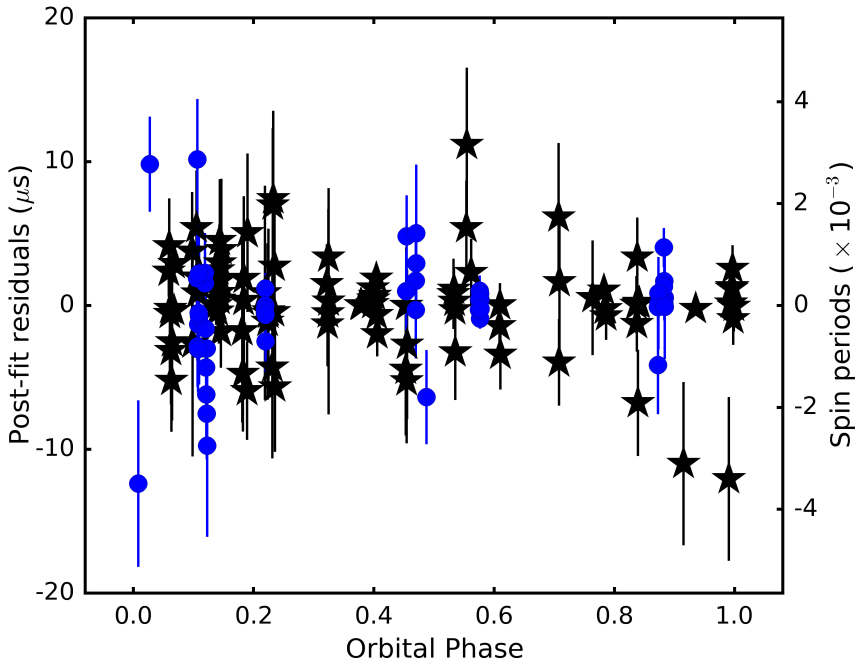

Figure 4.3: The timing residuals at 20 cm as a function of orbital phase, using the CPSR2 (circles) and CASPSR (stars) data.

4.3 Timing solution and high-precision potential

A total of 148 ToAs were formed in order to measure the orbital, spin characteristics and the astrometry of PSR J1933−6211. Since the eccentricity of the system is very low, we applied the ELL1 model (Lange et al., 2001), for which the eccentricity, e, the epoch and the longitude of periastron passage, T_0 and ω respectively, are replaced by the Laplace-Lagrange parameters, $\eta = e \sin\omega$ and $\kappa = e \cos\omega$ and the time of the ascending node passage T_{asc}.

We fit for pulsar parameters using least-squares fitting in order to minimize the differences between measured ToAs and the expected arrival times derived from the analytical model (Edwards et al., 2006). A phase offset was fitted between the CPSR2 and the CASPSR data account for any difference in instrumental delays. We furthermore multiplied the ToA uncertainties with error-scaling-factors (EFACs) of 0.8 and 1.4 for the data correspond to the two CPSR2 polarization bands and 0.9 CASPSR data respectively. These factors account for any possible underestimation of the ToA uncertainties, as described in Verbiest et al. (2016). We note that the phase offset between the backends is only 1.71 μs. Given this small offset, the fact that the timing model fits both sub-sets equally well and that the fit worsens considerably when an integer number of pulse-periods get either added or subtracted from this offset value, clearly indicates that phase-connection was achieved across the 6-year gap.

The TT(BIPM(2013)) terrestrial time standard and the DE421 solar system ephemeris were used in order to convert from topocentric to barycenter arrival times.

The resulting timing parameters that correspond to our best-fit residuals (Fig. 4.3) are presented in Table 4.2. The timing analysis led to significant measurements of the proper motion, the spin and spin-down and the keplerian parameters of the system. All these well

measured parameters led us to further investigate the geometry and the origin of the system.

With a weighted rms of only 1.23 μs, PSR J1933−6211 is a good candidate to be added in the Pulsar Timing Array (PTA) projects that aim to detect gravitational waves in the nHz regime as its timing rms compares well to that of most sources in the international PTA (Verbiest et al., 2016).

4.3.1 Mass constraints from timing

The lack of a Shapiro delay detection and precise post-Keplerian parameter measurements, $\dot{\omega}$ and $\dot{P}_{\rm b}$, has as a result that with the current timing direct system-mass measurements are not possible. Instead, we derived constraints on the masses and orientation of the system by mapping the goodness-of-fit (as determined by the χ^2 value of the fit) over a four-dimensional grid covering the companion mass $M_{\rm c}$, the inclination angle of the system i, the longitude of the ascending node Ω and the distance to the system D. At each pixel of this four-dimensional grid, these four parameters were held fixed, as were the post-Keplerian parameters $\dot{\omega}$ and $\dot{P}_{\rm b}$ that were derived from these. (Note while the distance does not enter in the post-Keplerian parameters, it was used to determine the parallax, which was kept fixed, and it entered in the calculation of the Kopeikin terms that define i and Ω; Kopeikin (1995, 1996)). Our grid had a step size of 0.01 $M_\odot$ in M_c, 0.01° in i, 1° in Ω and 20 pc in distance, so our results (see Table 4.2) are quantised at these levels.

In Fig. 4.4 our results are presented, with 95% confidence limit on the companion mass. The lower limit for the WD mass (0.1 $M_\odot$) comes directly from the mass function, evaluated for an edge-on orbit, provided that the pulsar mass is > 0.0 $M_\odot$. These limits do not allow us to identify the companion star as either a He or CO WD. In Section 4.5 we revisit this question based on some alternative, more theoretical, approaches.

4.3.2 Characteristic age

The age of pulsars is key for evolutionary models. But in order to measure it precisely we should know the pulsar's spin period at birth and the braking index. In order to approximate this problem we make some assumptions: the initial period of a pulsar is much lower than the one that we measure today, and the pulsar loses energy due to magnetic dipole radiation with a constant B-field (braking index equal to 3). We can then estimate the characteristic age τ:

$$\tau = \frac{P}{2\,\dot{P}}, \tag{4.1}$$

which is only a rough estimate of the real age (see below).

PSR J1933−6211 has a very low spin period derivate, as derived from timing (see Table 4.2). For pulsars with such low spin period derivates, effects like the Shklovskii effect and Galactic acceleration can have a significant impact on the observed spin period derivative. In order to calculate more accurately the characteristic age, we measured the contribution of these kinematic effects in $\dot{P}$.

Both effects are quite small in PSR J1933−6211, the Shklovskii effect that is calculated from:

$$\left(\frac{\dot{P}}{P}\right)_{\rm Shk} = 2.43 \times 10^{-21} \, \frac{\mu^2}{(\text{mass yr}^{-1})} \, \frac{d}{(\text{kpc})}, \tag{4.2}$$

is 1.8(3) $\times 10^{-19}$ s s^{-1}.

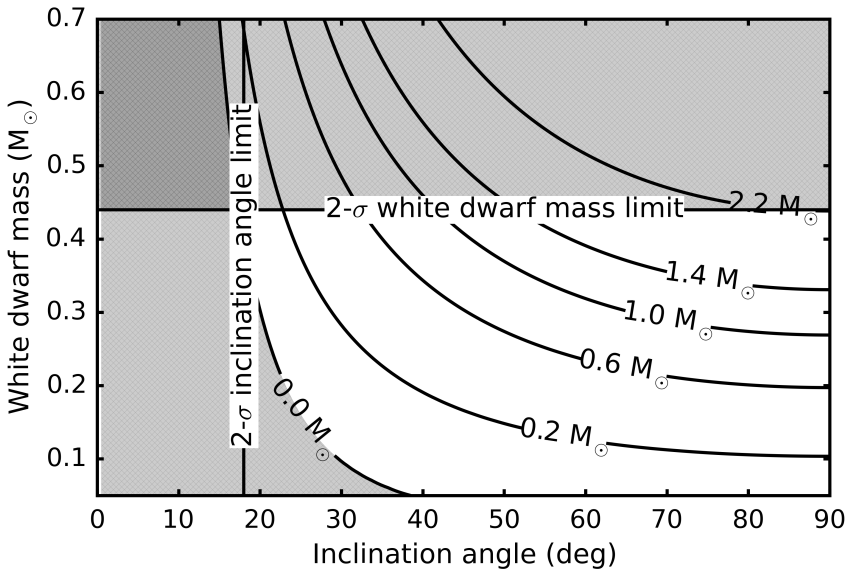

Figure 4.4: Mass – inclination angle diagram indicating the limits derived from timing. Specifically, the bottom-left region is excluded by the mass function and the requirement that $M_{psr} > 0$ and the 2-σ upper limit on the companion mass, derived from our goodness-of-fit mapping, is indicated by the horizontal line at $M_c = 0.44\ \mathrm{M}_\odot$ (see Section 4.3.1).

The Galactic acceleration contribution is defined by:

$$\left(\frac{\dot{P}}{P}\right)_{\text{Gal acc}} = \frac{\alpha_z \sin b}{\mathrm{c}} - \cos b \left(\frac{\Theta_0^2}{\mathrm{cR}_0}\right)\left(\cos l + \frac{\beta}{\sin^2 l + \beta^2}\right), \tag{4.3}$$

where the Galactic distance of the solar system: $\mathrm{R}_0 = 8.34$ kpc, the circular rotation speed of the Galaxy at R_0: $\Theta_0 = 240$ km s^{-1} (Reid et al., 2014), l the Galactic longitude, b the Galactic latitude and $\beta = (d/\mathrm{R}_0)\cos b - \cos l$. It is measured to be: 9.6(6) $\times 10^{-20}$ s s^{-1}. The resulting characteristic age after taken into account these effects is 14.6(4) Gyr, which exceeds the Hubble time. Such large characteristic ages have been pointed out before (Camilo et al., 1994), and are caused by the fact that the spin period derivate is too small to cause rapid changes in the pulsar spin period, so we observe the pulsar almost at its birth P and $\dot{P}$ values (Tauris et al., 2012), and thus eq. 4.1 above brakes down since it assumes $P_0 \ll P$, where P_0 is the birth spin period (after accretion). Instead, for MSPs the value of τ is a measure of its remaining lifetime as a radio pulsar.

4.4 Scintillation measurements

During our observations we measured strong scintillation. The mean S/N for observations that are fully averaged in time and frequency and polarization calibrated, is 29, but reaches ∼200 during scintillation maxima, for 15-min observation scans, a factor of almost seven stronger.

We managed to observe only two complete scintles due to the length of the scintillation time scale and the fact that the individual observations were conventionally ∼30 minutes

Table 4.3: Scintillation parameters and the derived scintillation speed of the two complete scintles. Both observations were taken with the CASPSR backend at 1382 MHz central frequency with 256-MHz observing bandwidth divided into 512 channels and 5-min time resolution.

Data	2011-05-03	2011-05-16
Δt (min)	181(5)	108(5)
Δf (MHz)	358(8)	155(8)
V_{ISS} based on NE2001 (km s^{-1})	34(3)	38(3)
Orbital phase (ϕ)	0.2	0.2

long. For the scintillation analysis we used only CASPSR data with 5-min integrations divided into 512 frequency channels (over a 256-MHz bandwidth). For each observation we removed the band edges, which corresponds to 10% of the band. We manually cleaned the remaining Radio Frequency Interference (RFI) for the cases where it was needed.

In order to measure the scintillation time scale and bandwidth we fitted 1-D Gaussian functions to the frequency (respectively time) averaged intensity-series of the dynamical spectrum. The number of Gaussians that are used to fit the data has been decided through a Kolmogorov-Smirnov test by requiring the post-fit intensities to follow a Gaussian distribution with 95% certainty (see Fig. 4.5). In Table 4.3 we present the scintillation parameters for the two available scintles as derived from the method that we explained above.

The scintillation properties allow transverse velocity measurements. The comparison with theoretical transverse velocity and further inclination angle limits are presented below.

4.4.1 Transverse velocity and inclination angle limit

Various studies have investigated the space velocity of pulsars. Desvignes et al. (2016), after investigating 42 MSPs pulsars, concluded that the mean transverse velocities of MSPs is 92±10 km s^{-1}, a factor of 4 lower than that of young pulsars (Hobbs et al., 2005). This difference can be understood from their dissimilar kick velocities at birth. Such a differentiation is thought to arise from a combination of different masses of the exploding stars forming neutron stars in isolation versus in close binaries (the latter being stripped prior to the explosion) and the absorption of the kick momentum in a binary system (Tauris & Bailes, 1996). Newborn pulsars are expected to receive a broad range of kicks – between 0 and more than 1000 km s^{-1} (Janka, 2016). The binaries that eventually give rise to MSPs, survived the SN kick, which could mean that the kick often was either small or fortuitously oriented.

Pulsar space velocities can be measured through scintillation properties of the pulsar. By assuming that the diffraction screen is located in the middle between the Earth and the pulsar and that the scattering medium is a uniform Kolmogorov medium, we calculate the scintillation speed from (Gupta et al., 1994):

$$V_{ISS}(\mathrm{km\ s^{-1}}) \;=\; 3.85\times10^{4}\,\frac{\sqrt{d(\mathrm{kpc})\,\Delta f(\mathrm{MHz})}}{f(\mathrm{GHz})\,\Delta t(\mathrm{s})}, \tag{4.4}$$

where d is the distance of the pulsar, f is the observing frequency and Δf and Δt are the scintillation bandwidth and time scale (see Table 4.3).

The dispersion measure can give an estimate of the pulsar distance. We consider two such distances derived from two different models: the widely used NE2001 model (Cordes &

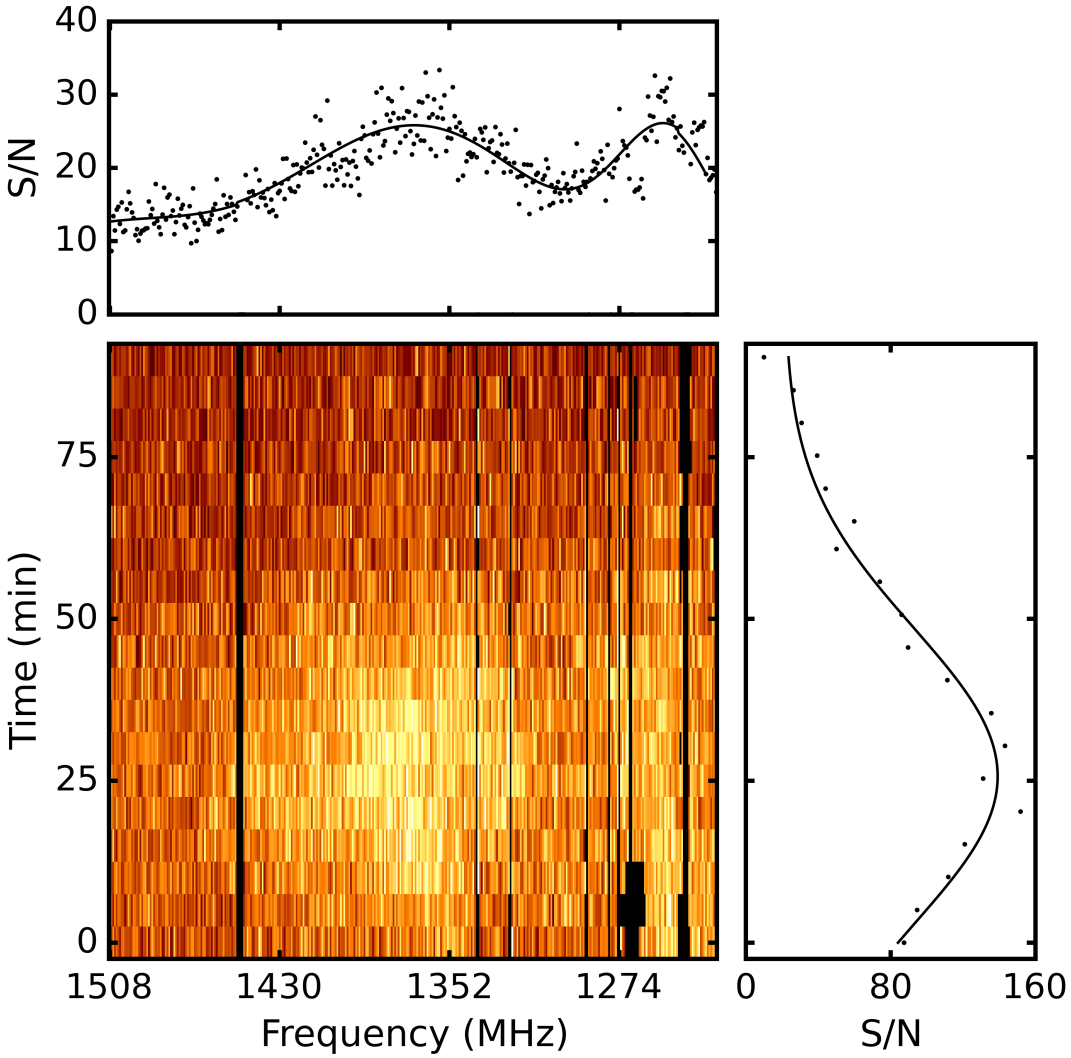

Figure 4.5: Dynamic spectrum of a full scintle of PSR J1933−6211 as observed on 16th of May 2011. In the top and right plots, the S/N in each frequency channel and in each sub-integration, are presented respectively. The solid line corresponds to a Gaussian fitting line to our observation.

Lazio, 2002) and the most recent YMW16 model (Yao et al., 2017). The NE2001 model has been widely scrutinised whenever new pulsar distances were measured (see, e.g. Matthews et al. 2016; Desvignes et al. 2016), leading to the conclusion that for pulsars at low and medium Galactic latitudes this model gives a good distance prediction, comparable to pulsar parallax measurements. For PSR J1933−6211 with Galactic latitude of −28.6315° and a dispersion measure equal to 11.520(2) pc cm^{-3} the model-predicted distance is 0.51(7) kpc, and 0.65 kpc based on NE2001 and YMW16, respectively. The scintillation speed that we measured based on NE2001 distance measurements is equal to 36(2) km s^{-1}.

The pulsar space velocity ($V_{\rm model}$), that we measured through scintillation speed, is composed of the pulsar's orbital velocity ($V_{\rm orb}$), proper motion ($V_{\rm pm}$), Earth's velocity ($V_{\rm Earth}$) and the velocity of the scattering screen (V_{ISM}).

$$V_{model} = \underbrace{V_{\rm orb}}_{\alpha_p,\, P_b,\, \omega,\, i,\, e,\, \phi} + \underbrace{V_{\rm pm}}_{\Omega,\, d,\, \mu_\alpha,\, \mu_\delta} + V_{\rm Earth} + V_{\rm ISM} \tag{4.5}$$

The proper motion and the orbital velocity, that either added or subtracted to the proper motion, contribute the most to the pulsar space velocity, since $V_{\rm ISM}$ can be neglected (Gupta, 1995) and $V_{\rm Earth}$ is considered as constant throughout the observation. Since the pulsar is moving, as we observe it we track it in different positions on the sky, having as a result to detect differences in V_{ISS}. By monitoring these changes in respect to orbital phase we can obtain useful information about the geometry of the system. For example, Lyne (1984) and Ord et al. (2002) measured the inclination angles of the PSR B0655+64 and J1141−6545 systems respectively, based on the orbital dependence of the scintillation speed. Unfortunately, based on our analysis, the fact that both scintles are detected at the same orbital phase (Table 4.3), did not allow us to perform a χ^2 mapping in order put constraints on the inclination angle of the system. Luckily, we can further investigate the geometry of the system based on the timing constraints on the longitude of the ascending node (Ω, see Section 4.3.1 and Table 4.2).

We compared the scintillation speed, measured with our data (Table 4.3), with the model of the pulsar space velocity (eq. 4.5). The ω, P_b, e, α_p and proper motion can be accurately measured through timing (Table 4.2). Our unknowns are two: Ω and i. The measured orbital velocity depends only on the unknown inclination angle:

$$V_{orb} = \frac{2\,\pi\,a_p}{\sin i \sqrt{1-e^2}\,P_b} = \frac{20.8868501(5)}{\sin\,i}\ {\rm km\ s^{-1}}. \tag{4.6}$$

Higher inclination angles correspond to lower orbital velocities and as a result to lower observed scintillation speeds. The highest probable orbital velocity that can be measured for this system, in the 0.2 orbital phase, is ∼120 km s^{-1} and the lowest is ∼2 km s^{-1}.

The other unknown is Ω for which we have a 2-σ limit through timing (see Table 4.2). Inside this Ω 2-σ parameter space we find the i values for which the $V_{\rm model}$ is consistent to our scintillation speed based on our observations. Our results are presented in Fig. 4.6. The fact that two regions of i are allowed, is due to the 180-degree ambiguity in Ω, raised from the fact that we can not determine which of the two orbit nodes is the ascending node.

4.5 Limits on the system masses

In addition to the timing-based constraints presented in Section 4.3.1, for LMXBs, there are theoretical relations between the orbital parameters and the pulsar and companion masses. We will now consider these theoretical models and their predictions, in order to investigate the nature of the white dwarf companion.

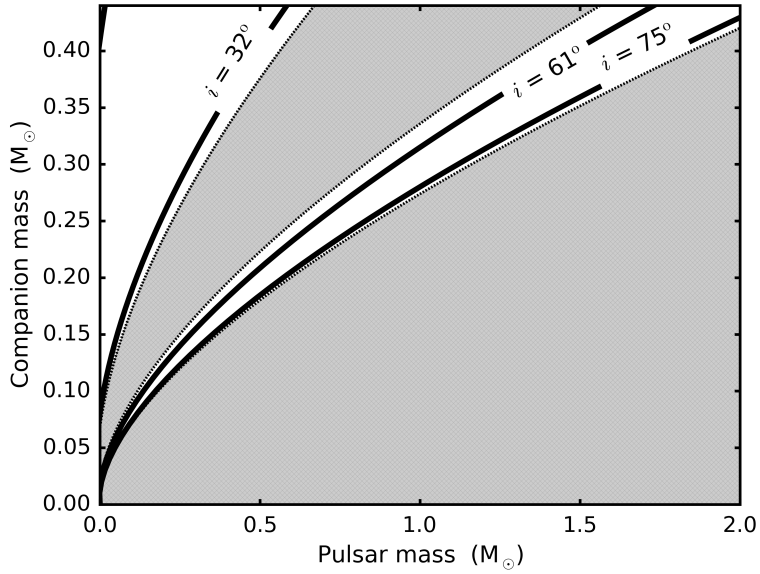

Figure 4.6: Pulsar mass – companion mass diagram. The grey areas indicate inclination angles excluded with 1-σ. With the solid lines the inclination angle 1-σ limits for this system are presented, as measured based on the scintillation speed. With the dotted lines the error is presented. Our two sets of solutions arise from the fact that we can not determine which of the two nodes is the ascending node.

4.5.1 Orbital eccentricity

Phinney & Kulkarni (1994) found a relationship between the orbital eccentricity and orbital period for cases where the pulsar is formed after stable mass transfer in an LMXB from a red giant filling its Roche lobe. For orbital periods of 12.8 days, the 95% lower limit on the eccentricity as predicted from this model is significantly higher than the value that we derived from timing (Table 4.2). This discrepancy is caused by the uncertainty in input physics applied for the modeling, i.e. related to tidal interactions and convection in the outer layers of the progenitor star. As a result, there is a large scatter in eccentricities for observed BMSPs with a given orbital period (cf. Fig. 4 in Tauris et al. (2012)).

4.5.2 Orbital period – WD mass relation

Different studies have investigated the relationship between the orbital period and the companion mass in MSP – WD binaries which originate from LMXBs (Savonije, 1987; Rappaport et al., 1995; Tauris & Savonije, 1999; Istrate et al., 2014). This relation has its basis in a correlation between the radius of a low-mass red-giant star and the mass of its degenerate He core.

Numerical stellar evolution calculations have been done by Tauris & Savonije (1999) to investigate this relationship for LMXBs with wide orbits (> 2 days). Based on computations of dynamically stable mass transfer in LMXBs, they obtained a relationship between the orbital period and the WD mass for different chemical compositions of the donor star. Based on this analysis, the derived WD mass varies from 0.251 to 0.277 $M_{\odot}$ (Table 4.4).

The mass of the WD is related to the mass of the neutron star (M_{ns}) and the orbital incli-

Table 4.4: WD mass estimates assuming different chemical compositions of its progenitor star, based on the orbital period – WD mass relation for He WD companions (Tauris & Savonije, 1999) and given that $P_b = 12.8$ d for PSR J1933−6211.

Population	WD mass ($M_\odot$)
I	0.251
I & II	0.264
II	0.277

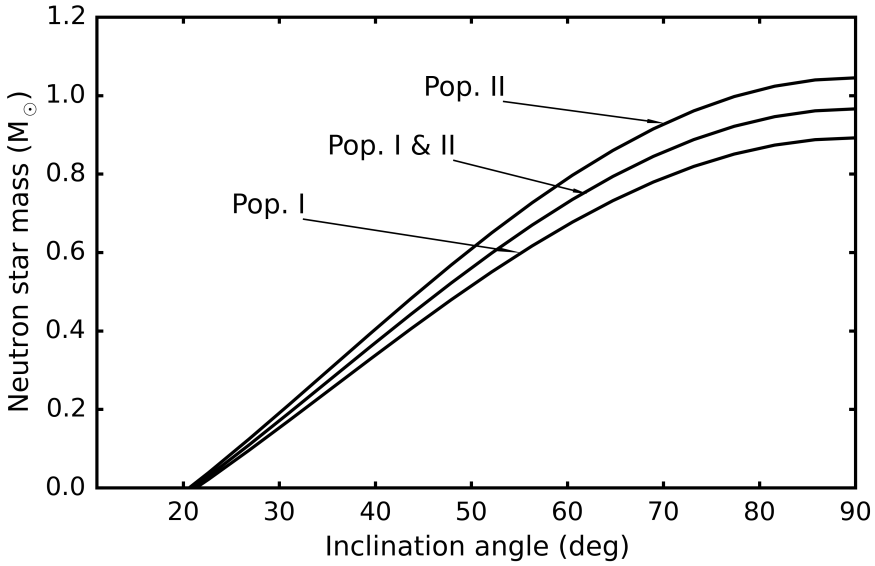

Figure 4.7: PSR J1933−6211 mass estimate as a function of inclination angle based on the theoretical orbital period – WD mass relations for He WD companions (see Section 4.5.2). The three neutron star mass lines are based on different chemical compositions of the progenitor star of the WD (Table 4.4).

nation angle (i) through the mass function:

$$f(M) = (M_{wd}\,\sin i)^3/(M_{ns} + M_{wd})^2, \tag{4.7}$$

In Fig. 4.7 we present this relation for three different WD masses, see Table 4.4 above. The derived upper limit for the neutron star mass is 0.96 ± 0.08 $M_\odot$. This very low pulsar mass limit, can be even lower if we combine it with the inclination angle limit: $i < 80°$, as calculated based on the scintillation speed measurements. Neutron star masses lower than 1.1 $M_\odot$ are not consistent with theoretical models of their formation (Timmes et al., 1996). For this reason it is very unlikely that the WD companion would be a He WD, and therefore we suggest that this system did not originate from an LMXB. Hence, the WD probably has a larger mass (and quite likely a CO composition), which also implies a larger mass of the neutron star.

The formation of a fully recycled MSP, like PSR J1933−6211, requires mass transfer on a long timescale which, until the discovery of PSR J1614−2230 (Hessels et al., 2005), has only been explained through an LMXB evolution. The discovery of the PSR J1614−2230 system brought a paradox, since the pulsar is an MSP with spin period 3.2 ms and yet it has a CO WD companion (Demorest et al., 2010). The formation of PSR J1614−2230 is explained with an

intermediate-mass X-ray binary (IMXB) which evolved from Case A Roche-lobe overflow (RLO) (Tauris et al., 2011; Lin et al., 2011). Another recently discovered candidate member of this class is PSR J1101−6424 (Ng et al., 2015). In the formation scenario of these systems the RLO begins when the progenitor of the WD is still on the main sequence (i.e. undergoing core hydrogen burning) and therefore the timescale of the RLO is relatively long, such that the amount of mass that is transfered to the neutron star is sufficient to form an MSP. In case of IMXBs in a close orbit, the mass of the remnant CO WD can be as low as 0.33 $M_\odot$ (Kippenhahn & Weigert, 1990; Tauris et al., 2000). This limit is consistent with our 2-σ WD upper limit of 0.44 $M_\odot$ derived from timing (Fig. 4.4). Finally, we note that the orbital period of PSR J1933−6211 (12.8 d) is also consistent with an IMXB forming a CO WD companion (Tauris et al., 2000). For optical constraints on the WD companion in PSR J1933−6211, see Mateo et al. (2017) (in preparation).

4.6 Conclusions

We have presented high-precision timing of PSR J1933−6211, a MSP with a WD companion, using the Parkes radio telescope. After applying the matrix template matching technique we managed to achieve ToAs precision of 1.23 μs and we reached an improvement of 15.5% in timing residuals, compared to the total intensity timing analysis. We determined precise spin and spin derivative values and the orbital parameters of the system.

The two scintles that we observed allowed us to determinate the scintillation parameters of the system. This information lead us to transverse velocity measurements of 26(2) km s^{-1}. Based on Ω 1-σ limits, obtained from χ^2 mapping, the Keplerian parameters, measured through timing, and the transverse velocity we put limits on the inclination angle of the system. We concluded that the inclination angle is likely lower than ∼80°.

The lack of Shapiro delay, $\dot{\omega}$ and $\dot{P}_p$ measurements prevents direct mass measurements. For this reason, we performed χ^2 mapping in order to put limits on the WD mass. Our 2-σ upper limit for the WD mass is 0.44 $M_\odot$. This limit corresponds to 2.2 $M_\odot$ as an upper pulsar mass limit for a high inclination angle. Based on this limit, we cannot distinguish between the possibility of a CO or a He WD. For this reason, we further investigated the possibility that the companion is a He WD. These type of MSP systems are very well studied. Based on the orbital period – WD mass relationship resulting from LMXB evolution (Tauris & Savonije, 1999), we derived an upper limit for the pulsar mass of 0.96 ± 0.08 $M_\odot$. Therefore, we conclude that if PSR J1933−6211 has indeed a He WD companion, then the mass of the pulsar is very light – in fact, too light to be consistent with current stellar evolution and SN explosion physics modeling. We therefore, conclude that the companion of PSR J1933−6211 is most likely a CO WD, and therefore this system has an origin in an IMXB system, somewhat similar to the BMSP J1614−2230.

Chapter 5

The beam geometry of PSR B1913+16

The work presented in this chapter is based on a publication in preparation:

Graikou, E., Kramer, M., Desvignes, G., Champion, D. J., Porayko N. K., Verbiest, J. P. W. *"The beam geometry of B1913+16"*, To be submitted to MNRAS

For this project I reanalysed the EPOS observations. I reduced the PSRIX Effelsberg PSR B1913+16 observations, and I polarisation calibrated them. I measured temporal changes of the separation, and relative height of the two main profile components, of the full width, and of the phase-averaged flux density. Finally, I determined the geometry of the system based on the total intensity.

Abstract

In this chapter we determine the geometry of the B1913+16 binary system by studying the impact of relativistic spin precession on the observed pulse profile shape and polarisation position angle (PPA) curve. For our analysis we used Arecibo data taken in the early 80s, as well as Effelsberg data from the middle of 1990 to the beginning of 2017. Changes in the separation, and the relative amplitude of the two main pulse components, in the phase-averaged flux density, and in the PPA curve are observed. Specifically, we found that the separation of the two components shrinks by $\sim$1.2% per year, and the relative amplitude of the leading and trailing components was reducing until the middle of 2010, after which it is started to increase again, an effect that is related to the emission beam structure. For extracting the emission geometry we used two independent models. The first one is purely geometrical and assumes a hollow-cone emission beam shape. This model is only applied to our total intensity observations. The second model is the Rotating-Vector model (RVM) and is fitted to the PPA curve measurements of our available polarization-calibrated data which cover only a small fraction of epochs compared to the total intensity observations. We concluded that the orbital inclination angle is 132.9° and the misalignment angle is $\sim$21°. Since the two models disagree on their predictions on how the line of sight cuts the emission beam we propose a new beam shape according to which the beam has a hollow-cone shape but the magnetic axis is not in the middle but is shifted by 10° from the center.

Contents

5.1 Introduction

Pulsars, the product of supernova explosions, can be found either isolated or in binary systems. Their companions, if any, can be either compact objects (white dwarfs, neutron stars, or black holes), or planets. So far planets, white dwarfs and neutron stars have been detected as pulsar companions. Pulsar-neutron star systems are rarely found, with only 21 such systems discovered thus far (Tauris et al., 2017). PSR B1913+16 was the first double neutron star system ever discovered (Hulse & Taylor, 1975), as part of an Arecibo observatory search campaign. It has a spin period of 59 ms, a very eccentric orbit (e = 0.6) and an orbital period of only 7.78 hours (Hulse & Taylor, 1975). PSR B1913+16 has been intensively observed and studied, so the orbital and spin characteristics are very accurately measured. Systems like this, composed of very compact objects in tight orbits, enable the study of various relativistic effects.

PSR B1913+16 was the first pulsar in which relativistic phenomena were observed and studied. One of this is GR's prediction of energy lose from binary systems in the form of GW emission. The result of this emission is the shrinkage of the orbit, which is observed as an orbital decay. The measured PK parameters of PSR B1913+16, already in 1979, set good constraints on the system masses allowing Taylor et al. (1979) to well predict the orbital decay of this system. Later measurements showed that the observed orbital decay of this system agrees with the expected emission of GWs to within 0.2% (Taylor & Weisberg, 1982; Weisberg et al., 2010). These observations were not only a confirmation of GR, but also the first indirect GW detection. Joseph Taylor and Russell Hulse for this discovery awarded a Nobel prize in physics in 1993. In this chapter we will focus on another relativistic effect, geodetic precession and how it affects the pulse profile and through this we will determine the emission beam geometry and map the emission beam of the pulsar.

Geodetic precession occurs when the total angular momentum of the system is misaligned with the pulsar's spin axis. A coupling of these two vectors causes a precession of the spin axis around the total angular momentum axis. The result is that the emission beam cuts the line of sight at different angles allowing us to see different parts of the beam at different epochs. It was first predicted by Damour & Ruffini (1974) that this phenomenon would be observable in pulsars. The strength of this effect can be expressed through the geodetic precession rate (Barker & O'Connell, 1975):

$$\Omega_{\rm p} = \frac{{\rm G}^{2/3}}{2{\rm c}^2}\left(\frac{2\pi}{P_{\rm b}}\right)^{5/3} \frac{m_{\rm c}(4m_{\rm p}+3m_{\rm c})}{(1-e^2)(m_{\rm p}+m_{\rm c})^{4/3}}, \tag{5.1}$$

where G in the gravitational constant, c is the speed of light, $P_{\rm b}$ the orbital period and m_c and $m_{\rm p}$ the companion and pulsar masses, respectively. Since all these pulsar characteristics have been accurately measured through timing (Weisberg & Huang, 2016), the expected geodetic precession rate for this system is 1.21° yr^{-1}, one of the shortest ever measured, which corresponds to a geodetic precession period of 300 years. The expected observational effects of this phenomenon are: changes in the shape, width and polarisation of the pulse profile through time. Multiple previous studies have been focused on measuring these effects in PSR B1913+16.

The most obvious changes are in the pulsar profile shape. Weisberg et al. (1989) were the first to report gradual evolution in the pulse profile of the pulsar. They used 1408 MHz observations from 1981 to 1987 and while they did not observe any changes in the component separation, they found that the flux density of the first component decreased relative to that of the second component. The changes followed the GR prediction, with the amplitude ratio decreasing by 1.2%±0.2% per year.

Kramer (1998) was the first to report changes in the separation of the two components. Specifically, he used Effelsberg 1400-MHz observations combined with older Arecibo data and found that the separation between the two components is reducing in a way that is expected from geodetic precession. By fitting those separation results to a beam model, in which the emission comes from a circular hollow-cone beam shape, he managed to measure the impact parameter β (the closest approach of the line of sight to the magnetic axis), the magnetic inclination angle α, the angle δ between the pulsar spin and orbital momentum axis and the inclination angle i of the system. According to his best solution $i = 132.9°$, $\alpha = 153°^{+3}_{-8}$, and $\delta = 22°^{+3}_{-8}$ (using a pulsar-centered coordinate system).

In addition to profile shape changes, geodetic precession affects the linear polarisation position angle (PPA) of the pulsar as well. In a significant number of pulsars, the PPA (Ψ) varies as a function of the rotational phase (ϕ) following a S-shape. Radhakrishnan & Cooke (1969) proposed a model, called the Rotating Vector Model (RVM), to explain this effect. In this model a perfectly dipolar pulsar magnetic field is assumed. The shape of the PPA depends on the geometry of the system. The mathematical expression of PPA variations through orbital phase, in this model, is:

$$\tan(\Psi - \Psi_0) = \frac{\sin a \, \sin(\phi - \phi_0)}{\sin(\alpha + \beta) \, \cos\alpha - \cos(\alpha + \beta) \, \sin a \, \cos(\phi - \phi_0)}, \tag{5.2}$$

where ϕ_0 is the pulse longitude when the magnetic meridian crosses the line of sight, α is the magnetic inclination angle, and β the impact parameter. At a longtitude of ϕ_0, Ψ is equal to Ψ_0. For pulsars that are affected by geodetic precession we expect to detect changes in the PPA shape as our line-of-sight changes. Kramer & Wex (2009) added geodetic precession's effect to the RVM and Manchester et al. (2010) fitted this model to the PPA shape of PSR J1141−6545, a slow pulsar with a white-dwarf companion.

Cordes et al. (1990) were the first to use PSR B1913+16 polarisation data, in order to detect PPA swing changes. Their data covered the epoch 1985 to 1988 at 21-cm wavelength. They did not detect any obvious changes in the PPA shape or in linear or circular polarisation.

Weisberg & Taylor (2002), had a large 20-year data set to investigate the emission geometry of PSR B1913+16. Apart from studying the differences in the profile shape, they also used polarisation data. They also did not detect any obvious changes in the PPA shape but they used these polarisation data to select a single preferred model solution, in which $i = 47.2°$, $\delta = 21.1°$ and $\alpha = 157.5°$ (using an Earth-centered coordinate system described by Damour & Taylor (1992)).

The combination of shape and polarisation changes led to a better understanding of the emission beam structure. Weisberg et al. (1989) observed only differences in the relative height

of the components so they concluded that the emission beam is not perfectly circular with a patchy conal component and that the line of sight cuts the hollow-cone beam in the middle. Cordes et al. (1990) argued that PSR B1913+16's emission has both core and cone origin, with core emission shifted in phase towards the trailing component. This model is supported by observations at lower frequencies in which the existence of a central component, which is strong in the middle 1980s but almost disappeared at the mids 2000s, is obvious (Weisberg & Taylor, 2005).

The most extensive work to understand the emission beam geometry has been done by Clifton & Weisberg (2008). For their analysis they assumed a precessing circular beam model. They concluded that only a small deviation from a perfect circular beam could explain the observational results, in contrast to previous studies (Weisberg & Taylor, 2002, 2005) in which on hourglass-shaped beam was needed to explain the observations.

Another by-product of geodetic precession monitoring of pulsars is the measurement of the misalignment angle (angle between spin and orbital momentum). The misalignment angle reveals information about the system formation and particularly about the asymmetry of the second supernova explosion. Precise measurement of this angle in a system helps to better understand the formation of double neutron star systems (e.g. Kalogera & Lorimer, 2000). Thus far, misalignment angle measurements (e.g. Kramer, 1998; Weisberg & Taylor, 2002) support the idea of an asymmetric second supernova explosion, which is thought to be necessary in order to observe geodetic precession in a pulsar system.

Now that we have available a significantly longer data set, including polarisation calibrated observations we can improve the emission beam geometry predictions of this system, study the time evolution of impact parameter, and form an emission beam model that best describe our observations, as will be presented in the following. The observations and data reduction are described in Section 5.2. The emission beam geometry as derived based on the total intensity profile shape changes is given in Section 5.3.1. The polarisation properties of the pulsar and the RVM fit results are presented in Section 5.3.2. Finally, the proposed new beam shape is given in Section 5.3.3, followed by our conclusions in Section 5.4.

5.2 Observations and data reduction

For our analysis we used data that have been taken at ∼1400 MHz with two telescopes and three different observing systems. For the earliest epoch, from 1981 to 1987, we used the Arecibo observations that were presented by Weisberg & Taylor (2002). From 1994 to 2017 we used the 100-m Effelsberg radio telescope of the Max Planck Institute for Radio astronomy. We divided these newest observations into two epochs: the Effelsberg Pulsar Observing System (EPOS) era, from 1994 to 2005 and the PSRIX era, from 2012 to 2017. The Effelsberg data are described in more detail below.

5.2.1 EPOS observations

For the EPOS (Jessner, 1996) observations a receiver centered at 1390 MHz was used. The backend system provided incoherently de-dispersed, real-time folded data.

The recording bandwidth of EPOS observations is 40 MHz. It is split into 60, 666-KHz wide frequency channels. Since de-dispersion is done incoherently, the signal in the whole band is aligned, but inside each frequency channel a small amount of dispersion smearing remains. In the case of PSR B1913+16, with dispersion measure equal to 168.77 pc cm^{-3}, this smearing is ∼0.33 ms.

Each observation consists of 1024 bins, each having a fixed sample time, in the case of PSR B1913+16 equal to 57.6 μs. This sampling time remains fixed for the whole observing time, resulting in the folding window being equal to 58.9824 ms and hence less than 59.03 ms (Weisberg & Huang, 2016), which is the full spin period of the pulsar. Since the sample time is fixed, in order to achieve a folding on phase, before each integration the Doppler-shift corrected topocentric pulse arrival time is calculated, so that every integration starts at the same pulse phase. The result is that, while the folding window does not cover the full pulse period, the integrations are aligned in phase.

The EPOS data we used in our analysis were total-intensity profiles, since polarisation calibration was not possible for these data. All the observations have been corrected for any drifts introduced by the use of the 30-MHz, 33-ns accurate maser clock. After this correction the observations were smoothed with a running mean of three samples.

5.2.2 PSRIX observations

The PSRIX (Lazarus et al., 2016) back-end provided coherently de-dispersion real-time folding data. The receivers that were used for our observations were either the central beam of the 7-beam receiver ("P217mm") with 200 MHz bandwidth or the single-feed receiver ("P200mm") with 140 MHz bandwidth, both centered at 1347.5 MHz. The whole bandwidth is divided into 256 channels. The sub-integration recording time is 10 s, and the pulse phase is recorded with 1024 sample bins. The effective time resolution is comparable to EPOS and Arecibo data.

In order to be able to compare observations from these two back-ends, since EPOS provides incoherent de-dispersion and PSRIX coherent de-dispersion, we smeared the PSRIX observations to a value that corresponds to the same smearing due to the dispersion in each EPOS frequency channel. After smearing, the PSRIX observations were smoothed to a running mean of three samples.

5.2.2.1 Polarisation and flux calibration

For our analysis, whenever possible, we used polarisation calibration observations. Only the PSRIX observations could be calibrated in polarimetry and flux. Before further processing our pulsar observations, we removed radio-frequency interference (RFI) using the COASTGUARD[1] reduction pipeline, which uses the PSRCHIVE package (Hotan et al., 2004).

In order to polarisation calibrate our pulsar observations we observed a noise diode directly prior to our pulsar observations. The noise diode signal is a 100% linearly polarised square wave, which illuminates equally and in phase both circular feeds. The duration of these observations were 2 minutes, with a 0.5° position offset from the pulsar position. We used the package PAC from PSRCHIVE, in order to determine and correct the differences in gain, amplitude, and phase of the two feeds. These corrections were then applied to the pulsar observations in order to derive the emitted polarimetric pulse information. As a result we have observations with correctly measured Stokes parameters.

In order to flux calibrate the observations we observed a source with stable, well-known flux density using the same system configuration. In our case we used the quasars 3C 218 and 3C 286. The noise diode, as described above, was observed on and off the quasar. Since the flux of the quasar is well known, we can determine the system temperature and as a result the flux density of the pulsar.

[1] https://github.com/plazar/coast_guard

5.2.3 Rotation measure

Most pulsars are highly polarised sources. Their polarised signal crosses the magnetic fields of the Galaxy on its way to Earth. Magnetic fields cause differences in the propagation speed of right and left hand circularly polarised waves. These differences result in a change in the apparent PPA. This change is proportional to the square of the observing wavelength (λ):

$$\Delta\Psi = \mathrm{RM} \times \lambda^2, \tag{5.3}$$

the RM factor is the rotation measure and is proportional to the integrated Galactic magnetic field strength along the line of sight, weighted by the electron density.

The non-zero RM causes harmonic oscillations in Stokes Q and U as a function of the square of the observation wavelength λ^2. The period of those variations is 2RM and can be probed via RM synthesis and related techniques (Burn, 1966; Brentjens & de Bruyn, 2005). Roughly, the classical RM synthesis technique implies a discrete Fourier transform of the complex polarization vector $P(\lambda^2) = Q + \mathrm{i}U$; the peak in the spectrum corresponds to the required RM and the uncertainties on the relative solution are estimated as $0.5\sigma_{\mathrm{RM}}/(\mathrm{S/N_L})$, where σ_{RM} is the full width at half maximum of the spectral peak and $\mathrm{S/N_L}$ is the signal to noise ratio of linearly polarised intensity of the fully scrunched pulsar observation (Noutsos et al., 2015). The results for PSR B1913+16 obtained with RM synthesis are demonstrated in Fig. 5.1 with open circles. With black circles we have shown the RMs, measured with method analogous to the RM synthesis approach but based on a Bayesian generalised Lomb-Scargle periodogram (BGLSP) (Mortier et al., 2015). The details of the application of the BGLSP are demonstrated in Porayko et al (in prep.). In this work the posterior probability of RM has been analytically marginalised over nuisance parameters, such as constant offsets in Q and U, and fit with a normal Gaussian distribution. The final RM uncertainty has been estimated as variance of the best-fit normal distribution, modified with an extra-scattering parameter ($\sim \sqrt{\chi^2}$), where needed. Fig. 5.1 shows that the results of the two methods are in a good agreement.

5.3 Results

The profile of PSR B1913+16 at 1400 MHz consists of two main components. In our observations, the effects of geodetic precession on the separation and relative height of the two components are clear (Fig. 5.2). Apart from these obvious changes, we further investigated any temporal changes in the width and polarisation properties of the pulsar. Our results are presented below.

5.3.1 Beam geometry based on total intensity analysis

In order to investigate the effect of geodetic precession on the pulse profile, from each observation we created a smoothed profile by fitting a sum of Gaussians to the observations. The Gaussian functions were applied to the whole pulse phase. The number of Gaussian functions fitted was decided through a Kolmogorov–Smirnov test with 5% significance level. The central part of the two local maxima of the overall Gaussian function defined the position and the amplitude of the leading and trailing components. For the EPOS data we took into account the fact that the folding window does not cover the whole pulse period, and we corrected our results accordingly in order to be comparable to the Arecibo and PSRIX observations.

Since the EPOS observations that we used in our analysis were part of the Kramer (1998) and Kramer et al. (2003) studies as well, we decided to compare our results with these studies, in order to check our method and data reduction process. In Kramer's method Gaussian

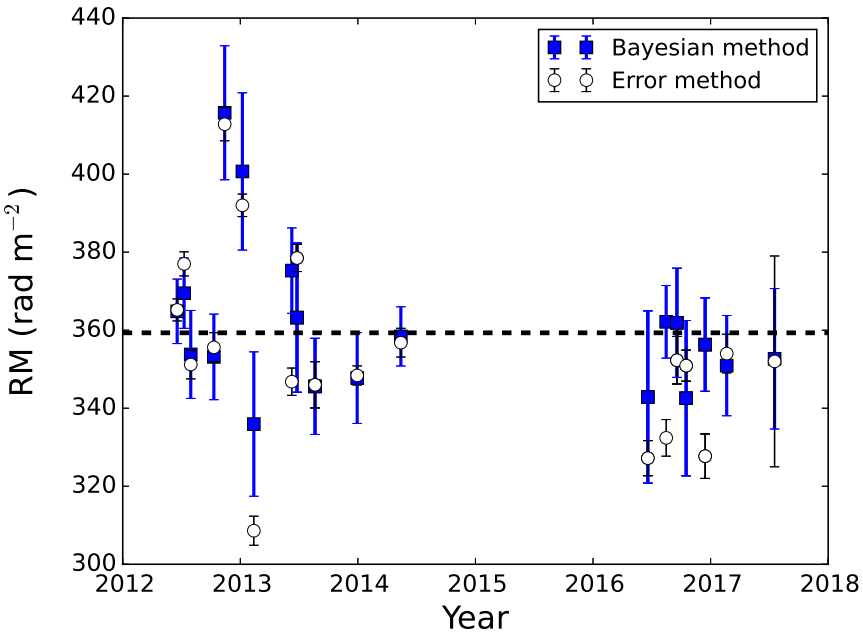

Figure 5.1: The RM of our PSRIX observations as a function of time. With open circles and blue squares we present respectively, the results obtained with the classical RM synthesis technique and the Bayesian approach (see text for details). The weighted mean after using the Bayesian method is 359±17 rad m^{-2}, and with the classical RM synthesis method 357±22 rad m^{-2}.

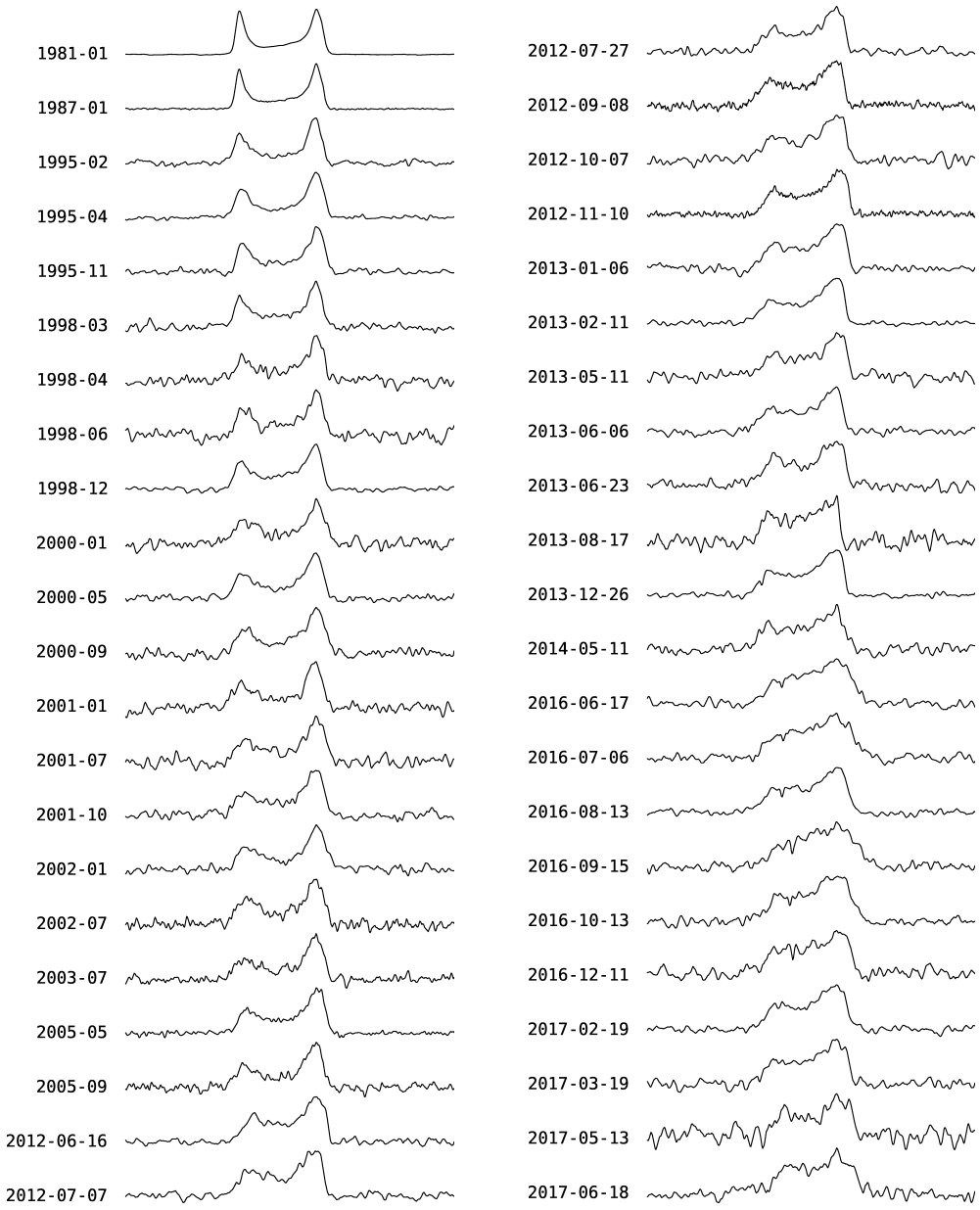

Figure 5.2: Total intensity PSR B1913+16 pulse profiles as a function of time. The 80s profiles are observed with the Arecibo telescope. From 1995 until 2005 the Effelsberg telescope with the EPOS system was used. These observations are corrected for a drift and smoothed with a running mean of width three bins. EPOS profiles that are presented here correspond to one observing scan. The profiles after 2012 are produced with the Effelsberg PSRIX back-end. They are smoothed identically to the EPOS data and a smearing that corresponds to the same smearing that dispersion measure causes to EPOS data is added, since the EPOS system provides no coherent de-dispersion of the signal. Changes in the separation and relative height of the two components are obvious.

functions are fitted to the central portion of each component to several intensity levels (95%, 90%, 80%, and 60% of the total intensity of the normalised profile), in order to better estimate the separation uncertainties. The two methods are in good agreement. We decided in order to be certain of our data reduction method, to apply Kramer's method to our EPOS data as well. The results are identical, within the 1-σ level. As a conclusion we are confident for both our data reduction and processing methods which are used to produce the results in this present text.

5.3.1.1 Relative amplitude changes

We report for the first time an increase in the relative amplitude of the leading and trailing components starting at around 2010 (see Fig. 5.3). So far in the previous analyses, the observed trend was a constant decrease of -1.9%±0.1% per year, as last measured by Kramer (1998).

Istomin (1991) created a model to explain the observed differences in the relative height and from this model extracted the emission beam geometry. For his analysis he used Arecibo data at 1400 MHz as presented by Weisberg et al. (1989). He assumed that the flux of the pulsar is proportional to the Goldreich–Julian matter density. Since there was no observational evidence of component separation changes in the data set that he had available, he concluded that the line of sight is very close to the magnetic axis, and as a natural conclusion he assumed that there should be an epoch in which the line of sight cuts the emission beam exactly in the middle. This event according to his calculation happened in 1977. In that epoch, according to his model, the two components had equal heights. His model has two free parameters: the misalignment angle (δ) and the precession phase, Φ_0, which defines the closest approach of the line of sight to the pulsar spin axis.

We fitted his model to our data by applying a Markov-chain Monte-Carlo (MCMC) analysis. Apart from, the two free parameters, δ and Φ_0, we introduced also a factor K, which accounts for any scaling miscalculations on our relative amplitude error measurements. The new uncertainties are measured as: $\sigma^2 = K^2\ \sigma^2_{\rm old}$. To reach $\chi^2 \approx 1$, $K = 0.2^{+0.04}_{-0.03}$, and $\delta = 31.9^{\circ}{}^{+5.8^{\circ}}_{-6.9^{\circ}}$, $\Phi_0 = 143.1^{\circ}{}^{+8.9^{\circ}}_{-9.2^{\circ}}$ with 1-σ confident level, as presented in Fig. 5.3. Although, our δ measurement does not deviate more than 1-σ from Istomin (1991) measurements our precesional phase corresponds to an epoch at which pulsar should be invisible according to his model. Therefore, we concluded that his model which assumes a linearly decrease in the relative amplitude is only a simplification of the reality and fails to explains our observations.

5.3.1.2 Profile width changes

We measured the change in the full width of the pulse profile at seven different intensity levels: 5%, 10%, 30%, 40%, 60%, 80%, and 95% relative to the peak of the component in question (Fig. 5.4). We observed that the width remains stable until 2015 when the pulse begins to broaden slightly.

We observed that the total profile width gradually increases at intensity levels 60%–95%. While at the intensity levels 5%, 10%, 30%, and 40% the total width increases from the middle of 1995, stays stable from 2003 to 2013 until increases again. We attribute these behavior to slight changes in the shape of the profile components.

5.3.1.3 Component separation changes

In Fig. 5.6 our results on the separation of the pulse components are presented. The model that we used in our analysis is described in Kramer (1998). In this model we assumed that

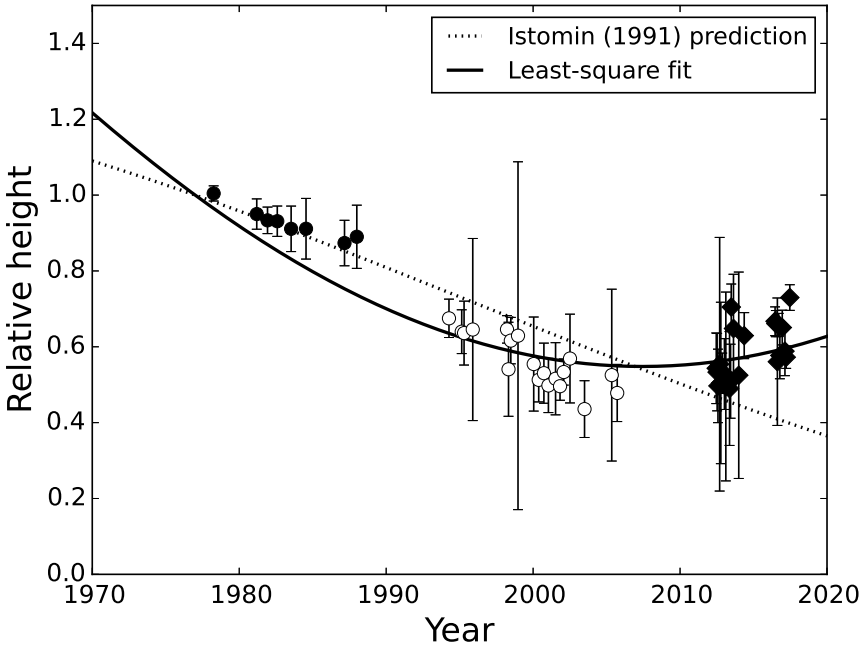

Figure 5.3: The amplitude ratio of the leading and trailing components as a function of time. Arecibo, and Effelsberg EPOS and PSRIX observations are shown with filled circles, open circles and diamonds, respectively. With a dotted line, the relative height as predicted from the Istomin (1991) model is presented. With the solid line the best MCMC fitting solution of this model to our observations is presented. For the first time a turn over in the, so far stably decreasing, relative amplitude is found.

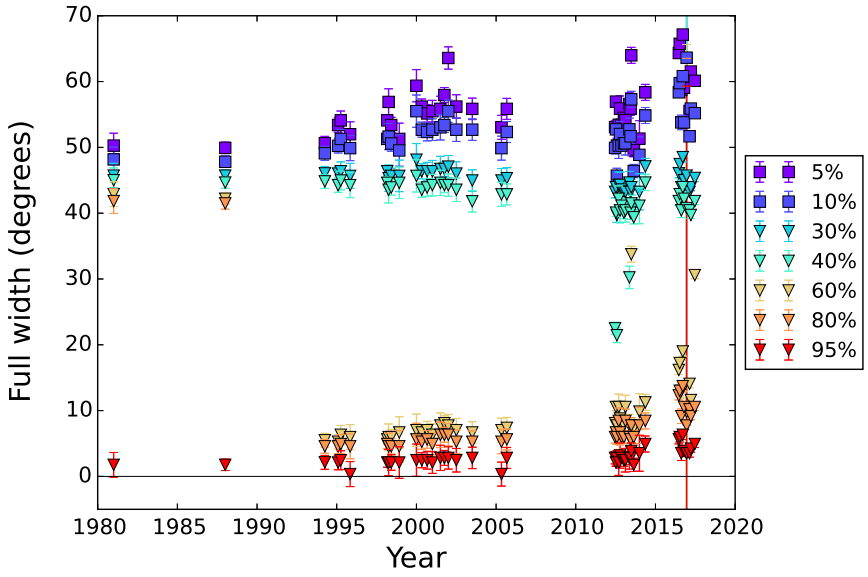

Figure 5.4: The width of the whole pulse profile as a function of time, at seven different intensity levels. The intensity levels 5%, 10%, 30%, 40%, 60%, 80%, and 95% are color-coded as given by the scale.

the emission beam has a hollow cone shape centered on the magnetic axis. The coordinate system that we used in our analysis is Earth-centered with the line of sight along the main axis, as explained in Kramer & Wex (2009) (see their Fig. 2), in contrast to the pulsar-centered coordinate system used in the Kramer (1998) analysis.

The basic geometric angles that we can determine with this analysis are: the magnetic angle α, which is the angle between pulsar spin axis and the magnetic axis; the misalignment angle δ, which is the angle between the orbital angular momentum and spin axes; the impact parameter β, which represents the closest approach of the line of sight to the magnetic axis; and the angle between the line of sight and spin axis ζ. The model that is used is purely geometric and correlates these angles with the observed pulse width. Since PSR B1913+16 has a measurable geodetic precession rate, the line of sight cuts the emission beam at different angles, this is seen by changes of ζ in time:

$$\cos\zeta(t) = \cos\delta\,\cos i - \sin\delta\,\sin i\,\cos\Phi(t), \tag{5.4}$$

where $\phi(t)$ is the precessional phase:

$$\Phi(t) = \Phi_0 + \Omega_\mathrm{p}\,\mathrm{d}t = \Phi_0 + \Omega_\mathrm{p}\,(t - T_0), \tag{5.5}$$

T_0 is a reference epoch set fixed and equal to MJD 56094, which corresponds to the first epoch in our data set; Φ_0 is the reference precessional phase at the epoch T_0; and Ω_p is the precession rate (see Eq. 5.1). The impact parameter is given by:

$$\beta(t) = \pi - \zeta(t) - \alpha. \tag{5.6}$$

The observed pulse width, as a function of time $w(t)$, measured in rotational longitude, can be expressed with simple geometry:

$$\sin^2\left(\frac{\mathrm{w(t)}}{4}\right) = \frac{\sin^2(\rho/2)\ -\ \sin^2(\beta/2)}{\sin\alpha\,\sin(\alpha+\beta)}. \tag{5.7}$$

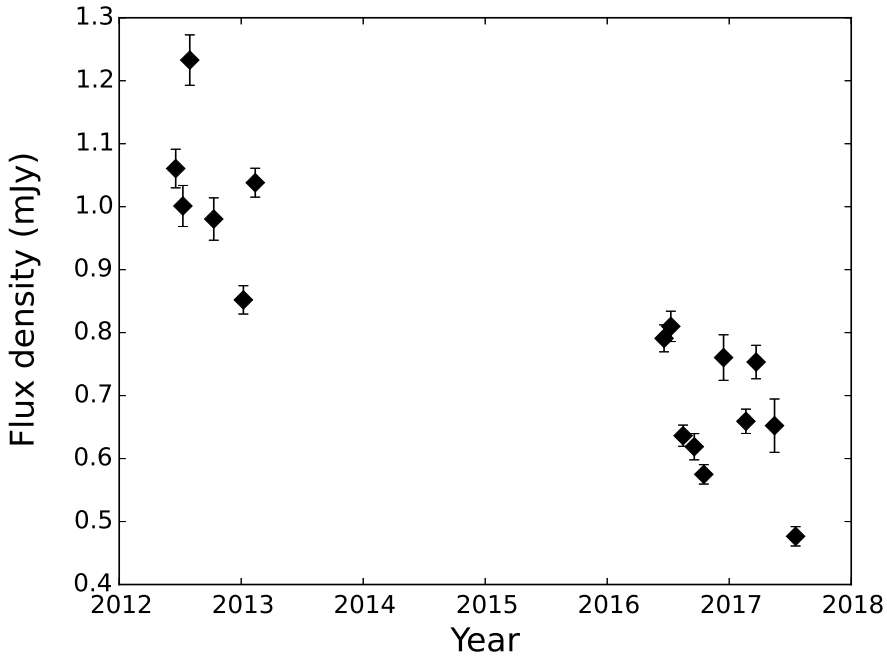

Figure 5.5: The phase-averaged flux densities of PSRIX observations as a function of time are presented here. Flux calibration of these data has been achieved with quasar observations. Not all our PSRIX observations could be flux calibrated, since in early 2012 quasar observations weren't carried out regularly and from November 2013 to August 2014 signs of system saturation made the quasar observations unreliable (Lazarus et al., 2016). A decrease of the pulsar's flux density is obvious. The measured mean flux density, based on the data presented here, is 0.81±0.21 mJy.

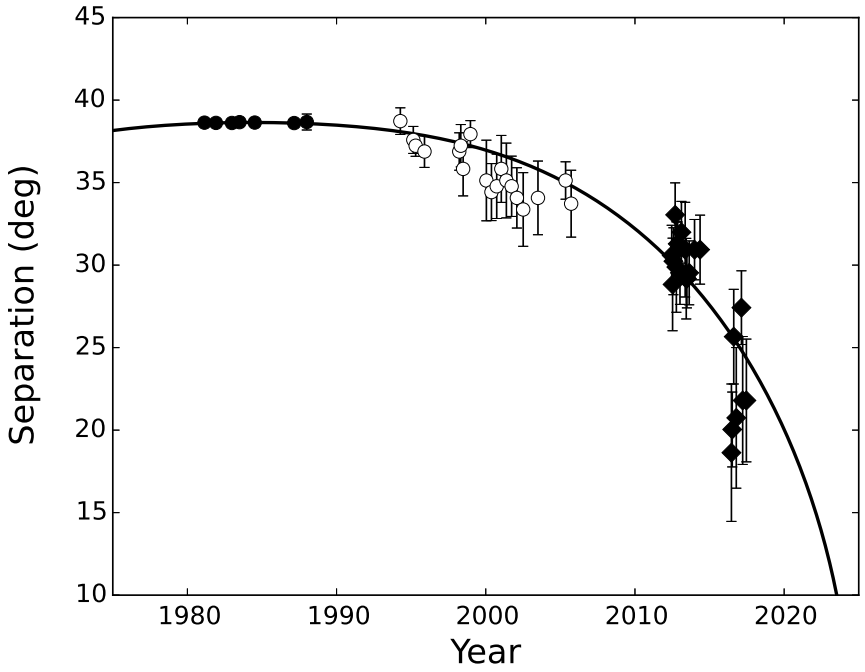

Figure 5.6: Separation of the two main pulse components of PSR B1913+16 as a function of time. With filled black circles Arecibo data as taken directly from Kramer (1998) are presented. Open circles and black triangles show Effelsberg observations with the EPOS observing system and the PSRIX back-end, respectively. The best-fit solution (see Table 5.1) of the model presented in Section 5.3.1.3 is presented with a solid line.

Table 5.1: Geometrical model solutions with 1-σ uncertainties.

Solutions	i (deg)	α (deg)	δ (deg)	Φ_0 (deg)	ρ_0 (deg)	K
I	47.1	$113.55^{+8.05}_{-9.80}$	$24.46^{+8.60}_{-6.88}$	$80.33^{+22.62}_{-11.23}$	$17.74^{+0.99}_{-1.46}$	$0.32^{+0.06}_{-0.03}$
II	47.1	$63.20^{+6.65}_{-6.91}$	$158.30^{+4.58}_{-5.48}$	$267.63^{+16.44}_{-10.21}$	$17.18^{+0.92}_{-1.21}$	$0.31^{+0.04}_{-0.03}$
III	132.9	$68.54^{+6.90}_{-6.14}$	$26.07^{+6.26}_{-5.16}$	$258.95^{+10.23}_{-8.13}$	$17.96^{+0.75}_{-0.91}$	$0.31^{+0.04}_{-0.03}$
IV	132.9	$113.12^{+9.04}_{-9.65}$	$155.54^{+6.88}_{-8.70}$	$79.40^{+18.38}_{-11.35}$	$17.79^{+1.04}_{-1.44}$	$0.32^{+0.05}_{-0.03}$

The parameters that are needed in order to describe the geometry of the system, are: α, δ, ρ, Φ_0, i, and Ω_p. We applied a MCMC in order to investigate the probability distribution of these parameters. The parameters that were set fixed are: i to values 47.1° and 132.9°, as measured by (Weisberg & Huang, 2016), T_0 to the first epoch of our data set, and Ω_p. All the remaining parameters were treated as free. We also introduced a scaling factor K to account for any miscalculations on the uncertainties of our measurements.

We found four possible solutions since we cannot distinguish the free parameter solutions from their complements (Table 5.1). For all cases the scaling factor K is < 1.0 meaning that we have overestimated our component separation uncertainties. As an example we present in Fig. 5.7 the posterior distribution of the free parameters around the solution III. All four solutions are psychical, however they predict different lines of sight. The solutions I and IV predict an inner line of sight, and positive impact parameter[2], while solutions II and III predict an outer line of sight, and negative impact parameter, at the observing epochs that cover our dataset. We can use the comparison of these solutions with the emission geometry that we obtain using PSRIX polarisation data (see next Section) to exclude of one or the other set of geometrical solutions presented here.

5.3.2 Emission beam geometry based on polarisation analysis

5.3.2.1 Polarisation properties

Pulsar emission is often polarised, in some cases it is even 100% linearly polarised. PSR B1913+16 exhibits significant levels of linear polarisation. The intensity of linear polarisation can be expressed through the Stokes parameters as: $L = \sqrt{Q^2 + U^2}$. Everett & Weisberg (2001) introduced a method to correct for the overestimation of the linear polarisation in the presence of noise. We applied this method in order to measure the true value of linear polarisation. Our results combined with the intensity of circular polarisation are presented in Fig. 5.8. A gradual decrease in L is observed.

5.3.2.2 RVM fitting

Following Damour & Taylor (1992), Kramer & Wex (2009) were the first to add the impact of relativistic spin precession to this model. The geodetic precession should change the shape of the PPA swing, but also the absolute values of PPA. Since the absolute value of the PPA is determined by the sky projection of the spin axis, changes in the orientation of the spin

[2]Using the coordinated system that is described in Kramer & Wex (2009)

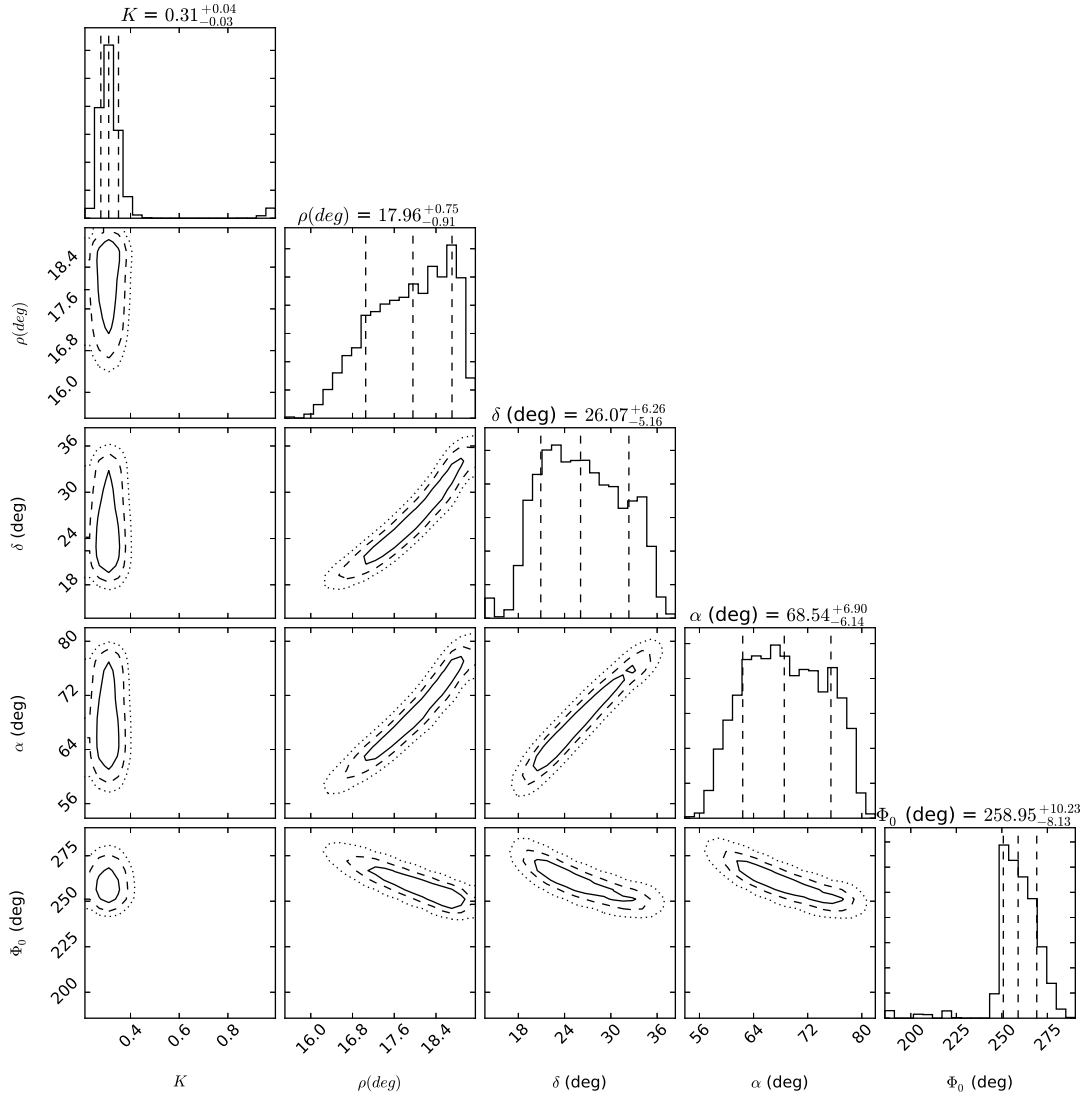

Figure 5.7: This corner plot shows the one and two dimensional projections of the posterior probability distributions of the emission beam opening angle ρ, the misalignment angle δ, the angle between the spin axis and the magnetic axis α, the reference precessional phase Φ_0, and the uncertainty scaling factor K. The covariance between all parameters other than k is obvious. The marginalized distributions for the parameters are measured based on one of our MCMC solution III (Table 5.1) obtained from the total intensity analysis with inclination angle and spin precession rate fixed to 132.9° and 1.21° yr^{-1}.

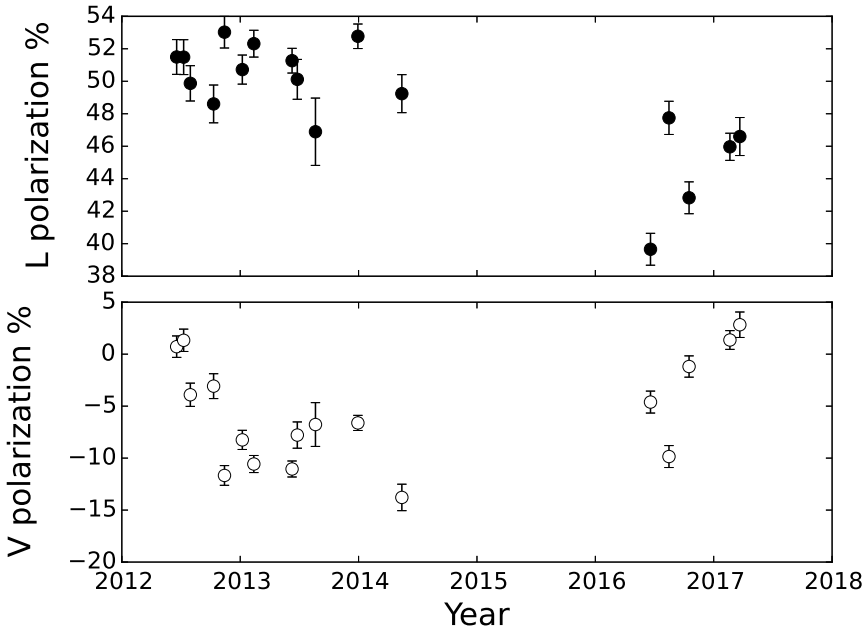

Figure 5.8: Average percentage of linear (top) and circular polarisation (bottom), based on our PSRIX observations, as a function of time. The error bars represent the 1-σ standard deviation.

axis will result in periodic changes in the absolute the PPA values, with period equal to the precessional period. The time-variable parameter $\Psi_0(t)$ is written as:

$$\Psi_0(t) = \Omega_{\rm asc} + \Delta\psi_{\rm F} + \Delta\psi_{\rm A} + \eta(t), \tag{5.8}$$

where $\Omega_{\rm asc}$ is the location of the ascending node, $\Delta\psi_{\rm F}$ accounts for unmodeled RM variations while $\Delta\psi_{\rm A}$ accounts for orbital aberration, and both are assumed constant, and $\eta(t)$ is the precessional longitude, which along with the polar angle, $\zeta(t)$, gives us the spatial orientation of the pulsar spin axis. Thus $\Psi_0(t)$ can be expressed as:

$$\Psi_0(t) = \eta(t) + \Delta\Psi_0. \tag{5.9}$$

The parameter $\eta(t)$ ($0 \leqslant \eta \leqslant 2\pi$), from simple geometrical considerations can be expressed as:

$$\begin{aligned} \cos\eta(t) &= \frac{\sin\delta\,\sin\Phi(\mathrm{t})}{\sin\zeta(\mathrm{t})}, \\ \sin\eta(t) &= \frac{\cos\zeta(\mathrm{t})\,\cos i - \cos\delta}{\sin i\,\sin\zeta(\mathrm{t})}, \end{aligned} \tag{5.10}$$

where $\Phi(t)$ is given by Eq. 5.5, and δ and $\zeta(t)$ are determined from Eq. 5.4. While $\Psi_0(t)$ is expressed based on the RVM[3] as:

$$\Psi_0(t) = \Psi - \tan^{-1}\left(\frac{\sin a\,\sin(\phi-\phi_0)}{\sin(\zeta(\mathrm{t}))\,\cos\alpha - \cos(\zeta(\mathrm{t}))\,\sin a\,\cos(\phi-\phi_0)}\right). \tag{5.11}$$

[3]The sign difference to Eq. 1.7 rise from the fact that different observing conventions are assumed.

Table 5.2: RVM solutions with 1-σ uncertainties.

i (deg)	α (deg)	δ (deg)	Φ_0 (deg)	Ψ_0 (deg)
47.1	$29.26^{+2.24}_{-2.04}$	$159.85^{+2.03}_{-1.86}$	$348.79^{+2.54}_{-3.11}$	$-37.45^{+1.66}_{-1.71}$
132.9	$28.27^{+2.10}_{-1.95}$	$20.88^{+1.78}_{-1.89}$	$347.62^{+2.16}_{-2.71}$	$-21.42^{+1.43}_{-1.39}$

Combining Eqs. 5.9–5.11 and Eqs. 5.4 and 5.5 we applied a global RVM fit to the PPA angle measurements derived from the PSR B1913+16 PSRIX polarization-calibrated data. For the fit we used 10 high S/N observations taken at epochs that span from mid 2012 to the end of 2016 (Figs. 5.9 and 5.10). We apply a RVM fit, not to the whole orbital phase, but to PPA angle measurements with phases that correspond to the trailing and leading profile components, since there are signs that the central component originates from a different emission cone or core (Cordes et al., 1990). All observations are corrected for Faraday rotation, using for all of them the same RM value, even though RM variations have been observed, meaning that the uncertainties on the model free parameters are likely to be underestimated.

For the global fit we used the MODELRVM[4] (Desvignes et al. in prep.) which uses the MULTINEST parameter space sampling algorithm (Feroz et al., 2009b). The inclination angle and $\Omega_{\rm p}$ are kept fixed during the fit: i to either 47.1° or 132.9°, and $\Omega_{\rm p}$ to 1.21° yr^{-1}. Since the impact parameter is related to the magnetic inclination angle through Eq. 5.6 there are 16 free parameters that are included in the model: α, δ, Φ_0, $\Delta\Psi_0$, and one ϕ_0 for each epoch.

For each inclination angle we determined one maximum likelihood result, both of them presented in Table 5.2, while the marginalized posterior distribution of the solution that corresponds to 132.9° inclination angle is presented in Fig. 5.11. These two RVM solutions correspond to solutions II and III derived from the total intensity analysis (Table 5.1). The comparison of these solutions as well as their predictions about the impact parameter and beam shape are given in the next sections.

5.3.2.3 Comparison of solutions

Misalignment angle measurements of geometrical model and RVM seem to agree within 1-σ, however α and Φ_0 measurements, as well as the predictions of the impact parameter strongly disagree. Firstly, we will focus on comparing the impact parameter predictions of these two models.

The impact parameter (β) is a very important angle since by knowing its value we can describe the way that the line of sight cuts the emission beam. β measurements combined with α give us the shape and orientation of the PPA. In all precessing pulsars β is not stable but changes as a function of time following a periodicity that is equal to the processional period. In Figs. 5.12 and 5.13 the β predictions based on geometrical model solutions II and III (Table 5.1) and the equivalent RVM solutions (Table 5.2) are presented, respectively.

This is not the first time that β measurements have been reported for PSR B1913+16. Cordes et al. (1990), Blaskiewicz et al. (1991), with data from mid 1985 until 1991 reported negative β values. Both did not find any obvious evolution in the linear or in the circular polarisation, or in the PPA S-shape during these epochs. Only the geometric solutions II and III seem to agree with these observations. These solutions predict that at the end of the 1970s β changed sign from positive to negative, meaning that we passed from an outer to an inner line

[4]https://github.com/gdesvignes/modelRVM

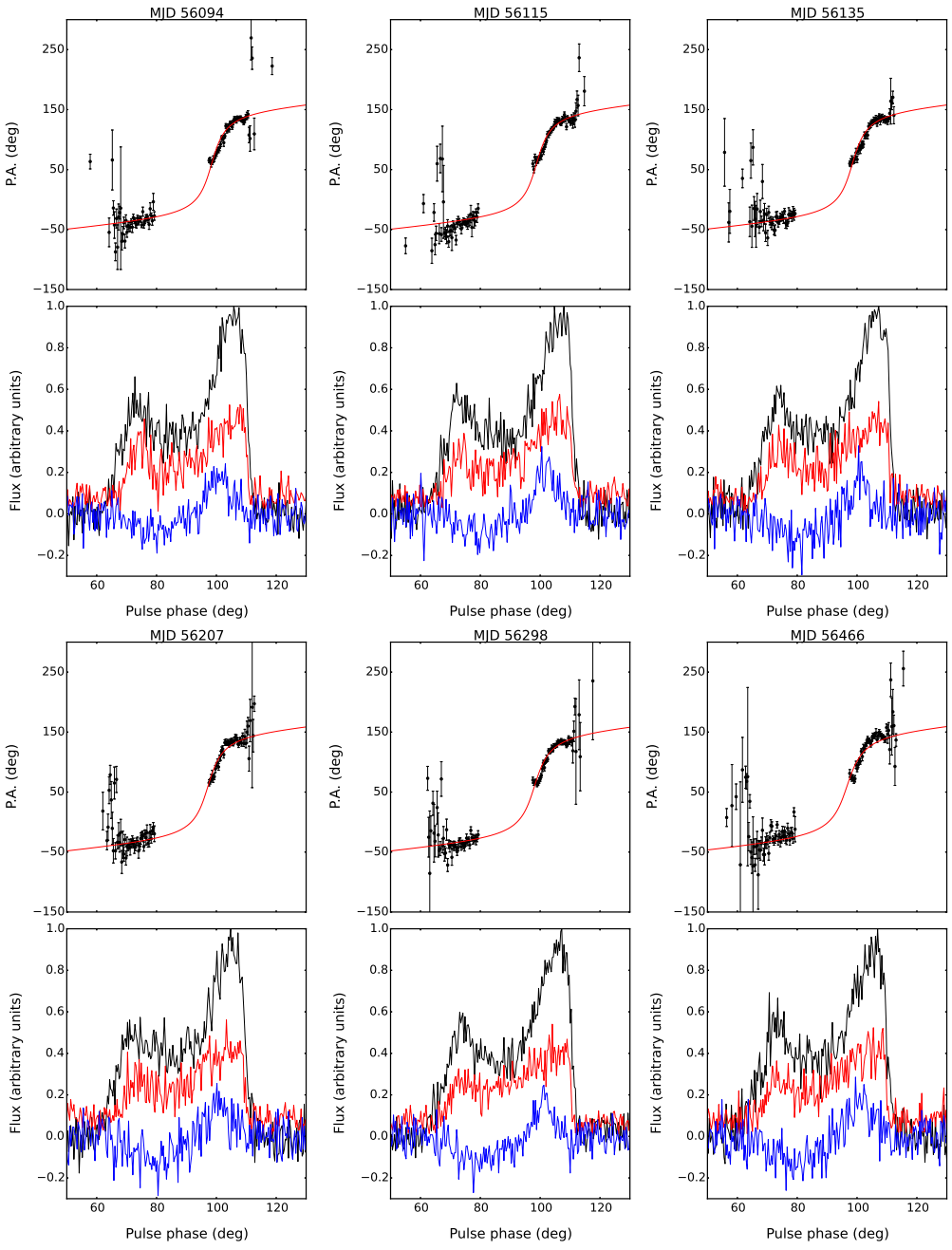

Figure 5.9: The averaged polarisation profiles and the PPA measurements of PSR B1913+16 at 10 different epochs. In the bottom panels the total intensity, linear and circular polarisation of the profiles are presented with black, red, and blue respectively, over a phase range zoomed around the profile. In the top panels, the data points correspond to measurements of the PPA of the linear polarisation, while the red line corresponds to the RVM best-fit results (Table 5.2).

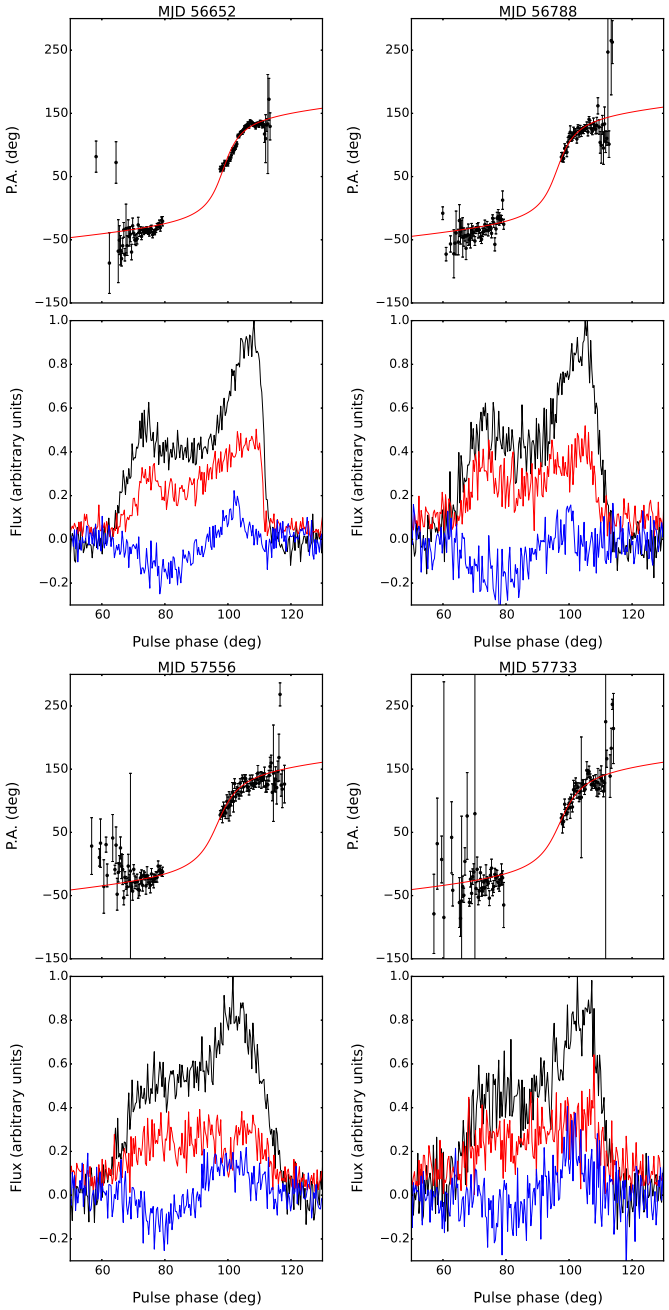

Figure 5.9: *–continued*

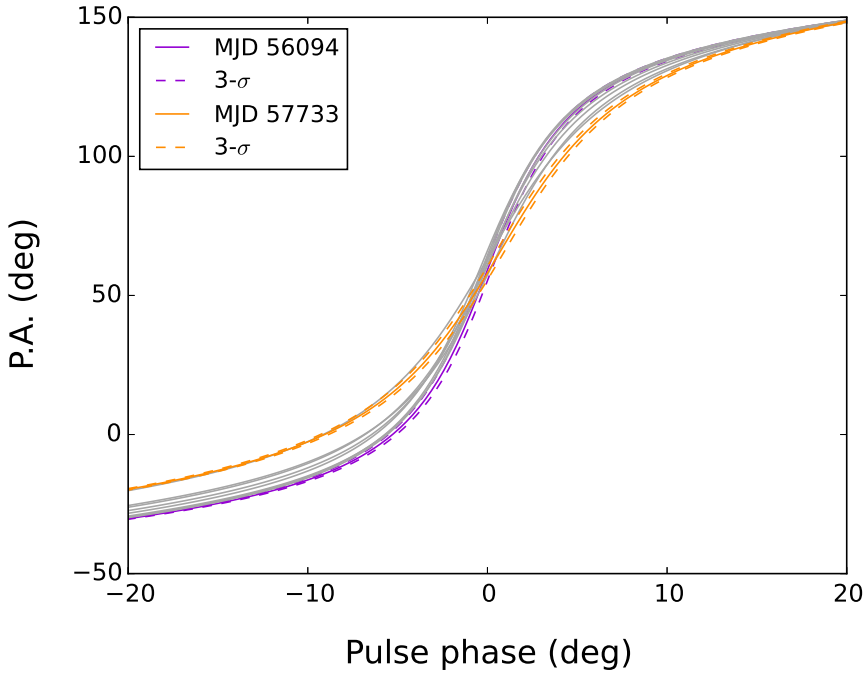

Figure 5.10: The PPA measurements of PSR B1913+16 as a function of pulse phase based on 10 PSRIX observations. With purple and orange solid lines we present the PPA values of our first and last observing epochs, respectively. The same color dashed lines indicate the 3-σ levels obtained for uncertainties on the pulse phase. All other observing epochs are given by the solid grey lines. The gradual flattening of PPA suggests that the line of sight moves away from the magnetic axis.

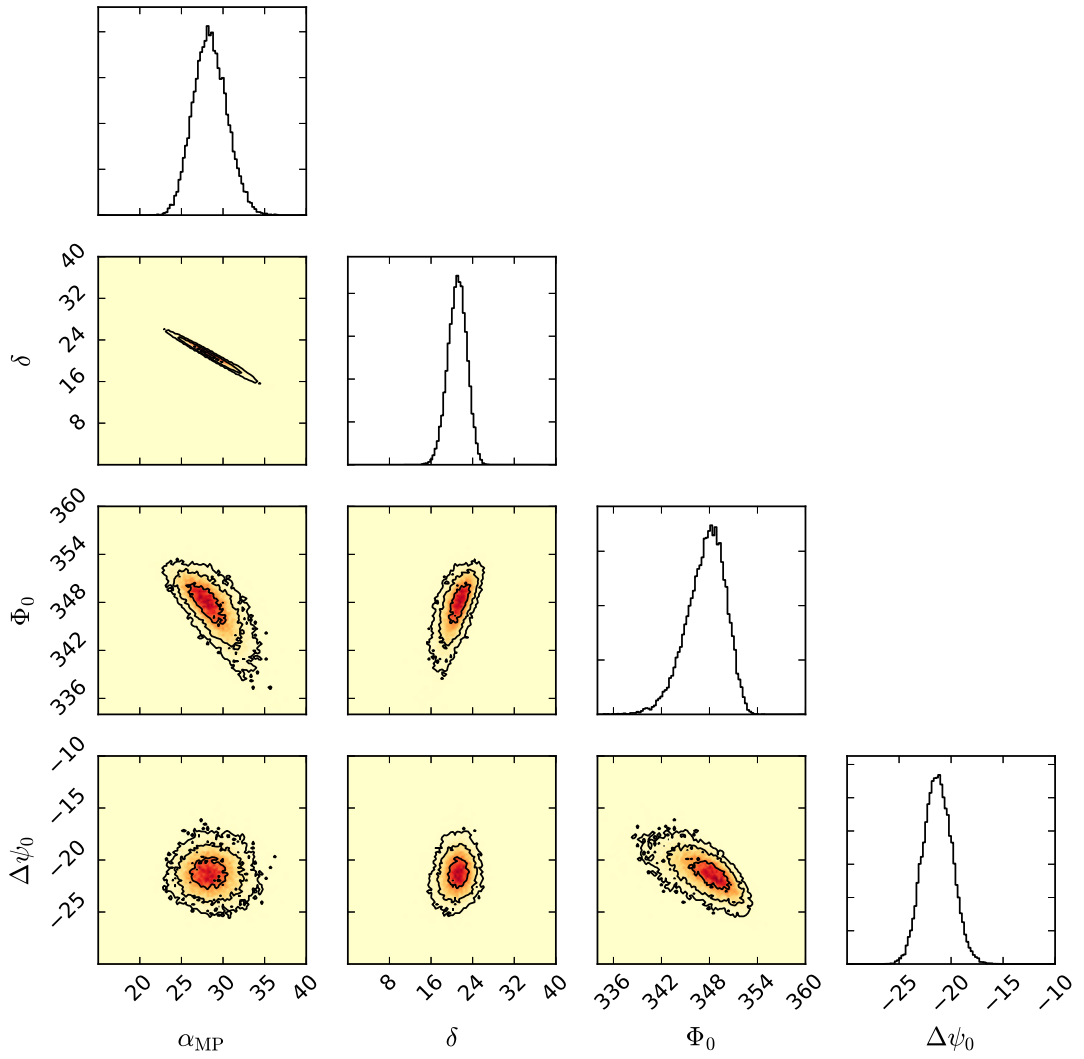

Figure 5.11: One and two-dimensional marginalised posterior distribution of the global RVM fit, computed with the MODELRVM code. From left to right and top to bottom, the represented parameters are the angle between the spin axis and the magnetic axis, α, the misalignment angle, δ, the reference precessional phase, Φ_0 and the constant PPA offset, $\Delta\Psi_0$. In the analysis the inclination angle and the geodetic precession rate are kept fixed to 132.9° and 1.21° yr^{-1}, respectively.

of sight, and thus a change of PPA shape orientation exactly at that epoch should have been observed. Unfortunately, polarisation calibrated observations at that epoch are not available to test this prediction. Since the end of 1970s, this model predicts that β has a gradually decreasing negative value, meaning that the PPA shape should get gradually flatten. This effect is observed in our PSRIX data (see Fig. 5.10), however these observations indicate a higher β value than this model's prediction. Nevertheless, β as measured from the RVM solutions seems to disagree with previously published observations and measurements derived from the geometrical model. More precisely, RVM predicts that β changed from positive to negative sign around 2005, something that indicates that a change in the orientation of the PPA should have been observed before that epoch, however, based on previously published results, no change has been observed. According to this model β reaches its lowest values in $\sim$2025, and then will start increasing again. During these epochs we expect the profile shape, the separation, the flux density, the polarisation properties to be identical to that of 2000–2030s. According to RVM solutions β will change sign in 2041^{+11}_{-6}, this also suggests that the PPA S-shape should flip orientation.

With impact parameter measurements we can also predict when the pulsar will stop being visible. This epoch is defined as when $\beta \geqslant \rho$. For PSR B1913+16 our two models disagree in their predictions of this epoch. According to the geometrical model PSR B1913+16 will stop beaming towards Earth in 2025^{+5}_{-4}, but according to RVM only in 2085^{+19}_{-10}. Future observations will allow to distinguish between the two models.

β measurements also allow us to make predictions about the pulse profile shape changes. Since the geometrical model is fitted to the observed component separation, we expect the predictions of this model (on how the line of sight cuts the emission beam) to be correct. For this model a hollow-cone beam with the magnetic axis in the center of the beam is assumed. According to this beam shape, we expect the separation of the main two components to have its maximum value at the epoch when the line of sight cuts the middle of the emission beam. In this case, due to the pulsar's precession, the line of sight moves away from the center of the beam the component separation should gradually decrease. Thus, according to our geometrical model solutions we see the middle of the beam exactly at the end of the 1970s, and while the beam moves north from Earth we observe the whole southern part of the beam until $\sim$2025 when the pulsar will not beam towards Earth anymore, as shown in the upper part of Fig. 5.14. On the other hand, for the RVM model, no component separation information is used for the fitting, and no emission beam model is assumed. However, assuming a hollow-cone emission beam, RVM solutions indicate a different precession movement. As shown in the bottom part of Fig. 5.14 at the beginning of the 1980s the northern part of the beam points towards Earth, and then as the pulsar precesses the beam moves slightly north towards Earth, crossing the center of the beam in $\sim$2005 and then again moves south until it is not pointing towards Earth any more.

The inconsistency of β, α, and Φ_0 measurements between the geometrical and RVM could arise from incorrect beam shape assumptions. In the next Section we will investigate how an alternative beam shape can explain these differences.

5.3.3 Beam shape

In this Chapter 5, so far have assumed a hollow-cone emission beam centered on the magnetic axis. However, assuming a different shape or construction for the emission beam we can make the two models' predictions about component separation consistent with each other, at least at the epochs that can be tested with our dataset. For example, if we assume that the magnetic

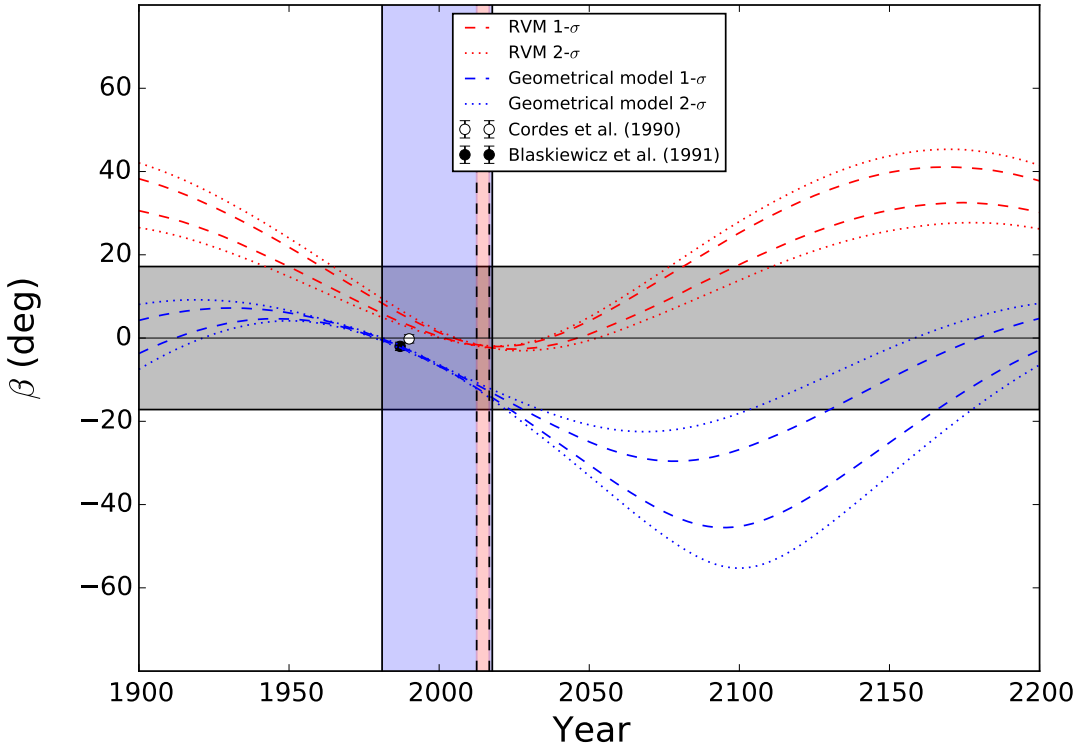

Figure 5.12: The impact parameter as a function of time for the RVM solution that corresponds to i=47.1° (red lines; Table 5.2) and the equivalent to this geometrical model solution II (blue lines; Table 5.1). The blue and red region represent the epochs in which total intensity and polarisation-calibrated observations, respectively, were available for our analysis. Within the dashed and the dotted lines, the 68 and 95 per cent confidence levels for the solutions are shown. In order for the pulsar to be visible the impact parameter should be lower than the emission beam opening angle, ρ. These regions, assuming a circular beam, are presented with a grey horizontal band.

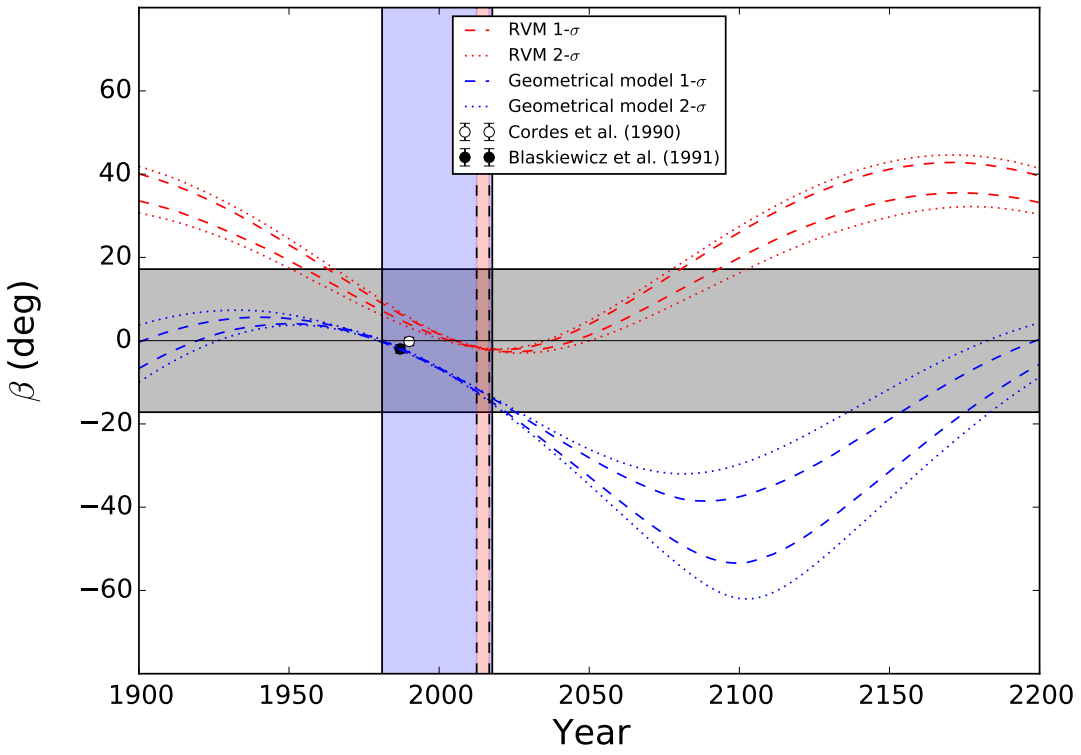

Figure 5.13: The impact parameter as a function of time for the RVM solution that corresponds to i=132.9° (red lines; Table 5.2) and the geometrical model solution III (blue lines; Table 5.1). See Fig. 5.12 for further details.

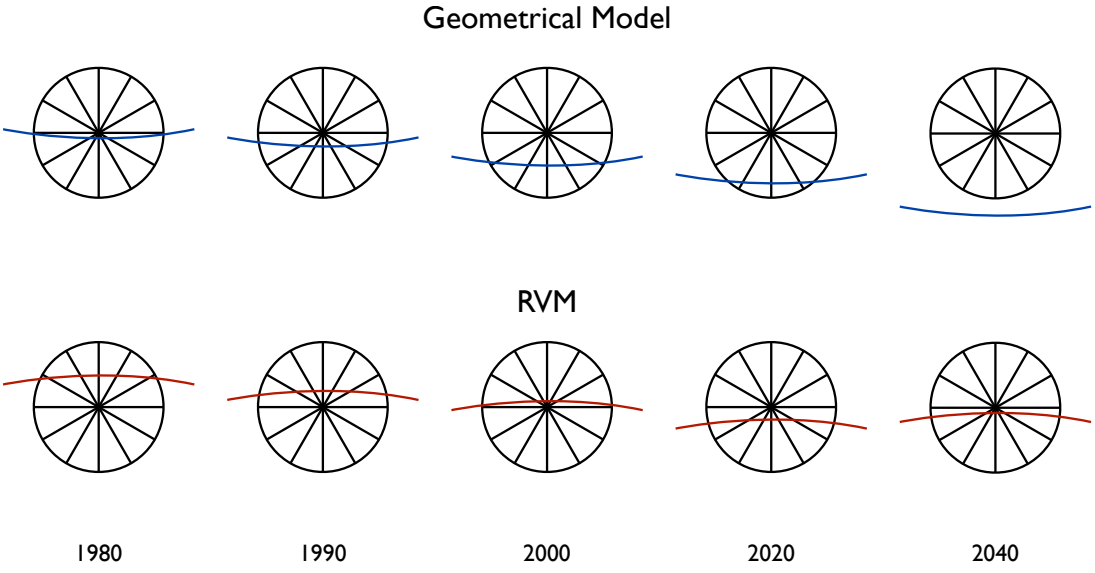

Figure 5.14: In this plot we present how the line of sight cuts the emission beam at different epochs based on the geometrical model (top panel) and RVM (bottom panel) predictions.

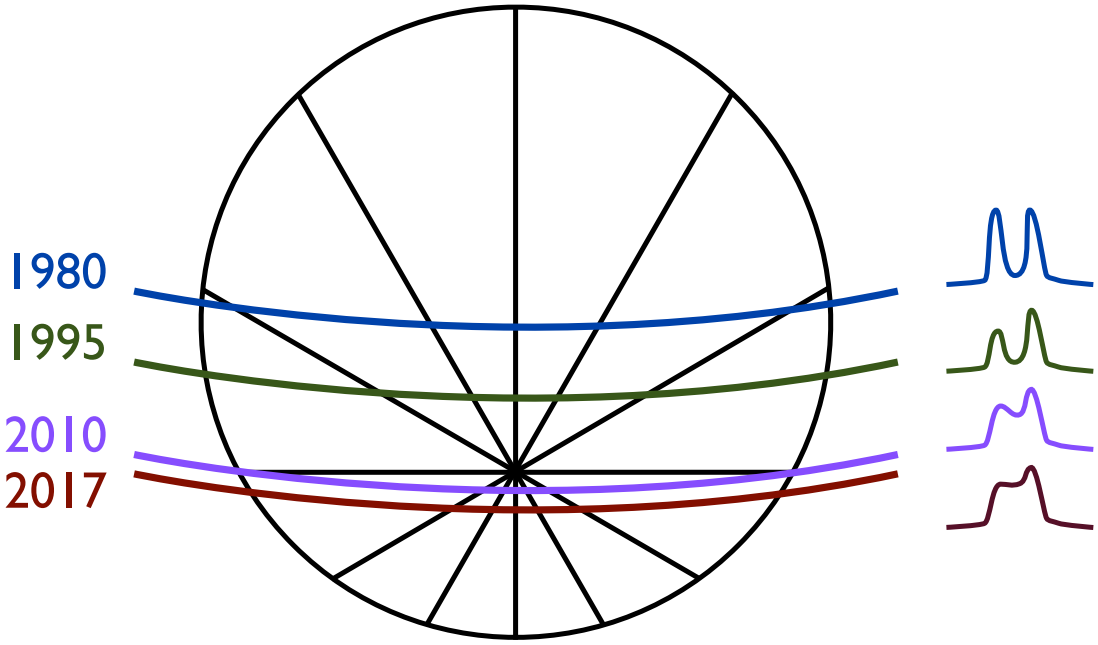

Figure 5.15: A beam model in which the magnetic axis is shifted around 10° from the center of the emission region is presented. With this model we can predict both the β measurements obtained from the RVM and the observed component separation for the epoch for which observations were available. However, the flip of PPA values that this model predicts around 2005 has not been observed.

axis is not in the middle of the beam but 10° south of the center, then as we see in Fig. 5.15, in the beginning of the 1980s the line of sight cuts the emission beam at the center, meaning that the separation has its maximum value but also β has positive value as predicted by RVM. Also according to this magnetic axis shift model, as the line of sight moves away from the center of the beam, the separation of the two main components decreases, as observed in our data. In the year 2005 we see the region of the beam that corresponds to the magnetic axis region and β measurements change from positive to negative sign as predicted from the RVM. This is not the only model that could explain both the β measurements and component separation, but a more complicated shape, for example a half hourglass shape could also explain our results.

Indeed, although this beam model can predict both the β measurements obtained from the RVM, and the observed separation of the two main components, it can not explain the fact that no flip in the PPA values around 2005 has been observed. One of possible explanations is that different observing convention than the one used by Cordes et al. (1990) and Blaskiewicz et al. (1991) has been used, thus a PPA value flip has indeed observed but has gone unnoticed. This would result in a sign change on β previously published measurements, but this would still be smaller than the expected β values based on RVM. However, this inconsistency can be also resolved if β measurements obtained from the RVM fit are underestimated due to the fact that temporal RM variations have not been taken into account. Another explanation could be that the assumptions made on RVM are very simplified and even though we observe a PPA S-shape, this model can not correctly explain the magnetic field of recycled pulsars which have undergone accretion, like PSR B1913+16

5.4 Conclusions

We have presented the effect of relativistic spin precession on PSR B1913+16 using early 80s Arecibo observations and Effelsberg observations from the mid 90s until the beginning of 2017. A gradual decrease of the separation of the two main profile components starting from the mid 90s has been observed, as well as a decrease in the phase-averaged flux density. For the first time we have observed an increase in the relative amplitude of the leading and trailing components starting in the middle of 2010.

We used a hollow-cone beam model to explain the temporal changes in the component separation, and the RVM to monitor changes in the PPA curve. Since with pulsar timing we cannot distinguish between the two possible orbital inclination angles (47.1° and 132.9°) with RVM we concluded two different system geometries, one for each possible inclination angle. We considered the i=132.9° solution to be the best to describe our data since it predicts a misalignment angle of λ=20.88$^{+1.78}_{-1.89}$. Misalignment angle less than 90° is required for an asymmetric kick during the second supernova explosion, which was already proposed for this pulsar. The equivalent to this geometrical model solution predicts similar λ values.

Our λ measurements come to an agreement with previously published values (Kramer, 1998; Weisberg & Taylor, 2002, 2005; Clifton & Weisberg, 2008). RVM measurements of α seem to agree within 1-σ with Kramer (1998), however geometrical model α measurements disagree. Also previously reported emission beam geometry based on polarisation observations by Weisberg & Taylor (2002) and Weisberg & Taylor (2005) suggests $i = 47.2°$ and the supplementary to our α values. Their model also suggests a flip on the PPA angle in late 80s that has not been observed. This model's predictions of β disagree with our PSRIX observations.

While the geometrical model and RVM appear to agree on their predictions for λ, they disagree on the way that the line of sight cuts the emission beam. We proposed a different orientation of the beam that can potentially explain this inconsistency. Alternative emission beam shapes has already been proposed in the literature. Weisberg & Taylor (2002) were the first to report deviations from a circular beam suggesting that an hourglass shape can explain the observations. Clifton & Weisberg (2008) extended this model concluded that minimal deviations from a circular beam can explain the observations. The model that we have suggested, which is not unique, assumes that the beam is circular and the magnetic axis is not in the middle of the beam but around 10° south. Although it can explain both RVM β measurements and component separation it fails to explain the fact that no flip of PPA values has been observed around 2005 as predicted by the RVM. This inconsistency may rise from the fact that both models used in our analysis are only a simplification of the real beam. The RVM probably can not accurately model the complex magnetic field of recycled pulsars, and the shape of the emission beam is more complicated than just a hollow-cone as previously indicated.

Further monitoring of the separation of the two main profile components and especially the PPA curve is crucial since according to RVM predictions, in the near future (starting in ∼2026), the line of sight will cross a part of the emission beam that we have already observed, meaning that the component separation, the flux density, the relative amplitude, and the PPA swing should appear the same as observed in the middle of the 2010s. Also, the time that the pulsar will not be visible also will distinguish the two models, since according to the RVM PSR B1913+16 will stop beaming towards Earth in 2085$^{+19}_{-10}$ but according to the geometrical model already in 2025$^{+5}_{-4}$. Thus these future observations will verify and expend the predictions of both of the models, revealing more precisely the emission geometry of this system.

Chapter 6

Conclusions

Pulsars are highly magnetised, fast spinning NSs, formed after a SN explosion. Their mass, which ranges from 1 to 2 $M_\odot$ is contained within a radius of only 10–12 km (Özel & Freire, 2016). Since their magnetic axis is usually misaligned to spin axis, the coherent polarised radiation that is emitted along each of their magnetic axes is detected as pulses on Earth like a lighthouse. Particularly interesting are MSPs (recycled pulsars that are spin-up pulsars form after transfer of mass and angular momentum from their companion star) whose rotational stability, over long timescales, approaches that of atomic clocks (Matsakis et al., 1997). MSPs are ideal for studying a wide range of phenomena, a few of them have been investigated in this thesis. The main technique for extracting the majority of the science that we can do with pulsars comes from timing, a technique that was discussed in Chapter 2. High precision timing was the tool used in this thesis, firstly for determining DM variations for increasing the PTA sensitivity to continuous GWs and the GWB, as discussed in Chapter 3, and also for investigating the nature of the companion of the high-spinning MSP PSR J1933−6211, as described is Chapter 4. In addition, the geometry of the geodetically precessing PSR B1913+16 system is investigating in Chapter 5.

No direct detection of GWs with pulsars has been achieved yet. The GW signal, despite is sourced from some of the most violent and energetic processes in the Universe, is expected to be very weak thus for a time scale of 5–10 years it can only be detected in the timing residuals of very stable PTA pulsars with a rms of < 100 ns (Jenet et al., 2005). In order to achieve a detection the red noise in pulse arrival times must be characterised. The main source of red noise in MSPs is DM variations. Since ISM effects are less prominent at high frequencies, in Chapter 3 we investigated the usage of the existing multi-frequency receivers used for Effelsberg EPTA observations and those under commissioning at Effelsberg and MeerKAT for measuring DM variations thus increasing the sensitivity to continuous GWs and the GWB. Currently the Effelsberg EPTA campaign consists of multi-frequency observations at 1.4 and 2.6 GHz. For the analysis we used the newest PSRIX observations taken since January 2012. For the 1.4-GHz observations we reported the phase-averaged flux densities and compared them with previously published values, for five of the pulsars these kinds of measurements are reported for the first time. We showed that with the available Effelsberg 4.85 GHz receiver we can detect 14 of the MSPs that we observe monthly for the EPTA. Motivated by these detections we investigated the performance of the Effelsberg C+ (centered at 5 GHz) and MeerKAT S-band (centered at 1.95 GHz) receiver on measuring temporal DM variations and the impact this has on the sensitivity to continuous GWs and a GWB. We concluded that the combination of Effelsberg 1.4 GHz and MeerKAT S-band observations provide the best precision in

DM variation measurements for flux density spectral indices $\lesssim -1.6$, and also the lowest uncertainty on the DM-corrected ToAs. Since correcting DM variations is always a process that removes red but adds white noise in the residuals, we have calculated which should be the reference ToA in order for the post-correction ToA precision to be 100 ns. Assuming that our primary observations are taken with the 1.4 GHz Effelsberg receiver ('P217 mm') and our secondary, for corrected DM variations, with the 2.6 GHz ('S110 mm'), 4.85 GHz ('S60 mm'), and 5 GHz ('C+') receivers, the pre-correction ToA uncertainty should be equal to 22 ns, 13 ns, and 26 ns, respectively. In the case that the MeerKAT S-band receiver is the primary and the 1.4 GHz system is the secondary, we need pre-correction ToA precision equal to 53 ns. Since the timing precision that we can achieve with PTAs is not yet of the order of tens of nanoseconds, a lot of effort should be done on achieving high timing precision with high frequency observations to enable the detection of GWs. We concluded, that with the current Effelsberg observing set up (1.4 GHz combined with 2.6 GHz observations), an addition of 6.7 years for a GWB and another 80 years of observations for continuous GWs are needed in order to achieve the same sensitivity as we expect with Effelbserg 1.4 GHz combined with MeerKAT S-band observations in 10 years.

A new generation of radio telescopes will soon be available for observations and will support PTA projects. One of these are located in the Northern hemisphere: FAST in China, while two others are located in the Southern hemisphere: SKA in South Africa and Australia, and MeerKAT in South Africa. The significantly larger collecting areas and much greater sensitivity of these telescopes will increase the S/N and correspondingly will reduce the ToA uncertainties of the currently observable PTA pulsars. Since all these next-generation telescopes will have projects that will aim to discover new pulsars, we expect some of them to become part of PTAs. These newly discovered pulsars are expected to have higher DMs, making the correction of ISM effects even more important in the future. As shown in Chapter 3 but also in previous studies (Lee et al., 2014), crucial factors for measuring DM-corrected ToAs are wider observing bands and better pre-correction ToA precision. Both requirements can be achieved with the next-generation large telescopes. Moreover, as shown in Chapter 3 it is very important not only to be able to achieve high pre-correction ToA precision at 1.4 GHz but also at higher observing frequencies. With the SKA, MeerKAT, and FAST we can achieve significant sensitivity at these frequencies as well. Another approach to correcting DM variations is to use low frequencies ($\sim$100–300 MHz) to determinate the DM values independently from the high-frequency timing data. The Low-Frequency Array (LOFAR) plays a major role in these observations in the Northern hemisphere. One potential problem for using these observations is that at these frequencies we may see different parts of the ISM as a result of interstellar scattering (Cordes et al., 2016, chromatic DM variations).

In Chapter 4 a phase-coherent solution for PSR J1933−6211, a 3.5-ms pulsar with a WD companion, using Parkes radio telescope observations, was given. For the analysis we applied the matrix template matching technique in which the ToAs are measured using full polarimetric information. The goal of applying this technique is to improve the timing residuals. Indeed the improvement that we got for this pulsar was 15.5% compared to the total intensity analysis. Based on the measured scintillation parameters and our timing analysis we concluded that the inclination angle is likely smaller than $\sim$80° and the upper limit on the companion mass is 0.44 $M_\odot$. With this limit we cannot distinguish between a He or CO WD companion. After investigating both possibilities we concluded that the pulsar has, as very few other fully recycled MSPs, a CO companion. The formation of the system is similar to PSRs J1614−2230 and J1101−6424 and can be explained with an IMXB which evolved from Case A RLO. In this case the transfer of mass started when the WD companion was still on the MS and thus the RLO timescale was long enough to fully recycle the pulsar.

PSR J1933−6211 is currently only observable with the Parkes radio telescope but will be observable with future facilities MeerKAT and SKA. Before these telescopes come online, Parkes will install a new Ultra–Wideband Low–frequency receiver (UWL), covering the bands from 0.7 GHz to 4.0 GHz, which will be ready for timing observations in late 2018. Observations of PSR J1933−6211 with this receiver will allow us to observe scintles at all orbital phases, making a Shapiro delay measurement possible. A Shapiro delay detection will put more constraints on the pulsar's mass revealing with more accuracy the nature of its companion. Moreover, UWL observations will lead to an improvement on the S/N of the pulse profile and consequently will decrease the uncertainty on the ToA measurements. If the expected improvement of the timing precision is sufficient this pulsar may be regularly observed by PTA projects depending on the amplitude and shape of the spin noise spectrum.

Even though the first direct GW detection happened 100 years after their prediction by LIGO the first indirect evidence for their existence came more than 30 years ago with the study of the decay of the ascending node of the first discovered DNS system, B1913+16. More than 40 years from its discovery this system remains a fascinating laboratory for studying relativistic effects. In Chapter 5 we focus on the relativistic effect of geodetic precession. Due to this effect the spin axis precesses about the total angular momentum of the system thus at different epochs we observe different parts of the emission beam. These temporal changes, for this pulsar have a periodicity of $\sim$300 years and can be seen in the total intensity profile and the polarisation properties. By studying these variations we derived the emission geometry of the system. For our analysis we used data at 21-cm, taken from early 80s to 2017 with the Arecibo and Effelsberg radio telescopes. We observed changes on the separation, and the relative height of the two main profile components, as well as on the phase-averaged flux density. To extract the emission geometry we used two independent models. The first one is purely geometrical, and assumes a hollow-cone emission beam fitted to the total intensity observations. The second model was the RVM and is fitted to the PPA curve of our available polarisation calibrated observations, which cover only a small fraction of the whole total intensity observations. We concluded that the orbital inclination angle is 132.9° while the misalignment angle is $\sim$21°. Since the two models disagree in their measurements of how the line of sight cuts the emission beam, a new emission beam shape is proposed in order to make these two models compatible with each other. According to this new model the beam has a hollow-cone shape but the magnetic axis is not located in the center of the beam but is shifted around 10° from the center.

By knowing the emission geometry of the pulsar we can predict which part of the emission beam we will observe in the future, and when the pulsar will stop being visible from Earth. The two models that we used disagree on these predictions. More precisely, according to the RVM model in the near future we should start observing parts of the emission beam that have been already observed in the past. Thus the component separation, the flux density, the relative amplitude, and the PPA swing at these two epochs should be identical. On the other hand, according to total intensity model we will not observe same parts of the beam, until the pulsar will not be visible any more. Thus with further monitoring of PSR B1913+16 with Effelsberg we can verify these predictions. Additionally with new observations we can extend and improve the predictions of both models by improving the emission geometry measurements of this system.

The future of pulsar astronomy is bright with the new generation of radio telescopes. The most important of which are: FAST, MeerKAT, and SKA. These telescopes, and especially SKA, will play a crucial role on the detection of GWs from individual sources or from the GWB. A lot of new pulsars will be discovered with these telescopes, some of them will be

added to PTAs. The observations of the already known pulsars are expected to provide us with lower ToA uncertainties, due to greater sensitivity of these telescopes. These high quality data sets will allow us to better characterize the noise of pulsars, especially DM noise, as explained in Chapter 3. The sensitivity that would be added to the PTAs from these changes will probably lead to the first detection of GWs in the nHz regime. Even if the detection is not achieved with these observations, more stringent constrains on galaxy evolution models will be set.

Even before the detection of GWs, these data sets will be interesting in their own right, since they can be used for producing other scientific results, like for example tests of theories of gravity, studies of the ISM. In the contest with this thesis, the discovery and timing of systems similar to PSR J1933−6211 will allow us to better understand the history and the evolution of these systems. Also, the discovery and probing of other geodetic precessing DNSs will lead to a better understanding of the pulsar beam structure and the emission mechanism of pulsars.

Bibliography

Abbott B. P., et al., 2016, Physical Review Letters, 116, 061102 (Cited on page 26.)

Abbott B. P., et al., 2017, Physical Review Letters, 119, 161101 (Cited on page 9.)

Abdalla H., et al., 2017, ApJ, 850, L22 (Cited on page 9.)

Abdo A. A., et al., 2009, Science, 325, 848 (Cited on page 11.)

Alpar M. A., Cheng A. F., Ruderman M. A., Shaham J., 1982, Nature, 300, 728 (Cited on pages 7 and 78.)

Altamirano D., et al., 2011, ApJ, 727, L18 (Cited on page 24.)

Amaro Seoane P., et al., 2013a, preprint, (arXiv:1305.5720) (Cited on page 26.)

Amaro-Seoane P., et al., 2013b, GW Notes, Vol. 6, p. 4-110, 6, 4 (Cited on page 26.)

Antoniadis J., et al., 2013, Science, 340, 448 (Cited on page 24.)

Antoniadis J., Tauris T. M., Ozel F., Barr E., Champion D. J., Freire P. C. C., 2016, preprint, (arXiv:1605.01665) (Cited on page 24.)

Arcavi I., et al., 2017, Nature, 551, 64 (Cited on page 9.)

Archibald A. M., et al., 2009, Science, 324, 1411 (Cited on pages 11 and 24.)

Archibald R. F., et al., 2016, ApJ, 819, L16 (Cited on page 6.)

Armstrong J. W., Rickett B. J., Spangler S. R., 1995, ApJ, 443, 209 (Cited on pages 46 and 70.)

Arnett D., 1996, Supernovae and Nucleosynthesis: An Investigation of the History of Matter from the Big Bang to the Present. Princeton University Press (Cited on page 3.)

Arzoumanian Z., et al., 2015, ApJ, 813, 65 (Cited on page 28.)

Arzoumanian Z., et al., 2018, ApJ, 859, 47 (Cited on page 28.)

Ashworth M., Lyne A. G., 1981, MNRAS, 195, 517 (Cited on page 11.)

Baade W., Zwicky F., 1934, Proceedings of the National Academy of Science, 20, 259 (Cited on page 2.)

Backer D. C., 1970, Nature, 228, 42 (Cited on pages 11 and 12.)

Backer D. C., 1972, ApJ, 174, L157 (Cited on page 13.)

Backer D. C., Rankin J. M., Campbell D. B., 1976, Nature, 263, 202 (Cited on page 19.)

Backer D. C., Kulkarni S. R., Heiles C., Davis M. M., Goss W. M., 1982, Nature, 300, 615 (Cited on pages 7 and 26.)

Barker B. M., O'Connell R. F., 1975, ApJ, 199, L25 (Cited on page 94.)

Barnard J. J., Arons J., 1986, ApJ, 302, 138 (Cited on page 18.)

Bates S. D., Lorimer D. R., Verbiest J. P. W., 2013, MNRAS, 431, 1352 (Cited on pages 12, 13 and 51.)

Bhat N. D. R., Cordes J. M., Camilo F., Nice D. J., Lorimer D. R., 2004, ApJ, 605, 759 (Cited on page 50.)

Bhat N. D. R., Bailes M., Verbiest J. P. W., 2008, Phys. Rev. D, 77, 124017 (Cited on page 25.)

Bhattacharya D., van den Heuvel E. P. J., 1991, Phys. Rep., 203, 1 (Cited on page 7.)

Bignami G. F., Caraveo P. A., De Luca A., Mereghetti S., 2003, Nature, 423, 725 (Cited on page 7.)

Bilitza D., Galkin I. A., Huang X. A., Reinisch B. W., Vesnin A., 2016, AGU Fall Meeting Abstracts, pp SA13A–2123 (Cited on page 50.)

Bisnovatyi-Kogan G. S., Komberg B. V., 1974, Soviet Ast., 18, 217 (Cited on page 78.)

Blaskiewicz M., Cordes J. M., Wasserman I., 1991, ApJ, 370, 643 (Cited on pages 109 and 117.)

Booth R. S., de Blok W. J. G., Jonas J. L., Fanaroff B., 2009, preprint, (arXiv:0910.2935) (Cited on page 29.)

Boyle L. A., Buonanno A., 2008, Phys. Rev. D, 78, 043531 (Cited on page 26.)

Brentjens M. A., de Bruyn A. G., 2005, A&A, 441, 1217 (Cited on page 98.)

Breton R. P., et al., 2008, Science, 321, 104 (Cited on page 25.)

Bruck Y. M., Ustimenko B. Y., 1973, Nature Physical Science, 242, 58 (Cited on page 12.)

Burbidge G. R., 1968, Nature, 218, 433 (Cited on page 2.)

Burgay M., et al., 2003, Nature, 426, 531 (Cited on page 25.)

Burgay M., et al., 2005, ApJ, 624, L113 (Cited on page 12.)

Burgay M., et al., 2013, MNRAS, 433, 259 (Cited on page 13.)

Burn B. J., 1966, MNRAS, 133, 67 (Cited on page 98.)

Camilo F., Thorsett S. E., Kulkarni S. R., 1994, ApJ, 421, L15 (Cited on page 86.)

Carroll B. W., Ostlie D. A., 2006, An introduction to modern astrophysics and cosmology. Addison-Wesley (Cited on page 3.)

Champion D. J., et al., 2010, ApJ, 720, L201 (Cited on page 46.)

Chen S., Middleton H., Sesana A., Del Pozzo W., Vecchio A., 2017, MNRAS, 468, 404 (Cited on page 28.)

Clifton T., Weisberg J. M., 2008, ApJ, 679, 687 (Cited on pages 96 and 118.)

Cognard I., Backer D. C., 2004, ApJ, 612, L125 (Cited on page 47.)

Cognard I., et al., 2011, ApJ, 732, 47 (Cited on page 57.)

Colgate S. A., White R. H., 1966, ApJ, 143, 626 (Cited on page 2.)

Colpi M., Shapiro S. L., Teukolsky S. A., 1993, ApJ, 414, 717 (Cited on page 78.)

Cordes J. M., 1978, ApJ, 222, 1006 (Cited on pages 12, 14 and 17.)

Cordes J. M., Downs G. S., 1985, ApJS, 59, 343 (Cited on page 11.)

Cordes J. M., Lazio T. J. W., 2002, in preprint. (arXiv:astro-ph/0207156) (Cited on pages 12, 20 and 87.)

Cordes J. M., Rickett B. J., 1998, ApJ, 507, 846 (Cited on page 23.)

Cordes J. M., Wasserman I., Blaskiewicz M., 1990, ApJ, 349, 546 (Cited on pages 95, 96, 109 and 117.)

Cordes J. M., Kramer M., Backer D. C., Lazio T. J. W., Science Working Groupthe Square Kilometer Array Team 2005, in American Astronomical Society Meeting Abstracts. p. 1390 (Cited on page 29.)

Cordes J. M., Shannon R. M., Stinebring D. R., 2016, ApJ, 817, 16 (Cited on pages 51 and 120.)

Damour T., Ruffini R., 1974, Academie des Sciences Paris Comptes Rendus Serie Sciences Mathematiques, 279, 971 (Cited on page 94.)

Damour T., Taylor J. H., 1992, Phys. Rev. D, 45, 1840 (Cited on pages 14, 23, 25, 44, 95 and 106.)

Davies J. G., Hunt G. C., Smith F. G., 1969, Nature, 221, 27 (Cited on page 3.)

Demorest P. B., Pennucci T., Ransom S. M., Roberts M. S. E., Hessels J. W. T., 2010, Nature, 467, 1081 (Cited on pages 9 and 91.)

Demorest P. B., et al., 2013, ApJ, 762, 94 (Cited on pages 40 and 51.)

Desvignes G., Cognard I., Kramer M., Lyne A., Stappers B., Theureau G., 2008, in Bassa C., Wang Z., Cumming A., Kaspi V. M., eds, AIP Conf. Proc. Vol. 983, 40 Years of Pulsars: Millisecond Pulsars, Magnetars and More. pp 482–484, doi:10.1063/1.2900280 (Cited on page 12.)

Desvignes G., et al., 2016, MNRAS, 458, 3341 (Cited on pages 28, 65, 67, 87 and 89.)

Detweiler S., 1979, ApJ, 234, 1100 (Cited on page 26.)

Dicke R. H., 1946, Rev. Sci. Instrument, 17, 268 (Cited on page 40.)

Drake F. D., Craft H. D., 1968, Nature, 220, 231 (Cited on page 11.)

Edwards R. T., Hobbs G. B., Manchester R. N., 2006, MNRAS, 372, 1549 (Cited on pages 39 and 84.)

Espinoza C. M., Lyne A. G., Kramer M., Manchester R. N., Kaspi V. M., 2011, ApJ, 741, L13 (Cited on page 6.)

Everett J. E., Weisberg J. M., 2001, ApJ, 553, 341 (Cited on page 106.)

Feroz F., Hobson M. P., 2008, MNRAS, 384, 449 (Cited on page 46.)

Feroz F., Hobson M. P., Bridges M., 2009a, MNRAS, 398, 1601 (Cited on page 46.)

Feroz F., Hobson M. P., Zwart J. T. L., Saunders R. D. E., Grainge K. J. B., 2009b, MNRAS, 398, 2049 (Cited on page 109.)

Flannery B. P., van den Heuvel E. P. J., 1975, A&A, 39, 61 (Cited on page 9.)

Fonseca E., et al., 2016, ApJ, 832, 167 (Cited on page 24.)

Frail D. A., Kulkarni S. R., 1991, Nature, 352, 785 (Cited on page 3.)

Freire P. C. C., Tauris T. M., 2014, MNRAS, 438, L86 (Cited on page 24.)

Freire P. C. C., Wex N., 2010, MNRAS, 409, 199 (Cited on page 78.)

Freire P. C., Camilo F., Kramer M., Lorimer D. R., Lyne A. G., Manchester R. N., D'Amico N., 2003, MNRAS, 340, 1359 (Cited on page 50.)

Freire P. C. C., et al., 2011, MNRAS, 412, 2763 (Cited on page 24.)

Freire P. C. C., et al., 2012, MNRAS, 423, 3328 (Cited on page 25.)

Fruchter A. S., et al., 1990, ApJ, 351, 642 (Cited on page 11.)

Gaensler B. M., Frail D. A., 2000, Nature, 406, 158 (Cited on page 6.)

Gangadhara R. T., Gupta Y., 2001, ApJ, 555, 31 (Cited on page 18.)

Gil J. A., Kijak J., Seiradakis J. H., 1993, A&A, 272, 268 (Cited on page 19.)

Gold T., 1968, Nature, 218, 731 (Cited on pages 2 and 3.)

Gold T., 1969, Nature, 221, 25 (Cited on page 3.)

Goldreich P., Julian W. H., 1969, ApJ, 157, 869 (Cited on page 17.)

Gould D. M., Lyne A. G., 1998, MNRAS, 301, 235 (Cited on page 17.)

Grishchuk L. P., 2005, Physics Uspekhi, 48, 1235 (Cited on page 26.)

Gupta Y., 1995, ApJ, 451, 717 (Cited on page 89.)

Gupta Y., Rickett B. J., Lyne A. G., 1994, MNRAS, 269, 1035 (Cited on pages 23 and 87.)

Haensel P., Zdunik J. L., Douchin F., 2002, A&A, 385, 301 (Cited on page 78.)

Hamilton P. A., Hall P. J., Costa M. E., 1985, MNRAS, 214, 5P (Cited on page 50.)

Han J. L., Manchester R. N., 2001, MNRAS, 320, L35 (Cited on page 19.)

Han J. L., Manchester R. N., Xu R. X., Qiao G. J., 1998, MNRAS, 300, 373 (Cited on page 13.)

Han J. L., Manchester R. N., Lyne A. G., Qiao G. J., van Straten W., 2006, ApJ, 642, 868 (Cited on page 21.)

Han J. L., Manchester R. N., van Straten W., Demorest P., 2018, ApJS, 234, 11 (Cited on page 21.)

Hankins T. H., 1971, ApJ, 169, 487 (Cited on page 33.)

Hankins T. H., Wright G. A. E., 1980, Nature, 288, 681 (Cited on page 19.)

Hassall T. E., et al., 2012, A&A, 543, A66 (Cited on page 18.)

Heiles C., et al., 2001, PASP, 113, 1274 (Cited on page 36.)

Helfand D. J., Manchester R. N., Taylor J. H., 1975, ApJ, 198, 661 (Cited on page 11.)

Hellings R. W., Downs G. S., 1983, ApJ, 265, L39 (Cited on page 26.)

Hemberger D. A., Stinebring D. R., 2008, ApJ, 674, L37 (Cited on page 46.)

Hessels J., Ransom S., Roberts M., Kaspi V., Livingstone M., Tam C., Crawford F., 2005, in Rasio F. A., Stairs I. H., eds, AIP Conf. Proc. Vol. 328, Binary Radio Pulsars. p. 395 (arXiv:astro-ph/0404167) (Cited on page 91.)

Hewish A., Bell S. J., Pilkington J. D. H., Scott P. F., Collins R. A., 1968, Nature, 217, 709 (Cited on page 2.)

Hickish J. e. a., 2016, Journal of Astronomical Instrumentation, 5, 1641001 (Cited on page 80.)

Hobbs G., Lorimer D. R., Lyne A. G., Kramer M., 2005, MNRAS, 360, 974 (Cited on page 87.)

Hobbs G. B., Edwards R. T., Manchester R. N., 2006, MNRAS, 369, 655 (Cited on pages 39, 65 and 81.)

Hobbs G., et al., 2012, MNRAS, 427, 2780 (Cited on pages 42 and 46.)

Hotan A. W., van Straten W., Manchester R. N., 2004, PASA, 21, 302 (Cited on pages 36, 54, 81 and 97.)

Hotan A. W., Bailes M., Ord S. M., 2005, ApJ, 624, 906 (Cited on page 12.)

Hotan A. W., Bailes M., Ord S. M., 2006, MNRAS, 369, 1502 (Cited on page 80.)

Hulse R. A., Taylor J. H., 1975, ApJ, 201, L55 (Cited on pages 24, 25, 26 and 94.)

Istomin Y. N., 1991, Soviet Astronomy Letters, 17, 301 (Cited on pages 101 and 102.)

Istrate A. G., Tauris T. M., Langer N., 2014, A&A, 571, A45 (Cited on page 90.)

Ivanova N., et al., 2013, A&A Rev., 21, 59 (Cited on page 10.)

Jacoby B. A., Cameron P. B., Jenet F. A., Anderson S. B., Murty R. N., Kulkarni S. R., 2006, ApJ, 644, L113 (Cited on page 12.)

Jacoby B. A., Bailes M., Ord S. M., Knight H. S., Hotan A. W., 2007, ApJ, 656, 408 (Cited on pages 57, 78, 80 and 82.)

Janka H.-T., 2016, preprint, (arXiv:1611.07562) (Cited on page 87.)

Janssen G. H., Stappers B. W., Bassa C. G., Cognard I., Kramer M., Theureau G., 2010, A&A, 514, A74 (Cited on page 57.)

Janssen G., et al., 2015, Advancing Astrophysics with the Square Kilometre Array (AASKA14), p. 37 (Cited on pages 29 and 32.)

Jenet F. A., Hobbs G. B., Lee K. J., Manchester R. N., 2005, ApJ, 625, L123 (Cited on pages 27, 28, 50 and 119.)

Jenet F. A., et al., 2006, ApJ, 653, 1571 (Cited on page 28.)

Jessner A., 1996, in van't Klooster C. G. M., van Ardenne A., eds, Large Antennas in Radio Astronomy. p. 185 (Cited on page 96.)

Johnston S., 2002, PASA, 19, 277 (Cited on page 54.)

Johnston S., Karastergiou A., Mitra D., Gupta Y., 2008, MNRAS, 388, 261 (Cited on page 17.)

Kalogera V., Lorimer D. R., 2000, ApJ, 530, 890 (Cited on page 96.)

Kapoor R. C., Shukre C. S., 1998, ApJ, 501, 228 (Cited on page 17.)

Karastergiou A., Johnston S., 2007, MNRAS, 380, 1678 (Cited on page 19.)

Kasen D., Metzger B., Barnes J., Quataert E., Ramirez-Ruiz E., 2017, Nature, 551, 80 (Cited on page 9.)

Kasian L., 2008, in Bassa C., Wang Z., Cumming A., Kaspi V. M., eds, AIP Conf. Proc. Vol. 983, 40 Years of Pulsars: Millisecond Pulsars, Magnetars and More. pp 485–487 (arXiv:0711.2690), doi:10.1063/1.2900281 (Cited on page 12.)

Keith M. J., et al., 2013, MNRAS, 429, 2161 (Cited on pages 43, 46, 50, 51 and 70.)

Kijak J., Gil J., 1998, MNRAS, 299, 855 (Cited on pages 17 and 18.)

Kippenhahn R., Weigert A., 1990, Stellar Structure and Evolution. Berlin Heidelberg: Springer-Verlag (Cited on page 92.)

Komesaroff M. M., 1970, Nature, 225, 612 (Cited on pages 11 and 19.)

Kopeikin S. M., 1995, ApJ, 439, L5 (Cited on page 85.)

Kopeikin S. M., 1996, ApJ, 467, L93 (Cited on page 85.)

Kramer M., 1998, ApJ, 509, 856 (Cited on pages 12, 95, 96, 98, 101, 103, 105 and 118.)

Kramer M., 2004, ArXiv Astrophysics e-prints, (Cited on page 29.)

Kramer M., 2014, International Journal of Modern Physics D, 23, 1430004 (Cited on page 12.)

Kramer M., Wex N., 2009, Classical and Quantum Gravity, 26, 073001 (Cited on pages 95, 103 and 106.)

Kramer M., Wielebinski R., Jessner A., Gil J. A., Seiradakis J. H., 1994, A&AS, 107, 515 (Cited on page 40.)

Kramer M., Xilouris K. M., Lorimer D. R., Doroshenko O., Jessner A., Wielebinski R., Wolszczan A., Camilo F., 1998, ApJ, 501, 270 (Cited on pages 11, 13 and 57.)

Kramer M., Lange C., Lorimer D. R., Backer D. C., Xilouris K. M., Jessner A., Wielebinski R., 1999, ApJ, 526, 957 (Cited on pages 11, 58 and 60.)

Kramer M., Löhmer O., Karastergiou A., 2003, in Bailes M., Nice D. J., Thorsett S. E., eds, AIP Conf. Proc. Vol. 302, Radio Pulsars. p. 99 (arXiv:astro-ph/0301146) (Cited on page 98.)

Kramer M., et al., 2006, Science, 314, 97 (Cited on page 25.)

Kuniyoshi M., Verbiest J. P. W., Lee K. J., Adebahr B., Kramer M., Noutsos A., 2015, MNRAS, 453, 828 (Cited on pages 13, 56, 60 and 61.)

Kuzmin A. D., Losovsky B. Y., 2001, A&A, 368, 230 (Cited on page 60.)

Lam M. T., Cordes J. M., Chatterjee S., Dolch T., 2015, ApJ, 801, 130 (Cited on page 51.)

Lam M. T., Cordes J. M., Chatterjee S., Jones M. L., McLaughlin M. A., Armstrong J. W., 2016, ApJ, 821, 66 (Cited on pages 43 and 50.)

Lange C., Camilo F., Wex N., Kramer M., Backer D. C., Lyne A. G., Doroshenko O., 2001, MNRAS, 326, 274 (Cited on page 84.)

Large M. I., Vaughan A. E., Mills B. Y., 1968, Nature, 220, 340 (Cited on page 2.)

Lattimer J. M., Prakash M., 2001, ApJ, 550, 426 (Cited on page 3.)

Lazaridis K., et al., 2009, MNRAS, 400, 805 (Cited on page 25.)

Lazarus P., Karuppusamy R., Graikou E., Caballero R. N., Champion D. J., Lee K. J., Verbiest J. P. W., Kramer M., 2016, MNRAS, 458, 868 (Cited on pages 36, 52, 67, 72, 97 and 104.)

Lee K. J., Wex N., Kramer M., Stappers B. W., Bassa C. G., Janssen G. H., Karuppusamy R., Smits R., 2011, MNRAS, 414, 3251 (Cited on page 29.)

Lee K. J., et al., 2014, MNRAS, 441, 2831 (Cited on pages 43, 72 and 120.)

Lentati L., Alexander P., Hobson M. P., Feroz F., van Haasteren R., Lee K. J., Shannon R. M., 2014, MNRAS, 437, 3004 (Cited on page 46.)

Lentati L., et al., 2015, MNRAS, 453, 2576 (Cited on pages 28 and 46.)

Lentati L., et al., 2016, MNRAS, 458, 2161 (Cited on pages 46 and 50.)

Levin L., et al., 2016, ApJ, 818, 166 (Cited on page 57.)

Lewin W. H. G., van Paradijs J., van den Heuvel E. P. J., 1997, X-ray binaries.. Cambridge Astrophysics Series (Cited on page 9.)

Lin J., Rappaport S., Podsiadlowski P., Nelson L., Paxton B., Todorov P., 2011, ApJ, 732, 70 (Cited on page 92.)

Liu K., Verbiest J. P. W., Kramer M., Stappers B. W., van Straten W., Cordes J. M., 2011, MNRAS, 417, 2916 (Cited on pages 46 and 47.)

Liu K., et al., 2014, MNRAS, 443, 3752 (Cited on page 40.)

Löhmer O., Mitra D., Gupta Y., Kramer M., Ahuja A., 2004, A&A, 425, 569 (Cited on page 51.)

Lommen A. N., Zepka A., Backer D. C., McLaughlin M., Cordes J. M., Arzoumanian Z., Xilouris K., 2000, ApJ, 545, 1007 (Cited on page 57.)

Lorimer D. R., Kramer M., 2012, Handbook of Pulsar Astronomy. Cambridge University Press (Cited on pages 4, 5, 15, 17, 20, 40, 42 and 78.)

Lorimer D. R., Yates J. A., Lyne A. G., Gould D. M., 1995, MNRAS, 273, 411 (Cited on page 13.)

Lorimer D. R., et al., 2006, MNRAS, 372, 777 (Cited on page 57.)

Lyne A. G., 1984, Nature, 310, 300 (Cited on pages 80 and 89.)

Lyne A. G., Manchester R. N., 1988, MNRAS, 234, 477 (Cited on page 19.)

Lyne A. G., Smith F. G., 1968, Nature, 218, 124 (Cited on page 13.)

Lyne A. G., Brinklow A., Middleditch J., Kulkarni S. R., Backer D. C., 1987, Nature, 328, 399 (Cited on page 24.)

Lyne A. G., Biggs J. D., Harrison P. A., Bailes M., 1993, Nature, 361, 47 (Cited on page 24.)

Lyne A. G., et al., 2004, Science, 303, 1153 (Cited on page 25.)

Lyne A., Hobbs G., Kramer M., Stairs I., Stappers B., 2010, Science, 329, 408 (Cited on page 46.)

Lyne A., Graham-Smith F., Weltevrede P., Jordan C., Stappers B., Bassa C., Kramer M., 2013, Science, 342, 598 (Cited on page 13.)

Manchester R. N., Hobbs G. B., Teoh A., Hobbs M., 2005, AJ, 129, 1993 (Cited on pages 7, 8, 61, 72 and 79.)

Manchester R. N., et al., 2010, ApJ, 710, 1694 (Cited on pages 12 and 95.)

Manchester R. N., et al., 2013, PASA, 30, e017 (Cited on page 57.)

Maron O., Kijak J., Kramer M., Wielebinski R., 2000, A&A, 147, 195 (Cited on pages 12, 13 and 51.)

Martynov D. V., et al., 2016, Phys. Rev. D, 93, 112004 (Cited on page 26.)

Mateo N. M., Antoniadis J., Tauris T. M., van Kerkwijk M., 2017, in prep. (Cited on page 92.)

Matsakis D. N., Taylor J. H., Eubanks T. M., 1997, A&A, 326, 924 (Cited on page 119.)

Matthews A. M., Nice D. J., Fonseca E., Arzoumanian Z., 2016, ApJ, 818, 92 (Cited on page 89.)

McKee J. W., et al., 2016, MNRAS, 461, 2809 (Cited on page 47.)

Mignani R. P., 2011, Advances in Space Research, 47, 1281 (Cited on page 11.)

Moore C. J., Taylor S. R., Gair J. R., 2015, Classical and Quantum Gravity, 32, 055004 (Cited on pages 74 and 75.)

Mortier A., Faria J. P., Correia C. M., Santerne A., Santos N. C., 2015, A&A, 573, A101 (Cited on page 98.)

Nan R., et al., 2011, International Journal of Modern Physics D, 20, 989 (Cited on page 29.)

Narayan R., 1992, Philosophical Transactions of the Royal Society of London Series A, 341, 151 (Cited on page 22.)

Ng C., Champion D. J., Bailes M., Barr E. D., 2015, MNRAS, 450, 2922 (Cited on page 92.)

Noutsos A., et al., 2015, A&A, 576, A62 (Cited on page 98.)

Oort J. H., Walraven T., 1956, Bull. Astron. Inst. Netherlands, 12, 285 (Cited on page 4.)

Oppenheimer J. R., Volkoff G. M., 1939, Physical Review, 55, 374 (Cited on pages 3 and 24.)

Ord S. M., Bailes M., van Straten W., 2002, ApJ, 574, L75 (Cited on pages 80 and 89.)

Osłowski S., van Straten W., Hobbs G. B., Bailes M., Demorest P., 2011, MNRAS, 418, 1258 (Cited on page 47.)

Ostriker J., 1968, Nature, 217, 1227 (Cited on page 2.)

Özel F., Freire P., 2016, ARA&A, 54, 401 (Cited on pages 24 and 119.)

Pacini F., 1967, Nature, 216, 567 (Cited on pages 2 and 3.)

Papitto A., et al., 2013, Nature, 501, 517 (Cited on pages 11 and 24.)

Pennucci T. T., Demorest P. B., Ransom S. M., 2014, ApJ, 790, 93 (Cited on page 40.)

Petrova S. A., 2000, A&A, 360, 592 (Cited on page 18.)

Phinney E. S., 1992, Philosophical Transactions of the Royal Society of London Series A, 341, 39 (Cited on page 78.)

Phinney E. S., Kulkarni S. R., 1994, ARA&A, 32, 591 (Cited on page 90.)

Pian E., et al., 2017, Nature, 551, 67 (Cited on page 9.)

Pilkington J. D. H., Hewish A., Bell S. J., Cole T. W., 1968, Nature, 218, 126 (Cited on page 2.)

Radhakrishnan V., Cooke D. J., 1969, Astrophys. Lett., 3, 225 (Cited on pages 14 and 95.)

Radhakrishnan V., Srinivasan G., 1982, Current Science, 51, 1096 (Cited on pages 7 and 24.)

Rajagopal M., Romani R. W., 1995, ApJ, 446, 543 (Cited on page 46.)

Rankin J. M., 1970, Nature, 227, 1330 (Cited on page 11.)

Rankin J. M., 1983, ApJ, 274, 333 (Cited on pages 17 and 19.)

Ransom S. M., et al., 2014, Nature, 505, 520 (Cited on pages 24 and 25.)

Rappaport S., Podsiadlowski P., Joss P. C., Di Stefano R., Han Z., 1995, MNRAS, 273, 731 (Cited on page 90.)

Ravi V., Wyithe J. S. B., Shannon R. M., Hobbs G., Manchester R. N., 2014, MNRAS, 442, 56 (Cited on page 28.)

Reardon D. J., et al., 2016, MNRAS, 455, 1751 (Cited on page 28.)

Reid M. J., et al., 2014, ApJ, 783, 130 (Cited on page 86.)

Rickett B. J., 1969, Nature, 221, 158 (Cited on page 22.)

Rickett B. J., 1970, MNRAS, 150, 67 (Cited on page 23.)

Rickett B. J., 1977, ARA&A, 15, 479 (Cited on pages 22 and 80.)

Ridolfi A., 2017, PhD thesis, Rheinische Friedrich-Wilhelms-Universitaet Bonn, `http://hss.ulb.uni-bonn.de/2017/4933/4933.htm` (Cited on page 44.)

Robinson B. J., Cooper B. F. C., Gardiner F. F., Wielebinski R., Landecker T. L., 1968, Nature, 218, 1143 (Cited on page 12.)

Romani R. W., 1989, in Ögelman H., van den Heuvel E. P. J., eds, NATO Advanced Science Institutes (ASI) Series C Vol. 262, NATO Advanced Science Institutes (ASI) Series C. p. 113 (Cited on page 26.)

Roy A. E., 1988, Orbital motion. IoP Publishing, Bristol (Cited on page 43.)

Roy J., et al., 2015, ApJ, 800, L12 (Cited on page 24.)

Sanidas S. A., Battye R. A., Stappers B. W., 2012, Phys. Rev. D, 85, 122003 (Cited on page 26.)

Saslaw W. C., 1968, Nature, 217, 1222 (Cited on page 2.)

Savonije G. J., 1978, A&A, 62, 317 (Cited on page 9.)

Savonije G. J., 1987, Nature, 325, 416 (Cited on pages 78 and 90.)

Sazhin M. V., 1978, Soviet Ast., 22, 36 (Cited on page 26.)

Scheuer P. A. G., 1968, Nature, 218, 920 (Cited on page 22.)

Sesana A., 2013, Classical and Quantum Gravity, 30, 244009 (Cited on page 26.)

Sesana A., Haardt F., Madau P., Volonteri M., 2004, ApJ, 611, 623 (Cited on page 46.)

Sesana A., Vecchio A., Colacino C. N., 2008, MNRAS, 390, 192 (Cited on page 26.)

Sesana A., Shankar F., Bernardi M., Sheth R. K., 2016, MNRAS, 463, L6 (Cited on page 75.)

Shaham J., 1992, in van den Heuvel E. P. J., Rappaport S. A., eds, X-Ray Binaries and the Formation of Binary and Millisecond Radio Pulsars. Dordrecht: kluwer Acad. Publ., pp 375–386 (Cited on page 9.)

Shannon R. M., Cordes J. M., 2012, ApJ, 761, 64 (Cited on page 47.)

Shannon R. M., et al., 2014, MNRAS, 443, 1463 (Cited on page 47.)

Shannon R. M., et al., 2015, Science, 349, 1522 (Cited on pages 28 and 41.)

Shao L., Wex N., 2016, Science China Physics, Mechanics, and Astronomy, 59, 699501 (Cited on page 25.)

Shao L., Caballero R. N., Kramer M., Wex N., Champion D. J., Jessner A., 2013, Classical and Quantum Gravity, 30, 165019 (Cited on page 25.)

Sieber W., 1973, A&A, 28, 237 (Cited on page 13.)

Siemens X., Ellis J., Jenet F., Romano J. D., 2013, Classical and Quantum Gravity, 30, 224015 (Cited on pages 28 and 75.)

Smarr L. L., Blandford R., 1976, ApJ, 207, 574 (Cited on page 24.)

Smartt S. J., et al., 2017, Nature, 551, 75 (Cited on page 9.)

Srinivasan G., van den Heuvel E. P. J., 1982, A&A, 108, 143 (Cited on page 24.)

Staelin D. H., Reifenstein III E. C., 1968, Science, 162, 1481 (Cited on pages 2 and 3.)

Stairs I. H., Thorsett S. E., Arzoumanian Z., 2004, Physical Review Letters, 93, 141101 (Cited on page 12.)

Stairs I. H., et al., 2005, ApJ, 632, 1060 (Cited on page 57.)

Staveley-Smith L., et al., 1996, PASA, 13, 243 (Cited on page 80.)

Stinebring D. R., Smirnova T. V., Hankins T. H., Hovis J. S., Kaspi V. M., Kempner J. C., Myers E., Nice D. J., 2000, ApJ, 539, 300 (Cited on page 13.)

Strom R. G., 1987, ApJ, 319, L103 (Cited on page 3.)

Tauris T. M., 2011, in Schmidtobreick L., Schreiber M. R., Tappert C., eds, AIP Conf. Proc. Vol. 447, Evolution of Compact Binaries. p. 285 (arXiv:1106.0897) (Cited on page 78.)

Tauris T. M., Bailes M., 1996, A&A, 315, 432 (Cited on page 87.)

Tauris T. M., Savonije G. J., 1999, A&A, 350, 928 (Cited on pages 9, 78, 90, 91 and 92.)

Tauris T. M., van den Heuvel E. P. J., 2006, Formation and evolution of compact stellar X-ray sources. Cambridge University Press, pp 623–665 (Cited on page 24.)

Tauris T. M., van den Heuvel E. P. J., Savonije G. J., 2000, ApJ, 530, L93 (Cited on page 92.)

Tauris T. M., Langer N., Kramer M., 2011, MNRAS, 416, 2130 (Cited on page 92.)

Tauris T. M., Langer N., Kramer M., 2012, MNRAS, 425, 1601 (Cited on pages 79, 86 and 90.)

Tauris T. M., et al., 2017, ApJ, 846, 170 (Cited on pages 24 and 94.)

Tavani M., Brookshaw L., 1992, Nature, 356, 320 (Cited on page 9.)

Taylor J. H., 1992, Philosophical Transactions of the Royal Society of London Series A, 341, 117 (Cited on pages 40, 41 and 81.)

Taylor J. H., Weisberg J. M., 1982, ApJ, 253, 908 (Cited on page 94.)

Taylor J. H., Weisberg J. M., 1989, ApJ, 345, 434 (Cited on page 45.)

Taylor J. H., Fowler L. A., McCulloch P. M., 1979, Nature, 277, 437 (Cited on page 94.)

Taylor S. R., Vallisneri M., Ellis J. A., Mingarelli C. M. F., Lazio T. J. W., van Haasteren R., 2016, ApJ, 819, L6 (Cited on page 29.)

Thorne K. S., Ipser J. R., 1968, ApJ, 152, L71 (Cited on page 2.)

Thorsett S. E., Stinebring D. R., 1990, ApJ, 361, 644 (Cited on page 60.)

Tiburzi C., Verbiest J., 2018, preprint, (arXiv:1804.04040) (Cited on page 50.)

Timmes F. X., Woosley S. E., Weaver T. A., 1996, ApJ, 457, 834 (Cited on pages 78 and 91.)

Tolman R. C., 1939, Physical Review, 55, 364 (Cited on page 3.)

Torne P., et al., 2017, MNRAS, 465, 242 (Cited on page 12.)

Toscano M., Bailes M., Manchester R. N., Sandhu J. S., 1998, ApJ, 506, 863 (Cited on page 13.)

Troja E., et al., 2017, Nature, 551, 71 (Cited on page 9.)

Truemper J., Pietsch W., Reppin C., Voges W., Staubert R., Kendziorra E., 1978, ApJ, 219, L105 (Cited on page 7.)

Verbiest J. P. W., et al., 2009, MNRAS, 400, 951 (Cited on page 41.)

Verbiest J. P. W., et al., 2016, MNRAS, 458, 1267 (Cited on pages 28, 46, 73, 84 and 85.)

Weisberg J. M., Huang Y., 2016, ApJ, 829, 55 (Cited on pages 25, 95, 97 and 106.)

Weisberg J. M., Taylor J. H., 2002, ApJ, 576, 942 (Cited on pages 95, 96 and 118.)

Weisberg J. M., Taylor J. H., 2005, in Rasio F. A., Stairs I. H., eds, AIP Conf. Proc. Vol. 328, Binary Radio Pulsars. p. 25 (arXiv:astro-ph/0407149) (Cited on pages 96 and 118.)

Weisberg J. M., Romani R. W., Taylor J. H., 1989, ApJ, 347, 1030 (Cited on pages 12, 95 and 101.)

Weisberg J. M., Nice D. J., Taylor J. H., 2010, ApJ, 722, 1030 (Cited on page 94.)

Weltevrede P., Stappers B. W., van den Horn L. J., Edwards R. T., 2003, A&A, 412, 473 (Cited on page 18.)

Woosley S. E., Weaver T. A., 1986, ARA&A, 24, 205 (Cited on page 3.)

Yao J. M., Manchester R. N., Wang N., 2017, ApJ, 835, 29 (Cited on pages 21 and 89.)

You X. P., et al., 2007, MNRAS, 378, 493 (Cited on page 51.)

Zhu W. W., et al., 2018, preprint, (arXiv:1802.09206) (Cited on page 25.)

van Straten W., 2004, ApJS, 152, 129 (Cited on pages 38 and 81.)

van Straten W., 2006, ApJ, 642, 1004 (Cited on pages 40 and 81.)

van Straten W., 2013, ApJS, 204, 13 (Cited on pages 38 and 81.)

van Straten W., Manchester R. N., Johnston S., Reynolds J. E., 2010, PASA, 27, 104 (Cited on page 81.)

van Straten W., Demorest P., Oslowski S., 2012, Astronomical Research and Technology, 9, 237 (Cited on pages 36 and 81.)

Erklärung

Ich versichere, dass ich die von mir vorgelegte Dissertation selbständig angefertigt, die benutzten Quellen und Hilfsmittel vollständig angegeben und die Stellen der Arbeiteinschlielich Tabellen, Karten und Abbildungen –, die anderen Werken im Wortlaut oder dem Sinn nach entnommen sind, in jedem Einzelfall als Entlehnung kenntlich gemacht habe; dass diese Dissertation noch keiner anderen Fakultät oder Universität zur Prfung vorgelegen hat; dass sie noch nicht verffentlicht worden ist sowie, da ich eine solche Veröffentlichung vor Abschluss des Promotionsverfahrens nicht vornehmen werde. Die Bestimmungen dieser Promotionsordnung sind mir bekannt. Die von mir vorgelegte Dissertation ist von Prof. Dr. Michael Kramer betreut worden.

Unterschift:
_____

Datum:
_____

Publications that account for major parts of the thesis

Refereed:

Graikou, E., Verbiest, J. P. W., Osłowski, S., Champion, D. J., Tauris, T. M., Jankowski, F., Kramer, M. *"Limits on the mass, velocity and orbit of PSR J1933−6211"*, 2017, MNRAS, 471, 4579

In preparation:

Graikou, E., Kramer, M., Desvignes, G., Champion, D. J., Porayko N. K., Verbiest, J. P. W. *"The beam geometry of B1913+16"*, To be submitted to MNRAS